Study of metal physical property estimation by analytical models of eddy-current testing

Progress report

2023

Zihan Xia

10901043

content

Acknowledgement

I would like to express my gratitude to Prof, Wuqiang Yang, Prof. Wuliang Yin and Prof. Tony Peyton. They support and care me during my study. I would express my sincere appreciation to Dr. Ruochen Huang who accompanies me and help me to know the meaning of life. I would like to extend my gratitude to my friends Dr. Gang Hu, Mr. Lei Xiong, Mr. Tian Meng and Ms. Xue Bai for their cooperation, and my group members as they help me improve. I would thank my family for their love and support and thank my country and the University of Manchester for study opportunity.

Abstract

Being a contactless non-destructive testing (NDT) technique, eddy-current (EC) testing plays a significant role in the measurement of metallic objects with the great potential of online measurement for various industrial applications. The theoretical study of EC testing mainly involves the forward and inverse problems. The forward problem aims to calculate the EC measurements for given metallic objects, while the inverse problem is to determine the physical properties from the EC measurement. To solve these problems, the analytical models have been extensively investigated due to the explicit expression and facilitation of physical understanding.

This study focuses on the solution to the forward and inverse problems for the physical property estimation of metallic objects. In the forward problem study, the analytical model of metallic object testing is simplified to accelerate computation and derive the functional relationship between the EC measurements and physical properties of objects. In the inverse problem, the key issues of optimization have been investigated, including the combination of optimized variables and the selection of variable initial guesses. These theoretical studies of multi-frequency EC testing and pulsed EC testing have been applied to the physical property analysis and estimation of metallic pipes, rods, spherical shells, bearing balls and plates. The performance of the proposed forward and inverse models has been comprehensively evaluated through numerical simulation and experiments.

1. Introduction

1.1 Research background

Non-destructive techniques are widely applied in the metal industry in order to control and evaluate the material properties without causing damage. The major non-destructive testing techniques include EC, magnetic-particle, liquid penetrant, radiographic, ultrasonic, and visual testing, of which the basic comparison is shown in Table 1.1. The EC technique is frequently utilized for the inspection of metallic materials such as copper, aluminum and stainless steel[1, 2].

Table 1.1 Major NDT methods, a comprehensive overview[3]

Technique	Principle	Advantages	Limitation
Visual testing	Uses reflected or transmitted light from test object that is image with the light sensing device.	Can be inexpensive and simple. Broad scope of uses and benefits.	Only surface conditions can be evaluated. Effective source of illumination required.
Penetrant testing	A liquid containing visible or fluorescent dye is applied to surface and enters discontinuities by capillary action.	Relatively easy and materials are inexpensive. Extremely sensitive, very versatile.	Discontinuities open to the surface only. Surface condition must be relatively smooth and free of contaminants.
Magnetic particle testing	Test part is magnetized, and fine ferromagnetic particle applied to surface, aligning at discontinuity.	Equipment/material usually inexpensive. Highly sensitive and fast compare to PT.	Only surface and a few subsurface discontinuities can be detected. Ferromagnetic.
Radiographic testing	Radiographic film is exposed when radiation passes through the test object. Discontinuities affect exposure.	Provides a permanent record and high sensitivity. Most widely used and accepted volumetric examination.	Limited thickness based on material. Density, orientation of planar discontinuities is critical. Radiation hazard.
Ultrasonic testing	High frequency sound pulses from a transducer propagate through the test material, reflecting at interfaces.	Provide precise, high sensitivity results quickly. Thickness, depth and flaw can be obtained.	No permanent record. Material attenuation, surface finish and contour. Required couplant.
EC testing	Electromagnetic field induced by the coil is changed by the eddy-current in metallic objects, reflecting electromagnetic properties.	Fast response. Non-contact. Thickness, electromagnetic properties and crack detection capability.	Low lift-off tolerance. Material attenuation (thin-skin effect). Electromagnetic shielding.

EC testing enables crack detection in a large variety of metallic materials, either

ferromagnetic or non-ferromagnetic. The advantage of the eddy current method over other techniques is that the inspection can be implemented without any direct physical contact between the sensor and the inspected piece[4-6].

Due to the characteristics (non-contact, fast response, relatively low cost, etc.) of this technique, it has been applied to a variety of inspections and measurement applications. Since the 1950s the role of eddy current testing has developed increasingly in the testing of materials, especially in the railway[7, 8], aircraft[9, 10], steel casting[11, 12] and nuclear industries[13, 14]. Furthermore, the development in eddy current sensors and instruments over the last decades enables the biomedical investigation, e.g., human brain pathophysiology[15].

The conventional EC testing system consists of the sensor, data acquisition system and host PC, as shown in Fig. 1.1. The sensor excites the electromagnetic field and receives the frequency-dependent secondary field caused by the measured objects, which is controlled and adjusted by the data acquisition system, while the host PC analyzes the measurement signal to calculate the physical properties of the measured objects.

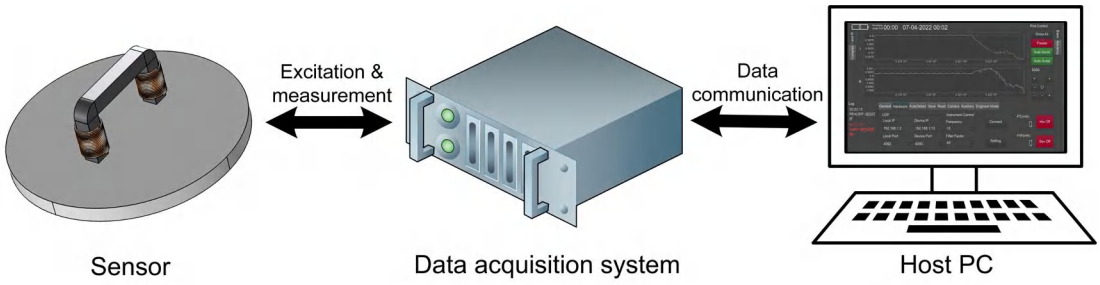

Figure. 1.1 Schematic of EC testing system

The principle of the EC technique is based on the electromagnetic theory which describes the interaction between the magnetic field and measured objects[13, 14, 16]. The induced eddy currents in the objects influence the electromagnetic field in the measuring space, thereby causing the variation of measurement signal which reflects the physical properties of objects, e.g., dimension, electromagnetic properties and crack, as shown in Fig. 1.2.

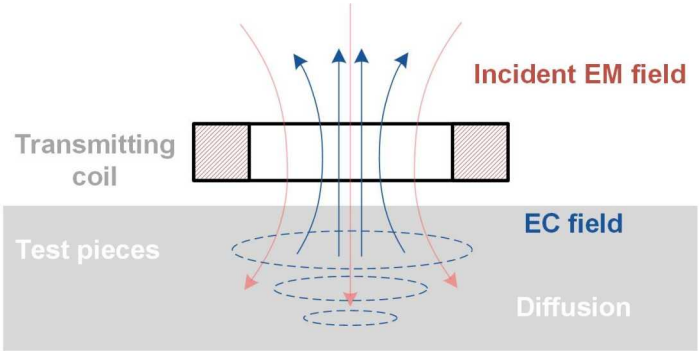

Figure. 1.2 Electromagnetic field of EC testing

1.2 Recent development of eddy-current computation

In the EC testing scenario, the forward and inverse problems are two major theoretical issues, which bridge the gap between the frequency-dependent electromagnetic field (measurements) and object properties. The representative methods to solve the forward and inverse problems are shown in Fig. 1.3.

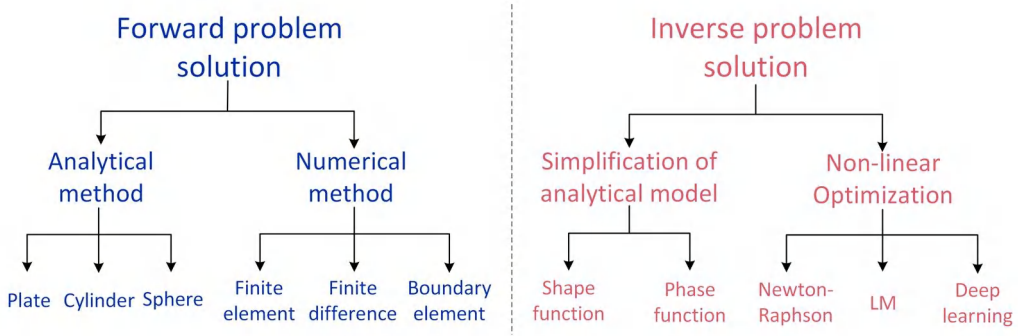

Figure 1.3 Main methods of EC computation

The forward problem involves solving the Helmholtz (diffusion) equation, derived from the Maxwell equation neglecting the displacement current, which describes the electromagnetic field in the EC testing condition. The numerical method can be categorized into the finite element and integral equation methods.

The finite element method (FEM) is frequently adopted in electromagnetic computing and has been explored for the calculation of curved plates[17], ferromagnetic modeling[18, 19] and conductive defect simulation[20]. Two common approaches are the $\boldsymbol{H}-\psi$ and $\boldsymbol{A}-\phi$ models[21]. Since the measurement region, usually several times larger than the sensor region, is required to be discretized into a variety of tiny mesh elements where the magnetic field is calculated simultaneously, the calculation of the model is time-consuming, especially for the 3-D model with complex geometry. The recent studies focus on the acceleration of calculation, which

can be realized through the combined FEM-BEM method[22, 23], developing a new shape function[24], optimizing the initial guess of each computational step[25] and strategy to update the perturbed field around the crack region separately[26, 27]. In addition, the commercial-grade software, e.g., Ansys Maxwell and COMSOL, makes the method convenient to implement.

The boundary element method (BEM) has a long history in engineering analysis applications[28]. Compared with FEM, only active regions require discretization in BEM. Instead of a system of equations where the unknown quantities are operated on by differential operators, the unknown quantities are operated on by integral operators[29]. According to Green's function method, the calculation of magnetic field in the presence of the crack can be achieved through the integral formulation, volume integral[30] for the scattered field. The direct and reflected field can be calculated due to the perturbance of the crack and meets the continuity for the boundary[24, 31, 32]. Q. Zhao et al. derive the magnetic polarization tensor from the scattered field calculated through boundary integration to estimate the properties of cylindrical objects[33]. M. Pham and A. Peyton proposed the BEM model to solve the forward problem of electromagnetic tomography (EMT)[34].

The analytical method can provide explicit solutions bridging the gap between the electromagnetic field and measurement configuration, which benefits solving both the forward and inverse problems. Dodd and Deeds (D&D) have initially derived the model for planar, cylindrical and spherical objects encircled by the coaxial coils, according to the separation of variables (Fourier) method[35-37]. The D&D model is axisymmetric, which indicates that the magnetic vector potential can be replaced by a scalar potential for simplification. For the model of arbitrary shaped coil above these objects, T. Theodoulidis, E. Kriezis et al introduced the second-order vector potential (hertz vector) to calculate the electromagnetic field[38-41], by assuming that the field can be separated into the transverse and longitudinal components described by two independent scalars. Compared with FEM and BEM, the analytical method provides the explicit expression of electromagnetic field, while the calculation is more accurate and computationally efficient without the discretization procedure.

To accelerate the calculation of analytical solution, a variety of studies have been performed. T. Theodoulidis and E. Kriezis proposed the truncated region eigenfunction expansion (TREE) method which only considers the computational region around the sensor[42, 43]. W. Yin et al. simplified the analytical solution of

planar structure model by characterizing the influence of test piece using its feature spatial frequency[25, 44]. Furthermore, R. Huang et al. discovered the relationship between the spatial frequency and corresponding cylindrical harmonics then subsequently proposed the finite region eigenfunction expansion (FREE) method for the finite-dimension planar model[45-47]. The extensive research of planar model facilitates the plate measurement[48-51], to some extent. Nevertheless, the analytical models of various geometric structures, including cylindrical[52, 53] and spherical models[49, 54], in different characteristics are still required to be investigated comprehensively. This could support the metallic measurement in numerous applications while better the understanding of scholars and engineers regarding the EC phenomenon.

The inverse problem of EC testing, for object property estimation, can be solved through the simplified model and non-linear optimization method. For the analytical solution of the planar model simplified by the feature spatial frequency, the influences of plate properties and sensor lift-off, distance between the sensor and plate affecting the feature spatial frequency, can be represented separately. Through the simplification of shape function, sensor term, using the elementary function, the lift-off distance and related feature spatial frequency can be estimated, which is then employed for the estimation of plate property[55, 56]. Aiming at the non-linear optimization problem, the New-Raphson and Levenberg–Marquardt (LM) algorithms are frequently adopted[57-59]. Since the LM algorithm interpolates between the New-Raphson and gradient descent methods, it reaches the convergence point slower than the New-Raphson method for a reasonable starting point. M. Lu et al. proposed the estimation method of plate properties based on the Newton Rapson method[60]. X. Chen et al. proposed the wall thickness estimation method for pipe measurement by solving the inverse problem of pulsed-eddy current (PEC) testing[61]. It has been discovered that the influences of conductivity and permeability on inductance measurement are strongly coupled[62, 63], which makes the variable updating process is unstable and it is difficult to optimize the properties simultaneously. There is still some space to elevate the performance of the inverse algorithm in terms of stability and computation efficiency.

1.3 Contributions

In this report, the main contributions are summarized as follows.

- The recent developments in EC computational models, systems, algorithms, and

measurement approaches for planar structures have been summarised in the review.

- The Dodd and Deeds (DD) model of pipes and spherical shells measured by coaxial coils is approximated by an elementary function. Due to the simple nature of the elementary function, the Jacobian matrix can be evaluated much more efficiently. Accordingly, a fast Newton-Raphson method-based optimization approach is developed for object property estimation.
- The Dodd and Deeds (DD) model of rods and plates measured by coaxial coils is approximated to derive the functional relationship between the object properties and coil inductance, to obtain the initial guesses of properties for optimization. The method decreases the influence of the local minimum issue on optimization.
- The variable combinations that severely affect the stability of simultaneous optimization of multiple object properties have been investigated for pipes, rods and spherical shells, according to the proposed indices of singular value feature and the variance-based Sobol index.
- The analytical model for fast computation of the pulsed EC measuring single-layer plates have been proposed through the inverse Laplace transform and model approximation. The proposed method reveals the diffusion time of EC in planar structures with large radial dimensions and is much more efficient than the Fourier transform-based method.

1.4 Organization of the report

This report includes the following sections.

Section 1 presents the basic introduction of EC computation, including the background, recent development of theoretical studies and research outline.

Section 2 introduces the theoretical basis of the analytical method for the calculation of planar, cylindrical and spherical objects encircled by the coaxial coils. Furthermore, the Newton-Raphson method is introduced for the physical property estimation.

Section 3 presents a review of recent studies of planar structure measurement.

Section 4 describes the fast estimation of metallic pipe radius and permeability using a simplified analytical solution.

Section 5 provides the rod radius and permeability estimation.

Section 6 shows the spherical shell radius and thickness estimation with a simplified analytical model.

Section 7 illustrates the bearing ball radius and permeability estimation through optimization.

Section 8 presents the physics-guided deep learning for plate permeability estimation with single to multiple frequency transformation.

Section 9 provides the thickness and permeability estimation of plates by triple-frequency eddy-current testing with probe lift-off.

Section 10 suggests the through thickness inspection of layered magnetic material using pulsed eddy current testing.

Section 11 draws the conclusion of this report and suggests future works.

2. Supporting theory

The supporting theory consists of the forward model to calculate the inductance and electromagnetic field measurements and inverse model to estimate the object physical properties. The forward model adopts the analytical solution for the measurement of planar, cylindrical and spherical objects, while in inverse model, the basic Newton-Raphson algorithm is introduced for the multi-variable optimization.

2.1 Analytical solution of coaxial plate and coil model

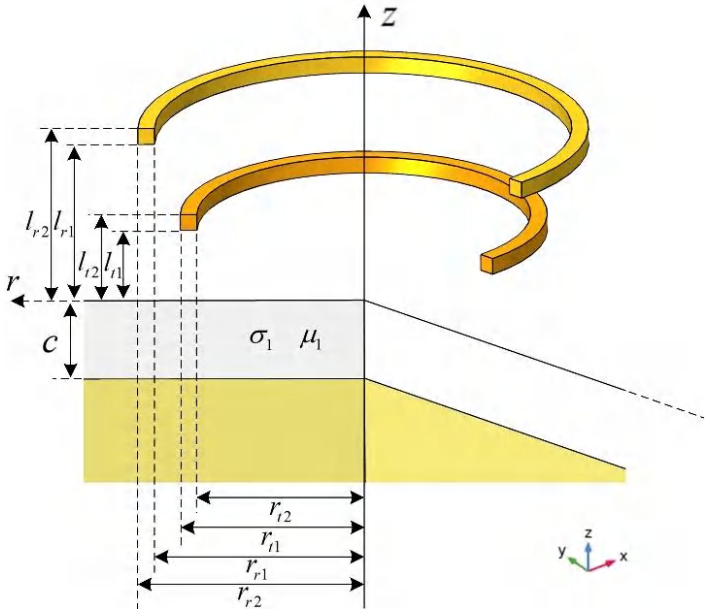

Figure 2.1 Metallic plate measured by the sensor composed of transmitting and receiving coils.

For the single-layered plate model measured by the sensor consisting of a transmitting and receiving coil, as shown in Fig. 2.1, according to the Dodd and Deeds model, the complex mutual inductance of the receiving coil caused by the metallic plate can be calculated by

$$\Delta \mathrm{L}(\omega) = \frac{\Delta Z}{\mathrm{j}\omega}$$

$$= \frac{\pi \mathrm{N_t N_r} \mu_0}{(\mathrm{l_{t2}} - \mathrm{l_{t1}})(\mathrm{l_{r2}} - \mathrm{l_{r1}})(\mathrm{r_{t2}} - \mathrm{r_{t1}})(\mathrm{r_{r2}} - \mathrm{r_{r1}})} \int_0^{\infty} \frac{J(\mathrm{r_{t2}}, \mathrm{r_{t1}}) J(\mathrm{r_{r2}}, \mathrm{r_{r1}})}{\alpha^6} \left(\mathrm{e}^{-\alpha \mathrm{l_{t1}}} - \mathrm{e}^{-\alpha \mathrm{l_{t2}}}\right)\left(\mathrm{e}^{-\alpha \mathrm{l_{r1}}} - \mathrm{e}^{-\alpha \mathrm{l_{r2}}}\right)$$

$$\times \phi(\alpha) \mathrm{d}\alpha \tag{2.1.1}$$

$$\phi(\alpha) = \frac{(\alpha_1 + \mu\alpha)(\alpha_1 - \mu\alpha) - (\alpha_1 + \mu\alpha)(\alpha_1 - \mu\alpha) e^{2\alpha_1 c}}{-(\alpha_1 - \mu\alpha)(\alpha_1 - \mu\alpha) + (\alpha_1 + \mu\alpha)(\alpha_1 + \mu\alpha) e^{2\alpha_1 c}} \tag{2.1.2}$$

$$J(r_{t2}, r_{t1}) = \int_{\alpha r_{t1}}^{\alpha r_{t2}} \tau J_1(\tau)\, \tau \tag{2.1.3}$$

where ω is the angular frequency of excitation, α denotes the spatial frequency, $\alpha_1 = \sqrt{\alpha^2 + j\omega\mu\sigma}$, $\mathrm{N_t}$ and $\mathrm{N_r}$ are turns of transmitting and receiving coils,

respectively.

The inductance could be calculated through numerical integration, whereas it is time-consuming. The TREE method proposed by T. Theodoulidis and E. Kriezis recasts the expression as sums rather than integrals, i.e.

$$\Delta L(\omega) = \frac{\pi N_t N_r \mu_0}{(l_{t2}-l_{t1})(l_{r2}-l_{r1})(r_{t2}-r_{t1})(r_{r2}-r_{r1})} \sum_{\alpha_i} \frac{J(r_{t2},r_{t1})J(r_{r2},r_{r1})}{\alpha_i^{\,6}} (e^{-\alpha_i l_{t1}} - e^{-\alpha_i l_{t2}})(e^{-\alpha_i l_{r1}} - e^{-\alpha_i l_{r2}})\phi(\alpha_i) \quad (2.1.4)$$

where α_i satisfies the condition on the truncated boundary, $J_1(\alpha_i h) = 0$, $i \in \{1,2,\ldots,n_\alpha\}$, which indicates that the electromagnetic field vanishes at the boundary $r = h$.

The series form accelerates the inductance calculation while guaranteeing the accuracy if the quantity of eigenvalues is appropriate. It can be seen from equation (2.1.4) that, the sensor structure and plate properties determine the inductance value, and the influence can be evaluated separately by rewriting it as

$$\Delta L(\omega) = \sum_{\alpha_i} A(\alpha_i)\phi(\alpha_i) \quad (2.1.5)$$

$$A(\alpha_i) = \frac{\pi N_t N_r \mu_0}{(l_{t2}-l_{t1})(l_{r2}-l_{r1})(r_{t2}-r_{t1})(r_{r2}-r_{r1})} \frac{J(r_{t2},r_{t1})J(r_{r2},r_{r1})}{\alpha_i^{\,6}} (e^{-\alpha_i l_{t1}} - e^{-\alpha_i l_{t2}})(e^{-\alpha_i l_{r1}} - e^{-\alpha_i l_{r2}}) \quad (2.1.6)$$

where $A(\alpha_i)$ is termed as the shape function and $\phi(\alpha_i)$ is the phase function/term related to the plate properties.

The analytical solution can be employed for the inductance calculation in the time domain through the inverse Fourier transform of the frequency spectrum, which is frequently investigated in PEC testing. For the receiving unit of the TMR sensor (Hall sensor or GMR sensor), as shown in Fig. 2.2, the response magnetic flux density in the frequency domain can be calculated by

$$\Delta B_z(\omega) = \frac{2\mu_0 i_0(\omega)}{r_0(c_2-c_1)} \sum_{\alpha_i} \frac{J(r_2,r_1)J_1(\alpha_i r_0)}{\alpha_i^5[hJ_0(\alpha_i h)]} (e^{\alpha_i c_2} - e^{\alpha_i c_1})(e^{-\alpha_i z_1} - e^{-\alpha_i z_2}) e^{-\alpha_i(c_1+c_2)} \phi(\alpha_i) \quad (2.1.7)$$

Furthermore, the magnetic field signal in the time domain can be calculated by

$$\Delta B_z(t) = \frac{2\mu_0}{r_0(c_2-c_1)} \sum_{\alpha_i} \frac{J(r_2,r_1)J_1(\alpha_i r_0)}{\alpha_i^5[hJ_0(\alpha_i h)]} (e^{\alpha_i c_2} - e^{\alpha_i c_1})(e^{-\alpha_i z_1} - e^{-\alpha_i z_2}) e^{-\alpha_i(c_1+c_2)} \int_{-\infty}^{-\infty} \phi(\alpha_i) i_0(\omega) d\omega \quad (2.1.8)$$

$$i_0(\omega) = \int_{-\infty}^{-\infty} i_0(t) e^{-i\omega t} dt \quad (2.1.9)$$

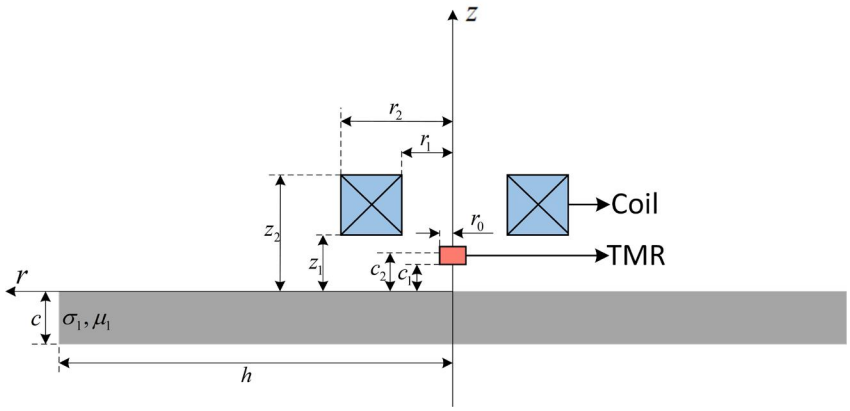

Figure 2.2 Metallic plate measured using coaxial transmitting coil and TMR sensor

2.2 Analytical solution of coaxial pipe and coil model

The analytical solution of infinite long metallic pipe can be obtained from the governing equation, through the separation of variables method. A typical model structure is shown in Fig. 2.3. According to the research on analytical solution for cylindrical object measurement[35], the inductance change due to the measured objects can be expressed as

$$\Delta L = k_L \int_0^{\infty} S(\alpha) L_s(\alpha) d\alpha \tag{2.2.1}$$

$$\begin{aligned} S(\alpha) = \frac{1}{bD(\alpha)K_1(\alpha b)} \{ & K_1(\alpha_2 b)\left[\beta_2 I_1(\alpha_1 a) I_0(\alpha_2 a)\right. \\ & \left. - \beta_1 I_1(\alpha_2 a) I_0(\alpha_1 a)\right] + I_1(\alpha_2 b)\left[\beta_1 K_1(\alpha_2 a) I_0(\alpha_1 a)\right. \\ & \left. + \beta_2 K_0(\alpha_2 a) I_1(\alpha_1 a)\right]\} - \frac{I_1(\alpha b)}{K_1(\alpha b)} \end{aligned} \tag{2.2.2}$$

$$\begin{aligned} D(\alpha) = & \left[\beta_2 K_0(\alpha_2 b) K_1(\alpha b) - \alpha K_0(\alpha b) K_1(\alpha_2 b)\right] \\ & \times \left[\beta_1 I_1(\alpha_2 a) I_0(\alpha_1 a) - \beta_2 I_1(\alpha_1 a) I_0(\alpha_2 a)\right] \\ & + \left[\beta_2 K_0(\alpha_2 a) I_1(\alpha_1 a) + \beta_1 K_1(\alpha_2 a) I_0(\alpha_1 a)\right] \\ & \times \left[\alpha I_1(\alpha_2 b) K_0(\alpha b) + \beta_2 I_0(\alpha_2 b) K_1(\alpha b)\right] \end{aligned} \tag{2.2.3}$$

$$L_s(\alpha) = K^2(r_2, r_1) f \cos(\alpha) / \alpha^6 \tag{2.2.4}$$

$$K(r_2, r_1) = \int_{\alpha r_1}^{\alpha r_2} \alpha r K_1(\alpha r) d\alpha r \tag{2.2.5}$$

$$\begin{aligned} f\cos(\alpha) = & 2\cos(\alpha d) - \cos\left(\alpha(l_2 - l_1 + d)\right) \\ & - \cos\left(\alpha(l_1 - l_2 + d)\right) \end{aligned} \tag{2.2.6}$$

where the phase function $S(\alpha)$ is determined by the pipe properties and frequency, the shape function $L_s(\alpha)$ relates to the sensor configuration, $k_L = 2N^2\mu_0 r_0 / \left[(r_2 - r_1)^2 (l_2 - l_1)^2\right]$, N is the turns of coil, μ_0 is the vacuum permeability,

α denotes the eigenvalue/spatial frequency, $\alpha_1=\beta_1=\alpha$, $\alpha_2=\sqrt{\alpha^2+j\omega\mu_0\mu_r\sigma}$, $\beta_2=\alpha_2/\mu_r$, $I(\cdot)$ and $K(\cdot)$ are modified Bessel functions of the first and the second kind, respectively, other parameters correspond to the dimensions of sensor.

According to the TREE method, it is computationally effective to employ the series form rather than the integral expression. Particularly, the eigenvalues are determined by $\cos(\alpha_k h)=0$, $k=1,2,...,n_\alpha$, h denotes the truncated longitudinal calculation region and n_α is the quantity of eigenvalues, which means $\alpha_k=(k\pi+\pi/2)/h$. In this way, equation (2.2.1) becomes

$$\Delta L \approx k_L \sum_k S(\alpha_k) L_s(\alpha_k) \tag{2.2.7}$$

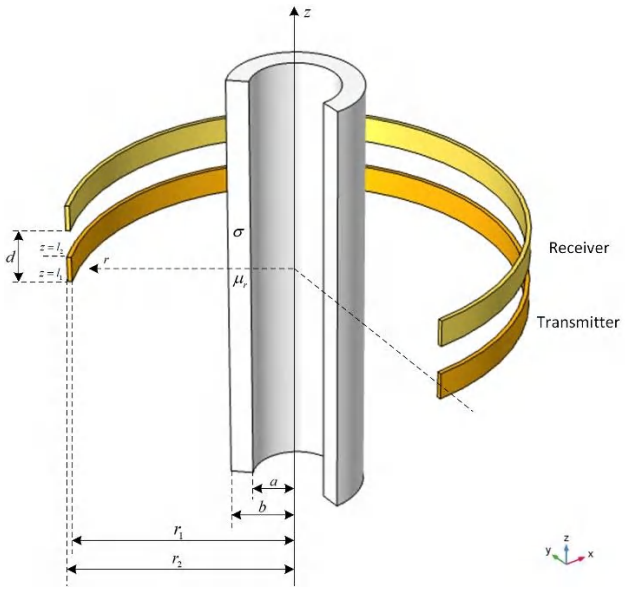

Figure. 2.3 Induction coils encircling a coaxial metallic pipe

2.3 Analytical solution of coaxial sphere and coil model

The analytical solution of the double-layered sphere, shown in Fig. 2.4, can derived using the separation of variables method. According to the research on the analytical solution of spherical model[64], the inductance change due to the measured objects can be expressed as

$$\Delta L = \sum_n \phi_n K_n \tag{2.3.1}$$

$$\phi_n = \frac{T_1\left\{i_n(\alpha_2 b)[(n+1)\mu_2 - 1] - \alpha_2 b i_n^{'}(\alpha_2 b)\right\} + T_2\left\{k_n(\alpha_2 b)[(n+1)\mu_2 - 1] - \alpha_2 b k_n^{'}(\alpha_2 b)\right\}}{T_1\left\{i_n(\alpha_2 b)[n\mu_2 + 1] - \alpha_2 b i_n^{'}(\alpha_2 b)\right\} + T_2\left\{k_n(\alpha_2 b)[n\mu_2 + 1] - \alpha_2 b k_n^{'}(\alpha_2 b)\right\}}$$

$$T_1 = \left\{\frac{i_n(\alpha_1 a)}{\mu_2}\left[k_n(\alpha_2 a) + \alpha_2 a k_n^{'}(\alpha_2 a)\right] - \frac{k_n(\alpha_2 a)}{\mu_1}\left[i_n(\alpha_1 a) + \alpha_1 a i_n^{'}(\alpha_1 a)\right]\right\} \Big/ D_n$$

$$T_2 = \left\{\frac{i_n(\alpha_2 a)}{\mu_1}\left[i_n(\alpha_1 a) + \alpha_1 a i_n^{'}(\alpha_1 a)\right] - \frac{i_n(\alpha_1 a)}{\mu_2}\left[i_n(\alpha_2 a) + \alpha_2 a i_n^{'}(\alpha_2 a)\right]\right\} \Big/ D_n$$

$$D_n = \frac{\alpha_2 a}{\mu_2}\left[i_n(\alpha_2 a) k_n^{'}(\alpha_2 a) - i_n^{'}(\alpha_2 a) k_n(\alpha_2 a)\right]$$

(2.3.2)

$$K_n = \frac{\pi \mu_0 N_{\mathrm{Tx}} N_{\mathrm{Rx}}}{(l_{t2} - l_{t1})(l_{r2} - l_{r1})(r_{t2} - r_{t1})(r_{r2} - r_{r1})} \frac{b^{2n+1}}{n(n+1)} P_{n,\mathrm{Tx}} P_{n,\mathrm{Rx}} \tag{2.3.3}$$

$$P_{n,\mathrm{Tx}} = \int_{S(\mathrm{Tx})} \frac{\sin\theta_o P_n^1(\cos\theta_o)}{r_o^n} dS \tag{2.3.4}$$

$$P_{n,\mathrm{Rx}} = \int_{S(\mathrm{Rx})} \frac{\sin\theta_o P_n^1(\cos\theta_o)}{r_o^n} dS \tag{2.3.5}$$

where the phase function ϕ_n is determined by the pipe properties and frequency, the shape function K_n relates to the sensor configuration, $i_n(\cdot)$ and $k_n(\cdot)$ are modified spherical Bessel functions of the first and the second kind, respectively, $P_n^1(\cdot)$ is the associated Legendre polynomials, $S(\mathrm{Tx})$ and $S(\mathrm{Rx})$ represent the cross-sectional area of transmitting and receiving coils, and other parameters correspond to the dimensions of sensor.

Noted that the integral in equation (2.3.4) and (2.3.5) are usually calculated through numerical integration, e.g. the Legendre integral. Considering the rectangular cross-sectional coil, equation (2.3.4) can be integrated in the spherical coordinates as

$$P_{n,\mathrm{Tx}} = \begin{cases} \int_{\theta_A}^{\theta_B} \frac{\sin\theta_0 P_n^1(\cos\theta_0)}{n-2}\left(\frac{\sin\theta_0}{r_{r1}}\right)^{n-2} d\theta_0 + \int_{\theta_B}^{\theta_C} \frac{\sin\theta_0 P_n^1(\cos\theta_0)}{n-2}\left(\frac{\cos\theta_0}{l_{r1}}\right)^{n-2} d\theta_0 \\ + \int_{\theta_C}^{\theta_D} \frac{\sin\theta_0 P_n^1(\cos\theta_0)}{n-2}\left(\frac{\sin\theta_0}{r_{r2}}\right)^{n-2} d\theta_0 + \int_{\theta_D}^{\theta_A} \frac{\sin\theta_0 P_n^1(\cos\theta_0)}{n-2}\left(\frac{\cos\theta_0}{l_{r2}}\right)^{n-2} d\theta_0 & n \neq 2 \\ \int_{\theta_A}^{\theta_B} \sin\theta_0 P_n^1(\cos\theta_0) \log\frac{r_{r1}}{\sin\theta_0} d\theta_0 + \int_{\theta_B}^{\theta_C} \sin\theta_0 P_n^1(\cos\theta_0) \log\frac{l_{r1}}{\cos\theta_0} d\theta_0 \\ + \int_{\theta_C}^{\theta_D} \sin\theta_0 P_n^1(\cos\theta_0) \log\frac{r_{r2}}{\sin\theta_0} d\theta_0 + \int_{\theta_D}^{\theta_A} \sin\theta_0 P_n^1(\cos\theta_0) \log\frac{l_{r2}}{\cos\theta_0} d\theta_0 & n = 2 \end{cases}$$

where θ_A, θ_B, θ_C and θ_D indicate the four vertices of coil cross-section from the

upper left corner in a clockwise direction.

Compared with the computation of the phase function, the numerical integration of the shape function is relatively time-consuming, whereas the shape function is required to be computed only once if the dimensions of coils are known and the coil position can be obtained beforehand.

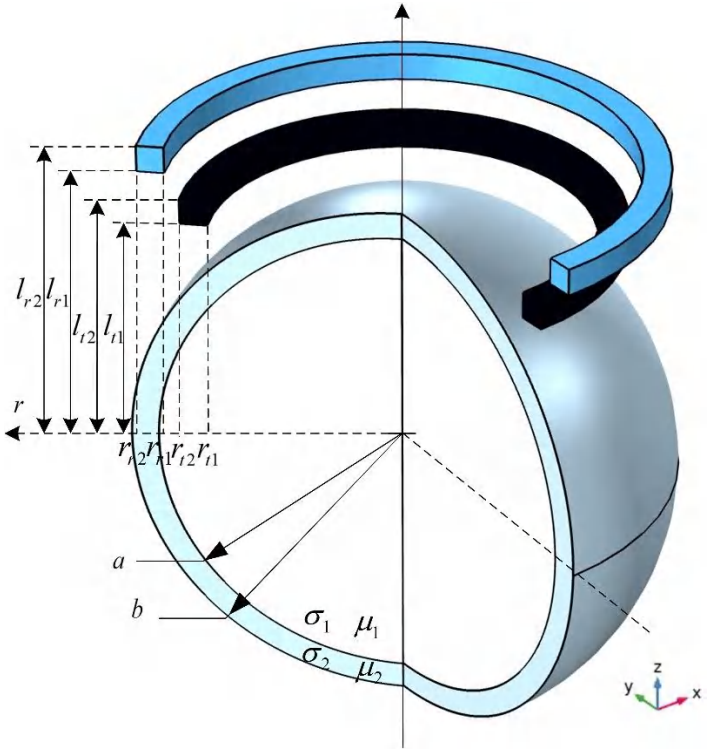

Figure. 2.4 Induction coils encircling a coaxial metallic double-layered sphere

2.4 Electromagnetic property estimation through optimization

The inverse problem is to determine the pipe properties from the frequency sweeping inductance/ inductance spectrum, which is realized by minimizing the distance between the calculated and measured inductance spectra based on the Newton-Raphson method.

A least-squares problem is defined as the objective function of optimization.

$$\min_{\mathbf{v}} f = \frac{1}{2}\left\|\Delta\mathbf{L}(\mathbf{v}) - \Delta\mathbf{L}_{\mathrm{m}}\right\|_2^2 \tag{2.4.1}$$

where $\mathbf{v} \in \mathbb{R}^{n_v \times 1}$ (n_v denotes the quantity of variables), $\|\cdot\|_2^2$ represents the ℓ_2-norm , $\Delta\mathbf{L}(\mathbf{v})$ and $\Delta\mathbf{L}_{\mathrm{m}}(\mathbf{v}) \in \mathbb{C}^{n_f \times 1}$ are calculated and measured inductance, respectively, which are written as $\mathbf{L}$ and $\mathbf{L}_{\mathrm{m}}$ in the following section for simplification (n_f is the quantity of recorded frequency points).

The local minimum $\mathbf{v}^*$ of optimization problem satisfies

$$\nabla f(\mathbf{v}^*) = \mathbf{0} \tag{2.4.2}$$

where $[\nabla f]_{i,j} = \partial f_i / \partial v_j$ and $\mathbf{0} \in \mathbb{R}^{n_v \times 1}$ is a zero vector.

Given a reference point $\mathbf{v}_r$ adjacent to $\mathbf{v}^*$, equation (2.4.2) can be approximated by the Taylor series as,

$$\nabla f(\mathbf{v}^*) = \nabla f(\mathbf{v}_r) + \nabla\nabla f(\mathbf{v}_r)\Delta\mathbf{v} \tag{2.4.3}$$

where $\Delta\mathbf{v} = \mathbf{v}^* - \mathbf{v}_r$ and $\nabla\nabla f(\mathbf{v}_r)$ denotes the Hessian matrix evaluated at $\mathbf{v}_r$ which is usually approximated by

$$\nabla\nabla f(\mathbf{v}_r) \approx [\nabla f(\mathbf{v}_r)]^{\mathrm{H}} \nabla f(\mathbf{v}_r) \tag{2.4.4}$$

where the superscript H denotes the conjugate transpose, and $\mathbf{H}(\mathbf{v}_r) = [\nabla f(\mathbf{v}_r)]^{\mathrm{H}} \nabla f(\mathbf{v}_r)$ is employed in the following analysis.

Furthermore, the first-order partial derivative of function f is

$$\begin{aligned} \nabla f(\mathbf{v}_r) &= \left[\nabla \mathbf{L}(\mathbf{v}_r)\right]^{\mathrm{H}} \left[\mathbf{L}(\mathbf{v}_r) - \mathbf{L}_{\mathrm{m}}\right] \\ &= \mathbf{S}(\mathbf{v}_r)^{\mathrm{H}} \left[\mathbf{L}(\mathbf{v}_r) - \mathbf{L}_{\mathrm{m}}\right] \end{aligned} \tag{2.4.5}$$

where $\mathbf{S} \in \mathbb{C}^{n_f \times n_v}$ is the sensitivity/Jacobian matrix, a linearized relationship between the variation of inductance spectrum and pipe properties, which can be calculated by both the original and approximate models.

Combining equation (2.4.2)-(2.4.5), one can obtain the variable difference, i.e.,

$$\Delta\mathbf{v} = -\left[\mathbf{S}(\mathbf{v}_r)^{\mathrm{H}} \mathbf{S}(\mathbf{v}_r)\right]^{-1} \mathbf{S}(\mathbf{v}_r)^{\mathrm{H}} \left[\mathbf{L}(\mathbf{v}_r) - \mathbf{L}_{\mathrm{m}}\right] \tag{2.4.6}$$

This is the variable updating form of the Newton-Raphson method, of which the optimization procedure is illustrated in Algorithm 1, providing the starting point $\mathbf{v}_1$ and residual threshold value ϵ. In addition, the computational complexity of this procedure is $\mathrm{O}(n_\alpha n_f n_i)$, n_i is the iterative steps.

Algorithm 1 Optimization of pipe properties

Input: $\mathbf{v}^1$, ϵ and n_i
Output: $\mathbf{v}$

initialize: Set $\mathbf{L}^1 = \mathbf{L}(\mathbf{v}^1)$
for $k = 1, 2, ..., n_i$ **do**
  $\mathbf{S}^k = \partial \mathbf{L}^k / \partial \mathbf{v}^k$
  $\mathbf{v}^{k+1} = \mathbf{v}^k - [(\mathbf{S}^k)^{\mathrm{T}} \mathbf{S}^k]^{-1} (\mathbf{S}^k)^{\mathrm{T}} (\mathbf{L}^k - \mathbf{L}_{\mathrm{m}})$
  $\mathbf{L}^{k+1} = \mathbf{L}(\mathbf{v}^{k+1})$
  if $\left\|\mathbf{L}^{k+1} - \mathbf{L}_{\mathrm{m}}\right\|_2^2 \leq \epsilon$ **then**
    Break;
  end if
end for

3. Eddy current measurement for planar structures

sensors

MDPI

Review

Eddy current measurement for planar structures

Zihan Xia[1], Ruochen Huang[2], Ziqi Chen[1], Kuohai Yu[1], Zhijie Zhang[3], J R Salas-Avila[4], and Wuliang Yin[1,*]

[1] School of Electrical and Electronic Engineering, University of Manchester, Manchester M60 1QD, UK; zihan.xia-5@postgrad.manchester.ac.uk (Z. X.); ziqi.chen@manchester.ac.uk (Z. C.); kuohai.yu@student.manchester.ac.uk (K. Y.);
[2] College of Electrical Engineering and Automation, Fuzhou University, Fuzhou 350108, China; ruochen_huang@fzu.edu.cn (R. H.)
[3] School of Instrument and Electronics, North University of China, Taiyuan 030051, China; zhangzhijie@nuc.edu.cn (Z. Z.)
[4] MAIERIC Ltd, Manchester, UK, M15 6SZ; jricardo.salas@gmail.com (J. R. S. A.)
* Correspondence: wuliang.yin@manchester.ac.uk (W. Y.)

Abstract: Eddy current (EC) testing has become one of the most common techniques for measuring metallic planar structures in various industrial scenarios such as infrastructures, automotive, manufacturing, and chemical engineering. There has been significant progress in measuring the geometry, electromagnetic properties, and defects of metallic planar structures based on electromagnetic principles. This review summarises the recent developments in EC computational models, systems, algorithms, and measurement approaches for planar structures. First, the computational models including analytical models, numerical methods and plate property estimation algorithms are introduced. Subsequently, the impedance measurement system and probes are presented. In plate measurements, sensor signals are sensitive to probe lift-off, and various algorithms for reducing the lift-off effect are reviewed. These approaches can be used for measuring thickness and electromagnetic properties of planar structures. Furthermore, defect detection for metallic plates is also discussed.

Keywords: eddy current testing; electromagnetic induction; planar structure; theoretical calculation; measurement

Citation: Xia, Z.; Huang, R.; Chen, Z.; Yu, K.; Zhang, Z.; Salas-Avila, J. R.; Yin, W. Eddy Current Measurement for Planar Structures. *Sensors* **2022**, *22*, x. https://doi.org/10.3390/xxxxx

Academic Editor(s): Firstname Lastname

Received: 29 September 2022
Accepted: 28 October 2022
Published: date

1. Introduction

Measuring the defect and physical properties (electromagnetic properties, dimensions *etc.*) of planar structure is important in a range of technological applications, for example, coating surface treatments [1] and quality inspections [2, 3]. Inspections during the manufacturing process and on-site monitoring of steel plates is key to the safety and efficiency of industrial applications in railway, aircraft and nuclear facilities [4-9]. Furthermore the measurement of nano-scale copper film thickness guarantees product quality of the integrated circuit manufacturing process in the semiconductor industry [10, 11] and chemical mechanical planarization process [12]. As one of the common non-destructive testing (NDT) techniques, for decades, EC testing has been intensively investigated for measuring planar structures, due to its characteristics of being non-invasive, contactless, fast response, and relatively low cost. The technique employs a time-varying magnetic field excited by coils covering the region of interest (ROI) in conductive structures. The eddy current is induced in the measured structures by an excitation magnetic field. Variations in the magnetic field caused by the eddy current contains the physical properties and geometric information of the ROI, which can be detected and employed for structural analysis.

Forward and inverse problems are the primary theoretical issues of EC testing. The forward problem aims to calculate the frequency-dependent measurements for given metallic objects, while the inverse problem determines the physical properties of the object from the frequency-dependent measurement. The forward problem can be solved by analytical and numerical methods. The analytical methods include the Dodd and Deeds model [13, 14] for symmetric geometry and the second-order vector potential (SOVP) method, also known as the hertz method, for asymmetric geometry [15]. The numerical methods cover the finite difference method, finite element method (FEM) and boundary element method (BEM). Recent studies on analytical models of plate measurement have focused on the solution to complex structures, for example, finite-size plates [16], and model simplification that facilitates the direct estimation of plate properties [17]. The FEM method has been implemented for complex geometry and anisotropic materials [18-21]. In addition, the 3-D models of FEM have been accelerated for defect plates [22, 23]. In the inverse problem, the plate properties can be estimated according to the linearized simplified analytical model with lift-off compensation strategy [24] and multivariable optimization algorithms [25, 26]. These methods deepen the understanding of the phenomenon in EC testing and account for the relationships between the measurement signals and plate properties.

The implementation of EC testing consists of a data acquisition system and probe which are used to obtain the measurement signal. The customised and commercial impedance analysers both enable the measurement of mutual inductance between coils and other magnetic field variables. In general, EC probes designed for plate property estimation and defect scanning contain transmitting (Tx) coils and receiving (Rx) elements. According to the required EM field for specific applications, the structure and dimensions of Tx coils can be selected and optimized. Furthermore, coils or magnetic field sensors are usually chosen as the Rx elements depending on the induced EM field by test pieces.

As compared with previous review articles on eddy-current testing [27-30], this work investigates recent improvements of multi-frequency EC testing in plate measurement, in terms of computational models and measurement system. In addition, the key issues affecting measurement signals, *i.e.* lift-off and tilt effect of the probe, are discussed theoretically.

The arrangement of the rest of the paper is as follows: In Section 2, we describe the computational methods of EC testing, including the solution of the forward problem by the analytical and FEM methods and the inverse problem by the optimization approach; In Section 3, we illustrate the recently developed impedance measurement systems with relevant calibration strategies and characteristics of EC probes for plate measurement; in Section 4, we explain the lift-off compensation methods and defect scanning applications.

2. Computational models

2.1. Analytical models

2.1.1. Dodd and Deeds and associated simplified models

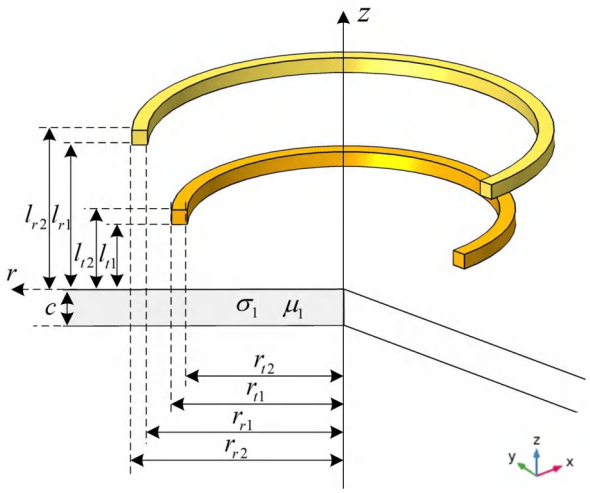

Figure 1. Metallic plate measured using probe with transmitting and receiving coils.

For the single-layered plate model placed near a probe consisting of Tx and Rx coils, as shown in Figure 1, according to the Dodd and Deeds model [13, 14], the complex mutual inductance [31], referred to as inductance hereinafter, between the Tx and the Rx coils caused by the metallic plate can be calculated by

$$\Delta L(\omega) = \frac{\Delta Z}{j\omega}$$

$$= \frac{\pi N_t N_r \mu_0}{(l_{t2}-l_{t1})(l_{r2}-l_{r1})(r_{t2}-r_{t1})(r_{r2}-r_{r1})} \int_0^{\infty} \frac{J(r_{t2},r_{t1})J(r_{r2},r_{r1})}{\alpha^6} (e^{-\alpha l_{t1}} - e^{-\alpha l_{t2}})(e^{-\alpha l_{r1}} - e^{-\alpha l_{r2}})\phi(\alpha)d\alpha \quad (1)$$

$$\phi(\alpha) = \frac{(\alpha_1+\mu_1\alpha)(\alpha_1-\mu_1\alpha) - (\alpha_1+\mu_1\alpha)(\alpha_1-\mu_1\alpha)e^{2\alpha_1 c}}{-(\alpha_1-\mu_1\alpha)(\alpha_1-\mu_1\alpha) + (\alpha_1+\mu_1\alpha)(\alpha_1+\mu_1\alpha)e^{2\alpha_1 c}} \quad (2)$$

$$J(r_{t2},r_{t1}) = \int_{\alpha r_{t1}}^{\alpha r_{t2}} \tau J_1(\tau)\,\tau \quad (3)$$

where ω is the angular frequency of excitation, α denotes the spatial frequency, $\alpha_1 = \sqrt{\alpha^2 + j\omega\mu_0\mu_1\sigma_1}$, σ_1 and μ_1 are electrical conductivity and relative magnetic permeability of plate, respectively, $J_1(\cdot)$ is the Bessel function of the first kind, N_t and N_r are the number of turns for the Tx and Rx coils, respectively.

The inductance can be calculated through numerical integration, whereas it is time-consuming. The truncated region eigenfunction expansion (TREE) method proposed by T. Theodoulidis and E. Kriezis recasts the expression as sums rather than integrals [15, 32], *i.e.*

$$\Delta L(\omega) = \frac{2\pi N_t N_r \mu_0}{(l_{t2}-l_{t1})(l_{r2}-l_{r1})(r_{t2}-r_{t1})(r_{r2}-r_{r1})} \sum_{\alpha_i} \frac{J(r_{t2},r_{t1})J(r_{r2},r_{r1})}{(h(J_0(\alpha_i \mathrm{h})))^2 {\alpha_i}^5} (e^{-\alpha_i l_{t1}} - e^{-\alpha_i l_{t2}})(e^{-\alpha_i l_{r1}} - e^{-\alpha_i l_{r2}})\phi(\alpha_i) \quad (4)$$

where α_i satisfies the condition on the truncated boundary, $J_1(\alpha_i \mathrm{h}) = 0$, $i \in \{1,2,\ldots,n_\alpha\}1$, which indicates that the electromagnetic field vanishes at the boundary $r = \mathrm{h}$. The series form accelerates the inductance calculation meanwhile guarantees accuracy if the range of spatial frequencies is appropriate.

Since the plate term $\phi(\alpha)$, sometimes referred to as phase term, varies relatively slowly as compared with the sensor term, as the representative curves shown in Figure 2, W. Yin, *et al.* employed the dominant value of plate term to approximate the original one [33], *i.e.*

$$\Delta L(\omega) = \phi(\alpha_0)\Delta L_0 \quad (5)$$

$$\Delta L_0 = \int_0^\infty A(\alpha)\, d\alpha \quad (6)$$

$$A(\alpha) = \frac{\pi N_t N_r \mu_0}{(l_{t2}-l_{t1})(l_{r2}-l_{r1})(r_{t2}-r_{t1})(r_{r2}-r_{r1})} \frac{J(r_{t2},r_{t1})J(r_{r2},r_{r1})}{\alpha^6} (e^{-\alpha l_{t1}} - e^{-\alpha l_{t2}})(e^{-\alpha l_{r1}} - e^{-\alpha l_{r2}}) \quad (7)$$

where α_0 is the characteristic/dominant spatial frequency corresponding to the maximum value of the sensor term $A(\alpha)$ which is determined by the sensor structure including the sensor lift-off.

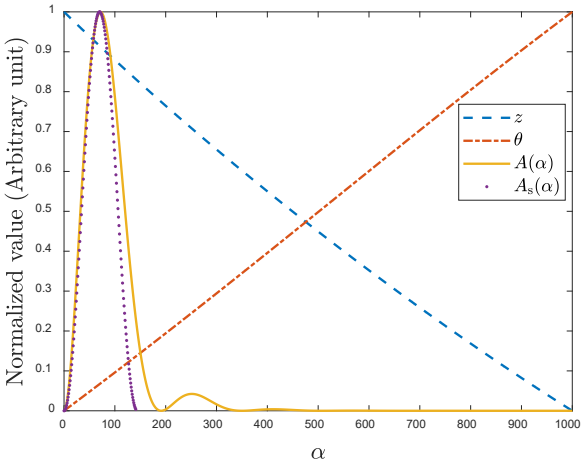

Figure 2. Comparison between the plate term $\phi(\alpha) = ze^{i\theta}$ and sensor term $A(\alpha)$ together with its approximation function $A_s(\alpha)$.

If the sensor structure is known or can be inferred, one can obtain ΔL_0 and α_0 before measurement. The approximation accelerates the inductance calculation and facilitates the estimation of plate properties using the plate term $\phi(\alpha_0)$. In addition, the sensor term $A(\alpha)$ which reaches its maximum value when $\alpha = \alpha_0$ can be approximated by an elementary function $A_s(\alpha)$,

$$A_s(\alpha) = A_m(\alpha_0)e^{-2\alpha l_0} \sin^2\left(\frac{\alpha\pi}{2\alpha_0}\right) \quad (8)$$

where $A_m(\alpha_0)$ is the maximum value of sensor term without the lift-off.

2.1.2. Model for the finite-size plate

In the theoretical analysis, the Dodd and Deeds model in Equation (1)-(3) calculates the inductance of plates with infinite radius, whereas in practical measurement, the plates normally have finite radii.

The TREE method indicates that the EC of finite-size geometry can be evaluated by considering a certain range of spatial frequencies in analytical model. By analysing the analytical solution, R. Huang, *et al.* proposed that the spatial frequency α was inversely proportional to the plate radius [16, 34, 35], as the relationship shown in Figure 3. This means that the limits of integration for α relates to the plate radius. For the plate with a radius of r_s, the range is $\alpha \in [\alpha_{r_s}, \infty]$, $\alpha_{r_s} = x_0/r_s$, and $x_0 = 3.518$. Consequently, the inductance change caused by the presence of the plate is

$$\Delta L(\omega) = \int_{\alpha_{r_s}}^\infty A(\alpha)\, \phi(\alpha) d\alpha \quad (9)$$

Then, based on the TREE method, the finite region eigenfunction expansion (FREE) method is proposed which confines the terms of series relating to the plate radius, *i.e.*;

$$\Delta L(\omega) = \sum_{\alpha=\alpha_{r_s}}^{\alpha=\alpha_{n_\alpha}} A(\alpha)\phi(\alpha)d\alpha \tag{10}$$

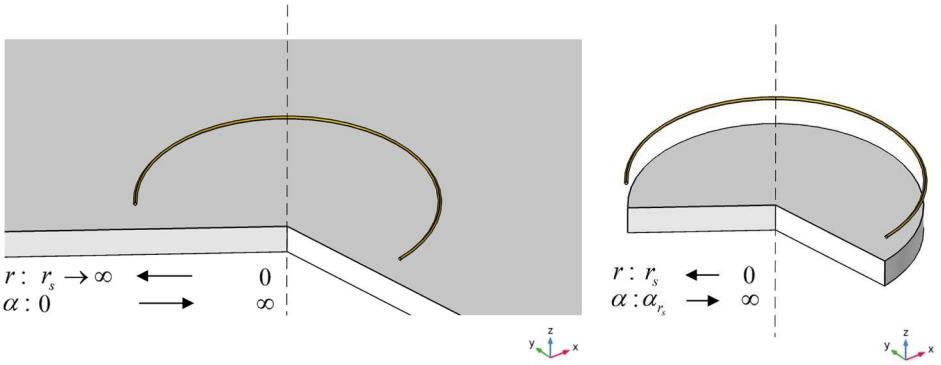

Figure 3. Relationship between the spatial frequency and radius, for the measurement of a finite-size plate.

2.2. Finite element method

The Finite element method (FEM) is a universal computation tool for arbitrary sensor setup and the geometry of target object. With the support of Galerkin equations [36], the unknown fields are subjected to the boundary conditions, and the approximated vector and scalar potentials are

$$\int_{\Omega_c} \nabla \times N_i \cdot v\nabla \times \mathbf{A}^n d\Omega + \int_{\Omega_c} j\omega\sigma N_i \cdot \mathbf{A}^n d\Omega + \int_{\Omega_c} j\omega\sigma N_i \cdot \nabla V^n d\Omega = \int_{\Omega_c} \nabla \times N_i \cdot v_0 \nabla \times \mathbf{A}_s \, d\Omega \quad i = 1,2,\ldots,6 \tag{11}$$

$$\int_{\Omega_c} j\omega\sigma \nabla L_i \cdot \mathbf{A}^n d\Omega + \int_{\Omega_c} j\omega\sigma \nabla L_i \cdot \nabla V^n d\Omega = 0 \quad i = 1,2,\ldots,4 \tag{12}$$

where v_0 is the reluctivity in the air, v is the reluctivity, ω is the excitation frequency, $\mathbf{A}^n$ and V^n are vector potential and scalar potential in element n, respectively.

As compared with analytical methods, the FEM can adapt to any geometry with high accuracy. However, it has a high computation load and requires a large amount of time to obtain the final solution for a single simulation. An equivalent phenomenon was observed for thin structures by using the analytical methods. From the principle of a plane wave reflected and transmitted at the surface of the non-magnetic plates, with a geometry of thin thickness, the inductance ΔL can be simplified as [37]

$$\Delta L = \frac{2\pi r E_0}{I} \frac{-\mu_0 \sigma c}{\alpha_0 + j\omega\mu_0\sigma c} \tag{13}$$

where r is the coil radius, E_0 is the electrical field in the air transmitted from the probe.

Then, considering two plates in different materials and thicknesses, the induced inductance is approximately equal when

$$\frac{D_1}{D_2} = \frac{\sigma_2}{\sigma_1} \tag{14}$$

where D_1 and D_2 are the thicknesses of the plates, and σ_1 and σ_2 are the corresponding conductivity.

The above relationship reduces the computational burden when modelling thin structure samples. Researchers have been devoted to speed up the computation speed to satisfy the users' requirements by using some approximations/techniques, *i.e.* zero-thickness defect [38], dedicated kernel [39], and the FEM-BEM hybrid method [40, 41]. M. Lu, and W. Yin *et al.* introduced a pre-conditioner in the computation for EC problems [42, 43]. The EC performance using this accelerated method for a co-axial air-cored probe above a defect is shown in Figure 4.

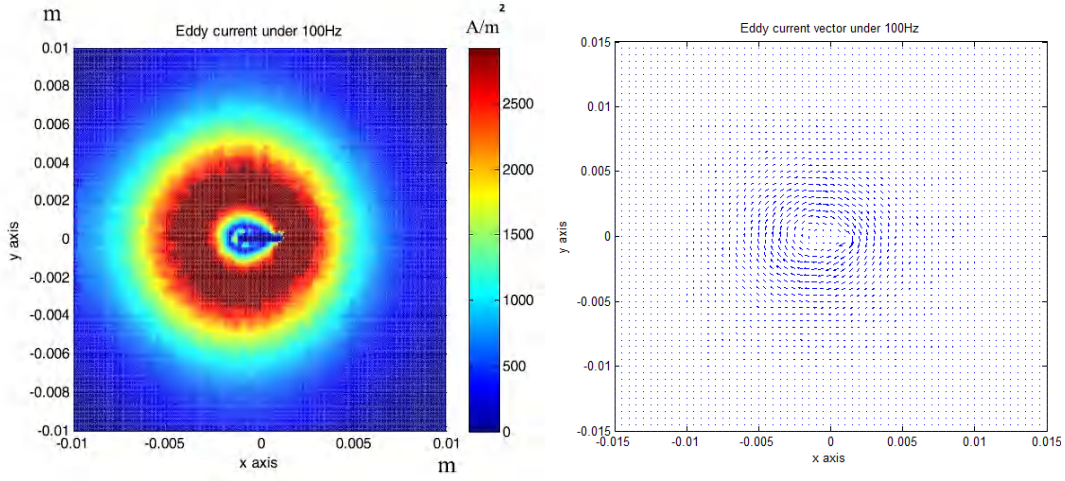

(a) (b)

Figure 4. Eddy current performance using an accelerated FEM solver: (a) Colour map; (b) quiver map [42].

The proposed pre-conditioning method optimises the initial guess for solving the system algebraic equations. Combined with the perturbed matrix inversion (PMI) method, a fast FEM approach was proposed which can effectively shrinks the time needed for the crack computation due to the small perturbation [23]. Furthermore, by exploiting the fact that the perturbed field exists in the surrounding region of the crack, the simulation solution can be calculated by combining the crack affected field and the original field without crack [22]. Table 1 lists the acceleration rate and computation deviation using the proposed method under different mesh elements. It can be noticed that, for the mesh including 139k elements, the computation time employing the accelerated method can be decreased by 34 times. As can be seen from Figure 5, the iteration number is reduced, especially for large-scale mesh models.

Table 1. The computation and accelerated times under different mesh elements [22]

Element number	Calculation time of the method without acceleration (s)	Calculation time of the proposed method (s)	Accelerated rate (times)	Calculation deviation (%)
10 k	7.69	2.03	3.79	2.56
51 k	57.74	3.56	16.22	3.22
139 k	306.79	8.96	34.24	3.56

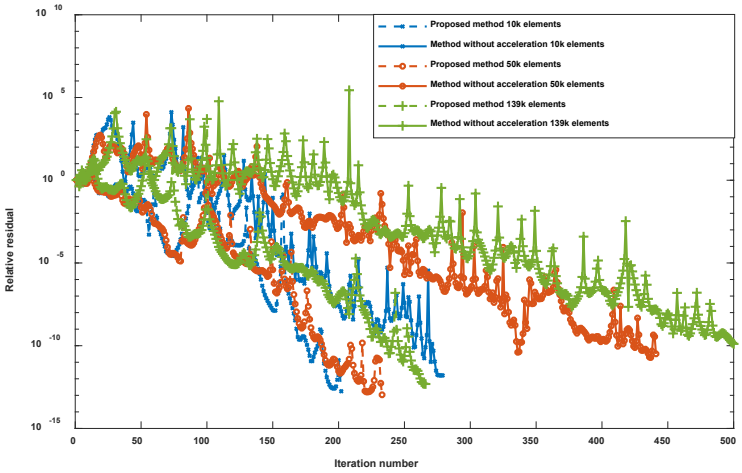

Figure 5. The relative residual with different mesh elements [22].

2.3. Tilted structure measurement

The probe tilt is identified as one of the major sources of noise in EC surface inspections [44]. The FEM and BEM methods can model the tilted probes naturally [45] while for the analytical model, the geometry is no longer axisymmetric and special treatments are required to represent the electromagnetic field [15]. The tilt effect has been studied for decades employing the methods including the SOVP [46], and the electromagnetic field of arbitrary current source above a conductive half-space [47]. The latter approach is analysed as described below.

Following studies [44, 48], applying the 2-D Fourier transform and according to the Parseval theorem, the general expression of mutual inductance change due to the conductive half-space is

$$\Delta L = 2\mu_0 \int_0^\infty \int_0^\infty \frac{1}{\kappa} \tilde{\mathrm{h}}_\mathrm{T}(u,v)\tilde{\mathrm{h}}_\mathrm{R}(-u,-v)\frac{\mu_r\kappa - \kappa_1}{\mu_r\kappa + \kappa_1}dudv$$
$$\tilde{\mathrm{h}}_\mathrm{T}(u,v) = \frac{N_t}{2(r_{t2}-r_{t1})(l_{t2}-l_{t1})\kappa^3} J(\kappa r_{t1}, \kappa r_{t2})(e^{-\kappa l_{t2}} - e^{-\kappa l_{t1}}) \quad (15)$$
$$\tilde{\mathrm{h}}_\mathrm{R}(u,v) = \frac{N_r}{2(r_{r2}-r_{r1})(l_{r2}-l_{r1})\kappa^3} J(\kappa r_{r1}, \kappa r_{r2})(e^{-\kappa l_{r2}} - e^{-\kappa l_{r1}})$$

where the source terms $\tilde{\mathrm{h}}_\mathrm{T}(u,v)$ and $\tilde{\mathrm{h}}_\mathrm{R}(u,v)$ indicate the 2-D Fourier transformed magnetic field intensity on surface of plane induced by the Tx and Rx coils, respectively, $\kappa = \sqrt{u^2+v^2}$ and $\kappa_1 = \sqrt{\kappa^2 + j\omega\mu_0\mu_r\sigma}$.

As the 2-D Fourier transform can characterize the rotation and translation function, for the probe shown in Figure 6. which is rotated around the y axis, the source terms become

$$\tilde{\mathrm{h}}_\mathrm{T}'(u,v) = \frac{jN_t}{2(r_{t2}-r_{t1})(l_{t2}-l_{t1})\psi^3} M(\psi r_{t1}, \psi r_{t2}) e^{-\kappa d_t} \sin\left(\frac{\psi(l_{t2}-l_{t1})}{2}\right)$$
$$\tilde{\mathrm{h}}_\mathrm{R}'(u,v) = \frac{jN_r}{2(r_{r2}-r_{r1})(l_{r2}-l_{r1})\psi^3} M(\psi r_{r1}, \psi r_{r2}) e^{-\kappa d_r} \sin\left(\frac{\psi(l_{r2}-l_{r1})}{2}\right) e^{jux_0} \quad (16)$$
$$M(\psi r_{t1}, \psi r_{t2}) = \int_{\psi r_{t1}}^{\psi r_{t2}} \tau I_1(\tau) d\tau$$

where $\psi = u\sin\varphi + j\kappa\cos\varphi$.

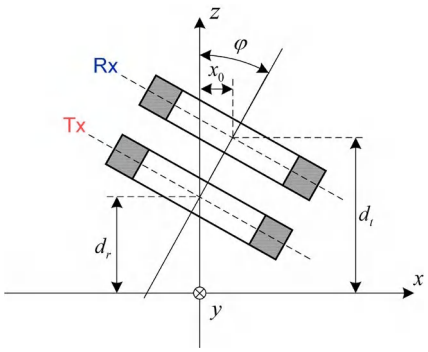

Figure 6. Cross-sectional view of tilted Tx-Rx coils, other dimensions similar as the counterparts without tilt angle

Substituting the source terms in Equation (15) by $\tilde{h}_T'(u,v)$ and $\tilde{h}_R'(u,v)$, the inductance variation of the tilted probe can be calculated. The source terms in Equation (16) can be derived from the model of perpendicular coils [48].

For the measurement of a plate with an infinitely long crack, according to the thin-skin model in high-frequency regime [49, 50], the inductance variation is

$$\Delta L = \frac{-j\mu_0}{2\pi}\int_{-\infty}^{\infty}\frac{1}{v^2}\tilde{H}_{y,\mathrm{T}}(v)\tilde{H}_{y,\mathrm{R}}(-v)\gamma dv$$
$$\tilde{H}_{y,\mathrm{T}}(v) = jv\int_{-\infty}^{\infty}\frac{1}{\kappa\psi^3}M(\psi r_{t1},\psi r_{t2})e^{-\kappa d_t}\sin\left(\frac{\psi(l_{t2}-l_{t1})}{2}\right)\frac{\kappa_1}{\kappa_1+\kappa\mu_r}e^{jux_0}du \quad (17)$$

where the term γ is determined by the crack parameters and plate properties, which is defined in [44, 51].

The measurements of probe impedance scanning through the finite-size test pieces can reflect the electromagnetic properties of the plate under measurement [52]. However, the tilt effect makes it difficult to estimate the electromagnetic properties from the measurements. Through extensive experiments, it has been observed that at several specific excitation frequencies, for example, 40 kHz, the endpoint of inductance trajectory on the complex plane can characterize the conductivity of test pieces, and the phase of the point is almost invariant regarding the tilt angle ranging from 0^o to 16.7^o [53]. This phenomenon is shown in Table 2. In addition, the approximate linear relationship between the endpoint inductance phase and conductivity can be obtained through the curve fitting employing the least squares method. This facilitates the classification of non-magnetic metals [54, 55].

Table 2. Relationships between the end point of inductance trajectory (marked by circles) and tilt angles [53]

Material	Copper	Aluminium
Inductance trajectory	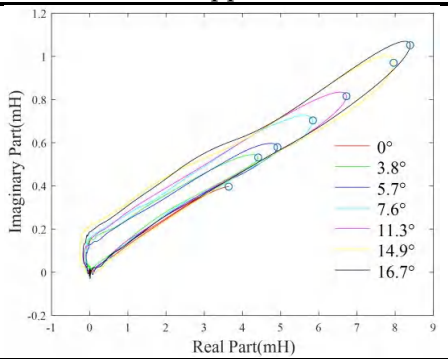	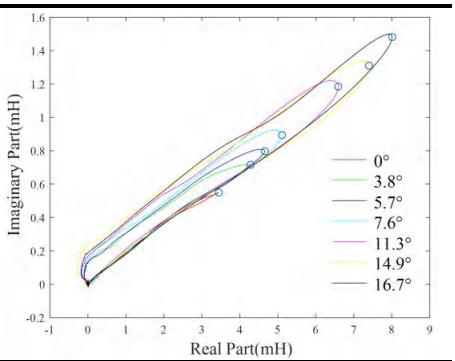

2.4. Multivariable inversion

The inverse methods, closely related to the forward model, retrieve the plate properties and parameter distributions, for example, conductivity profile and defect shape from the measurements. Even though the forward model varies from different governing equation and object geometry, similar inverse methods have been widely employed for a variety of objects under measurement, including pipes and spheres. The notable implementation of inverse methods in EC testing are summarised in Figure 7. The prevalent inversion algorithms for parameter estimation can be found in the literature [25, 56], without being exhaustive.

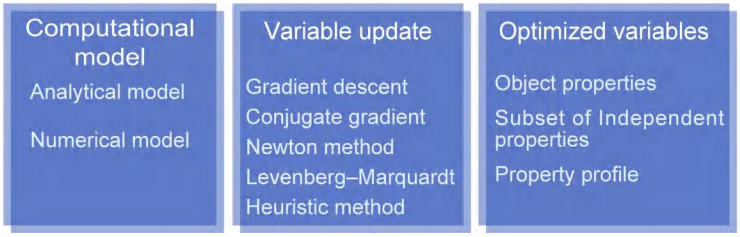

Figure 7. Primary issues of parameter inversion

The inversion of physical properties is realized through optimization by minimizing the discrepancy between the measured and calculated electromagnetic measurements. A least square index is usually adopted as the objective function, which represents the Euclidean distance between the measured and calculated values. For instance, the objective function employing the coil inductance reads

$$\min_{\mathbf{v}} f = \frac{1}{2}\|\Delta\mathbf{L}(\mathbf{v}) - \Delta\mathbf{L}_{\mathrm{m}}\|_2^2 \tag{18}$$

where $\mathbf{v} \in \mathbb{R}^{n_v \times 1}$ (n_v denotes the quantity of variables), $\|\cdot\|_2^2$ represents the ℓ_2-norm, $\Delta\mathbf{L}(\mathbf{v})$ and $\Delta\mathbf{L}_{\mathrm{m}}(\mathbf{v}) \in \mathbb{C}^{n_f \times 1}$ are calculated and measured inductance spectrum due to the test piece, respectively (n_f is the quantity of frequency points).

However, the inverse problem suffers from ill-posed and ill-conditioning problems which makes the optimization extremely sensitive to measurement noise. To stabilize the optimization, the regularization methods originated from Tikhonov impose the prior knowledge as a regularization term to Function (18), which functions as a spectral filter. The objective function becomes

$$\min_{\mathbf{v}} f = \frac{1}{2}\|\Delta\mathbf{L}(\mathbf{v}) - \Delta\mathbf{L}_{\mathrm{m}}\|_2^2 + \beta R(\mathbf{v}) \tag{19}$$

where β is the relaxation factor and the term $R(\mathbf{v})$ for ℓ_2 regularization is $R(\mathbf{v}) = \|\mathbf{v}\|_2^2$.

The measurements in the objective function can be the impedance of the Rx coil [57] and magnetic field values from magnetic field sensors [58]. The corresponding calculated values are usually obtained from the analytical and numerical models. The number of independent measurement points affect the estimation results, to some extent [59]. The numerical simulation is usually time-consuming whereas the analytical models are only suitable for the homogenous isotropic materials. For the isotropic material in axisymmetric geometry, the Dodd and Deeds model and its simplification have been intensively investigated [26, 60], while for the asymmetric model, the SOVP method can be applied [61]. To analyse the complex structures consisting of the heterogeneous electromagnetic property distribution [62] and anisotropic materials, for example, carbon fibre reinforced polymer (CFRP) [63], the FEM as well as hybrid FEM and boundary element method (BEM) can be adopted.

The combination of optimized variables influences the optimization performance. It is expected that the non-linear objective function reaches its global minimum in the

variable space, which only exists when the objective function is convex. This corresponds to the situation that $\nabla_{\mathbf{v}}\nabla_{\mathbf{v}}f \succcurlyeq 0$. The second-order derivative, the Hessian matrix, is usually approximated by $\nabla_{\mathbf{v}}\nabla_{\mathbf{v}}f \approx \mathbf{H}(\mathbf{v}) = (\nabla_{\mathbf{v}}f)^{\mathrm{H}}\nabla_{\mathbf{v}}f$, and $\mathbf{S}(\mathbf{v}) = \nabla_{\mathbf{v}}f$ is referred to as the sensitivity/Jacobian matrix. If the influences of various variables on measurements are correlated, for example, coupling effect of permeability and conductivity on inductance [64-66] and correlation between the derivatives in terms of thickness and electromagnetic parameters [61], the condition number of the Hessian matrix will be large, and the function convexity can hardly be satisfied. Furthermore, the variable correlation renders the optimization process unstable when the inversion of the Hessian matrix is required [67]. The appropriate variable combination can be determined according to local and global sensitivity analysis. The local sensitivity analysis focuses on the Jacobian matrix evaluated on specific points, *e.g.* the singular value analysis, while the global analysis can reflect the correlations between variables, *e.g.* the variance-based methods [68, 69]. The ill-conditioning degree of the inverse problem can be represented by the singular value spectrum of sensitivity/Hessian matrix[70]. If there is no extremely small singular value, the optimization process would be stable and affected little by the measurement noise. The singular value feature of the Hessian matrix can be represented by $S_f: \mathbb{C}^{\mathrm{n_v}\times\mathrm{n_v}} \to \mathbb{R}$,

$$S_f\big(\mathbf{H}(\mathbf{v}_{\mathrm{r}})\big) = -20\log_{10}\left(|\lambda_{\min}|/\lambda_{\max}|\right) \tag{20}$$

where $\lambda_{\min}$ and $\lambda_{\max}$ are the minimum and maximum singular values of $\mathbf{H}(\mathbf{v}_{\mathrm{r}})$, respectively.

In the optimization process, the variables can be updated by various strategies according to the gradient of the non-linear objective function. The representative methods and their characteristics are shown in Table 3. The variables are updated in an iterative manner,

$$\mathbf{v}_{k+1} = \mathbf{v}_k + \Delta\mathbf{v}_k \tag{21}$$

Table 3. Characteristics of non-linear optimization algorithms

Algorithm	Updating direction, $\Delta\mathbf{v}_k = \mathbf{d}_k(\Delta\mathbf{L} - \Delta\mathbf{L}_{\mathrm{m}})$	Convergence rate	Stability
Gradient descent	$\mathbf{d}_k = -\mathbf{S}_k^{\mathrm{H}}$	Slow	High
Conjugate gradient	$\mathbf{d}_k = -\mathbf{S}_k^{\mathrm{H}} + \beta_k\mathbf{d}_k,\ \beta_k = \max\left\{0, \mathbf{s}_k^{\mathrm{H}}\frac{(\mathbf{s}_k - \mathbf{s}_{k-1})}{\|\mathbf{s}_k\|_2^2}\right\}$	Fast	Medium
Newton method	$\mathbf{d}_k = -(\mathbf{S}_k^{\mathrm{H}}\mathbf{S}_k)^{-1}\mathbf{S}_k^{\mathrm{H}}$	Fast	Low
LM	$\mathbf{d}_k = -\left[\mathbf{S}_k^{\mathrm{H}}\mathbf{S}_k + \beta\mathrm{diag}(\mathbf{S}_k^{\mathrm{H}}\mathbf{S}_k)\right]^{-1}\mathbf{S}_k^{\mathrm{H}}$	Medium	Medium
PSO	$\Delta\mathbf{v}_k = \Delta\mathbf{v}_{k-1} + \boldsymbol{U}(\mathbf{0}, \boldsymbol{\phi_1}) \otimes \left(\mathbf{v}_{\mathrm{pBest},k} - \mathbf{v}_k\right)$ $+\boldsymbol{U}(\mathbf{0}, \phi_2) \otimes (\mathbf{v}_{\mathrm{gBest},k} - \mathbf{v}_k)$ (details in [71])	Medium	High

For a small number of optimized variables, the heuristic methods which employ various solution searching strategies, including classic genetic algorithm (GA) and particle swarm optimization (PSO), are usually implemented in conjunction with other methods. These methods decrease the influence of starting point selection meanwhile improve the algorithm's convergence and maintaining its correctness as long as the heuristic is admissible [71-73].

In previous studies, the electromagnetic properties and thickness of metallic plates have been estimated by the modified Newton-Raphson method [74]. The aforementioned algorithms have been evaluated in the reconstruction of conductivity profile in the graphite blocks [56, 75]. In addition, the reconstruction of defects in the anisotropic materials

employing the GA method has been proposed in the study [63]. The shape reconstruction of conductive clogging deposits in the steam generator is realized in research [62], using the gradient descent method employing the shape derivatives.

3. Measurement system

3.1. Impedance measurement system

3.1.1 Overview of EC testing instruments

EC testing techniques are widely applied in various industrial applications [27]. In practice, the system configuration, *e.g.* hardware and software implementation, differs from instrument to instrument and highly depends on each particular application. In general, the system contains an excitation source, which can be pulsed excitation signal [76], single frequency signal [28, 77, 78] and multi-frequency signal [79-83], *etc.* The hardware, data acquisition system (DAQ), normally includes analogue and digital conditioning electronics, which implement signal generation, signal amplification, demodulation and filtering. Typically, a control unit is in charge of the operation in the hardware, which can be a digital signal processor (DSP), a field programmable gate array (FPGA) or a microcontroller, *etc.* For software, normally it varies from the programming language for the user interface such as C or C++ [84, 85] and LabVIEW graphical programming language [82, 86, 87]. Due to different requirements of measuring speed, the electromagnetic (EM) instruments can also be divided into on-line or off-line instruments [88]. In addition, there are more variations when the system is interfaced to sensors of different configurations, such as the electromagnetic tomography (EMT) sensor array, which requires multiplexing operation of the instrument [89, 90].

Although much work has been carried out for EM system development, there is still a further expectation in improving hardware and software system design. With the development of technology and higher demand in the industry, the hardware and the software have kept advancing. The development of analogue EM systems has a long history, which relies on constructing physical circuits by using electronic components as in [90], [91]. Compared with analogue systems, digital systems are of increasing interest as they are more reliable, robust and less complex in hardware configuration [84]. The digital systems commonly apply a DSP or an FPGA as cornerstone, which can process the detected signals digitally and quickly. Generally, a digital instrument consists of a processing unit, a control logic, front-ends and possibly a power management part. A generical block diagram of digital system is shown in Figure 8.

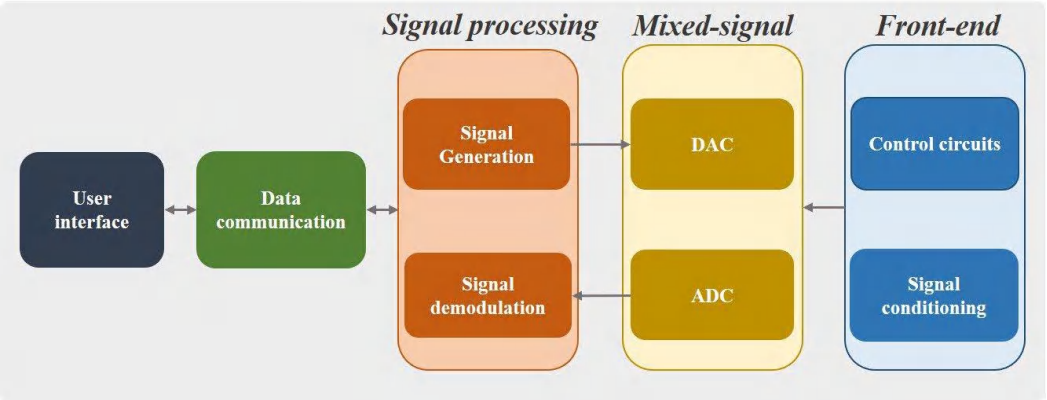

Figure 8. Generic block diagram of EM instruments.

3.1.2. Customised EC testing instrument

The EC testing instruments have been developed for various measurement applications. The recent studies and system characteristics are summarised in Table 4.

Table 4. Characteristics of customised EC testing instruments in recent studies

Researcher	Controller	Applied excitation frequency	SNR	Software	Main application
M. Kekelj *et al*. [92]	Cyclone V SoC	100~400 kHz	Up to 56 dB	MATLAB	Pipe defects
M. Hamel *et al*. [93]	NI DAQ	50~150 kHz	-	LabVIEW	Plate with crack
N. Zhang *et al*. [94]	NI DAQ	0.1~1 kHz	-	MATLAB	Cylindrical samples
A. K. Soni *et al*. [95]	NI DAQ with lock-in amplifier	0.5~80 kHz	38 dB	LabVIEW	Plate with crack
D. E. Aguiam *et al*. [96]	ADSP	Up to 10MHz	-	LabVIEW	Block with crack
G. Zhang *et al*. [97]	NI DAQ with lock-in amplifier	50 kHz	-	LabVIEW	Plate with crack
G. Dingley *et al*. [98]	AVR MCU	0.1~100 kHz	Up to 90 dB	-	EMT

The EC testing instrument developed in the EM sensing group led by W. Yin at the University of Manchester is shown in Figure 9. The cornerstone of the instrument is an FPFA SoC, which integrates an ARM dual Cortex-9-based processor and a Xilinx 7-series FPGA. The FPGA module is responsible for excitation signal generation, implementation of in-phase and quadrature phase (IQ) demodulation, multiplexing control and data transfer. Generally, the FPGA is preferable for implementing a high-speed logic, arithmetic and dataflow subsystem. Therefore, it is suitable for real-time online detection and imaging of defects, which requires high data speed. The ARM processor is in charge of data transfer and communication. With ethernet communication, the instrument has a fast and robust transmission, and it can provide a data rate up to 10k samples/s. Under this configuration, the interference between the FPGA and the processor is minimised.

Figure 9. Self-designed and constructed EC testing instrument.

A block diagram of the system architecture is shown in Figure 10. In addition to the SoC, the instrument also consists of front-end circuits including excitation circuits, detection circuits and mixed-signal circuits. Depending on the probe structure, it may also involve multiplexing when using multi-channel probes. The excitation circuit generates a sinusoidal signal to energise the Tx coils, and the detection circuit receives the induced voltage on the Rx elements. The excitation frequency ranges from 1 kHz to 1 MHz, which is applicable for most EC testing applications. A typical loop-back signal-to-noise ratio (SNR) can reach up to 100 dB. However, the real SNR including sensor elements depends on the measurement configuration.

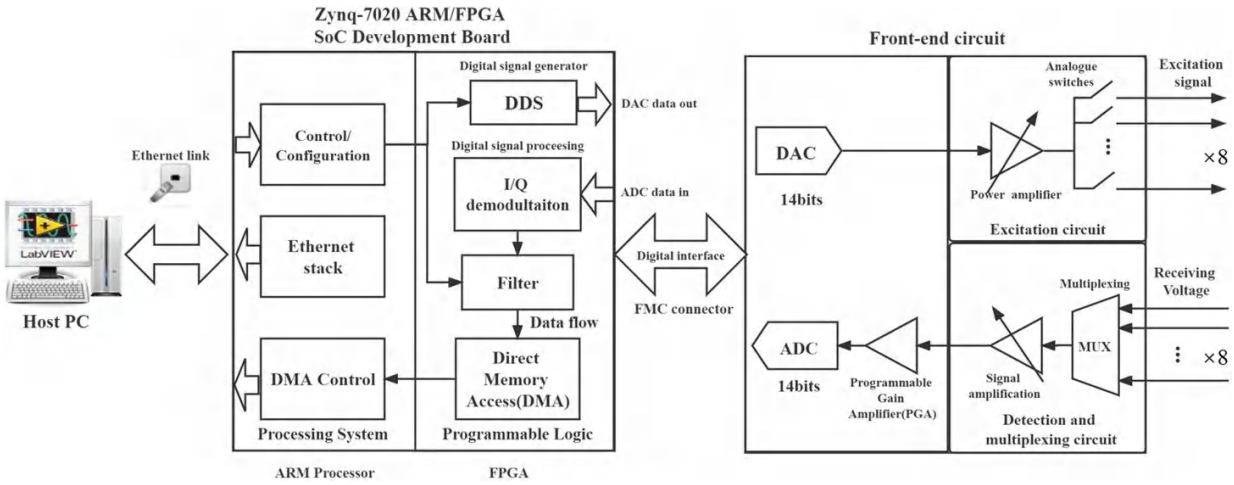

Figure 10. System architecture of the customised EC testing instrument.

A built-in user interface running on the host PC was also developed. The user interface provides a convenient way to display and log data. It also allows the user to send configurations such as operating frequency, filter width and coil pairs assignment during the experiments. After measurements, the data is saved in a database format (.db), which can be directly fed into further signal processing algorithms.

The instrument integrates all elements in a case with a size of 288 mm x 208 mm x 135 mm, which makes it portable for in-situ tests. There are also USB and HDMI interfaces that can connect to external devices. Notably, the instrument can operate with or without the power connection as it includes an internal battery with automatic power management and can last for more than 8 hours during typical use once fully charged.

3.1.3. Commercial impedance analysers

Impedance is an important parameter characterising the frequency response of EC probes. In the analytical solution of Dodd and Deeds, the inductance of Rx coil is calculated as the result in the presence of test pieces [13, 14]. Generally, impedance is defined as the total opposition a device or circuit offers to the flow of an alternating current at a given frequency and is represented as a complex quantity [99]. The impedance vector consists of a real part R and an imaginary part X. The real part represents the resistance while the imaginary part denotes reactance which can be either inductive or capacitive. To acquire the impedance, both the real part and the imaginary part need to be measured [99]. The representative frequency responses of the imaginary and real parts of EC probes are shown in Figure 11.

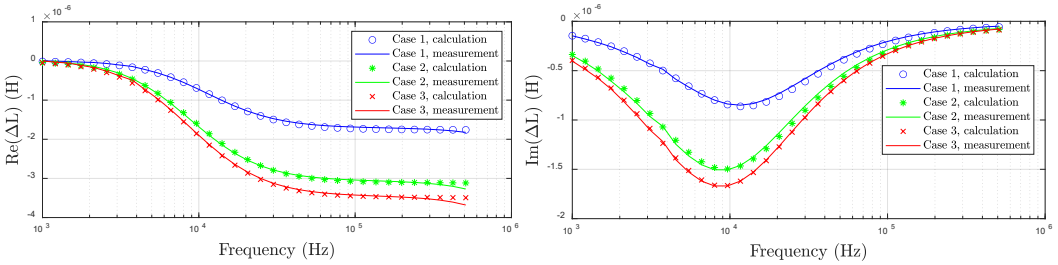

Figure 11. Frequency responses of eddy current probes.

As compared with using off-the-self commercial impedance analysers, the development of customised instruments can be complicated and time-consuming. Therefore, commercial impedance analysers play essential roles in laboratory-based experiments of EC testing as they may have a wider operating ranges and better performances in terms of accuracy and precision than customised instruments.

Typically, commercial impedance analysers implement 4-port measurement, where both voltage and current are measured. The terminal arrangements are shown in Figure 12 a,b when measuring a single element and mutual inductance between coils, respectively. Table 5 illustrates the characteristics of two commercial impedance analysers that have been intensively used in previous studies [100, 101].

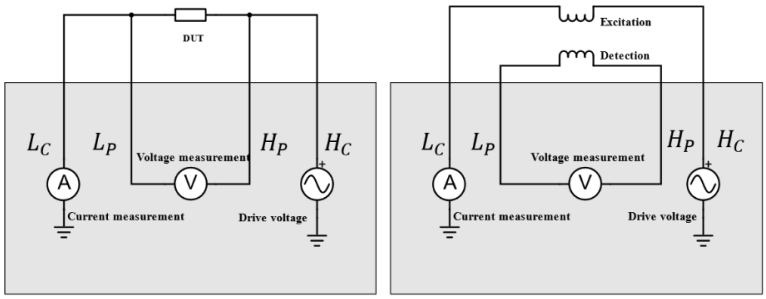

(a) (b)

Figure 12. Terminal arrangement of commercial impedance analysers for: (a) impedance measurement of DUT; (b) mutual inductance measurement between the excitation and detection coils

Table 5. Comparison of two commercial impedance analysers

-	Basic accuracy	Frequency range	Impedance range	Data Speed	No. of channels
Zurich MFIA 	0.05%	1 mHz to 500 kHz/5 MHz	1 mΩ to 1 TΩ	20 msec/point for f > 10 kHz	1 Current, 1 Voltage
Solartron 1260A Impedance Analyzer 	0.1%, 0.1°	10 μHz to 32 MHz	100 mΩ to 100 TΩ	No specified	1 Current, 2 Voltage

3.1.4. Calibration

Generally, electronic components such as op-amps introduce phase shifts at different frequencies in acquisition channels. To reduce these phase shifts, calibration is normally required for the measuring system. Typically, it can be achieved by taking a set of measurements using a small permeable or conductive object in air space. As the expected signal in these cases has only a real (or imaginary) component, the phase shift can be manually adjusted for each frequency to minimize the imaginary (or real) component. Then the obtained phase for each channel can be stored and subtracted automatically from all posterior measurements using other objects [102]. A conductive brass sphere was used in [102], which was supposed to only provide a real component. In [87, 103], a ferrite object was used for calibration, which was magnetically permeable but not electrically conductive. Therefore, the measurements should only change along the imaginary part in the complex plane. In this way, the errors and phase shifts introduced in the acquisition channels can be effectively attenuated.

An alternative calibration method using a current sensing transformer was proposed in [104], where both induced voltage and excitation current were measured. As compared with current sensing resistors, it provides a better dynamic range when employing coil probes. Furthermore, the transformer has quite a flat magnitude response under different frequencies and introduces little phase shift between the primary side and the secondary side. The diagram of calibrations is shown in Figure 13, with a current sensing transformer.

The relative inductance in the presence of a sample can be calculated by using Equations (22) and (23):

$$V_{\text{transformer}} = j\omega MI \tag{22}$$

$$\Delta L = \frac{V_{\text{sample}} - V_{\text{air}}}{j\omega I} = (V_{\text{sample}} - V_{\text{air}}) \times \frac{M}{V_{\text{transformer}}} \tag{23}$$

where V_{sample} is the induced voltage in the Rx coil in the presence of a sample, V_{air} is the induced voltage in the Rx coil in free space, $V_{\text{transformer}}$ is the induced voltage at the secondary side of the transformer, M is the mutual inductance between the primary side and secondary side of the transformer, I is the excitation current and ω is the angular frequency of the excitation signal.

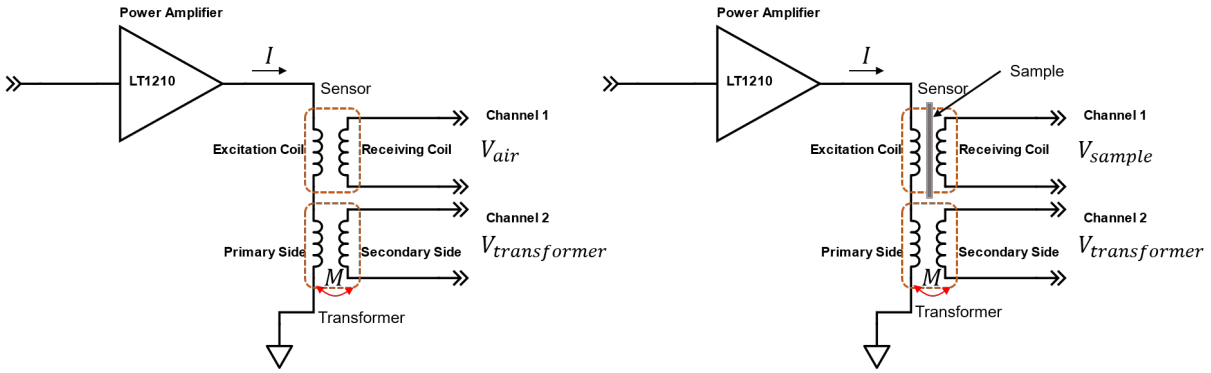

Figure 13. Calibration with a current sensing transformer.

3.2. Probe design

The EC probes can be categorized according to the operation mode and configuration of applications [105, 106], as shown in Figure 14. The EC probes and related signal processing techniques have been summarised in previous studies [29, 30, 107-109]. The characteristics of the conventional probes are briefly analysed below.

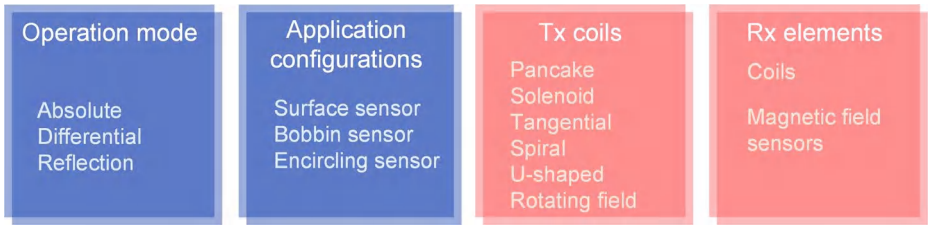

Figure 14. Categories of the eddy-current probes

For the operation modes, the absolute mode usually measures the absolute impedance of Rx coil, which reflects the thickness, conductivity, permeability and defect information; the differential mode measures the defect on the test pieces using the differential signal of coils that is insensitive to the slowly varying properties and environmental influences; the reflection mode conventionally referred to as driver/pickup mode adopts the Tx and Rx coils which are optimized separately for various purposes.

In the reflection mode, the Tx and Rx coils are considered separately. There exist various structures of Tx coils, for example, pancake, tangential, planar and U-shaped/U-cored coils. The basic structures of several representative Tx coils and sensitive region on measured plates are illustrated in Table 6.

Table 6. Transmitting coils and corresponding magnetic field on the surface and longitudinal section of measured plates

Coil structure	Magnetic field distribution, normalized |**H**|	Coil structure	Magnetic field distribution, normalized |**H**|
Pancake coil 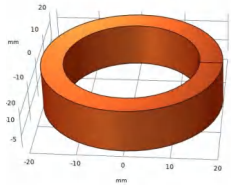	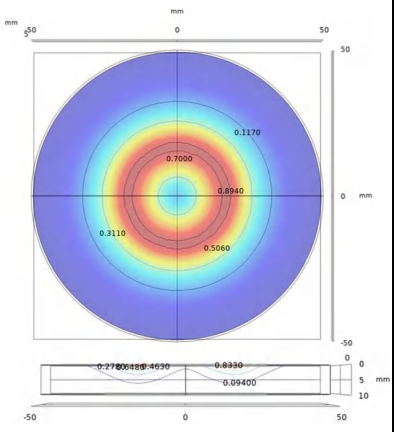	Spiral coil 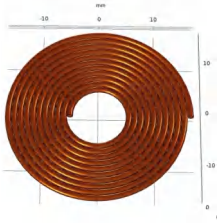	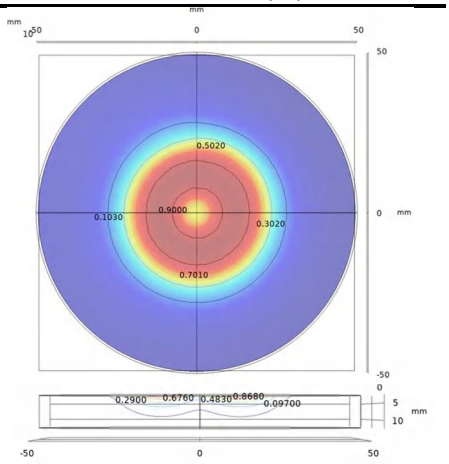
Solenoid coil 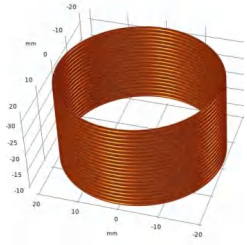	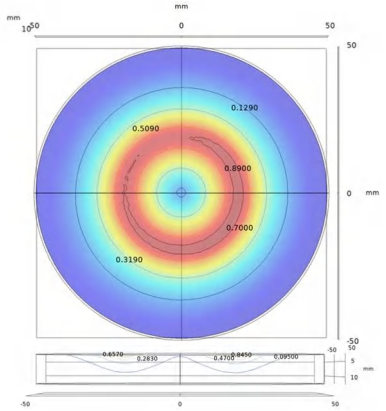	U-shaped (ferrite core) coil 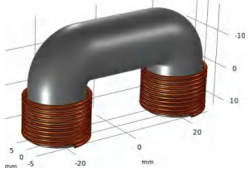	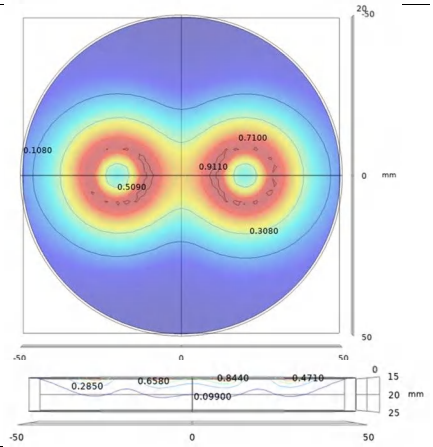
Tangential coil (rectangular) 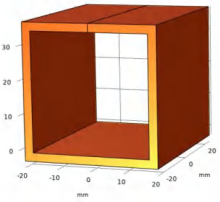	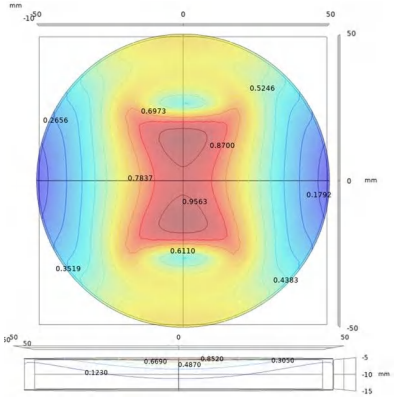	Rotating field coils 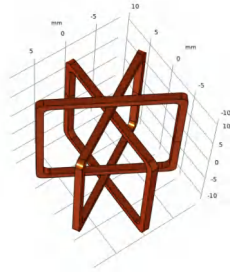	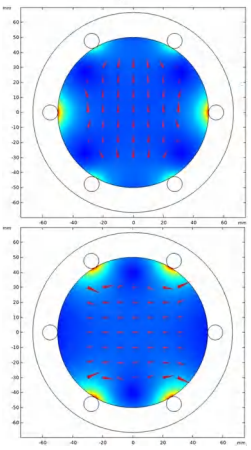 (Varying with time)

To measure thick plates and pipes, the EC penetration depth is limited by;

$$\delta = \frac{1}{\sqrt{\pi f \mu \sigma}} \tag{24}$$

The defined penetration depth corresponds to the planar wave excitation and is usually higher than that of the practical Tx coils in finite dimensions. The normalized standard penetration depth can represent the influence of variables in Equation (24) [110], *i.e.*

excitation frequency, conductivity and permeability. The factors that affect the penetration depth including the coil dimensions have been summarised in the study [111]. It has been suggested that the tangential coil is more suitable for the thick plate measurement, as the induced EC of the widely adopted pancake coils suffers from the diffusion and axial cancellation effect, resulting in more obvious longitudinal EC decay [110, 112, 113].

The U-shaped coil usually contains a ferrite core that constitute the magnetic circuit and concentrates the magnetic field beneath the two ends, which increases the signal amplitude caused by the defects [114-116]. The planar coil fabricated by flexible printed circuit (FPC) and printing electronic technology (PET) elevates the detection capability of micro-surface defects [117, 118]. Furthermore, by employing a suitable track width of the planar spiral coils, the coil impedance consists of both the capacitance and inductance, reflecting various electromagnetic properties simultaneously [119]. To measure the defects in an arbitrary direction, it is efficient to employ a rotating magnetic field probe composed of several Tx coils with different excitation signal phase and position [105, 120-123]. The most significant variation of EC field due to the crack occurs when it is perpendicular to the defect direction.

The Rx elements include coils and magnetic field sensors which measure the coil impedance and magnetic field, respectively. In comparison, the coils are characterized by their linear response, no saturation, small hysteresis and high flexibility, while the magnetic field sensors, for example, Hall sensor, anisotropic magneto resistor (AMR), giant magneto resistor (GMR), tunneling magneto resistance (TMR) and superconducting quantum interference device (SQUID), are in small dimensions and capable of low-frequency measurement in the sensitive direction. Nevertheless, the magnetic field sensors are limited in the dynamic range, to some extent, and provide the non-linear response signal. The detailed characteristics and comparison of the magnetic field sensors are summarised in the literature [124-126]. Increasing the number of Rx elements accounts for an increase in the independent measurement signals, thereby enriching the prior information to estimate the physical properties of objects. The plate thickness and permeability, for instance, can be derived using the single frequency inductance from multiple Rx coils with the simplified analytical model [100, 127, 128]. Furthermore, to better the accuracy solving the inverse problem, the optimum design of coil array has been discussed for electromagnetic tomography (EMT) [129, 130], while few studies have considered this issue in plate measurement applications.

Probe shielding reduces the interaction of the exciting magnetic field with the non-relevant region in proximity of the probe, which is usually applied to reduce edge effects. In addition, probe loading employs the ferrite cores which are ferromagnetic concentrating the magnetic field for the sensing area. These strategies are significant, especially for remote field EC testing [131] and for reducing the size of the device.

The EC probes can integrate with the sensors of other sensing modalities, for example, capacitance electrodes. An integrated sensor can obtain complementary information and is sensitive to more electromagnetic properties of the test pieces. The dual-modality inductive and capacitive sensor facilitates plate thickness measurement using the single frequency inductance [132], as the lift-off can be directly derived from the capacitance between the surfaces of probe and plates.

4. Planar structure measurements and applications

4.1. Reducing the lift-off effects

The EC testing of planar structure suffers from the lift-off effect, which attenuates the magnitude and changes the phase of measured signals, causing errors in property estimation. To address this issue, researchers have investigated a range of methods including compensation strategies, algorithms, and lift-off invariance phenomenon.

4.1.1. Lift-off compensation using multiple measurements

Analytical models are frequently adopted to estimate plate properties, due to explicit expressions and fast calculation. Although asymmetric problems exist in applications, a variety of cases of planar structure measurement can be approximated using the axial-symmetric model employing the Dodd and Deeds model with adequate accuracy.

In the Dodd and Deeds model, the plate term of the coil inductance is a function of excitation frequency, spatial frequency and plate properties. In the approximate model expressed by Equation (5), the characteristic spatial frequency α_0 of coil probes is affected by the lift-off. The compensation methods estimate the lift-off and calculate the compensated characteristic spatial frequency α_{0r}, then a specific plate property can be estimated from the phase of inductance. As the unknown parameters are lift-off and plate property, the measurements of various Rx coils (or different positions of single Rx coil) are implemented to solve the linear equations of the simplified analytical model. The representative measurement configuration is shown in Figure 15.

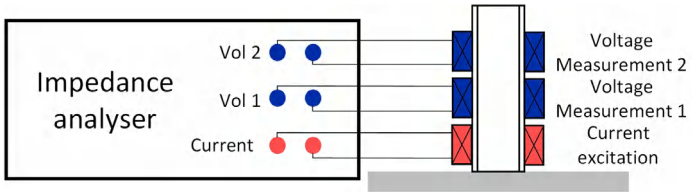

Figure 15. Measurement configuration for lift-off compensation employing triple-coil probe

For the non-magnetic plates, according to the model in Equation (5), the phase of inductance is determined by the plate term $\phi(\alpha_0)$. In the low excitation frequency, the approximation that $\alpha_1 c \to 0$, $e^{2\alpha_1 c} \sim 1 + 2\alpha_1 c$ can be satisfied. Consequently, $\phi(\alpha_0)$ can be simplified to [133]

$$\begin{aligned} \phi(\alpha_0) &\approx \frac{j\omega\sigma\mu_0 c}{j\omega\sigma\mu_0 c + 2{\alpha_0}^2 c + 2\alpha_0 + 2\alpha_0\alpha_1 c} \\ &= \frac{j\frac{\omega}{\omega_0}}{1 + \frac{2\alpha_0\alpha_1 c}{2{\alpha_0}^2 c + 2\alpha_0} + j\frac{\omega}{\omega_0}} \end{aligned} \quad (25)$$

where $\omega_0 = 2\alpha_0/(\sigma\mu_0 c)$.

When the plate thickness c is a small value, the plate term can be simplified by the first-order system [101], of which the peak frequency is ω_0, *i.e.*;

$$\phi(\alpha_0) \approx \frac{j\omega/\omega_0}{1 + j\omega/\omega_0} \quad (26)$$

The simplified plate term indicates that the plate thickness is inversely proportional to the peak frequency of imaginary part of inductance [133]. Providing the characteristic spatial frequency and phase of inductance, the plate thickness can be estimated using Equation (26).

Alternatively, for the magnetic plates employing the high excitation frequency ($\alpha_1 c \to \infty$), the plate term in Equation (2) can be approximated by [127, 134, 135];

$$\phi(\alpha_0) \approx -\frac{\alpha_1 - \mu_1\alpha_0}{\alpha_1 + \mu_1\alpha_0} \quad (27)$$

Applying the approximation $\alpha_1 = \sqrt{\alpha^2 + j\omega\mu_0\mu_1\sigma} \approx \sqrt{j\omega\mu_0\mu_1\sigma} = (1+j)\,\alpha', \alpha' = \sqrt{2\omega\mu_0\mu_1\sigma}/2$, Equation (27) can be approximated by

$$\phi(\alpha_0) \approx -\frac{2\alpha'^2 - {\mu_1}^2{\alpha_0}^2 + j2\mu_1\alpha_0\alpha'}{(\alpha' + \mu_1\alpha_0)^2 + \alpha'^2} \quad (28)$$

In this way, the real part of the plate term relating to the real part of inductance can be simplified as

$$\begin{aligned} \mathrm{Re}[\phi(\alpha_0)] &\approx -\frac{2\alpha'^2 - {\mu_1}^2{\alpha_0}^2}{(\alpha' + \mu_1\alpha_0)^2 + \alpha'^2} \\ &= \frac{2{\mu_1}^2{\alpha_0}^2 + 2\mu_1\alpha_0\alpha'}{2\alpha'^2 + {\mu_1}^2{\alpha_0}^2 + 2\mu_1\alpha_0\alpha'} - 1 \end{aligned} \tag{29}$$

Since $\alpha' \gg \alpha_0$ for the high excitation frequency, the real part can be approximated by [127];

$$\mathrm{Re}[\phi(\alpha_0)] \approx \frac{\mu_1\alpha_0}{\alpha'} - 1 = \sqrt{\frac{2\mu_1}{\omega\mu_0\sigma}}\alpha_0 - 1 \tag{30}$$

The relative permeability can be estimated if α_0 is obtained. For the unknown lift-off, the compensated characteristic spatial frequency α_{0r}, relating to the maximum value in the sensor term series, is calculated by [17];

$$\alpha_{0r} = \alpha_0 - \frac{4\alpha_0^2 l_0}{\pi^2} \tag{31}$$

For the plates in a large radius, according to Equation (8), the inductance magnitude can be calculated by

$$\begin{aligned} L_0 &\approx A_m(\alpha_0)\int_0^{2\alpha_0} e^{-2\alpha l_0}\sin^2\left(\frac{\alpha\pi}{2\alpha_0}\right)d\alpha \\ &= A_m(\alpha_0)\frac{\pi^2\alpha_0(1 - e^{-2\alpha_0 l_0})}{2\alpha_0 l_0[(\alpha_0 l_0)^2 + \pi^2]} \end{aligned} \tag{32}$$

where l_0 indicates the lift-off of Rx coil and the upper limit of integral relates to the range of the first peak of the sensor term, as shown in Figure 2.

In Equation (32), the linear relationship between the lift-off l_0 and magnitude of inductance L_0 can be obtained through simplification. The relationship can be applied to estimate l_0 from the inductance measured by Rx coils [17]. Combining Equation (25) for low excitation frequency, or Equation (30) for relatively high frequency, and inductance magnitude, the thickness and lift-off can be estimated for non-magnetic plates [100, 101, 115, 127], while the permeability and lift-off can be calculated for the magnetic plates [24, 134]. The experimental evaluation of aforementioned methods are shown in Table 7.

In addition, it is observed that a series of quadratic-like curves relating to the plate thickness can approximately describe the relationships between the phase and logarithmic amplitude performing the lift-off scan with the inductor–capacitor (LC) resonant probe. The plate thickness can be estimated employing the curve fitting method [136].

Table 7. Experimental evaluation results of representative probes for lift-off compensation

Probe type	Plate materials	Applied frequency for estimation	Lift-off (mm)	Estimated variables and range	Relative error of estimation
Triple-coil [101]	Al	Peak frequency	Up to 6	Thickness (22~100 um)	<5%
Triple-coil [134]	DP 800, DP 1000	Zero-crossing frequency	Up to 4	μ_r	<2%
Triple-coil [135]	DP 600, Cr-Mo	Dual frequency	Up to 20	μ_r	<4.5%
Triple-coil [127]	Al, Cu	Single frequency (16 kHz)	Up to 5	Thickness (~66 um)	<5%
Triple-coil [100]	Al, Cu	Single frequency (200 kHz)	Up to 4	Thickness (0.4, 0.5 mm)	<3%

4.1.2. Lift-off compensating algorithms

A variety of algorithms have been proposed to address the influence due to the probe lift-off on the electromagnetic property estimation of planar structures. W. Yin, *et al.* proposed the characteristic frequency which relates to the thickness and conductivity of the planar plate [33]. Furthermore, it was observed that the characteristic frequency decreases with an increase of the lift-off. By utilizing the triple-coil probe with fixed coil separations, the change of characteristic frequency under the range of lift-offs tested remains a constant value [101]. Avoiding the requirement for precise magnetic balance, the compensation algorithm was proposed to tackle the lift-off variation by using the compensated peak frequency feature. Accordingly, the accuracy is increased while the mechanical configuration can be simplified [17]. Furthermore, M. Lu *et al.* employed the zero-crossing frequency of the real part of inductance to inspect the properties of both non-magnetic and magnetic materials [137]. The magnetic permeability prediction approach was given based on the phase compensating algorithm to reduce the inaccuracy of impedance phase for ferrous steels caused by the probe lift-offs. The error in permeability prediction was less than 2% within the evaluated range [134]. In addition, H. Wang, *et al.* proposed that the slope of the lift-off curve (LOC) in the RL impedance plane can characterize the target thickness which is independent of lift-off variation [138, 139].

For heterogenous plates, the material property profiles can be reconstructed from frequency sweeping measurements [24, 26, 57, 140]. By adopting the iterative optimization algorithms or simply fitting the EM measurements calculated by analytical models, the profiles for test pieces can be reconstructed. For magnetic materials, the induced eddy current concentrates near the surface of plates, due to the thin skin effect. Based on this effect, the simplified material-independent algorithm was derived to estimate the probe lift-off and plate permeability [24]. In [100], the proposed algorithm employs the inductance phase of two Rx coils in a single low excitation frequency to infer the probe lift-off, which is applied to compensate the estimated thickness of non-magnetic plates. These compensation algorithms increase the lift-off tolerance to about 10 mm, while maintaining the high accuracy of plate property estimation.

4.1.3. Lift-off invariance phenomenon

Measurements based on the electromagnetic induction method are sensitive to probe lift-off. In an investigation attenuating the lift-off effect, the lift-off invariance phenomenon was observed and applied to measure the conductive plates. As shown in Figure 16, it was found that at a certain range of lift-off, there exists a certain lift-off that makes the influence of the conductivity/permeability on the inductance unchangeable, which is termed the conductivity invariance phenomenon (CIP) [141] and permeability invariance phenomenon (PIP) [142]. This phenomenon can decouple the correlation between electrical conductivity and magnetic permeability at an optimal lift-off. In [143] and [144], the authors have found that the phase curves of measurements for different lift-offs maintain a stable value. H. Wang *et al.* observed that, for a large distance of lift-off, the approximate linear relationship holds between the logarithms of the phase signal and the plate conductivity [138]. C. S. Angani *et al.* indicated that the magnetic field measurements of various lift-offs intersects at a certain point in the frequency domain when performing the transient EC oscillation method [145].

With the aid of LII and LIF, optimization methods have been applied to calculate plate properties.

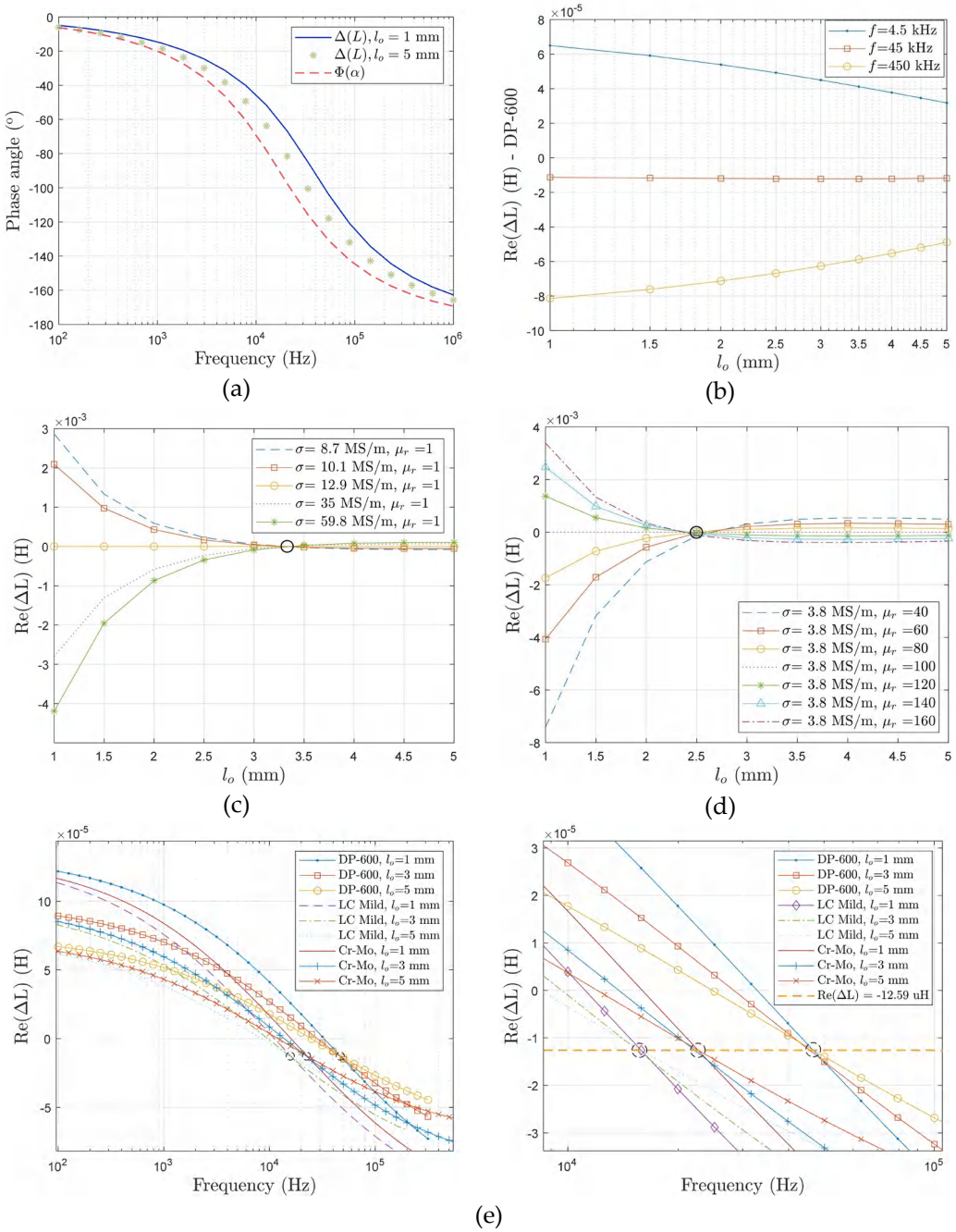

Figure 16. lift-off invariance features: (a) phase invariance phenomenon; (b) lift-off invariance inductance; (c) conductivity invariance phenomenon; (d) permeability invariance phenomenon; (e) lift-off invariance frequency

Under high excitation frequency, it was proposed that there exists a linear relationship between the ratio of inductance change and the probe lift-off, namely the dual-frequency linearity of lift-off (DFL) feature [135]. This can be formulated as

$$l_0 = \frac{5.56(4{\alpha_0}^2(g+h_c)^2+\pi^2)(g+h_c)\Delta L_2}{\pi^2(1-e^{-4\alpha_0(g+h_c)})\Delta L_1} - \frac{1.39}{\alpha_0} \quad (33)$$

where g and h_c are gap between coils and the height of coil, respectively.

It has been noticed that there was a lift-off invariance inductance (LII) for different samples under various excitation frequencies, termed the lift-off invariance frequency

(LIF) [146]. The estimation of plate properties employing the inductance measurement phenomenon is summarized in Table 8.

Table 8. Experimental evaluation of plate property estimation employing the representative coil inductance phenomenon

Phenomenon	Plate materials	Applied frequency for estimation	Lift-off (mm)	Estimated variables and range	Relative error of estimation
Phase invariance Phenomenon [144]	Al, Cu	100 Hz ~ 1 MHz	-	Thickness (22 um~5 mm)	<3%
Lift-off invariance inductance [24]	DP 600, DP 800	Single frequency depending on material	Up to 12	μ_r	<1%
Lift-off invariance inductance [146]	DP 600, LC-Mild, Cr-Mo	Single frequency depending on material	Up to 5	σ *or* μ_r	<1%
Conductivity invariance phenomenon [141]	DP 600, DP 800, DP 1000	Single frequency (90 kHz)	1.9	μ_r	<3%
Permeability-independent frequency [143]	Al, Al alloy, SUS304	4~200 kHz	-	Thickness (1~8 mm)	-
Slope of lift-off curve [138]	Cu, Al, SS, Ti	1 MHz	0.04 to 0.4	Thickness (~100 um)	<3%

4.2. Defect scanning

The defect evaluation is one of the major applications of the EC system in metallic plate measurement. The measurement features of signals in the time and frequency domain are extracted to infer the defect information. The recent research highlights are shown in Figure 17. Representative probes, measurement features and inference methods are illustrated below.

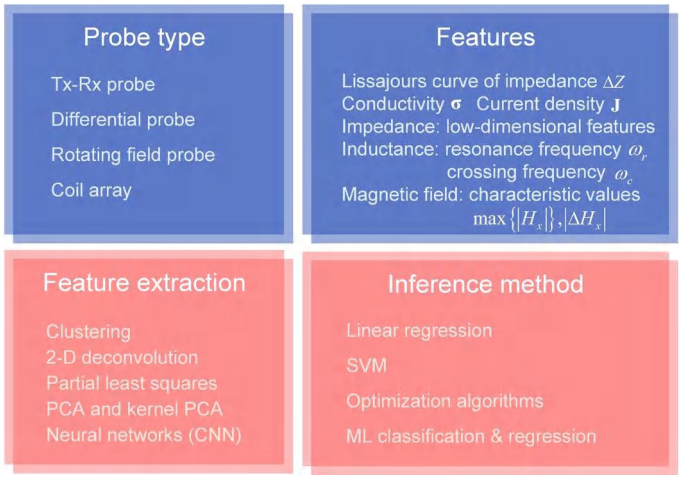

Figure 17. Key factors estimating the defect information

The probes suitable for the surface defect measurement include the Tx and Rx coils as well as magnetic field sensors. The measured time series and frequency spectrum when scanning the probe above the test pieces, as shown in Figure 18, reflects the properties of defects. The experiments indicate that the probe is sensitive to the defect especially when the induced eddy current is perpendicular to the defect orientation [147]. Accordingly, the rotating field coils, constructed by the planar and ferrite-core coils, have been designed to generate the magnetic field for the measurement of crack directions [148, 149]. The signals of differential probe are featured as the so-called Lissajous curve, as shown in Figure 19, of which the geometric features reflect the depth of defects [150]. In addition, the probe lift-off affects the signals of Rx elements, and the influence is expected to be a fixed value

during the scanning process [149]. In addition, the variation of scanning signals due to lift-off can be applied to estimate the surface corrosion of plates [151].

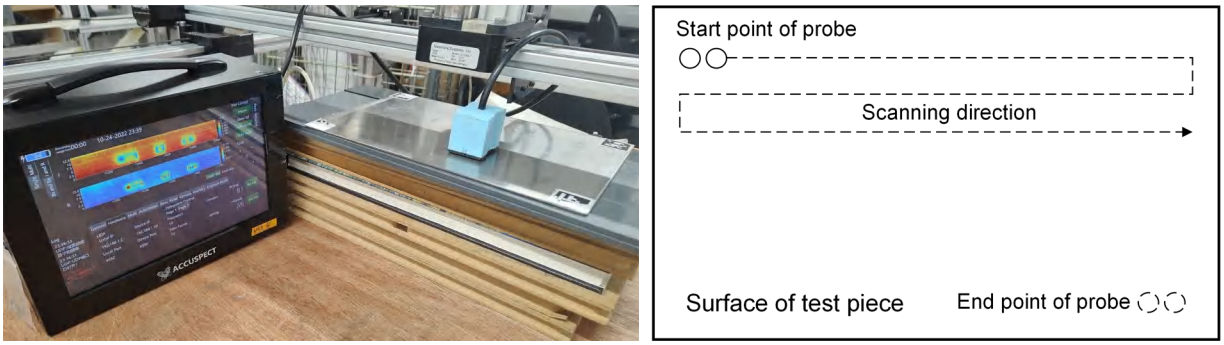

(a) (b)

Figure 18. (a) experimental setup of EC system (b) diagram of defect scanning

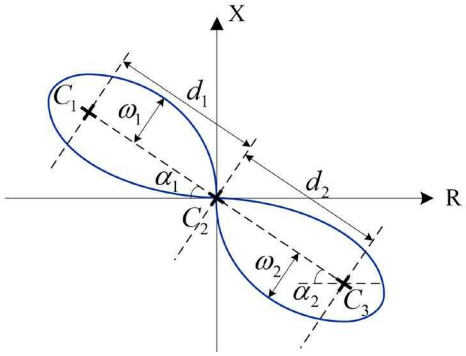

Figure 19. Geometric features of the Lissajous curve in the impedance plane, C_1, C_2 and C_3 are clustered centres of a variety of impedance curves.

The defect information can be obtained from electromagnetic measurements and corresponding statistical features. The electromagnetic measurements are measured from coils and magnetic field sensors. The statistical features are obtained from the electromagnetic measurements through the linear and non-linear feature extraction methods of machine learning and pattern recognition, which is intended to be informative and non-redundant, facilitating the subsequent estimation of plate properties and defect information.

The measurements of coil at the characteristic frequencies, for example, peak and zero-crossing frequencies, contain the information of plate properties and probe lift-off, while the pattern of measured magnetic field parameters relates to the geometry of defects. It has been observed that the crossing frequency of a specific real part of the coil inductance corresponds to the permeability, which relates to the hardness of magnetic materials [152]. The lift-off effect of probe employing magnetic field sensors can be compensated for in the Fourier domain [153]. Furthermore, the conductivity distributions reconstructed in the ROI by inverse methods can represent the arbitrary defect location and shape [154, 155]. Through the various scanning modes shown in Figure 20, it has been proposed that among the features of $|H(f,x,y)|$, $\mathrm{Arg}\{H(f,x,y)\}$, $|\Gamma(t,x,y)|$, and $\mathrm{Arg}\{\Gamma(t,x,y)\}$ ($\Gamma(t,x,y) = H(t,x,y) + j\mathcal{H}\{H(t,x,y)\}$, $\mathcal{H}\{\cdot\}$ represents the Hilbert transform), $\mathrm{Arg}\{\Gamma(t,x,y)\}$ can characterize the defects in relatively deeper locations of test pieces [156]. The distribution of the measured magnetic field approximates to the Hermite-Gaussian (HG) modes which are solutions of analytical function [157], *i.e.* paraxial wave equation in Cartesian coordinates [158]. Furthermore, the Biot-Savart law implies that the variation of EC distribution reflecting the defect contour, as shown in Figure 21, can be

approximated by the 2-D deconvolution of magnetic field change and dipole current map [149, 157], since

$$[B_x] = [\mathrm{conv}([b_x], [J_d])]$$

where $[B_x]$ is a matrix that maps the magnetic field perturbation, $[J_d]$ is the matrix that maps the EC perturbation induced in the metallic surface, $[b_x]$ is a transfer matrix that represents the field produced by a unit dipole current and $\mathrm{conv}(\cdot,\cdot)$ indicates the 2-D convolution operation.

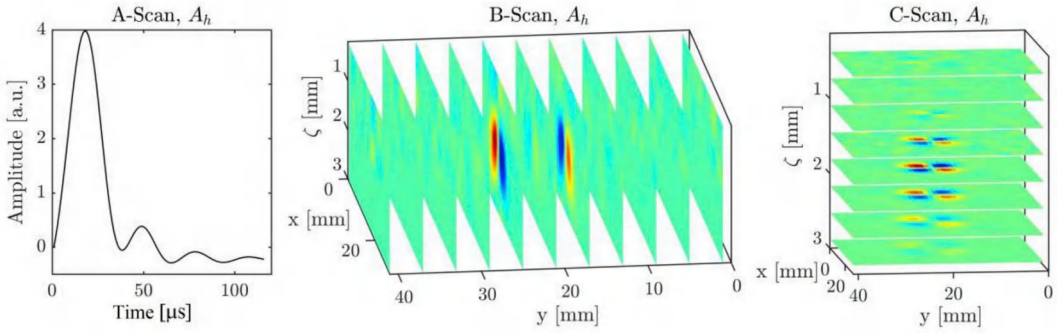

Figure 20. Various scanning modes where A-Scan is the pulse response of a single point, x, y and ζ indicate the width, length and depth of a rectangular plate, respectively [156].

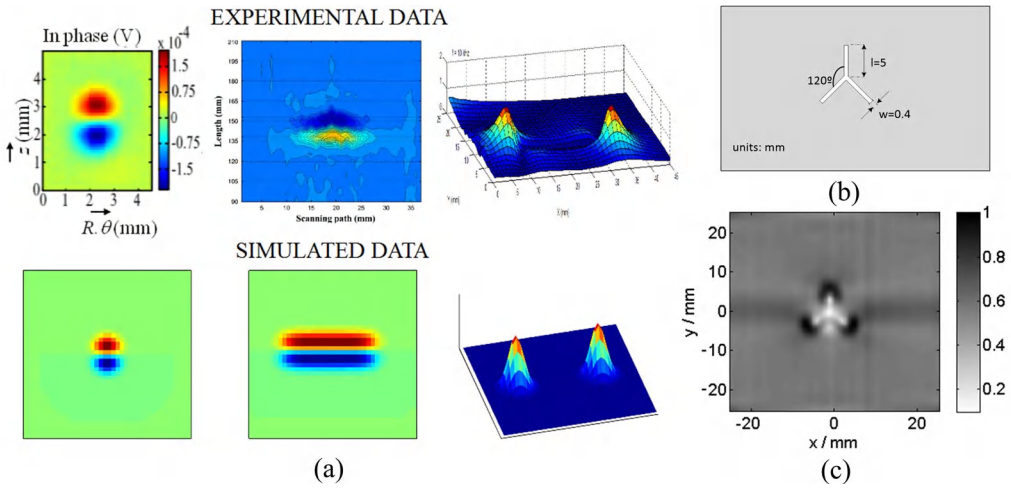

Figure 21. (a) comparison between the measured magnetic field signal (experimental data) and $HG_{0.1}$ pattern (simulated data) [157]; (b) shape of defect; (c) normalized sum of eddy current density distributions [149].

The statistical features of measurements in lower dimensional space can be extracted employing the linear methods including principal component analysis (PCA), partial least squares (PLS) [159], clustering methods [150], and non-linear methods, for example, kernel PCA [160] and neural networks of machine learning (ML) [161, 162]. The non-linear mapping from the statistical features to defect dimensions is usually modelled implicitly by ML. In ML models, it is expected that the measurement features of training and test samples are uniformly distributed in a similar region of the lower dimensional space. This implies that the independent identical distribution hypothesis of samples can be satisfied, so that the high prediction accuracy and generalization can be achieved. The adaptive sampling scheme, for example, output surface filling can be adopted to realize this condition.

Specifically, the discrete defect depth and lift-off can be estimated by classification methods, for example, support vector machine (SVM) and other ML models

implementing the classification loss functions, while the continuous dimensions and shape of defects can be obtained by the regression models [159].

Although the emerging deep learning (DL) models have demonstrated advantages regarding defect reconstruction and lift-off tolerance [163], the robustness of DL models is still one of the primary challenges. For instance, when measuring anisotropic ferromagnetic plates and unknown materials, the prediction errors tend to increase, due to large discrepancies between the available training samples prepared beforehand and test samples [164]. In the on-line monitoring process where the estimation speed and safety are in high requirement, it is difficult to deploy the large-scale DL models. The DL method for defect scanning still requires investigation of the state-of-the-art models, dataset construction and deployment in various conditions, to test its performance and reliability.

5. Conclusions

This review summarises the recent developments of EC testing for planar structures. The key issues in computational models, measurement systems and parameter estimation are summarised. In the theoretical analysis, the forward and inverse problems are described, elaborating the basic principles of the analytical model and FEM for the forward problem as well as simplification and optimization algorithms for the inverse problem. The system development consists of a customized and commercial grade impedance measurement system including the calibration method, and probe design which is task specific. In applications of plate property measurement, the lift-off compensation methods are addressed. Furthermore, in defect scanning, the joint application of probes, measurement feature extraction and defect parameter inference methods are investigated.

Computational models are being developed for complex geometry and for real world applications, while, at the same time, simplified methods increase the speed of computation for real-time measurements. The sensitivity and spatial resolution of measurements can be improved by system improvements as well as customised and application-specific probe optimization. Lift-off tolerance/elimination methods are still topics worth investigation. In summary, the combination of cutting-edge models and high-performance measurement systems is still required and needs to be explored through continuous efforts for many existing and potential industrial applications.

Author Contributions: Conceptualization, W. Y.; methodology, Z. X., R. H., Z. C., J. R. S. A., Z. Z and W. Y.; software, Z. X., R. H., Z. C. and J. R. S. A.; validation, Z. X., R. H., Z. C. and J. R. S. A.; formal analysis, Z. X. and W. Y.; data curation, Z. X., R. H., Z. C. and J. R. S. A.; writing—original draft preparation, Z. X., R. H., Z. C., Y. K.; writing—review and editing, Z. X. and W. Y.; administration, W.Y.; All authors have read and agreed to the published version of the manuscript.

Funding: This research was financially supported from The Chinese NSF 52166004, The Royal Society IEC\NSFC\211165, China Scholarship Council (CSC) and 2022 IEEE I&M Society Graduate Fellowship Award.

Institutional Review Board Statement: Not applicable.

Informed Consent Statement: Not applicable.
Data Availability Statement: Not applicable.

Conflicts of Interest: Not applicable.

References

1. Xu, J.; Wu, J.; Xin, W.; Ge, Z. L., Measuring Ultrathin Metallic Coating Properties Using Swept-Frequency Eddy-Current Technique. *IEEE Transactions on Instrumentation and Measurement* **2020,** 69, (8), 5772–5781.
2. Cheng, W. Y., Swept-frequency eddy current testing to characterize a nonmagnetic metallic plate and a nonconductive coating over it. *International Journal of Applied Electromagnetics and Mechanics* **2019,** 59, (3), 1169 −1178.

3. Xu, J.; Wu, J.; Xin, W.; Ge, Z. L., Fast Measurement of the Coating Thickness and Conductivity Using Eddy Currents and Plane Wave Approximation. *IEEE Sensors Journal* **2021,** 21, (1), 306−314.
4. AbdAlla, A. N.; Faraj, M. A.; Samsuri, F.; Rifai, D.; Ali, K.; Al-Douri, Y., Challenges in improving the performance of eddy current testing: Review. *Measurement & Control* **2019,** 52, (1−2), 46−64.
5. Hohmann, R.; Lomparski, D.; Krause, H. J.; Von Kreurzbruck, M.; Becker, W., Aircraft wheel testing with remote eddy current technique using a HTS SQUID magnetometer. *IEEE Transactions on Applied Superconductivity* **2001,** 11, (1), 1279−1282.
6. Qi, G. J.; Lei, H.; Fu, G. Q.; Jing, P.; Lin, J. M., In Situ Eddy-Current Testing on Low-Pressure Turbine Blades of Aircraft Engine. *Journal of Testing and Evaluation* **2012,** 40, (4), 553−556.
7. Liu, Z.; Li, W.; Xue, F. Q.; Xiafang, J. Y.; Bu, B.; Yi, Z., Electromagnetic Tomography Rail Defect Inspection. *IEEE Transactions on Magnetics* **2015,** 51, (10).
8. Augustyniak, M.; Borzyszkowski, P.; Bulawa, M., Towards an Universal Method for Predicting Eddy-Current Sensor Characteristics in the Railway Industry. *Journal of Nondestructive Evaluation* **2019,** 38, (1).
9. Guilizzoni, R.; Finch, G.; Harmon, S., Subsurface corrosion detection in industrial steel structures. *IEEE Magnetics Letters* **2019,** 10, 1−5.
10. Qu, Z.; Zhao, Q.; Meng, Y., Improvement of sensitivity of eddy current sensors for nano-scale thickness measurement of Cu films. *NDT & E International* **2014,** 61, 53−57.
11. Qu, Z.; Meng, Y.; Zhao, Q., Eddy current measurement of the thickness of top Cu film of the multilayer interconnects in the integrated circuit (IC) manufacturing process. *Frontiers of Mechanical Engineering* **2015,** 10, (1), 1−6.
12. Li, H.; Zhao, Q.; Lu, X.; Luo, J., Signal processing and analysis for copper layer thickness measurement within a large variation range in the CMP process. *Review of Scientific Instruments* **2017,** 88, (11), 115103.
13. Dodd, C. V.; Luquire, J.; Deeds, W.; Spoeri, W. *Some eddy-current problems and their integral solutions*; Oak Ridge National Lab., Tenn.: United States, 1969.
14. Dodd, C.; Deeds, W., Analytical solutions to eddy-current probe-coil problems. *Journal of applied physics* **1968,** 39, (6), 2829−2838.
15. Theodoulidis, T.; Kriezis, E. E., Application of the TREE method to Axisymmetric Problems. In *Eddy Current Canonical Problems (with Applications to Nondestructive Evaluation)*, Tech Science Press: Contemporary research on emerging science and technology, 2006; p 152−182.
16. Huang, R.; Lu, M.; Zhang, Z.; Zhao, Q.; Xie, Y.; Tao, Y.; Meng, T.; Peyton, A.; Theodoulidis, T.; Yin, W., Measurement of the radius of metallic plates based on a novel finite region eigenfunction expansion (FREE) method. *IEEE Sensors Journal* **2020,** 20, (24), 15099−15106.
17. Lu, M.; Yin, L.; Peyton, A. J.; Yin, W., A novel compensation algorithm for thickness measurement immune to lift-off variations using eddy current method. *IEEE Transactions on Instrumentation and Measurement* **2016,** 65, (12), 2773−2779.
18. Zeng, Z. W.; Jiao, S. N.; Du, F.; Sun, L.; Li, J., Eddy Current Testing of Delamination in Carbon Fiber Reinforced Polymer (CFRP): A Finite Element Analysis. *Research in Nondestructive Evaluation* **2018,** 29, (4), 199−211.
19. Tian, Q. Z.; Zeng, Z. W., Hybrid Formulation Domain-Decomposition Finite-Element Method for Simulating Eddy-Current Testing. *IEEE Transactions on Magnetics* **2020,** 56, (7).
20. Barbato, L.; Poulakis, N.; Tamburrino, A.; Theodoulidis, T.; Ventre, S., Solution and Extension of a New Benchmark Problem for Eddy-Current Nondestructive Testing. *Ieee Transactions on Magnetics* **2015,** 51, (7).
21. Tesfalem, H.; Fletcher, A. D.; Brown, M.; Chapman, B.; Peyton, A. J., Study of asymmetric gradiometer sensor configurations for eddy current based non-destructive testing in an industrial environment. *NDT & E International* **2018,** 100, 1−10.
22. Huang, R.; Lu, M.; Chen, Z.; Shao, Y.; Xia, Z.; Hu, G.; Peyton, A.; Yin, W., A novel acceleration method for crack computation using finite element analysis in eddy current testing. *IEEE Transactions on Instrumentation and Measurement* **2022,** 71, 1−9.

23. Huang, R.; Lu, M.; Peyton, A.; Yin, W., A novel perturbed matrix inversion based method for the acceleration of finite element analysis in crack-scanning eddy current NDT. *IEEE Access* **2020,** 8, 12438−12444.
24. Lu, M.; Meng, X.; Huang, R.; Chen, L.; Peyton, A.; Yin, W., Inversion of distance and magnetic permeability based on material-independent and liftoff insensitive algorithms using eddy current sensor. *IEEE Transactions on Instrumentation and Measurement* **2020,** 70, 1−9.
25. Cui, Z.; Wang, Q.; Xue, Q.; Fan, W.; Zhang, L.; Cao, Z.; Sun, B.; Wang, H.; Yang, W., A review on image reconstruction algorithms for electrical capacitance/resistance tomography. *Sensor Review* **2016,** 36, (4), 429−445.
26. Lu, M.; Xie, Y.; Zhu, W.; Peyton, A.; Yin, W., Determination of the magnetic permeability, electrical conductivity, and thickness of ferrite metallic plates using a multifrequency electromagnetic sensing system. *IEEE Transactions on Industrial Informatics* **2018,** 15, (7), 4111−4119.
27. Ali, K. B.; Abdalla, A. N.; Rifai, D.; Faraj, M. A., Review on system development in eddy current testing and technique for defect classification and characterization. *IET Circuits, Devices & Systems* **2017,** 11, (4), 338−351.
28. García-Martín, J.; Gómez-Gil, J.; Vázquez-Sánchez, E., Non-destructive techniques based on eddy current testing. *Sensors* **2011,** 11, (3), 2525−2565.
29. Liu, S.; Sun, Y.; Jiang, X.; Kang, Y., A review of wire rope detection methods, sensors and signal processing techniques. *Journal of Nondestructive Evaluation* **2020,** 39, (4), 1−18.
30. Sophian, A.; Tian, G.; Fan, M., Pulsed eddy current non-destructive testing and evaluation: A review. *Chinese Journal of Mechanical Engineering* **2017,** 30, (3), 500−514.
31. Cheng, W., Measurement of magnetic plates at a few hertz with two concentric coils and thickness estimation using mutual inductance. *IEEE Transactions on Instrumentation and Measurement* **2021,** 70, 1−10.
32. Theodoulidis, T. P.; Bowler, J. R., The Truncated Region Eigenfunction Expansion Method for the Solution of Boundary Value Problems in Eddy Current Nondestructive Evaluation. *AIP Conference Proceedings* **2005,** 760, (1), 403-408.
33. Yin, W.; Peyton, A. J.; Dickinson, S. J., Simultaneous measurement of distance and thickness of a thin metal plate with an electromagnetic sensor using a simplified model. *IEEE Transactions on Instrumentation and Measurement* **2004,** 53, (4), 1335−1338.
34. Huang, R.; Lu, M.; He, X.; Peyton, A.; Yin, W., Measuring coaxial hole size of finite-size metallic disk based on a dual-constraint integration feature using multifrequency eddy current testing. *IEEE Transactions on Instrumentation and Measurement* **2020,** 70, 1−7.
35. Huang, R.; Lu, M.; Peyton, A.; Yin, W., Thickness measurement of metallic plates with finite planar dimension using eddy current method. *IEEE Transactions on Instrumentation and Measurement* **2020,** 69, (10), 8424−8431.
36. Pavo, J.; Miya, K., Reconstruction of crack shape by optimization using eddy current field measurement. *IEEE transactions on magnetics* **1994,** 30, (5), 3407−3410.
37. Yin, W.; Tang, J.; Lu, M.; Xu, H.; Huang, R.; Zhao, Q.; Zhang, Z.; Peyton, A., An equivalent-effect phenomenon in eddy current non-destructive testing of thin structures. *IEEE Access* **2019,** 7, 70296−70307.
38. Bowler, J. R.; Theodoulidis, T. P.; Poulakis, N., Eddy current probe signals due to a crack at a right-angled corner. *IEEE transactions on magnetics* **2012,** 48, (12), 4735−4746.
39. Du, Y.; Xie, S.; Li, X.; Chen, Z.; Uchimoto, T.; Takagi, T., A fast forward simulation scheme for eddy current testing of crack in a structure of carbon fiber reinforced polymer laminate. *IEEE Access* **2019,** 7, 152278−152288.
40. Zhao, K.; Vouvakis, M. N.; Lee, J.-F., Solving electromagnetic problems using a novel symmetric FEM-BEM approach. *IEEE Transactions on magnetics* **2006,** 42, (4), 583−586.
41. Bíró, O., Edge element formulations of eddy current problems. *Computer methods in applied mechanics and engineering* **1999,** 169, (3-4), 391−405.

42. Lu, M.; Peyton, A.; Yin, W., Acceleration of frequency sweeping in eddy-current computation. *IEEE Transactions on Magnetics* **2017,** 53, (7), 1–8.
43. Yin, W.; Lu, M.; Yin, L.; Zhao, Q.; Meng, X.; Zhang, Z.; Peyton, A., Acceleration of eddy current computation for scanning probes. *Insight-Non-Destructive Testing and Condition Monitoring* **2018,** 60, (10), 547–555.
44. Theodoulidis, T., Analytical model for tilted coils in eddy-current nondestructive inspection. *IEEE Transactions on Magnetics* **2005,** 41, (9), 2447–2454.
45. Chao, X.; Li, Y.; Nie, J., Tilt angle measurement based on arrayed eddy current sensors. *Journal of Magnetics* **2016,** 21, (4), 524–528.
46. Burke, S., Eddy-current induction in a uniaxially anisotropic plate. *Journal of applied physics* **1990,** 68, (7), 3080–3090.
47. Beissner, R.; Sablik, M., Theory of eddy currents induced by a nonsymmetric coil above a conducting half-space. *Journal of applied physics* **1984,** 56, (2), 448–454.
48. Burke, S.; Ibrahim, M., Mutual impedance of air-cored coils above a conducting plate. *Journal of Physics D: Applied Physics* **2004,** 37, (13), 1857.
49. Harfield, N.; Bowler, J. R., Theory of thin-skin eddy-current interaction with surface cracks. *Journal of applied physics* **1997,** 82, (9), 4590–4603.
50. Ditchburn, R.; Burke, S.; Posada, M., Eddy-current nondestructive inspection with thin spiral coils: Long cracks in steel. *Journal of Nondestructive Evaluation* **2003,** 22, (2), 63–77.
51. Lu, M.; Meng, X.; Huang, R.; Peyton, A.; Yin, W., Analysis of tilt effect on notch depth profiling using thin-skin regime of driver-pickup eddy-current sensor. *Sensors* **2021,** 21, (16), 5536.
52. O'Toole, M. D.; Karimian, N.; Peyton, A. J., Classification of nonferrous metals using magnetic induction spectroscopy. *IEEE Transactions on Industrial Informatics* **2017,** 14, (8), 3477–3485.
53. Liu, Y.; Zhang, Z.; Yin, W.; Chen, H.; Yu, Z.; Wang, Q., A Novel Conductivity Classification Technique for Nonmagnetic Metal Immune to Tilt Variations Using Eddy Current Testing. *IEEE Access* **2021,** 9, 135334–135342.
54. Du, Y.; Zhang, Z.; Yin, W.; Zhu, S.; Chen, Z.; Xu, H., Conductivity classification of non-magnetic tilting metals by eddy current sensors. *Sensors* **2020,** 20, (9), 2608.
55. Du, Y.; Zhang, Z.; Yin, W.; Tytko, G., Sloping-invariance for nonferrous metallic slabs at multiple frequencies by eddy current sensors. *IEEE Access* **2021,** 9, 59949–59956.
56. Hampton, J.; Fletcher, A.; Tesfalem, H.; Peyton, A.; Brown, M., A comparison of non-linear optimisation algorithms for recovering the conductivity depth profile of an electrically conductive block using eddy current inspection. *NDT & E International* **2022,** 125, 102571.
57. Uzal, E.; Moulder, J.; Rose, J., Experimental determination of the near-surface conductivity profiles of metals from electromagnetic induction (eddy current) measurements. *Inverse Problems* **1994,** 10, (3), 753.
58. Cai, W.; Jomdecha, C.; Zhao, Y.; Wang, L.; Xie, S.; Chen, Z., Quantitative evaluation of electrical conductivity inside stress corrosion crack with electromagnetic NDE methods. *Philosophical Transactions of the Royal Society A* **2020,** 378, (2182), 20190589.
59. Ge, J.; Yusa, N.; Fan, M., Frequency component mixing of pulsed or multi-frequency eddy current testing for nonferromagnetic plate thickness measurement using a multi-gene genetic programming algorithm. *NDT & E International* **2021,** 120, 102423.
60. Meng, X.; Lu, M.; Yin, W.; Bennecer, A.; Kirk, K. J., Inversion of lift-off distance and thickness for nonmagnetic metal using eddy current testing. *IEEE Transactions on Instrumentation and Measurement* **2020,** 70, 1–8.
61. Chen, X.; Li, J.; Wang, Z., Inversion method in pulsed eddy current testing for wall thickness of ferromagnetic pipes. *IEEE Transactions on Instrumentation and Measurement* **2020,** 69, (12), 9766–9773.

62. Haddar, H.; Jiang, Z.; Riahi, M. K., A robust inversion method for quantitative 3D shape reconstruction from coaxial eddy current measurements. *Journal of Scientific Computing* **2017,** 70, (1), 29−59.
63. Du, Y.; Li, X.; Xie, S.; Yang, S.; Chen, Z., Reconstruction of cracks in a carbon fiber-reinforced polymer laminate plate from signals of eddy current testing. *Journal of Composite Materials* **2020,** 54, (24), 3527−3536.
64. Adewale, I. D.; Tian, G. Y., Decoupling the influence of permeability and conductivity in pulsed eddy-current measurements. *IEEE Transactions on Magnetics* **2012,** 49, (3), 1119−1127.
65. Vasic, D.; Bilas, V.; Ambrus, D., Validation of a coil impedance model for simultaneous measurement of electromagnetic properties and inner diameter of a conductive tube. *IEEE Transactions on Instrumentation and Measurement* **2006,** 55, (1), 337−342.
66. Vasić, D.; Bilas, V. Lumped representation in inductive measurement of metal casing properties, In 2010 IEEE Instrumentation & Measurement Technology Conference Proceedings, 2010.
67. Ghaffari, A.; Krstić, M.; Nešić, D., Multivariable Newton-based extremum seeking. *Automatica* **2012,** 48, (8), 1759−1767.
68. Schöbi, R., Surrogate models for uncertainty quantification in the context of imprecise probability modelling. *IBK Bericht* **2019,** 505.
69. Zhang, J.; Yin, J.; Wang, R., Basic framework and main methods of uncertainty quantification. *Mathematical Problems in Engineering* **2020,** 2020, 6068203.
70. Aster, R. C.; Borchers, B.; Thurber, C. H., Chapter Three-Rank Deficiency and Ill-Conditioning. In *Parameter Estimation and Inverse Problems (Third Edition)*, Aster, R. C.; Borchers, B.; Thurber, C. H., Eds. Elsevier: 2019; p 55−91.
71. Poli, R.; Kennedy, J.; Blackwell, T., Particle swarm optimization. *Swarm Intelligence* **2007,** 1, (1), 33−57.
72. Salcedo-Sanz, S., Modern meta-heuristics based on nonlinear physics processes: A review of models and design procedures. *Physics Reports* **2016,** 655, 1−70.
73. Parouha, R. P.; Verma, P., State-of-the-art reviews of meta-heuristic algorithms with their novel proposal for unconstrained optimization and applications. *Archives of Computational Methods in Engineering* **2021,** 28, (5), 4049−4115.
74. Lu, M. Forward and inverse analysis for non-destructive testing based on electromagnetic computation methods. PhD Thesis, The University of Manchester (United Kingdom), 2018.
75. Hampton, J.; Tesfalem, H.; Dorn, O.; Fletcher, A.; Peyton, A.; Brown, M., Calibration of a Finite Element Forward Model in Eddy Current Inspection. *IEEE Sensors Journal* **2022,** 22, (11), 10699−10707.
76. Wu, J.; Zhou, D.; Wang, J.; Guo, X.; You, L.; An, W.; Zhang, H. Surface crack detection for carbon fiber reinforced plastic (CFRP) materials using pulsed eddy current testing, In 2014 IEEE Far East Forum on Nondestructive Evaluation/Testing, 2014.
77. O'Toole, M. D.; Karimian, N.; Peyton, A. J. Fast classification of non-magnetic metal targets using eddy-current based impedance spectroscopy, In 2017 IEEE SENSORS, 2017.
78. Tao, Y.; Xu, H.; Chen, Z.; Huang, R.; Yin, W. Automatic feature extraction method for crack detection in eddy current testing, In 2019 IEEE International Instrumentation and Measurement Technology Conference (I2MTC), 2019.
79. Tao, Y.; Ktistis, C.; Zhao, Y.; Yin, W.; Peyton, A. J., A Class D Power Amplifier for Multifrequency Eddy Current Testing Based on Multisimultaneous-Frequency Selective Harmonic Elimination Pulsewidth Modulation. *IEEE Transactions on Industrial Electronics* 67, (10), 8799−8807.
80. Bernieri, A.; Betta, G.; Ferrigno, L.; Laracca, M. Multi-frequency ECT method for defect depth estimation, In IEEE Sensors Applications Symposium, 2012.
81. Yin, W.; Dickinson, S. J.; Peyton, A. J., A multi-frequency impedance analysing instrument for eddy current testing. *Measurement Science and Technology* **2006,** 17, (2), 393−402.

82. Avila, J.; Chen, Z.; Xu, H.; Yin, W. A multi-frequency NDT system for imaging and detection of cracks, In 2018 IEEE International Symposium on Circuits and Systems (ISCAS), 2018.
83. Betta, G.; Ferrigno, L.; Laracca, M.; Burrascano, P.; Ricci, M. Optimized complex signals for eddy current testing, In 2014 IEEE International Instrumentation and Measurement Technology Conference (I2MTC) Proceedings, 2014.
84. Yin, W.; Chen, G.; Chen, L.; Wang, B., The Design of a Digital Magnetic Induction Tomography (MIT) System for Metallic Object Imaging Based on Half Cycle Demodulation. *IEEE Sensors Journal* **2011,** 11, (10), 2233–2240.
85. Yin, W.; Chen, G.; Jian, J.; Cui, Z. The design of a FPGA-based digital magnetic induction tomography (MIT) system for metallic object imaging, In IEEE Instrumentation & Measurement Technology Conference, 2010.
86. Wei, H. Y.; Soleimani, M., Hardware and software design for a National Instrument-based magnetic induction tomography system for prospective biomedical applications. *Physiological Measurement* **2012,** 33, (5), 863.
87. Hanyang; Avila, S.; Ricardo, J.; Fanfu; Roy; Matthew, J.; Xie; Yuedong; Zhou; Frank, Imaging x70 weld cross-section using electromagnetic testing. *NDT & E International: Independent Nondestructive Testing and Evaluation* **2018,** 98, 155–160.
88. Zhu, W.; Yang, H.; Luinenburg, A.; Van, d. B., F.; Dickinson, S.; Yin, W.; Peyton, A. J., Development and deployment of online multifrequency electromagnetic system to monitor steel hot transformation on runout table of hot strip mill. *Ironmaking & Steelmaking* **2014,** 41, (9), 685–693.
89. Yin, W.; Peyton, A. J., A planar EMT system for the detection of faults on thin metallic plates. *Measurement Science & Technology* **2006,** 17, (8), 2130–2135.
90. Chao, W.; He, H.; Cui, Z.; Cao, Q.; Ping, Z.; Wang, H., A novel EMT system based on TMR sensors for reconstruction of permeability distribution. *Measurement Science and Technology* **2018,** 29, (10), 104008.
91. Ma, X.; Peyton, A. J.; Higson, S. R.; Lyons, A.; Dickinson, S. J., Hardware and software design for an electromagnetic induction tomography (EMT) system for high contrast metal process applications. *Measurement Science & Technology* **2006,** 17, (1), 111–118.
92. Kekelj, M.; Bulic, N.; Sucic, V. An FPGA implementation of the Goertzel algorithm in a Non-Destructive Eddy current Testing, In 2017 International Conference on Signals and Systems (ICSigSys), 16–18 May, 2017.
93. Hamel, M.; Mohellebi, H., A LabVIEW-based real-time acquisition system for crack detection in conductive materials. *Mathematics and Computers in Simulation* **2020,** 167, 381–388.
94. Zhang, N.; Peng, L.; He, Y.; Ye, C., Flexible Probe With Array Tunneling Magnetoresistance Sensors for Curved Structure Inspection. *IEEE Transactions on Instrumentation and Measurement* **2022,** 71, 1–9.
95. Soni, A. K.; Rao, B. P., Lock-in Amplifier Based Eddy Current Instrument for Detection of Sub-surface Defect in Stainless Steel Plates. *Sensing and Imaging* **2018,** 19, (1), 32.
96. Aguiam, D. E.; Rosado, L. S.; Ramos, P. M.; Piedade, M., Heterodyning based portable instrument for eddy currents non-destructive testing. *Measurement* **2015,** 73, 146–157.
97. Zhang, G.; Xie, X.; You, Y., Multi-Channel Eddy Current Detector Based on Virtual Instrument Technology and Self-Balancing Technology. *Sensing and Imaging* **2021,** 22, (1), 12.
98. Dingley, G.; Soleimani, M., Multi-Frequency Magnetic Induction Tomography System and Algorithm for Imaging Metallic Objects. *Sensors* **2021,** 21, (11), 3671.
99. Technologies, K. Impedance Measurement Handbook. www.keysight.com (18 Oct. 2022),
100. Lu, M.; Meng, X.; Yin, W.; Qu, Z.; Wu, F.; Tang, J.; Xu, H.; Huang, R.; Chen, Z.; Zhao, Q., Thickness measurement of non-magnetic steel plates using a novel planar triple-coil sensor. *NDT & E International* **2019,** 107, 102148.
101. Yin, W.; Xu, K., A novel triple-coil electromagnetic sensor for thickness measurement immune to lift-off variations. *IEEE Transactions on Instrumentation and Measurement* **2015,** 65, (1), 164–169.

102. Rosell-Ferrer, J.; Merwa, R.; Brunner, P.; Scharfetter, H., A multifrequency magnetic induction tomography system using planar gradiometers: data collection and calibration. *Physiological Measurement* **2006,** 27, (5).
103. Abdel-Rehim, O. A.; Davidson, J. L.; Marsh, L. A.; O'Toole, M. D.; Peyton, A. J., Magnetic Polarizability Tensor Spectroscopy for Low Metal Anti-personnel Mine Surrogates. *IEEE Sensors Journal* **2016,** 16, (10), 3775–3783.
104. Chen, Z.; Salas-Avlia, J. R.; Tao, Y.; Yin, W.; Ricardo, J., A novel hybrid serial/parallel multi-frequency measurement method for impedance analysis in eddy current testing. *Review of Scientific Instruments* **2020,** 91, (2), 024703.
105. Xu, Z.; Wang, X.; Deng, Y., Rotating focused field Eddy-current sensing for arbitrary orientation defects detection in carbon steel. *Sensors* **2020,** 20, (8), 2345.
106. Center for Nondestructive Evaluation, N.-E. o. Nondestructive Evaluation Techniques. https://www.nde-ed.org/NDETechniques/EddyCurrent/ProbesCoilDesign/ProbesConfig.xhtml (18 Oct. 2022),
107. Gao, P.; Wang, C.; Li, Y.; Cong, Z., Electromagnetic and eddy current NDT in weld inspection: A review. *Insight-Non-Destructive Testing and Condition Monitoring* **2015,** 57, (6), 337–345.
108. Sharif, N. A.; Ramli, R.; Nuawi, M. Z.; Mohamed, A. Z., Theory and development of magnetic flux leakage sensor for flaws detection: A review. *Jurnal Kejuruteraan* **2020,** 32, (3), 385–395.
109. Halchenko, V.; Trembovetskaya, R.; Tychkov, V., Surface Eddy Current Probes: Excitation Systems of the Optimal Electromagnetic Field (Review). *Devices and Methods of Measurements* **2020,** 11, 91–104.
110. Hoshikawa, H.; Koyama, K., Eddy current distribution using parameters normalized by standard penetration depth. In *Review of Progress in Quantitative Nondestructive Evaluation*, Springer: 1999; p 515–521.
111. Mook, G.; Hesse, O.; Uchanin, V., Deep penetrating eddy currents and probes. *Materials Testing* **2007,** 49, (5), 258–264.
112. Jiao, S.; Liu, X.; Zeng, Z., Intensive study of skin effect in eddy current testing with pancake coil. *IEEE Transactions on Magnetics* **2017,** 53, (7), 1-8.
113. Zeng, Z.; Ding, P.; Li, J.; Jiao, S.; Lin, J.; Dai, Y., Characteristics of Eddy Current Attenuation and Thickness Measurement of Metallic Plate. *Chinese Journal of Mechanical Engineering* **2019,** 32, 106.
114. Hayashi, M.; Saito, T.; Nakamura, Y.; Sakai, K.; Kiwa, T.; Tanikura, I.; Tsukada, K., Extraction Method of Crack Signal for Inspection of Complicated Steel Structures Using A Dual-Channel Magnetic Sensor. *Sensors* **2019,** 19, (13).
115. Yin, W.; Peyton, A. J., Thickness measurement of non-magnetic plates using multi-frequency eddy current sensors. *NDT & E International* **2007,** 40, (1), 43–48.
116. Mori, H.; Kagaya, H.; Inamoto, Y.; Izumi, S. I.; Yashima, K.; Takagi, T., Numerical Analysis of Eddy Current Distribution in Submental Region Induced by Magnetic Stimulation for Treating Dysphagia. *IEEE Transactions on Neural Systems and Rehabilitation Engineering* **2020,** 28, (5), 1178–1186.
117. Chen, D.; Li, Y.; Pan, M.; Tian, W., Flexible planar electromagnetic sensor array fabricated with printing electronic technology. *Measurement* **2018,** 129, 499–503.
118. Daura, L. U.; Tian, G.; Yi, Q.; Sophian, A., Wireless power transfer-based eddy current non-destructive testing using a flexible printed coil array. *Philosophical Transactions of the Royal Society A* **2020,** 378, (2182), 20190579.
119. Avila, J. R. S.; How, K. Y.; Lu, M.; Yin, W., A novel dual modality sensor with sensitivities to permittivity, conductivity, and permeability. *IEEE Sensors Journal* **2017,** 18, (1), 356–362.
120. Hamia, R.; Cordier, C.; Dolabdjian, C., Eddy-current non-destructive testing system for the determination of crack orientation. *Ndt & E International* **2014,** 61, 24–28.
121. Dogaru, T.; Smith, C.; Schneider, R.; Smith, S. Deep crack detection around fastener holes in airplane multi-layered structures using GMR - based eddy current probes, In AIP Conference Proceedings, 2004.
122. Ye, C.; Huang, Y.; Udpa, L.; Udpa, S. S., Differential sensor measurement with rotating current excitation for evaluating multilayer structures. *IEEE Sensors Journal* **2015,** 16, (3), 782–789.

123. Ye, C.; Rosell, A.; Haq, M.; Stitt, E.; Udpa, L.; Udpa, S., EC probe with orthogonal excitation coils and TMR sensor for CFRP inspection. *International Journal of Applied Electromagnetics and Mechanics* **2019,** 59, (4), 1247−1255.
124. Ripka, P.; Janosek, M., Advances in magnetic field sensors. *IEEE Sensors journal* **2010,** 10, (6), 1108−1116.
125. Hainz, S.; de la Torre, E.; Güttinger, J. Comparison of magnetic field sensor technologies for the use in wheel speed sensors, In 2019 IEEE International Conference on Industrial Technology (ICIT), 2019.
126. Hadjigeorgiou, N.; Asimakopoulos, K.; Papafotis, K.; Sotiriadis, P. P., Vector Magnetic Field Sensors: Operating Principles, Calibration, and Applications. *IEEE Sensors Journal* **2020,** 21, (11), 12531−12544.
127. Lu, M.; Meng, X.; Huang, R.; Chen, L.; Peyton, A.; Yin, W.; Qu, Z., Thickness measurement of circular metallic film using single-frequency eddy current sensor. *NDT & E International* **2021,** 119, 102420.
128. Lu, M.; Meng, X.; Huang, R.; Chen, L.; Peyton, A.; Yin, W., A high-frequency phase feature for the measurement of magnetic permeability using eddy current sensor. *NDT & E International* **2021,** 123, 102519.
129. Wang, C.; Wang, R. C.; Liang, X.; Ye, J. M.; Chen, X. Y., Design and optimization of electromagnetic tomography and electrical resistance tomography dual-modality sensor. *Measurement Science and Technology* **2022,** 33, (10).
130. Arellano, Y.; Hunt, A.; Haas, O.; Ahmed, H.; Ma, L., Multiple regression-based prediction correlations for enhanced sensor design of magnetic induction tomography systems. *Measurement Science and Technology* **2019,** 31, (2), 024002.
131. She, S.; Chen, Y.; He, Y.; Zou, X., Optimal design of remote field eddy current testing probe for ferromagnetic pipeline inspection. *Measurement* **2021,** 168, 108306.
132. Avila, J. R. S.; Lu, M.; Huang, R.; Chen, Z.; Zhu, S.; Yin, W., Accurate measurements of plate thickness with variable lift-off using a combined inductive and capacitive sensor. *NDT & E International* **2020,** 110, 102202.
133. Yin, W.; Peyton, A., Thickness measurement of non-magnetic plates using multi-frequency eddy current sensors. *NDT & E International* **2007,** 40, (1), 43−48.
134. Lu, M.; Huang, R.; Yin, W.; Zhao, Q.; Peyton, A., Measurement of permeability for ferrous metallic plates using a novel lift-off compensation technique on phase signature. *IEEE Sensors Journal* **2019,** 19, (17), 7440−7446.
135. Lu, M.; Meng, X.; Huang, R.; Chen, L.; Peyton, A.; Yin, W., Measuring lift-off distance and electromagnetic property of metal using dual-frequency linearity feature. *IEEE Transactions on Instrumentation and Measurement* **2020,** 70, 1−9.
136. Dinh, C.-H.; Jeng, J.-T.; Huang, G.-W.; Chen, J.-Y.; Chiang, Y.-S.; Doan, V.-D.; Pham, T.-T., Real-time thickness measurement using resonant eddy-current sensor. *IEEE Transactions on Instrumentation and Measurement* **2021,** 70, 1−9.
137. Lu, M.; Zhu, W.; Yin, L.; Peyton, A. J.; Yin, W.; Qu, Z., Reducing the lift-off effect on permeability measurement for magnetic plates from multifrequency induction data. *IEEE Transactions on Instrumentation and Measurement* **2017,** 67, (1), 167−174.
138. Wang, H.; Li, W.; Feng, Z., Noncontact thickness measurement of metal films using eddy-current sensors immune to distance variation. *IEEE Transactions on Instrumentation and Measurement* **2015,** 64, (9), 2557−2564.
139. Li, W.; Wang, H.; Feng, Z., Non-contact online thickness measurement system for metal films based on eddy current sensing with distance tracking technique. *Review of Scientific Instruments* **2016,** 87, (4), 045005.
140. Yin, W.; Dickinson, S. J.; Peyton, A., Imaging the continuous conductivity profile within layered metal structures using inductance spectroscopy. *IEEE Sensors Journal* **2005,** 5, (2), 161−166.
141. Lu, M.; Xu, H.; Zhu, W.; Yin, L.; Zhao, Q.; Peyton, A.; Yin, W.; Senior Member, I., Conductivity Lift-off Invariance and measurement of permeability for ferrite metallic plates. *NDT & E International* **2018,** 95, 36−44.
142. Yin, W.; Meng, X.; Lu, M.; Zhao, Q.; Xu, H.; Zhang, Z.; Peyton, A., Permeability invariance phenomenon and measurement of electrical conductivity for ferrite metallic plates. *Insight-Non-Destructive Testing and Condition Monitoring* **2019,** 61, (8), 472−479.
143. Cheng, W., Thickness measurement of metal plates using swept-frequency eddy current testing and impedance normalization. *IEEE Sensors Journal* **2017,** 17, (14), 4558−4569.

144. Yin, W.; Peyton, A. J., Thickness measurement of metallic plates with an electromagnetic sensor using phase signature analysis. *IEEE Transactions on Instrumentation and Measurement* **2008,** 57, (8), 1803–1807.
145. Angani, C. S.; Ramos, H. G.; Ribeiro, A. L.; Rocha, T. J.; Baskaran, P., Lift-off point of intersection feature in transient eddy-current oscillations method to detect thickness variation in stainless steel. *IEEE Transactions on Magnetics* **2016,** 52, (6), 1–8.
146. Lu, M.; Meng, X.; Huang, R.; Chen, L.; Peyton, A.; Yin, W., Lift-off invariant inductance of steels in multi-frequency eddy-current testing. *NDT & E International* **2021,** 121, 102458.
147. Mohseni, E.; Habibzadeh Boukani, H.; Ramos França, D.; Viens, M., A study of the automated eddy current detection of cracks in steel plates. *Journal of Nondestructive Evaluation* **2020,** 39, (1), 1–12.
148. Li, W.; Chen, G.; Ge, J.; Yin, X.; Li, K., High sensitivity rotating alternating current field measurement for arbitrary-angle underwater cracks. *NDT & E International* **2016,** 79, 123–131.
149. Pasadas, D. J.; Ribeiro, A. L.; Ramos, H. G.; Rocha, T. J., Inspection of cracks in aluminum multilayer structures using planar ECT probe and inversion problem. *IEEE Transactions on Instrumentation and Measurement* **2017,** 66, (5), 920–927.
150. Yin, L.; Ye, B.; Zhang, Z.; Tao, Y.; Xu, H.; Avila, J. R. S.; Yin, W., A novel feature extraction method of eddy current testing for defect detection based on machine learning. *NDT & E International* **2019,** 107, 102108.
151. Bajracharya, S.; Sasaki, E.; Tamura, H., Numerical study on corrosion profile estimation of a corroded steel plate using eddy current. *Structure and Infrastructure Engineering* **2019,** 15, (9), 1151–1164.
152. Xu, H.; Lu, M.; Avila, J.; Zhao, Q.; Zhou, F.; Meng, X.; Yin, W., Imaging a weld cross-section using a novel frequency feature in multi-frequency eddy current testing. *Insight-Non-Destructive Testing and Condition Monitoring* **2019,** 61, (12), 738–743.
153. Ribeiro, A. L.; Alegria, F.; Postolache, O. A.; Ramos, H. M. G., Liftoff correction based on the spatial spectral behavior of eddy-current images. *IEEE Transactions on Instrumentation and Measurement* **2010,** 59, (5), 1362–1367.
154. Yin, W.; Peyton, A., A planar EMT system for the detection of faults on thin metallic plates. *Measurement Science and Technology* **2006,** 17, (8), 2130.
155. Shao, Y.; Meng, T.; Yu, K.; Xia, Z.; Huang, R.; Tao, Y.; Chen, Z.; Avila, J. R. S.; Yin, W., Automatic Detection and Imaging of Rivet Hole Defects for Aircraft Structures with Optimised Sensor Array Using Eddy Current Method and Image Analysis. *IEEE Sensors Journal* **2022**, (early access).
156. Ferrigno, L.; Laracca, M.; Malekmohammadi, H.; Tian, G. Y.; Ricci, M., Comparison of time and frequency domain features' immunity against lift-off in pulse-compression eddy current imaging. *NDT & E International* **2019,** 107, 102152.
157. Betta, G.; Ferrigno, L.; Laracca, M.; Ramos, H.; Ricci, M.; Ribeiro, A.; Silipigni, G. Fast 2D crack profile reconstruction by image processing for Eddy-Current Testing, In 2015 IEEE Metrology for Aerospace (MetroAeroSpace), 2015.
158. Wang, Y.; Chen, Y.; Zhang, Y.; Chen, H.; Yu, S., Generalised Hermite–Gaussian beams and mode transformations. *Journal of Optics* **2016,** 18, (5), 055001.
159. Ahmed, S.; Reboud, C.; Lhuillier, P.-E.; Calmon, P.; Miorelli, R., An adaptive sampling strategy for quasi real time crack characterization on eddy current testing signals. *NDT & E International* **2019,** 103, 154–165.
160. Fan, M.; Wang, Q.; Cao, B.; Ye, B.; Sunny, A. I.; Tian, G., Frequency optimization for enhancement of surface defect classification using the eddy current technique. *Sensors* **2016,** 16, (5), 649.
161. Rosado, L. S.; Janeiro, F. M.; Ramos, P. M.; Piedade, M., Defect characterization with eddy current testing using nonlinear-regression feature extraction and artificial neural networks. *IEEE Transactions on Instrumentation and Measurement* **2013,** 62, (5), 1207–1214.
162. Deng, W.; Bao, J.; Ye, B., Defect Image Recognition and Classification for Eddy Current Testing of Titanium Plate Based on Convolutional Neural Network. *Complexity* **2020,** 2020, 8868190.

163. Meng, T.; Tao, Y.; Chen, Z.; Avila, J. R. S.; Ran, Q.; Shao, Y.; Huang, R.; Xie, Y.; Zhao, Q.; Zhang, Z., Depth evaluation for metal surface defects by eddy current testing using deep residual convolutional neural networks. *IEEE Transactions on Instrumentation and Measurement* **2021,** 70, 1–13.

164. Hampe, N.; Katscher, U.; Van den Berg, C. A.; Tha, K. K.; Mandija, S., Investigating the challenges and generalizability of deep learning brain conductivity mapping. *Physics in Medicine & Biology* **2020,** 65, (13), 135001.

4. Fast estimation of pipe properties using simplified analytical solution in eddy-current testing

Fast estimation of metallic pipe properties using simplified analytical solution in eddy-current testing

Zihan Xia, Jiangjiang Yan, Ruochen Huang, Mingyang Lu, *Member, IEEE,* Ziqiang Cui, *Member, IEEE,* Anthony Peyton, Wuliang Yin*, *Senior Member, IEEE,* and Wuqiang Yang, *Fellow, IEEE*

***Abstract*—The eddy-current testing technique has been extensively explored for the measurement of metallic pipes in various industrial processes. In this study, a simplified analytical model of metallic pipes encircled by a coaxial sensor is derived according to the asymptotic forms of modified Bessel functions. The original Dodd and Deeds (DD) model is thus approximated by an elementary function describing the relationship between the measured inductance spectrum and the pipe properties. Due to the simple nature of the elementary function, the Jacobian matrix can be evaluated much more efficiently. Accordingly, a fast Newton-Raphson method-based optimization approach is developed. The proposed method has been evaluated by comparing with the numerical simulation of finite element method (FEM) and experimental measurements which indicate its effectiveness for the measurement of metallic pipe properties.**

***Index Terms*—Electromagnetic sensing, eddy current testing, analytical model, inverse problem, wall thickness measurement.**

I. Introduction

Being non-invasive and non-destructive, the electromagnetic (EM) sensing method is a well-established technique for the measurement of oil-well casing and metallic pipes/tubes, ensuring the safety and efficiency of industrial production. Especially, the eddy current testing method has demonstrated its effectiveness in the measurement of the crucial properties of metallic pipes [1, 2, 3], *i.e.* radius, conductivity together with permeability.

In the eddy-current testing scenario, the forward and inverse problems are two major issues, which bridges the gap between the inductance spectrum (a variety of the frequency-dependent mutual inductance between coils) and pipe properties. The forward problem aims to calculate the inductance spectrum for given metallic pipe properties, while the inverse problem is to determine the pipe properties from the inductance spectrum measurement.

On the one hand, it is prevailing to adopt the analytical method, initially investigated by Dodd and Deeds [4, 5], and FEM to solve the forward problem [6, 7]. In comparison, the analytical method characterized by the explicit solution is usually more efficient. Furthermore, the computational cost of the analytical model has been reduced through the approximation of integral equation, by employing the truncated region eigenfunction expansion (TREE) method [8, 9]. In addition, the computational efficiency can be elevated by simplifying the analytical expression, which has been explored for the plate model [10, 11] but has been rarely discussed for the pipe model yet. Compared with the former studies relating to analytical model simplification in [7, 12, 13, 14], this study focuses on the analytical model of pipe encircled by a coaxial coil sensor. In the analytical expression of inductance calculation, the term determined by the pipe properties is simplified according to the asymptotic forms of the modified Bessel function. The simplification involves a range of spacial frequencies of cylindrical harmonics rather than merely retaining a dominant spacial frequency component [15] which requires being updated for various measuring objects.

On the other hand, the inverse problem also depends on the forward modeling. Most of the previous studies explore the relationships between the properties of metallic objects and characteristic frequency of the inductance spectrum, *e.g.* zero-crossing frequency (the frequency at which the real part of inductance change is zero), peak frequency (the frequency where the imaginary part of inductance change reaches its maximum), conductance invariant phenomenon [16, 17, 18], *etc.* This is commonly achieved by extracting the relations according to the simplified analytical model, or performing the numerical analysis based on the comprehensive simulation results [19, 20, 21]. There exists a few studies investigating the optimization approaches which minimize the discrepancies, *e.g.* in terms of the Euclidean distance, between the calculated and measured inductance to estimate the object properties [22, 23, 24, 25]. Previous studies have reported that the conductivity and permeability are difficult

Manuscript updated March 12, 2023, and submitted xxx xx, 2021.

This research is financially supported from China Scholarship Council (CSC).

Mr. Zihan Xia, Mr. Jiangjiang Yan, Prof. Anthony Peyton, Dr. Wuliang Yin and Prof. Wuqiang Yang are with the School of Electrical and Electronic Engineering, University of Manchester, Manchester M13 9PL, U.K. (*Corresponding author: Wuliang Yin. email: wuliang.yin@manchester.ac.uk*)

Dr. Ruochen Huang was with the School of Electrical and Electronic Engineering, University of Manchester, Manchester M13 9PL, U.K., and now with the College of Electrical Engineering and Automation, Fuzhou University, Fuzhou 350108, China.

Dr. Mingyang Lu was with the School of Electrical and Electronic Engineering, University of Manchester, Manchester M13 9PL, U.K.

Dr. Ziqiang Cui is with the School of Electrical and Information Engineering, Tianjin University, Tianjin 300072, China.

to be estimated simultaneously, as their influences on inductance measurement are strongly coupled [26, 27, 28], which is indicated by the permeability-to-conductivity ratio [29] and by the inductance iso-surface in the logarithm domain of pipe properties [30]. Recently, the property estimation of metallic plate have been investigated based on the Newton-Raphson method, with the updating strategy of sensitivity matrix [31]. Nevertheless, the efficiency and stability of property estimation by optimization still require further improvement, which can be achieved by employing the simplified analytical model and selecting the appropriate estimated variables. Aiming at the non-linear optimization problem, the Newton-Raphson and Levenberg–Marquardt (LM) algorithm are frequently adopted [32, 33, 34]. Since the LM algorithm interpolates between the Newton-Raphson and gradient descent methods, it reaches the convergence point slower than the Newton-Raphson method for a reasonable starting point. Therefore, the pipe property estimation is studied based on the Newton-Raphson method, following the previous research.

In this study, the DD analytical pipe model is simplified to an elementary function according to the asymptotic forms of modified Bessel functions. The simplification facilitates the estimation of pipe properties and accounts for a simple estimation approach of inductance peak frequency for the non-magnetic thin thickness pipes. In addition, both numerical simulation and experiments have been conducted for the comprehensive evaluation of pipe property estimation, which indicates the improved optimization stability and computational speed, due to the model simplification.

The rest of the paper is arranged as follows. Section II-A introduces the simplified analytical solution of metallic pipe encircled by a coaxial sensor. The algorithm estimating the pipe properties is illustrated in section II-B. The numerical and experimental evaluations are summarized in section III then conclusions are presented in section IV.

II. Methods

The schematic of the forward and inverse problem for metallic pipe measurement is illustrated in Fig. 1. In the forward problem, the classic Dodd and Deeds (DD) and truncated region eigenfunction expansion (TREE) models are briefly introduced, from which the simplified analytical model is derived by employing the asymptotic forms of the modified Bessel functions. Subsequently, the peak frequency estimation method for the non-magnetic thin thickness pipes is obtained from the simplified model. In the inverse problem, the optimization method for pipe properties estimation is described, including the strategies to improve the accuracy and stability.

A. Simplification of analytical solution

The analytical solution of infinite long metallic pipe encircled by the coaxial coil sensor, as shown in Fig. 2, can be obtained from the governing equation, through the separation of variables method. The mutual inductance

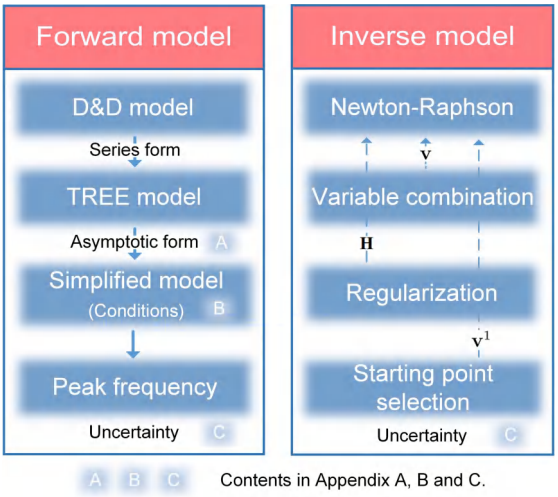

Fig. 1. Flowchart of proposed method for pipe property estimation

variation due to the measured pipe (referred to as inductance hereinafter) is expressed by $\Delta M = M - M_a$, where M and M_a indicate the inductance measuring the pipe and in free space, respectively. According to the analytical solution for the cylindrical model [4], ΔM can be calculated by

$$\Delta M = k_M \int_0^\infty S(\alpha) M_{\mathrm{s}}(\alpha) d\alpha \tag{1}$$

$$\begin{aligned} S(\alpha) = \frac{1}{bD(\alpha)K_1(\alpha b)} \{ & K_1(\alpha_2 b) [\beta_2 I_1(\alpha_1 a) I_0(\alpha_2 a) \\ & - \beta_1 I_1(\alpha_2 a) I_0(\alpha_1 a)] + I_1(\alpha_2 b) [\beta_1 K_1(\alpha_2 a) I_0(\alpha_1 a) \\ & + \beta_2 K_0(\alpha_2 a) I_1(\alpha_1 a)] \} - \frac{I_1(\alpha b)}{K_1(\alpha b)} \end{aligned} \tag{2}$$

$$\begin{aligned} D(\alpha) = & [\beta_2 K_0(\alpha_2 b) K_1(\alpha b) - \alpha K_0(\alpha b) K_1(\alpha_2 b)] \\ & \times [\beta_1 I_1(\alpha_2 a) I_0(\alpha_1 a) - \beta_2 I_1(\alpha_1 a) I_0(\alpha_2 a)] \\ & + [\beta_2 K_0(\alpha_2 a) I_1(\alpha_1 a) + \beta_1 K_1(\alpha_2 a) I_0(\alpha_1 a)] \\ & \times [\alpha I_1(\alpha_2 b) K_0(\alpha b) + \beta_2 I_0(\alpha_2 b) K_1(\alpha b)] \end{aligned} \tag{3}$$

$$M_{\mathrm{s}}(\alpha) = K^2(r_2, r_1) f \cos(\alpha) / \alpha^6 \tag{4}$$

$$K(r_2, r_1) = \int_{\alpha r_1}^{\alpha r_2} \alpha r K_1(\alpha r) d\alpha r \tag{5}$$

$$\begin{aligned} f \cos(\alpha) = & \, 2\cos(\alpha d) - \cos\left(\alpha(l_2 - l_1 + d)\right) \\ & - \cos\left(\alpha(l_1 - l_2 + d)\right) \end{aligned} \tag{6}$$

where the phase term $S(\alpha)$ is determined by the pipe properties and excitation frequency, the sensor term $M_{\mathrm{s}}(\alpha)$ relates to the sensor configuration, $k_M = 2N^2\mu_0 r_0 / \left[(r_2 - r_1)^2 (l_2 - l_1)^2\right]$, N is the turns of coil, μ_0 is the vacuum permeability, α is the spacial frequency, $\alpha_1 = \beta_1 = \alpha$, $\alpha_2 = \sqrt{\alpha^2 + j\omega\mu_0\mu_{\mathrm{r}}\sigma}$, $\beta_2 = \alpha_2/\mu_r$, $I(\cdot)$ and $K(\cdot)$ are the modified Bessel functions of the first and

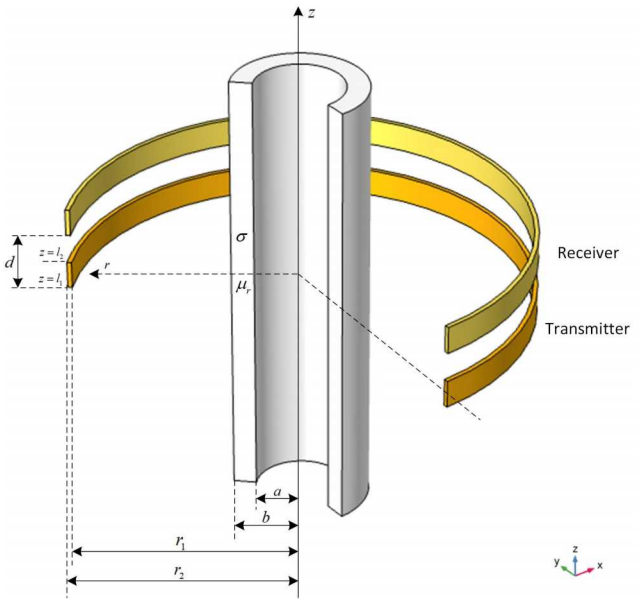

Fig. 2. Induction coils encircling a coaxial metallic pipe

the second kind, respectively. Other parameters correspond to the dimensions of sensor.

The computational efficiency becomes higher by employ the series approximation rather than the integral expression in equation (1), which is known as the TREE method. Particularly, the spacial frequencies are determined by $\cos(\alpha \mathrm{h}) = 0$, h denotes the truncated longitudinal calculation region, which means $\alpha_k = (k\pi + \pi/2)/h$, $k \in [1, 2, ..., n_\alpha]$. In this way, equation (1) becomes

$$\Delta M \approx k_M \sum_k S(\alpha_k) M_\mathrm{s}(\alpha_k) \tag{7}$$

The asymptotic forms of the modified Bessel functions [35] can be introduced to simplify $S(\alpha)$. Given $z \in \mathbb{C}$, when z tends to infinity, the asymptotic forms are

$$\begin{cases} I_0(z) = I_1(z) \sim \mathrm{e}^z/\sqrt{2\pi z} & , |\arg z| < \pi/2 \\ K_0(z) = K_1(z) \sim \sqrt{\pi/(2z)}\mathrm{e}^{-z} & , |\arg z| < 3\pi/2 \end{cases} \tag{8}$$

As z approaches to zero, the asymptotic forms are

$$\begin{cases} I_0(z) \sim 1, \\ I_1(z) \sim z/2, \\ K_0(z) \sim -\ln(z), \\ K_1(z) \sim 1/z \end{cases} \tag{9}$$

Assume that $\alpha a \to 0$ and $\alpha_2 a \to \infty$, then the modified Bessel functions can be approximated according to the asymptotic forms in equation (8) and (9), *i.e.*,

$$\begin{cases} I_0(\alpha a) \approx 1, & I_0(\alpha_2 a) \approx \mathrm{e}^{\alpha_2 a}/\sqrt{2\pi\alpha_2 a} \\ I_1(\alpha a) \approx \alpha a/2, & I_1(\alpha_2 a) \approx \mathrm{e}^{\alpha_2 a}/\sqrt{2\pi\alpha_2 a} \\ K_0(\alpha a) \approx -\ln(\alpha a), & K_0(\alpha_2 a) \approx \sqrt{\pi}\mathrm{e}^{-\alpha_2 a}/\sqrt{2\alpha_2 a} \\ K_1(\alpha a) \approx 1/\alpha a, & K_1(\alpha_2 a) \approx \sqrt{\pi}\mathrm{e}^{-\alpha_2 a}/\sqrt{2\alpha_2 a} \end{cases} \tag{10}$$

The above approximation can also be applied to the variables αb and $\alpha_2 b$, as a close to b.

Subsequently, the phase term $S(\alpha)$ can be simplified to $S_\mathrm{s}(\alpha)$, through the derivation provided in appendix A,

$$S(\alpha) \approx S_\mathrm{s}(\alpha) = \frac{\alpha^2\beta_2 a + 2\alpha^2 \tanh(\alpha_2(b-a))}{\frac{2\beta_2}{b} - \alpha^2\beta_2 a \ln(\alpha b) + \left[\frac{a{\beta_2}^2}{b} - 2\alpha^2\ln(\alpha b)\right]\tanh(\alpha_2(b-a)) - \alpha^2 b^2/2} \tag{11}$$

The high accuracy of simplification can be achieved if the approximate conditions ($\alpha a \to 0, \alpha a \to 0, \alpha_2 a \to \infty$ and $\alpha_2 b \to \infty$) are satisfied, which is analyzed following appendix B.

For the measurement of non-magnetic metallic pipe, the permeability $\mu_r \approx 1$ and $\beta_2 \approx \alpha_2$, equation (11) becomes

$$S_\mathrm{s}(\alpha) = \frac{\alpha^2\alpha_2 a + 2\alpha^2 \tanh(\alpha_2(b-a))}{\frac{2\alpha_2}{b} - \alpha^2\alpha_2 a \ln(\alpha b) + \left[\frac{a{\alpha_2}^2}{b} - 2\alpha^2\ln(\alpha b)\right]\tanh(\alpha_2(b-a)) - \alpha^2 b^2/2} \tag{12}$$

Since a and b are usually small values, and the spacial frequencies dominating the inductance calculation are small (referring to Fig. 11), the relationships $\alpha_2 \gg \alpha^2 a \ln(\alpha b)$ and ${\alpha_2}^2 a/b \gg 2\alpha^2 \ln(\alpha b)$ hold. This means that the denominator of the first fraction in $S_\mathrm{s}(\alpha)$ is dominated by $2\alpha_2/b + a{\alpha_2}^2 \tanh(\alpha_2(b-a))/b$. Consequently, $S_\mathrm{s}(\alpha)$ can be simplified to

$$S_\mathrm{s}(\alpha) \approx \frac{\alpha^2\alpha_2 a + 2\alpha^2 \tanh(\alpha_2(b-a))}{\frac{2\alpha_2}{b} + \frac{a{\alpha_2}^2}{2b}\tanh(\alpha_2(b-a))} - \frac{\alpha^2 b^2}{2} \tag{13}$$

For the thin thickness pipes, it has $(b-a) \ll 1$ and $\alpha_2(b-a) \to 0$, implying that the approximation $\tanh(\alpha_2(b-a)) \approx \alpha_2(b-a)$ is satisfied. In this way, equation (13) becomes

$$\begin{aligned} S_\mathrm{s}(\alpha) &\approx \frac{\alpha^2\left[ab + 2b(b-a)\right]}{2 + a{\alpha_2}^2(b-a)} - \frac{\alpha^2 b^2}{2} \\ &= \frac{\alpha^2\left[ab + 2b(b-a)\right]}{2 + \alpha^2 a(b-a) + j\omega\mu_0\sigma a(b-a)} - \frac{\alpha^2 b^2}{2} \\ &= \frac{\alpha^2\left[ab + 2b(b-a)\right]/\omega_\mathrm{s}}{1 + j\omega\mu_0\sigma a(b-a)/\omega_\mathrm{s}} - \frac{\alpha^2 b^2}{2} \end{aligned} \tag{14}$$

where $\omega_\mathrm{s} = 2 + \alpha^2 a(b-a)$.

According to the corner frequency of the first-order system [36], the imaginary part of equation (14) reaches its maximum when $\omega = \omega_p$, $\omega_p = \left[2 + \alpha^2 a(b-a)\right]/\left[\mu_0\sigma a(b-a)\right]$. In addition, as $2 \gg \alpha^2 a(b-a)$, the peak (angular) frequency can be approximated by

$$\omega_p \approx 2/\left[\mu_0\sigma a(b-a)\right] \tag{15}$$

B. Estimation of pipe properties

The inverse problem is to estimate the pipe properties by minimizing the squared Euclidean distance between

the calculated and measured inductance spectra, $\Delta\mathbf{M} = (\Delta M_i), \Delta\mathbf{M}_{\mathrm{m}} = (\Delta M_{\mathrm{m},i}) \in \mathbb{C}^{n_f \times 1}$ (n_f is the number of frequency points), i.e.,

$$\min_{\mathbf{v}} f_0 = \|\Delta\mathbf{M}(\mathbf{v}) - \Delta\mathbf{M}_{\mathrm{m}}\|_2^2 \tag{16}$$

where $\|\cdot\|_2^2$ represents the ℓ_2-norm, $\mathbf{v} \in \mathbb{R}^{n_v \times 1}$ is the optimized pipe property vector (n_v denotes the quantity of variables) influencing the calculated inductance spectra $\Delta\mathbf{M}(\mathbf{v})$, and the symbol Δ is omitted in the following content.

The local minimum $\mathbf{v}^*$ of optimization problem satisfies

$$\nabla f(\mathbf{v}^*) = \mathbf{0} \tag{17}$$

where $[\nabla f]_{i,j} = \partial f_i / \partial v_j$ and $\mathbf{0} \in \mathbb{R}^{n_v \times 1}$ is a zero vector.

Given a reference point $\mathbf{v}_r$ adjacent to $\mathbf{v}^*$, the partial derivative in equation (17) can be approximated by the Taylor series as,

$$\nabla f(\mathbf{v}^*) = \nabla f(\mathbf{v}_r) + \nabla\nabla f(\mathbf{v}_r)\Delta\mathbf{v} \tag{18}$$

where $\Delta\mathbf{v} = \mathbf{v}^* - \mathbf{v}_r$ and $\nabla\nabla f(\mathbf{v}_r)$ denotes the Hessian matrix evaluated at $\mathbf{v}_r$ which is usually approximated by

$$\nabla\nabla f(\mathbf{v}_r) \approx [\nabla f(\mathbf{v}_r)]^{\mathrm{H}} \nabla f(\mathbf{v}_r) \tag{19}$$

where the superscript H denotes the conjugate transpose, and $\mathbf{H}(\mathbf{v}_r) = [\nabla f(\mathbf{v}_r)]^{\mathrm{H}} \nabla f(\mathbf{v}_r)$ is employed in the following analysis.

Furthermore, the first-order partial derivative is

$$\begin{aligned} \nabla f(\mathbf{v}_r) &= [\nabla\mathbf{M}(\mathbf{v}_r)]^{\mathrm{H}} [\mathbf{M}(\mathbf{v}_r) - \mathbf{M}_{\mathrm{m}}] \\ &= \mathbf{S}(\mathbf{v}_r)^{\mathrm{H}} [\mathbf{M}(\mathbf{v}_r) - \mathbf{M}_{\mathrm{m}}] \end{aligned} \tag{20}$$

where $\mathbf{S} \in \mathbb{C}^{n_f \times n_v}$ is the sensitivity/Jacobian matrix, a linearized relationship between the variation of pipe properties and inductance spectrum, which can be calculated by both the DD and simplified models.

Combining equation (17) to (20), one can obtain the variable difference, *i.e.*

$$\Delta\mathbf{v} = -\left[\mathbf{S}(\mathbf{v}_r)^{\mathrm{H}}\mathbf{S}(\mathbf{v}_r)\right]^{-1} \mathbf{S}(\mathbf{v}_r)^{\mathrm{H}} [\mathbf{M}(\mathbf{v}_r) - \mathbf{M}_{\mathrm{m}}] \tag{21}$$

Accordingly, the variable optimization procedure is illustrated in Algorithm 1, providing the starting point $\mathbf{v}_1$ and residual threshold value ϵ. The corresponding computational complexity is $\mathrm{O}(n_\alpha n_f n_i)$, n_i indicate the iterative steps.

Algorithm 1 Optimization of pipe properties

Input: $\mathbf{v}^1$, ϵ and n_i
Output: $\mathbf{v}$

initialize: Set $\mathbf{M}^1 = \mathbf{M}(\mathbf{v}^1)$
for $k = 1, 2, ..., n_i$ **do**
  $\mathbf{S}^k = \partial\mathbf{M}^k / \partial\mathbf{v}^k$
  $\mathbf{v}^{k+1} = \mathbf{v}^k - [(\mathbf{S}^k)^{\mathrm{H}}\mathbf{S}^k]^{-1}(\mathbf{S}^k)^{\mathrm{H}}(\mathbf{M}^k - \mathbf{M}_{\mathrm{m}}) - \lambda$
  $\mathbf{M}^{k+1} = \mathbf{M}(\mathbf{v}^{k+1})$
  if $\left\|\mathbf{M}^{k+1} - \mathbf{M}_{\mathrm{m}}\right\|_2^2 \leq \epsilon$ **then**
    Break;
  end if
end for

Noted that the combination of variables to be optimized plays a significant role in determining the algorithm performance. The ill-conditioning degree of inverse problem could be represented by the singular value spectrum of sensitivity/Hessian matrix [37]. If there is no extremely small singular value, the optimization would be stable and affected little by the measurement noise. The singular value feature of the Hessian matrix can be represented by $S_f : \mathbb{R}^{n_v \times n_f} \to \mathbb{R}$,

$$S_f\left(\mathbf{H}(\mathbf{v}_r)\right) = -20\log_{10}\left(|\lambda_{\min}| / \lambda_{\max}\right) \tag{22}$$

where $\lambda_{\min}$ and $\lambda_{\max}$ are the minimum and maximum singular values of $\mathbf{H}(\mathbf{v}_r)$, respectively.

This index also reflects the uncertainty of inversion [28], which is desired to be a small value indicating the weak correlation between the derivatives of various variables. The investigated variable combinations include $(a, b), (\sigma, \mu_r), (a, b, \sigma), (a, b, \mu_r)$ and (a, b, σ, μ_r).

Considering the range of $\mathbf{v}_r$, it is expected to calculate the average value of $\overline{S_f} = \sum_p S_f(\mathbf{v}_r^{(p)})/n_p$ ($\mathbf{v}_r^{(p)}$ denotes the p-th evaluating point and n_p is the quantity of points) on a set of points in the hyper-rectangle variable domain defined by $\mathcal{D} = [\underline{a}, \overline{a}] \times [\underline{b}, \overline{b}] \times [\underline{\sigma}, \overline{\sigma}] \times [\underline{\mu_r}, \overline{\mu_r}]$, $\underline{a}$ and $\overline{a}$ represent the upper and lower boundaries of a, respectively.

For a certain measurement application, domain $\mathcal{D}$ is constructed according to the possible range of variables, from which the interior point set $\mathbf{v}^{\mathcal{D}}, \mathbf{v}^{\mathcal{D}} \subset \mathcal{D}$ can be sampled for evaluation. For instance, $\mathbf{v}^{\mathcal{D}}$ consists of 625 equally spaced interior points in $\mathcal{D}$, corresponding to the pipe properties in the range of $a \in [5, 15]$ mm, $b \in [0.2, 3]$ mm, $\sigma \in [1, 61]$ MS/m and $\mu_r \in [1, 201]$. The index $\overline{S_f}$ evaluated on $\mathbf{v}^{\mathcal{D}}$ is shown in Table I, which indicates that the variable combinations of (a, b) and (a, b, μ_r) are relatively suitable. To estimate the variables as many as possible while maintaining a low value of $\overline{S_f}$, the combination (a, b, μ_r) is selected and σ is recommended to be measured beforehand. Because the influence of conductivity on inductance is coupled with permeability [27].

TABLE I
SINGULAR VALUE FEATURE OF HESSIAN MATRIX FOR VARIOUS VARIABLE COMBINATIONS

#	(a, b)	(σ, μ_r)	(a, b, σ)	(a, b, μ_r)	(a, b, σ, μ_r)
$\overline{S_f}$	56.9	277.9	407.2	184.1	552.9

To further improve the optimization stability, a regularization strategy can be implemented to avoid the extremely small singular value. The Hessian matrix is decomposed by singular value decomposition (SVD) as $\mathbf{H} = \mathbf{U}\mathbf{\Sigma}\mathbf{V}^{\mathrm{H}}$, and the strategy applies $\mathbf{H}^* = \mathbf{U}\mathbf{\Sigma}^*\mathbf{V}^{\mathrm{H}}$,

$$\mathbf{\Sigma}^* = \begin{bmatrix} \Sigma_{11} & 0 & 0 \\ 0 & \Sigma_{22} + \beta_b\Sigma_{11} & 0 \\ 0 & 0 & \Sigma_{33} + \beta_\mu\Sigma_{11} \end{bmatrix} \tag{23}$$

where β_b and β_μ are constants to be determined, Σ_{11}, Σ_{22} and Σ_{33} are elements in the diagonal matrix $\mathbf{\Sigma}$.

For the measurement of non-magnetic pipe, of which the real part of inductance spectra approximates to 0H in the low-frequency range, one can adopt a relatively large β_μ, or merely optimize the pipe dimensions.

The starting point for optimization, $\mathbf{v}_1$, influences the convergence point to be reached, due to the local optimality feature of the Newton-Raphson method. By comparing the inductance difference between the measurement and candidate points in $\mathbf{v}^{\mathcal{D}}$, *i.e.* $\min_{\mathbf{v}_s}\left\{\|\Delta\mathbf{M}(\mathbf{v}_s)-\Delta\mathbf{M}_{\mathrm{m}}\|_2^2\right\}, \mathbf{v}_s \in \mathbf{v}^{\mathcal{D}}$, an appropriate starting point corresponding to the minimum difference can be determined.

III. Results and Discussions

In the numerical simulation and experiments, the inductance spectra calculated by the simplified model are compared with the DD model and measurements from the FEM and impedance analyzer, while the pipe properties are estimated separately according to the simplified and DD models. The numerical simulation and analysis are performed on a PC with CPU AMD Ryzen 7 5800H 3.2 GHz and RAM 32 GB.

A. Numerical simulations

In the numerical simulations, the performance of the forward and inverse models, as well as peak frequency estimation are evaluated quantitatively and qualitatively.

The coil dimensions adopt the design provided in appendix B. to measure the aluminum (Al) ($\sigma = 38$ MS/m, $\mu_r = 1$) and magnetic pipes ($\sigma = 6.6$ MS/m, $\mu_r = 125$). A FEM model, corresponding to its analytical counterpart, is constructed employing the COMSOL software. The model employs the two-dimensional axisymmetric structure, in which the infinite-long pipes are approximated by the pipes in the length of 600 mm. The applied signal is in 1 A, and there are 100 frequency points at logarithmic intervals between 10 Hz to 1 MHz. The representative solution is shown in Fig. 3.

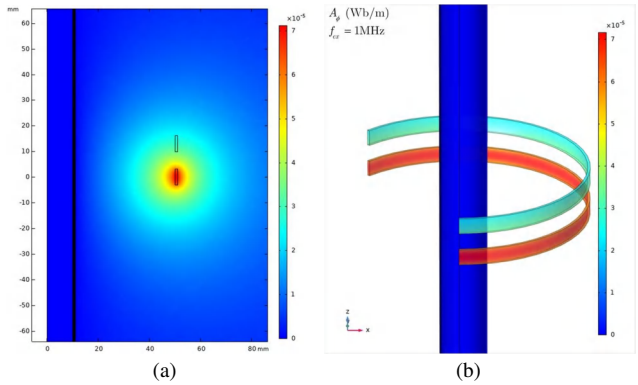

(a) (b)

Fig. 3. FEM solution of a magnetic pipe in (a) shaft section view and (b) 3D (rotating) view

To assess the forward model, the aluminum and magnetic pipes in the inner radius of 5 mm and 15 mm, and thickness 0.1 mm and 1 mm are measured. As a result, the inductance spectra are shown in Fig. 4 and Fig. 5 for aluminum and magnetic pipes, respectively. In addition, the mean absolute error (MAE) and correlation coefficient (CC) [38] of inductance spectra with respect to the DD model are provided in Table II. These indices are defined as,

$$\begin{aligned}
\mathrm{MAE} &= \frac{1}{n_f}\sum_{i=1}^{n_f}|M_{\mathrm{s},i}-M_{\mathrm{D},i}| \\
\mathrm{CC} &= \left|\frac{\sigma_{\mathbf{M}_\mathrm{s}\mathbf{M}_\mathrm{D}}}{\sigma_{\mathbf{M}_\mathrm{s}}\sigma_{\mathbf{M}_\mathrm{D}}}\right| \\
\sigma^2_{\mathbf{M}_\mathrm{D}} &= \frac{1}{n_f}\sum_{i=1}^{n_f}(M_{\mathrm{D},i}-\overline{\mathbf{M}}_\mathrm{D})^*(M_{\mathrm{D},i}-\overline{\mathbf{M}}_\mathrm{D}) \\
\sigma_{\mathbf{M}_\mathrm{s}\mathbf{M}_\mathrm{D}} &= \frac{1}{n_f}\sum_{i=1}^{n_f}(M_{\mathrm{s},i}-\overline{\mathbf{M}}_\mathrm{s})^*(M_{\mathrm{D},i}-\overline{\mathbf{M}}_\mathrm{D})
\end{aligned} \tag{24}$$

where the operator $(\cdot)^*$ represents the complex conjugate, $M_{\mathrm{s},i}$ and $M_{\mathrm{D},i}$ denote the i-th frequency-dependent inductance calculated by the simplified and DD models, respectively, while $\overline{\mathbf{M}}_\mathrm{s}$ and $\overline{\mathbf{M}}_\mathrm{D}$ indicate the corresponding arithmetic mean.

TABLE II
MAE and CC of inductance spectra calculation by the simplified equation

Radii	(a, b) (mm)	(5.5.1)	(5.6)	(15.15.1)	(15.16)
Aluminum pipe	MAE (μH)	0.06	0.58	2.4	3.2
	CC (%)	99.99	99.95	99.99	99.98
Magnetic pipe	MAE (μH)	0.2	6.1	5.7	9.4
	CC (%)	99.98	99.96	99.99	99.98

The inductance spectra in Fig. 4 and Fig. 5 indicate that the solutions of the simplified model are approximate to the DD model and results of FEM. The accuracy is relatively higher for thin thickness pipes in small radii. Specifically, for the pipe in the inner radius of 5 mm, the inductance discrepancy becomes obvious in the low frequency range where the approximation error relating to the assumption that $\alpha_2 a \to \infty$ and $\alpha_2 b \to \infty$ are relatively large, as $\alpha_2 a$ and $\alpha_2 b$ are small values. The inductance calculation error of pipes in the inner radius of $a = 15$ mm is mainly caused by the approximate error of $I_0(\alpha a) \approx 1$, $I_1(\alpha a) \approx \alpha a/2$, $K_0(\alpha a) \approx -\ln(\alpha a)$ and $K_1(\alpha a) \approx 1/\alpha a$ (also for variable αb), as αa and αb are too large to meet the conditions of $\alpha a \to 0$ and $\alpha b \to 0$.

The peak frequency of aluminum thin thickness pipes is estimated employing equation (15). The inner radius ranges from 5 mm to 15 mm and thickness from 0.1 mm to 1 mm. As a results, the relative estimation error is shown in Fig. 6, which are generally lower than 15%.

In the evaluation of pipe property estimation, there exist 10 frequency points in each inductance spectrum, $n_f = 10$, at logarithmic intervals between 1 kHz and 500 kHz. The quantity of spacial frequencies n_α is 100. In addition, the additive white Gaussian noise is applied to the inductance

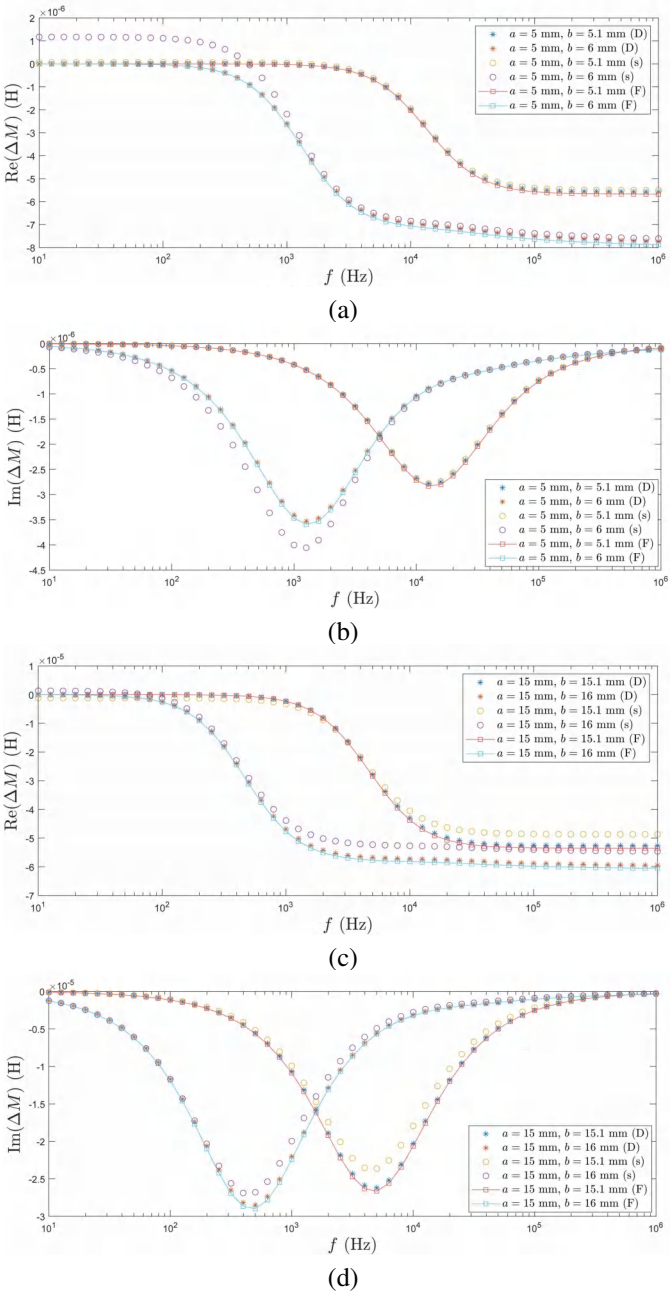

Fig. 4. Inductance spectra of aluminum pipes in the numerical simulation. The pipe inner radius in (a) and (b) is 5 mm, and in (c) and (d) is 15 mm. D: DD model, s: simplified model and F: results of FEM

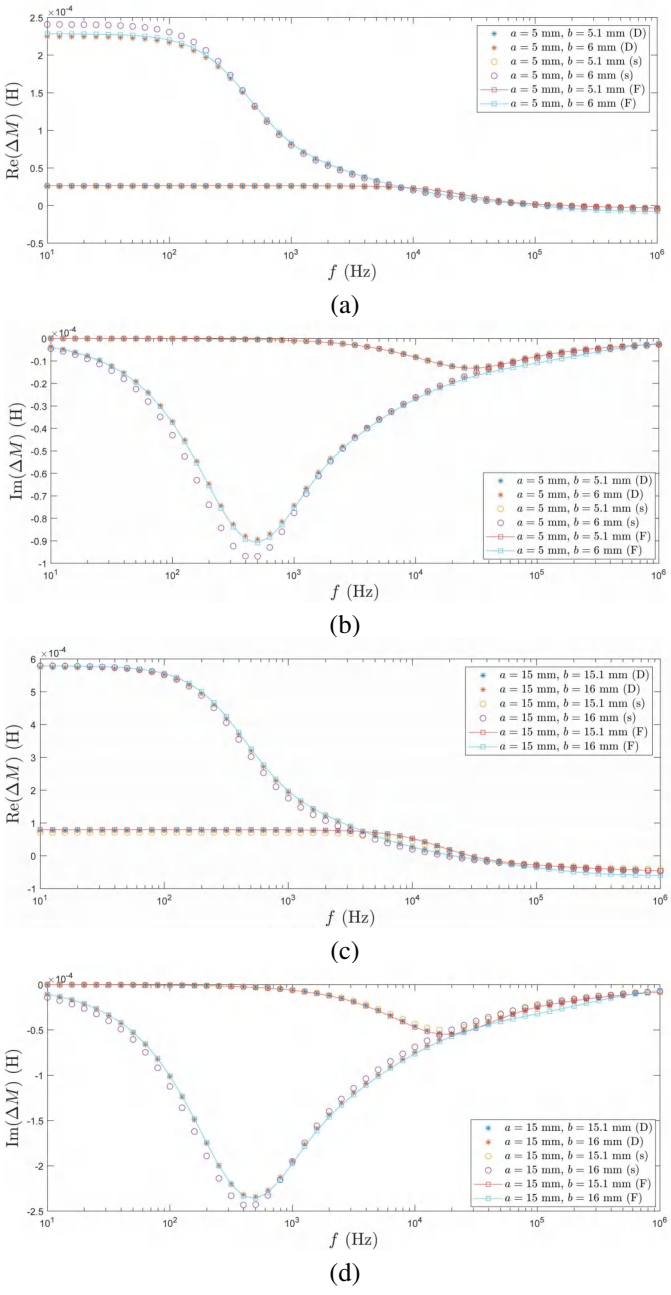

Fig. 5. Inductance spectra of magnetic pipes in the numerical simulation. The pipe inner radius in (a) and (b) is 5 mm, and in (c) and (d) is 15 mm. D: DD model, s: simplified model and F: results of FEM

spectra, leading to an equivalent signal-to-noise ratio of 60 dB. For the inverse model, the starting point of optimization is selected from the point set $\mathbf{v}^{\mathcal{D}}$ defined in section II-B. The regularization parameters are $\beta_b = 10^{-5}$ and $\beta_\mu = 10^{-7}$ for conductive pipes while $\beta_b = 10^{-5}$ and $\beta_\mu = 1 \times 10^{-13}$ for magnetic pipes. In addition, the residual threshold value is $\epsilon = 10^{-15}$ and maximum iterative steps is $n_i = 10$. The inverse results are shown in Table III. Due to the characteristics of the least-squares objective function, the algorithm is more sensitive to the thickness variation rather than the exact radii. The thickness error of the simplified model is smaller than 0.2 mm and permeability error within 27 for the magnetic pipes.

Noted that the optimization stability decreases obviously measuring the thin thickness pipes, mainly because of the larger index $\overline{S_f}$, as shown in Fig. 7.

B. Experiments

In the experiments, both conductive (non-magnetic stainless-steel) pipes and magnetic pipes are measured for evaluation. The conductivity of stainless-steel pipes is 1.1 MS/m, while that of magnetic pipes measured by the

TABLE III
COMPARISON OF PREDICTED RESULTS AND COMPUTATIONAL TIME IN SIMULATION

	#	(a, b)(mm)	$(a_{\rm s}, b_{\rm s})$ (mm) [1]	$(a_{\rm D}, b_{\rm D})$ (mm) [1]	$b_{\rm s} - a_{\rm s}$(mm)	$b_{\rm D} - a_{\rm D}$(mm)	μ_r	$\mu_{r\rm s}$	$\mu_{r\rm D}$	$T_{\rm s}$ (s)	$T_{\rm D}$ (s)
Aluminum pipe	1	(5, 5.1)	(5.0, 5.1)	(4.1, 4.5)	0.1	0.5	1	1.2	1.2	0.10	2.42
	2	(10, 11)	(10.5, 11.4)	(10.2, 11.2)	0.9	1.0	1	1.2	1.2	0.09	2.35
	3	(15, 17)	(16.1, 18)	(15.1, 17.1)	1.9	2.0	1	1.2	1.0	0.09	2.33
Magnetic pipe	4	(5, 5.1)	(5.6, 5.7)	(4.1, 4.3)	0.1	0.2	125	98.3	87.2	0.10	2.43
	5	(10, 11)	(10.0, 10.9)	(10.1, 11.1)	0.9	1.0	125	132.8	126.5	0.08	2.25
	6	(15, 17)	(14.9, 16.8)	(15.4, 17.4)	1.8	2.0	125	135.4	121.9	0.08	2.12

[1] The subscript s and D indicate the estimation adopting the simplified and DD models, respectively.

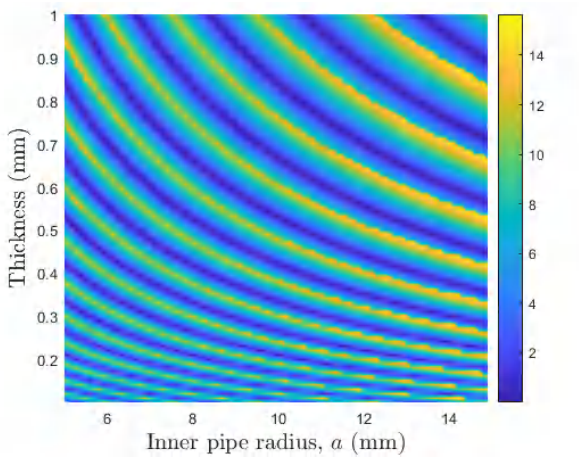

Fig. 6. Relative error of peak frequency estimation measuring aluminum pipes

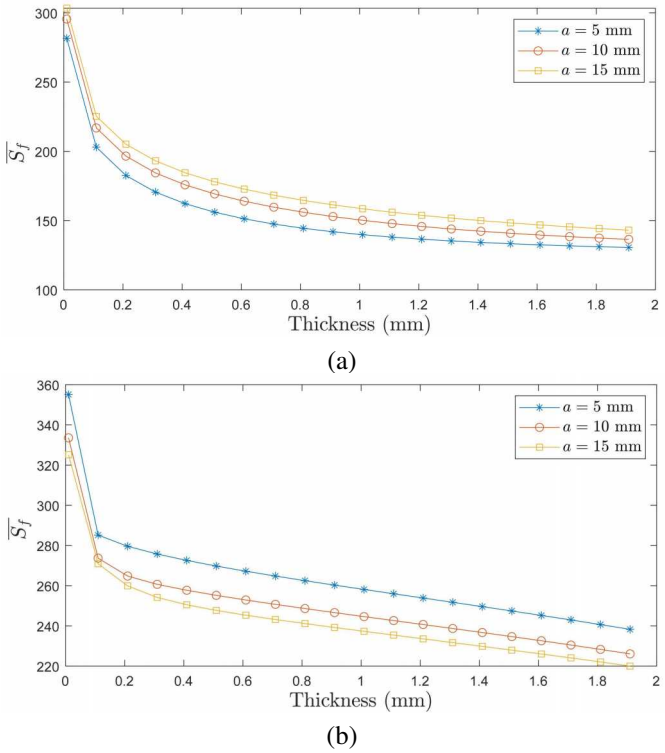

Fig. 7. Singular value feature of Hessian matrix for various thickness when measuring (a) aluminum and (b) magnetic pipes, in the inner radius of a

micro Ohm meter (Keysight Technologies 34420A) is 3.1 MS/m and the relative permeability obtained through the curve fitting method is 60.

The inductance spectra are measured via the Zurich impedance analyzer (MFIA) [39] with the excitation frequency ranging from 1 kHz to 510 kHz, which attains the measurement accuracy of 0.05%, *i.e.* inductance absolute error less than 4.357×10^{-8}H in this case. The experimental facilities are shown in Fig. 8, with corresponding parameters listed in Table IV. There are three representative conductive pipes in the radii (2.75 mm, 3 mm), (4 mm, 5 mm), and (4.75 mm, 5 mm), together with two magnetic pipes in the radii (7.5 mm, 10.5 mm) and (10.5 mm, 13.5 mm).

The measured and calculated inductance spectra are shown in Fig. 9. In addition, the inductance peak frequency estimation of conductive pipes by equation (15) is illustrated in Table V where $\epsilon_{re}(\omega_{\rm p})$ denotes the relative estimation error of peak frequency. The results indicate that the simplified model provides the inductance spectra close to the measured results, especially for thin thickness pipes. Furthermore, the relative error of peak frequency estimation for the conductive pipes is lower than 10 %.

In the pipe property estimation, the parameters of inverse algorithm are identical to the counterparts in the numerical simulation. The pipe properties estimated according to the DD and simplified models are summarized in Table VI (the estimation results for all pipes are shown in Table IX). The results indicate that both models can estimate the approximate pipe properties. For the conductive pipes,

TABLE IV
PARAMETERS OF MEASUREMENT SETUP

Parameters	Value [1]
Inner coil radius r_1 (mm)	11 (53.5)
Outer coil radius r_2 (mm)	11.125 (54)
Coil hight $l_2 - l_1$ (mm)	6 (5)
Span between coils (mm)	16.5 (21.5)
Coil turns	30 (15)
Conductivity of pipe (MS/m)	1.1 (3.5)
Relative permeability of pipe	1 (60)
Range of exciting frequency (kHz)	1 $\sim$ 510

[1] Values in parentheses relate to magnetic pipe measurement.

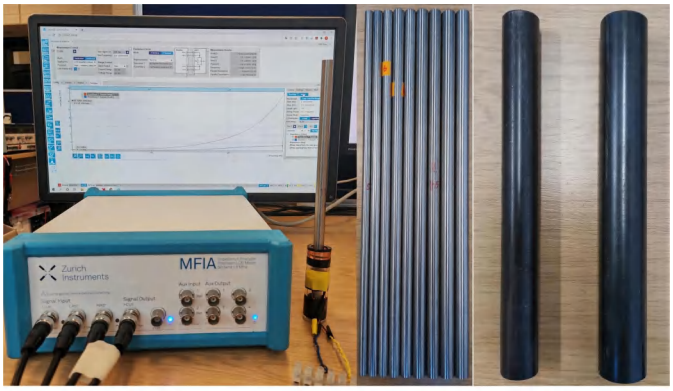

(a) (b) (c)

Fig. 8. (a) experimental setup, (b) conductive pipes and (c) magnetic pipes

TABLE V
INDUCTANCE PEAK FREQUENCY ESTIMATION OF CONDUCTIVE PIPES

#	(a, b) (mm)	Peak frequency (krad/s)	ω_{p} (krad/s)	$\epsilon_{re}(\omega_{\mathrm{p}})$ (%)
1	(2.75, 3)	1901.3	1780.7	9.7
2	(4, 4.5)	613.9	611.9	0.3
3	(4.75, 5)	1080.7	1030.4	4.8

the pipe thickness error of the simplified model is smaller than 0.1 mm, while for the magnetic pipes, the thickness error is within 0.5 mm and relative permeability error is smaller than 5. Furthermore, the simplified model is much more computational efficient and more stable for estimation, obtaining the approximate properties within 0.1 s.

IV. CONCLUSION

The analytical solution to metallic pipes encircled by a coaxial coil is simplified by introducing the approximation of the modified Bessel functions. The simplification is effective for pipe measurement if the asymptotic approximate conditions can be satisfied. Furthermore, the pipe properties can be efficiently estimated by the proposed optimization algorithm. In both numerical simulation and experiments, the simplified model provides the inductance spectra approximating to the DD model. The estimation of metallic pipe properties can be achieved within 0.1 s for each inductance spectrum, which is more than 20 times faster than implementing the DD model, and the absolute error of pipe thickness estimation is less than 0.4 mm.

In the future, the forward and inverse solvers of eddy-current testing system can be developed based on the simplified model and property estimation algorithm. The solvers could be integrated into the measurement system for specific applications.

APPENDIX A

The phase term $S(\alpha)$ in the DD model can be simplified into $S_{\mathrm{s}}(\alpha)$, according to the following procedure.

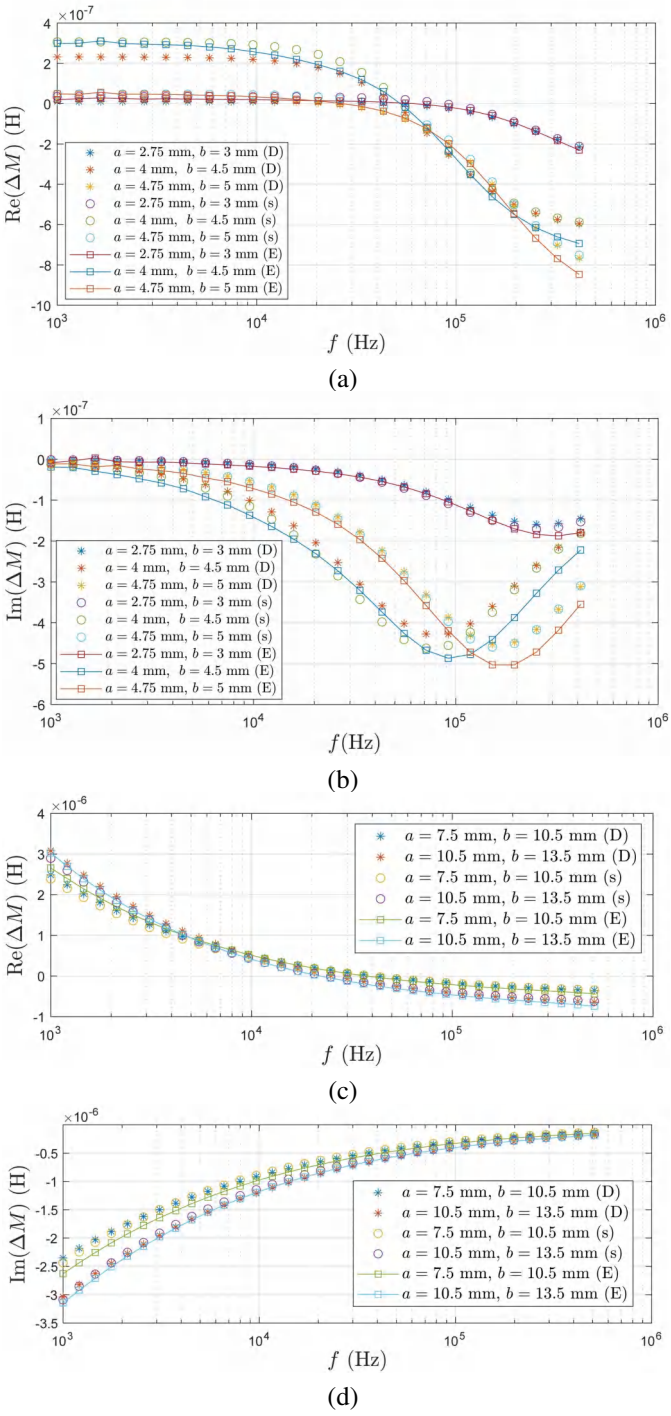

Fig. 9. Experimental inductance spectra including (a) real part of conductive pipes, (b) imaginary part of conductive pipes, (c) real part of magnetic pipes and (d) imaginary part of magnetic pipes. D: DD model, s: simplified model and E: experimental measurements

The phase term in the DD model is

$$S(\alpha) = \frac{1}{bD(\alpha)K_1(\alpha b)} \{K_1(\alpha_2 b)\,[\beta_2 I_1(\alpha_1 a) I_0(\alpha_2 a) - \beta_1 I_1(\alpha_2 a) I_0(\alpha_1 a)] + I_1(\alpha_2 b)\,[\beta_1 K_1(\alpha_2 a) I_0(\alpha_1 a) + \beta_2 K_0(\alpha_2 a) I_1(\alpha_1 a)]\} - \frac{I_1(\alpha b)}{K_1(\alpha b)} \tag{25}$$

TABLE VI
COMPARISON OF PREDICTED RESULTS AND COMPUTATIONAL TIME IN EXPERIMENTS

	#	(a, b) (mm)	$(a_\mathrm{s}, b_\mathrm{s})$ (mm) [1]	$(a_\mathrm{D}, b_\mathrm{D})$[1](mm)	$b_\mathrm{s} - a_\mathrm{s}$ (mm)	$b_\mathrm{D} - a_\mathrm{D}$ (mm)	μ_r	$\mu_{r\mathrm{s}}$	$\mu_{r\mathrm{D}}$	T_s (s)	T_D (s)
Conductive pipe	1	(2.8, 3)	(2.9 3.1)	(6.2, 1.7)	0.2	-4.5	1	1.2	2.3	0.08	2.17
	2	(4, 4.5)	(4.0, 4.5)	(4.2, 4.7)	0.5	0.5	1	2.0	2.6	0.10	2.35
	3	(4.8, 5)	(4.7, 4.9)	(4.8, 5.0)	0.2	0.2	1	1.0	1.4	0.09	2.31
Magnetic pipe	4	(7.5, 10.5)	(8.2, 11.3)	(8.7, 11.1)	3.1	2.4	60	64.1	58.9	0.09	2.43
	5	(10.5, 13.5)	(10.8, 14.2)	(11.3, 13.9)	3.4	2.6	60	58.9	56.1	0.09	2.37

[1] The subscript s and D indicate the estimation adopting the simplified and DD models, respectively.

The above equation can be written as

$$\begin{aligned} S(\alpha) &= \frac{S_0}{bD(\alpha)K_1(\alpha b)} - \frac{I_1(\alpha b)}{K_1(\alpha b)} \\ S_0 &= K_1(\alpha_2 b)S_{01} + I_1(\alpha_2 b)S_{02} \\ S_{01} &= \beta_2 I_1(\alpha_1 a)I_0(\alpha_2 a) - \beta_1 I_1(\alpha_2 a)I_0(\alpha_1 a) \\ S_{02} &= \beta_1 K_1(\alpha_2 a)I_0(\alpha_1 a) + \beta_2 K_0(\alpha_2 a)I_1(\alpha_1 a) \end{aligned} \tag{26}$$

In the first fraction of $S(\alpha)$, function $D(\alpha)$ is

$$\begin{aligned} D(\alpha) = &[\beta_2 K_0(\alpha_2 b)K_1(\alpha b) - \alpha K_0(\alpha b)K_1(\alpha_2 b)] \\ &\times [\beta_1 I_1(\alpha_2 a)I_0(\alpha_1 a) - \beta_2 I_1(\alpha_1 a)I_0(\alpha_2 a)] \\ &+ [\beta_2 K_0(\alpha_2 a)I_1(\alpha_1 a) + \beta_1 K_1(\alpha_2 a)I_0(\alpha_1 a)] \\ &\times [\alpha I_1(\alpha_2 b)K_0(\alpha b) + \beta_2 I_0(\alpha_2 b)K_1(\alpha b)] \end{aligned} \tag{27}$$

Substituting S_{01} and S_{02} into $D(\alpha)$, it can be expressed as

$$\begin{aligned} D(\alpha) &= S_{02}\left[\alpha I_1(\alpha_2 b)K_0(\alpha b) + \beta_2 I_0(\alpha_2 b)K_1(\alpha b)\right] \\ &\quad + S_{01}\left[\beta_2 K_0(\alpha_2 b)K_1(\alpha b) - \alpha K_0(\alpha b)K_1(\alpha_2 b)\right] \\ &= \alpha K_0(\alpha b)S_0 + \beta_2 K_1(\alpha b)\left[I_0(\alpha_2 b)S_{02}\right. \\ &\quad \left. + K_0(\alpha_2 b)S_{01}\right] \end{aligned} \tag{28}$$

Bringing equation (26) and the second equation in (28) into (25), $S(\alpha)$ becomes

$$\begin{aligned} S(\alpha) &= \frac{1}{bK_1(\alpha b)\left[\alpha K_0(\alpha b) + \beta_2 K_1(\alpha b)\frac{S_\mathrm{nu}}{S_\mathrm{de}}\right]} \\ &\quad - I_1(\alpha b)/K_1(\alpha b) \\ S_\mathrm{nu} &= I_0(\alpha_2 b)S_{02} + K_0(\alpha_2 b)S_{01} \\ S_\mathrm{de} &= K_1(\alpha_2 b)S_{01} + I_1(\alpha_2 b)S_{02} \end{aligned} \tag{29}$$

By separating the terms relating to α_2 and others (α and α_1), S_nu and S_de becomes

$$\begin{aligned} S_\mathrm{nu} &= \beta_2 I_1(\alpha_1 a)\left[K_0(\alpha_2 a)I_0(\alpha_2 b) - I_0(\alpha_2 a)K_0(\alpha_2 b)\right] \\ &\quad + \beta_1 I_0(\alpha_1 a)\left[K_1(\alpha_2 a)I_0(\alpha_2 b) + I_1(\alpha_2 a)K_0(\alpha_2 b)\right] \\ S_\mathrm{de} &= \beta_2 I_1(\alpha_1 a)\left[K_1(\alpha_2 b)I_0(\alpha_2 a) + K_0(\alpha_2 a)I_1(\alpha_2 b)\right] \\ &\quad + \beta_1 I_0(\alpha_1 a)\left[K_1(\alpha_2 a)I_1(\alpha_2 b) - K_1(\alpha_2 b)I_1(\alpha_2 a)\right] \end{aligned} \tag{30}$$

Employing the asymptotic form (for large variable) of modified Bessel functions in the brackets of equation (30), *i.e.* $I_0(\alpha_2 a) = I_1(\alpha_2 a) \approx \mathrm{e}^{\alpha_2 a}/\sqrt{2\pi\alpha_2 a}$, $I_0(\alpha_2 b) = I_1(\alpha_2 b) \approx \mathrm{e}^{\alpha_2 b}/\sqrt{2\pi\alpha_2 b}$, $K_0(\alpha_2 a) = K_1(\alpha_2 a) \approx \sqrt{\pi}\mathrm{e}^{-\alpha_2 a}/\sqrt{2\alpha_2 a}$ and $K_0(\alpha_2 b) = K_1(\alpha_2 b) \approx \sqrt{\pi}\mathrm{e}^{-\alpha_2 b}/\sqrt{2\alpha_2 b}$, the terms S_nu and S_de are approximated by

$$\begin{aligned} S_\mathrm{nu} &\approx \beta_2 I_1(\alpha_1 a)\sinh\left[\alpha_2(b-a)\right]/(\alpha_2\sqrt{ab}) \\ &\quad + \beta_1 I_0(\alpha_1 a)\cosh\left[\alpha_2(b-a)\right]/(\alpha_2\sqrt{ab}) \\ S_\mathrm{de} &\approx \beta_2 I_1(\alpha_1 a)\cosh\left[\alpha_2(b-a)\right]/(\alpha_2\sqrt{ab}) \\ &\quad + \beta_1 I_0(\alpha_1 a)\sinh\left[\alpha_2(b-a)\right]/(\alpha_2\sqrt{ab}) \end{aligned} \tag{31}$$

Substituting equation (31) into (29), the phase term $S(\alpha)$ becomes

$$\begin{aligned} S(\alpha) \approx &\left\{bK_1(\alpha b)\left[\alpha K_0(\alpha b) + \beta_2 K_1(\alpha b)\right.\right. \\ &\left.\left. \times \frac{\beta_2 I_1(\alpha_1 a)\tanh(\alpha_2(a-b)) + \beta_1 I_0(\alpha_1 a)}{\beta_2 I_1(\alpha_1 a) + \beta_1 I_0(\alpha_1 a)\tanh(\alpha_2(a-b))}\right]\right\}^{-1} \\ &- I_1(\alpha b)/K_1(\alpha b) \end{aligned} \tag{32}$$

Subsequently, by adopting $\alpha_1 = \beta_1 = \alpha$ and applying the asymptotic form (for small variable) of Bessel functions, *i.e.* $I_0(\alpha_1 a) \approx 1$, $I_1(\alpha_1 a) \approx \alpha_1 a/2$, $K_0(\alpha_1 a) \approx -\ln(\alpha_1 a)$, $K_1(\alpha_1 a) \approx 1/\alpha_1 a$, $I_0(\alpha_1 b) \approx 1$, $I_1(\alpha_1 b) \approx \alpha_1 b/2$, $K_0(\alpha_1 b) \approx -\ln(\alpha_1 b)$ and $K_1(\alpha_1 b) \approx 1/\alpha_1 b$, the phase term can be simplified to $S_\mathrm{s}(\alpha)$,

$$\begin{aligned} S_\mathrm{s}(\alpha) &= \alpha^2\beta_2 a + 2\alpha^2\tanh(\alpha_2(b-a)) \\ &\quad \times \left\{\frac{2\beta_2}{b} - \alpha^2\beta_2 a\ln(\alpha b) + \left[\frac{a{\beta_2}^2}{b} - 2\alpha^2 ln(\alpha b)\right]\right. \\ &\quad \left. \times \tanh(\alpha_2(b-a))\right\}^{-1} - \alpha^2 b^2/2 \end{aligned} \tag{33}$$

APPENDIX B

The conditions of asymptotic approximation are analyzed in this section.

Given the minimum and maximum radii of pipes to be measured, a_min and b_max. Since $a < b$, the asymptotic approximation requires $\alpha b \to 0$ and $\alpha_2 a \to \infty$, which implies $\max\{\alpha b\} < l_\mathrm{m}$ and $\min\{\alpha_2 a/\sqrt{i}\} > u_\mathrm{m}$. Accordingly, the applicable conditions are shown in Fig. 10. The limits of l_m and u_m can be set according to the approximate error of each modified Bessel function.

The condition $\max\{\alpha b\} < l_\mathrm{m}$ indicates that the spacial frequencies dominating the inductance calculation should be as small as possible. Providing the vector of spacial frequencies $\alpha_\mathrm{m} = [\alpha', \alpha''] \in \mathbb{R}^{n_\alpha \times 1}$, which consists of the elements from small to large, a part of small spacial frequencies $\alpha' = [\alpha_1, ..., \alpha_b]$ dominates the inductance calculation, while

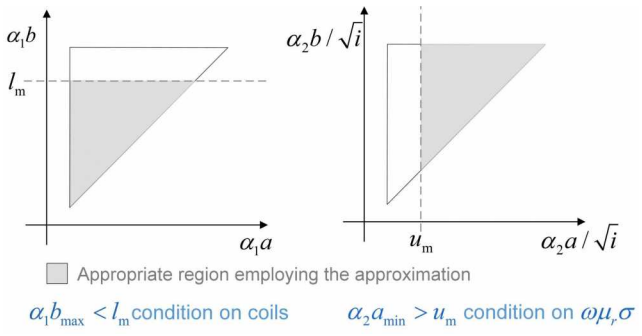

Fig. 10. Schematic of approximate conditions

the other part α'' has a relatively smaller influence. The trend of integrand in equation (1) regarding the variation of spacial frequency is shown in Fig. 11. It has been confirmed that the range of α' is inversely proportional to the spacial coverage of EM field which is influenced by the transmitting coil radii [21, 40]. Noted that the magnitude of integrand is determined by the sensor term $M_s(\alpha)$ which is dominated by its component $f_K(r_1, r_2, \alpha) = K^2(r_2, r_1)/\alpha^6$. The influence of the coil radius on function $f_K(r_1, r_2, \alpha)$ can be obtained through the monotonicity analysis, which remains to readers. When the coil inner radius r_1 is adequately large and coil thickness $r_2 - r_1$ is small, the dominant spacial frequencies α' are in small values. In addition, to maintain the high measurement sensitivity, r_1 should approximate to b_{max}, to some extent. Other coil parameters play a less important role in improving the approximation accuracy and can be selected empirically.

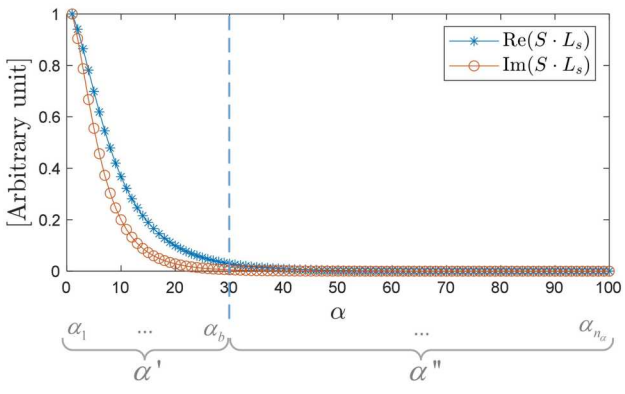

Fig. 11. Relationship between the spacial frequency and integrand in equation (1), where α' indicates the dominant spacial frequencies

The condition $\min\{\alpha_2 a/\sqrt{i}\} > u_m$ confines that $\mu_r\sigma\omega > (u_m/\alpha_{min})^2/\mu_0$. If the electromagnetic properties of pipe (μ_r and σ) are known, the lower limit of the suitable excitation frequency ω_{min} can be obtained. Alternatively, the lower limit of the suitable pipe properties $\mu_r\sigma$ can be estimated for a certain range of excitation frequencies.

The following illustration examines if the above two approximate conditions can be satisfied for the measurement of pipes in the minimum inner radius of $a_{min} = 5$mm and maximum inner radius of $b_{max} = 20$mm. To confine the relative approximation errors within 15%, the limits of l_m and u_m could be 0.353 and 2.008, respectively. The condition $\max\{\alpha b\} < l_m$ limiting the coil radii requires that the magnitude of integrand corresponding to the spacial frequencies α' should be much greater than α''. Setting $\alpha_b = \alpha_{27} = 17.28$ and selecting $r_1 = 50$ mm and $r_2 = 51$ mm, it has $f_K(r_1, r_2, \alpha_b)/f_K(r_1, r_2, \alpha_1) = 3.7 \times 10^{-6}$, which meets the requirement, to some extent. Other coil parameters include the distance between coils of $d = 13$ mm, coil height of $l_2 - l_1 = 6.25$ mm and number of turns $N = 100$ for the wire diameter of 0.25 mm. Furthermore, the condition $\min\{\alpha_2 a/\sqrt{i}\} > u_m$ limits the lumped parameters $\mu_r\sigma\omega$. When measuring the aluminum pipes $\sigma = 38$ MS/m, $\mu_r = 1$ and magnetic pipes $\sigma = 6.6$ MS/m, $\mu_r = 125$, the lower limit of excitation frequency could be 537 Hz and 25 Hz, respectively.

APPENDIX C

The uncertainty of both forward and inverse models applying simplification is analyzed in this section.

The interval and Gaussian processes [41, 42] are frequently adopted for uncertainty quantification (UQ) in various applications [43, 44]. In this case, the available measurements are limited, and it is time-consuming to obtain a large amount of data in simulation. The Gaussian process is introduced to model the error of experimental pipe property inversion. The interval process which does not need the detailed statistical characteristics of uncertain parameters is employed to quantify the uncertainty of results in the simulation.

In the numerical simulation, the aluminum ($\sigma = 3.8 \times 10^7$ S/m, $\mu_r = 1$) and magnetic pipes ($\sigma = 6.6 \times 10^6$ S/m, $\mu_r = 125$) in the measurement range of inner radius $a \in [5, 15]$ mm and pipe thickness $t = b - a, t \in [0.5, 3]$ mm are considered to analyze the uncertainty of forward and inverse models. It is assumed that the inner radius and thickness are independent and follow the uniform distributions, *i.e.* $a \sim U(5, 15)$ and $t \sim U(0.5, 3)$. The unit of variables is neglected hereinafter for simplification.

Following the interval process, the outer discretization method, a slicing algorithm, is applied to discretize the range of a and t into a number of intervals [45]. Given the lower and upper boundaries of these intervals by $\underline{c}^{(j)}$ and $\overline{c}^{(j)}$, $j = 1, ..., n_c$, the variable intervals $\left[\underline{a}^{(j)}, \overline{a}^{(j)}\right]$ and $\left[\underline{t}^{(j)}, \overline{t}^{(j)}\right]$ are obtained from the corresponding cumulative distribution function $\underline{a}^{(j)} = F_a^{-1}(\underline{c}^{(j)})$, $\overline{a}^{(j)} = F_a^{-1}(\overline{c}^{(j)})$, $\underline{t}^{(j)} = F_t^{-1}(\underline{c}^{(j)})$ and $\overline{t}^{(j)} = F_t^{-1}(\overline{c}^{(j)})$. Here $\underline{c}^{(j)} \in \{0, 0.04, ..., 0.96\}$, $\overline{c}^{(j)} = \underline{c}^{(j)} + 0.04$ and $n_c = 25$ is adopted, which means that $\underline{a}^{(j)} \in \{5, 5.4, ..., 14.6\}$, $\overline{a}^{(j)} = \underline{a}^{(j)} + 0.4$, $\underline{t}^{(j)} \in \{0.5, 0.6, ..., 3\}$ and $\overline{t}^{(j)} = \underline{t}^{(j)} + 0.1$. This essentially discretizes the two-dimensional variable domain into 625 hyper-rectangle $\mathcal{D}^{\mathbf{k}} = \left[\underline{a}^{(k_a)}, \overline{a}^{(k_a)}\right] \times \left[\underline{t}^{(k_b)}, \overline{t}^{(k_b)}\right]$, with its indices $\mathcal{K} = \{\mathbf{k} = (k_a, k_b), k_a, k_b \in \{1, 2, ..., n_c\}\}$. The probability density associated to $\mathcal{D}^{\mathbf{k}}$ is $p^{(\mathbf{k})} = p_a^{(k_a)} \cdot p_b^{(k_b)} = 1/625$.

Noted that there are 3 equally spaced interior points in each interval of a and of t. In each hyper-rectangle $\mathcal{D}^{\mathbf{k}}$, the associated bounds of result, $\mathbf{y} = \{y_i\}, i = 1, ..., n_y$, n_y is the quantity of error indices, are estimated from the interior points by

$$\underline{y}_i^{(\mathbf{k})} = \min_{(a,b)\in\mathcal{D}^{\mathbf{k}}} \mathcal{M}(a,b),\ \overline{y}_i^{(\mathbf{k})} = \max_{(a,b)\in\mathcal{D}^{\mathbf{k}}} \mathcal{M}(a,b) \quad (34)$$

where $\mathcal{M}(\cdot)$ indicates the evaluation function of the forward and inverse problem solutions.

For the forward model, $\mathbf{y}_{\text{for}} = (\varepsilon_{\text{MAE}}(\mathbf{M}), \varepsilon_{\text{CC}}(\mathbf{M}))$ consists of the MAE and CC of inductance calculation in terms of the DD model, while $\mathbf{y}_{\text{inv}} = (\varepsilon_{\text{re}}(a), \varepsilon_{\text{re}}(b), \varepsilon_{\text{re}}(\mu_r))$ indicate the relative estimation errors, and $\varepsilon_{\text{re}}(\mu_r)$ is neglected for the aluminum pipes. The corresponding error bounds are shown in Table VII and Table VIII, respectively.

TABLE VII
ERROR BOUNDS OF INDUCTANCE SPECTRA CALCULATED BY THE SIMPLIFIED MODEL

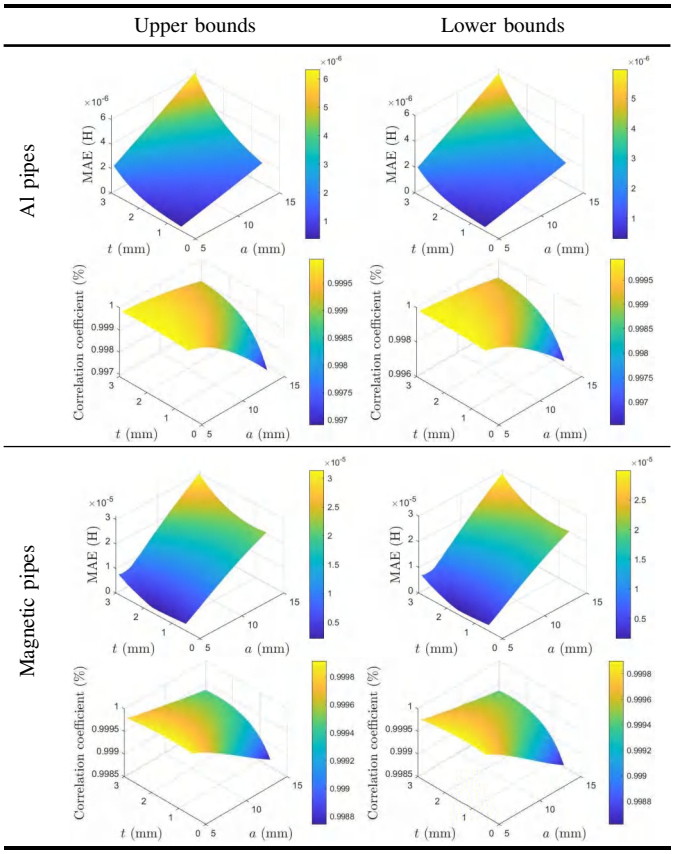

The inductance calculation results in Table VII indicate that the CC of magnetic pipes are higher than conductive pipes. In addition, the forward modeling error increases with the pipe radius and thickness. Furthermore, the pipe property estimation error in Table VIII shows that the simplified inverse model is more accurate for the aluminum pipes, especially for the small pipe radius and thin thickness. Specifically, when measuring the aluminum pipes, the relative errors $\varepsilon_{\text{re}}(a)$ and $\varepsilon_{\text{re}}(t)$ are lower than 9% and 5%,

TABLE VIII
ERROR BOUNDS OF PIPE PROPERTY ESTIMATION APPLYING THE SIMPLIFIED MODEL

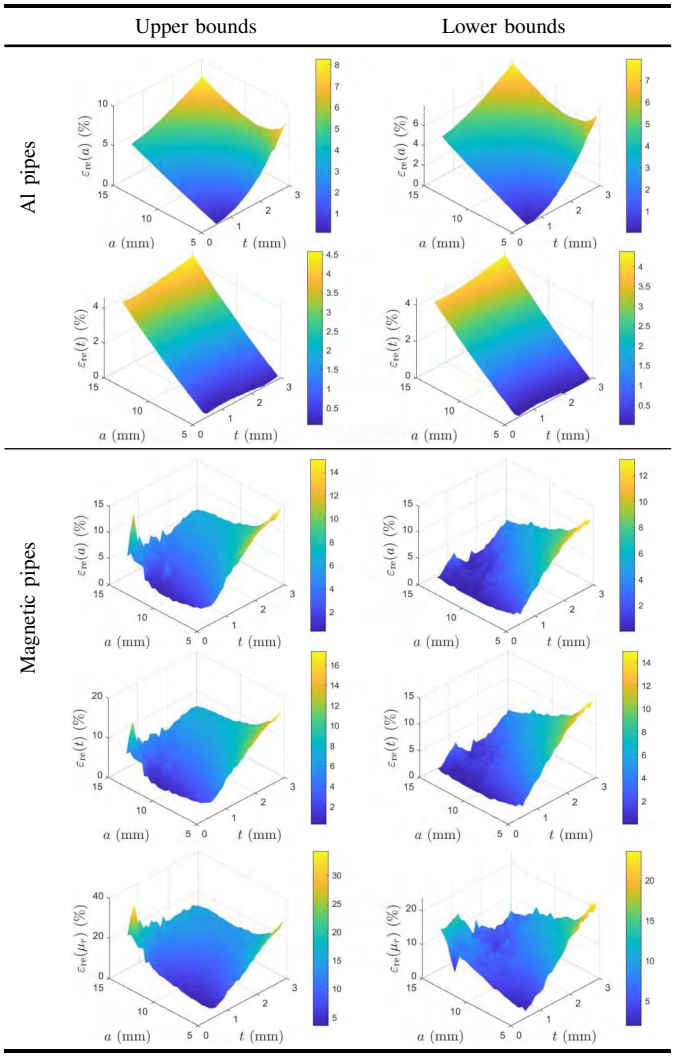

while for the magnetic pipes, the indices $\varepsilon_{\text{re}}(a)$, $\varepsilon_{\text{re}}(t)$ and $\varepsilon_{\text{re}}(\mu_r)$ are within 15%, 17% and 35%, respectively.

In the experiments, to evaluate the uncertainty of pipe property estimation results induced by various factors, the Kenndy & O'Hagan model [46] is employed, which expresses the errors as a Gaussian process. Several assumptions are introduced, *i.e.* neglecting the observation error term and assuming the linear correlation between errors. In this way, the relationship between the estimation and actual pipe properties $\mathbf{v}$ is expressed by

$$\mathbf{v} = f_{\text{inv}}(\mathbf{M}_{\text{m}}) + \delta \quad (35)$$

where $f_{\text{inv}}(\cdot)$ indicates the inverse model introduced in section II-B and $\delta \sim N(\mu, \widetilde{\mathbf{V}})$, with the mean vector $\mu \in \mathbb{R}^{3\times 1}$ and covariance matrix $\widetilde{\mathbf{V}} \in \mathbb{R}^{3\times 3}$.

Through the measurement of 11 metallic pipes shown in Fig. 8 (the data is attached in Table IX), the mean error relates to the DD and simplified model is $\mu_{\text{D}} =$

$(-0.53, 0.34, -0.34)$ and $\mu_{\rm s} = (-0.05, -0.11, -0.38)$, while the covariance is

$$\widetilde{\mathbf{V}}_{\rm D}=\begin{bmatrix} 0.56 & -0.23 & 0.20 \\ -0.23 & 1.47 & -0.15 \\ 0.20 & -0.15 & 3.03 \end{bmatrix}, \quad \widetilde{\mathbf{V}}_{\rm s}=\begin{bmatrix} 0.07 & 0.08 & 0.24 \\ 0.08 & 0.105 & 0.22 \\ 0.24 & 0.22 & 1.76 \end{bmatrix} \tag{36}$$

This means that compared with the DD model, the simplified model is more accurate and suitable for the pipe radius estimation, with a smaller variance of estimation error.

ACKNOWLEDGMENT

The authors would like to thank the financial supports from The Chinese NSF 52166004, The Royal Society IEC\NSFC\211165, China Scholarship Council (CSC) and 2022 IEEE I&M Society Graduate Fellowship Award. The authors are grateful for all the valuable comments and suggestions provided by the anonymous reviewers.

REFERENCES

[1] S. L. Asher, A. Boenisch, and K. Reber, "Development of a magnetic eddy current in-line inspection tool," in *International Pipeline Conference*, vol. 1: Pipelines and Facilities Integrity, 09 2016.

[2] S. Duchesne, N. Bouzida, and J.-P. Villeneuve, "Performance estimation of a remote field eddy current method for the inspection of water distribution pipes," *Journal of Water Resources Planning and Management*, vol. 137, no. 6, pp. 521–530, 2011.

[3] Y. Song and X. Wu, "An analytical solution for vertical coils near a multi-layered metallic pipe in pulsed eddy current testing," *NDT & E International*, vol. 125, p. 102570, 2022.

[4] C. V. Dodd and W. E. Deeds, "Analytical solutions to eddy-current probe-coil problems," *Journal of Applied Physics*, vol. 39, no. 6, pp. 2829–2838, 1968.

[5] C. Dodd and W. Deeds, *Some Eddy-current Problems and Their Integral Solutions*, ser. ORNL.: Oak Ridge National Laboratory. Oak Ridge National Laboratory, 1969.

[6] Z. Zeng, L. Udpa, S. S. Udpa, and M. S. C. Chan, "Reduced magnetic vector potential formulation in the finite element analysis of eddy current nondestructive testing," *IEEE Transactions on Magnetics*, vol. 45, no. 3, pp. 964–967, 2009.

[7] R. Huang, M. Lu, A. Peyton, and W. Yin, "A novel perturbed matrix inversion based method for the acceleration of finite element analysis in crack-scanning eddy current ndt," *IEEE Access*, vol. 8, pp. 12 438–12 444, 2020.

[8] T. Theodoulidis and E. Kriezis, *Eddy Current Canonical Problems (with Applications to Nondestructive Evaluation)*, ser. Contemporary research on emerging science and technology. Tech Science Press, 2006.

[9] J. R. Bowler and T. P. Theodoulidis, "Eddy currents induced in a conducting rod of finite length by a coaxial encircling coil," *Journal of Physics D: Applied Physics*, vol. 38, no. 16, pp. 2861–2868, aug 2005.

[10] M. Lu, A. Peyton, and W. Yin, "Acceleration of frequency sweeping in eddy-current computation," *IEEE Transactions on Magnetics*, vol. 53, no. 7, pp. 1–8, 2017.

[11] M. Lu, X. Meng, R. Huang, L. Chen, A. Peyton, and W. Yin, "A high-frequency phase feature for the measurement of magnetic permeability using eddy current sensor," *NDT & E International*, vol. 123, p. 102519, 2021.

[12] W. Yin, M. Lu, L. Yin, Z. Qian, X. Meng, Z. Zhang, and A. Peyton, "Acceleration of eddy current computation for scanning probes," *Insight - Non-Destructive Testing and Condition Monitoring*, vol. 60, pp. 547–555, 10 2018.

[13] Z. Jin, G. Qin, H. Fan, R. Huang, Z. Chen, Q. Zhao, M. Lu, Z. Zhang, A. Peyton, and W. Yin, "Boundary-element analysis of magnetic polarization tensor for metallic cylinder," *IEEE Access*, vol. 9, pp. 63 250–63 256, 2021.

[14] W. Yin and A. Peyton, "Thickness measurement of non-magnetic plates using multi-frequency eddy current sensors," *Ndt & E International*, vol. 40, no. 1, pp. 43–48, 2007.

[15] M. Lu, *Forward and inverse analysis for non-destructive testing based on electromagnetic computation methods*. The University of Manchester (United Kingdom), 2018.

[16] M. Lu, W. Zhu, L. Yin, A. J. Peyton, W. Yin, and Z. Qu, "Reducing the lift-off effect on permeability measurement for magnetic plates from multifrequency induction data," *IEEE Transactions on Instrumentation and Measurement*, vol. 67, no. 1, pp. 167–174, 2018.

[17] W. Yin, X. Meng, M. Lu, Z. Qian, H. Xu, Z. Zhang, and A. Peyton, "Permeability invariance phenomenon and measurement of electrical conductivity for ferrite metallic plates," *Insight - Non-Destructive Testing and Condition Monitoring*, vol. 61, pp. 472–479, 08 2019.

[18] M. Lu, X. Meng, R. Huang, L. Chen, A. Peyton, and W. Yin, "Inversion of distance and magnetic permeability based on material-independent and liftoff insensitive algorithms using eddy current sensor," *IEEE Transactions on Instrumentation and Measurement*, vol. 70, pp. 1–9, 2021.

[19] M. Lu, L. Yin, A. J. Peyton, and W. Yin, "A novel compensation algorithm for thickness measurement immune to lift-off variations using eddy current method," *IEEE Transactions on Instrumentation and Measurement*, vol. 65, no. 12, pp. 2773–2779, 2016.

[20] G. Hu, R. Huang, M. Lu, L. Zhou, and W. Yin, "Measurement of radius of a metallic ball using eddy current testing based on peak frequency difference feature," *Measurement*, vol. 184, p. 109876, 07 2021.

TABLE IX
EXPERIMENTAL RESULTS OF PIPE PROPERTY ESTIMATION

	Conductive pipes									Magnetic pipes	
(a, b) mm	(2.8, 3)	(3.3, 3.5)	(3, 3.5)	(3.8,4)	(3.5,4)	(4.3,4.5)	(4, 4.5)	(4.8, 5)	(4.6, 5)	(7.5, 10.5)	(10.5, 13.5)
$(a_{\rm s}, b_{\rm s})$ mm [1]	(2.9, 3.1)	(3.3, 3.5)	(2.9, 3.4)	(3.7,4.0)	(3.3,3.9)	(4.2,4.4)	(4.0, 4.5)	(4.7, 4.9)	(4.4, 4.9)	(8.2, 11.3)	(10.8, 14.2)
$(a_{\rm D}, b_{\rm D})$ mm [1]	(6.2, 1.7)	(3.8, 0.1)	(3.0, 3.5)	NaN [2]	(3.5,4.0)	(4.3,4.5)	(4.2, 4.7)	(4.8, 5.0)	(4.6, 5.1)	(8.7, 11.1)	(11.3, 13.9)
μ_r	1	1	1	1	1	1	1	1	1	60	60
$\mu_{r\rm s}$	1.2	1.0	0.9	1.0	0.8	1.0	2.0	1.0	1.2	64.1	58.9
$\mu_{r\rm D}$	2.3	1.4	1.1	NaN [2]	1.0	1.1	2.6	1.4	1.7	62.7	56.1

[1] The subscript s and D indicate the estimation adopting the simplified and DD models, respectively.
[2] NaN denotes not a number.

[21] R. Huang, M. Lu, Z. Zhang, Q. Zhao, Y. Xie, Y. Tao, T. Meng, A. Peyton, T. Theodoulidis, and W. Yin, "Measurement of the radius of metallic plates based on a novel finite region eigenfunction expansion (FREE) method," *IEEE Sensors Journal*, vol. 20, no. 24, pp. 15 099–15 106, 2020.

[22] X. Chen and Y. Lei, "Inverse problem of pulsed eddy current field of ferromagnetic plates," *Chinese Physics B*, vol. 24, no. 3, p. 030301, feb 2015.

[23] X. Chen, J. Li, and Z. Wang, "Inversion method in pulsed eddy current testing for wall thickness of ferromagnetic pipes," *IEEE Transactions on Instrumentation and Measurement*, vol. 69, no. 12, pp. 9766–9773, 2020.

[24] C. Xingle and X. Rongrong, "A pulsed eddy current testing method for relative thickness of ferromagnetic components considering local hysteresis characteristics," *NDT & E International*, vol. 124, p. 102541, 2021.

[25] H. Sun, Y. Shi, W. Zhang, and Y. Li, "Rfec based oil downhole metal pipe thickness measurement," *Journal of Nondestructive Evaluation*, vol. 40, no. 2, pp. 1–9, 2021.

[26] H. J. . S. Y. Lee, K. H.; Kim, "Electromagnetic method for analyzing the property of steel casing," University of California, Tech. Rep., 1988.

[27] W. Yin, X. Hao, A. Peyton, M. Strangwood, and C. Davis, "Measurement of permeability and ferrite/austenite phase fraction using a multi-frequency electromagnetic sensor," *NDT & E International*, vol. 42, no. 1, pp. 64–68, 2009.

[28] I. D. Adewale and G. Y. Tian, "Decoupling the influence of permeability and conductivity in pulsed eddy-current measurements," *IEEE Transactions on Magnetics*, vol. 49, no. 3, pp. 1119–1127, 2013.

[29] D. Vasic, V. Bilas, and D. Ambrus, "Validation of a coil impedance model for simultaneous measurement of electromagnetic properties and inner diameter of a conductive tube," *IEEE Transactions on Instrumentation and Measurement*, vol. 55, no. 1, pp. 337–342, 2006.

[30] D. Vasić and V. Bilas, "Lumped representation in inductive measurement of metal casing properties," in *2010 IEEE Instrumentation Measurement Technology Conference Proceedings*, 2010, pp. 841–844.

[31] M. Lu, Y. Xie, W. Zhu, A. Peyton, and W. Yin, "Determination of the magnetic permeability, electrical conductivity, and thickness of ferrite metallic plates using a multifrequency electromagnetic sensing system," *IEEE Transactions on Industrial Informatics*, vol. 15, no. 7, pp. 4111–4119, 2019.

[32] D. R. Hunter and K. Lange, "A tutorial on mm algorithms," *The American Statistician*, vol. 58, no. 1, pp. 30–37, 2004.

[33] W. Yang and L. Peng, "Image reconstruction algorithms for electrical capacitance tomography," *Measurement science and technology*, vol. 14, no. 1, p. R1, 2002.

[34] W. Yin, S. J. Dickinson, and A. Peyton, "Imaging the continuous conductivity profile within layered metal structures using inductance spectroscopy," *IEEE Sensors Journal*, vol. 5, no. 2, pp. 161–166, 2005.

[35] M. Abramowitz and I. A. Stegun, *Handbook of mathematical functions with formulas, graphs, and mathematical tables*. US Government printing office, 1964, vol. 55.

[36] W. Bolton, "11 - frequency response," in *Instrumentation and Control Systems*, W. Bolton, Ed. Oxford: Newnes, 2004, pp. 252–281.

[37] R. C. Aster, C. H. Thurber, and B. Borchers, "Parameter estimation and inverse problems (second edition)," *International Geophysics*, vol. 67, pp. 411–421, 2010.

[38] B. Hanson, K. Klink, K. Matsuura, S. M. Robeson, and C. J. Willmott, "Vector correlation: review, exposition, and geographic application," *Annals of the Association of American Geographers*, vol. 82, no. 1, pp. 103–116, 1992.

[39] "MFIA 5MHz impedance analyzer and precision lcr meter," https://www.zhinst.com/sites/default/files/documents/2021-12/zi_mfia_leaflet_latest.pdf., accessed on: Apr. 4, 2022. [Online].

[40] W. Yin, R. Huang, M. Lu, Z. Zhang, and A. Peyton, "Measurements of thickness for metallic plates with co-axial holes using a novel analytical method with the modified integration range," *IEEE Access*, vol. 8, pp. 198 301–198 306, 2020.

[41] J. Zhang, J. Yin, and R. Wang, "Basic framework and main methods of uncertainty quantification," *Mathematical Problems in Engineering*, vol. 2020, 2020.

[42] I. Bilionis and N. Zabaras, *Bayesian Uncertainty*

Propagation Using Gaussian Processes. Cham: Springer International Publishing, 2017, pp. 555–599. [Online]. Available: https://doi.org/10.1007/978-3-319-12385-1_16

[43] R. Schöbi and B. Sudret, "Structural reliability analysis for p-boxes using multi-level meta-models," *Probabilistic Engineering Mechanics*, vol. 48, pp. 27–38, 2017.

[44] C. Wang, Z. Qiu, X. Wang, and D. Wu, "Interval finite element analysis and reliability-based optimization of coupled structural-acoustic system with uncertain parameters," *Finite Elements in Analysis and Design*, vol. 91, pp. 108–114, 2014.

[45] R. Schöbi, "Surrogate models for uncertainty quantification in the context of imprecise probability modelling," *IBK Bericht*, vol. 505, 2019.

[46] M. C. Kennedy and A. O'Hagan, "Bayesian calibration of computer models," *Journal of the Royal Statistical Society: Series B (Statistical Methodology)*, vol. 63, no. 3, pp. 425–464, 2001.

5. Model-based Cylinder Radius and Permeability Estimation Using Eddy Current Testing

Model-based Cylinder Radius and Permeability Estimation Using Eddy Current Testing

Abstract

The material quality of metallic cylinders including microstructure is reflected in their physical properties. Eddy current testing techniques play an important role in the measurement of metallic cylinder measurement. In this paper, a cylinder radius and permeability estimation method is proposed based on the combined analytical and optimisation method. The Dodd and Deeds analytical model has been first simplified, which suggests an approximate linear relationship between the cylinder radius, permeability and coil inductance. Based on the proposed relation, the pre-estimated radius and permeability are used as the initial guess for the modified Newton-Raphson algorithm to solve the least squares problem between the measured and calculated coil inductance spectra. This method avoids the local minimum issue that occurs otherwise, to some extent. The effectiveness of the proposed method has been evaluated by numerical simulations and experiments, which indicates that fast estimation can be achieved with high accuracy.

Keywords: Electromagnetic sensing, eddy current testing, cylinder measurement, analytical model, inverse problem.

1. Introduction

Metallic rods play an important structural role in industries, *e.g.* in building structures to balance the horizontal thrusts and avoid the overturning of vertical supports [1]. In the fabrication of metallic rods, the heating process changes the microstructure of materials which affects the physical properties of rods [2]. The presence of contaminants in heating systems, overloading, electrical shocks, and material fatigue lead to various types of quality problems. Microstructure testing is a crucial issue of rod quality inspection.

The electromagnetic properties, *i.e.* electrical conductivity and permeability, are closely related to the material microstructure [3, 4] and can be measured by the eddy current (EC) testing technique. The EC testing technique has been extensively studied for the property measurement of various metals, including metallic cylinders[5, 6, 7, 8]. The measurement of cylindrical properties according to EC measurement requires the theoretical analysis of EC signals. The relationships between the coil inductance and electromagnetic properties are described by the forward and inverse problems.The forward problem calculates the frequency-dependent coil inductance for known electromagnetic properties while the inverse problem solves the electromagnetic properties according to the inductance.

The forward problem can be solved by numerical and analytical methods. The finite element method (FEM) can be used to calculate the electromagnetic field for arbitrary geometries by discretising the computational domain into numerous elements. It has been widely applied to models with complex geometry. The calculation for the model with a dense mesh is usually time-consuming, previous studies accelerated the calculation by employing strategies including initial value estimation [9], partial solution update [10] and combination with boundary element method

[11]. Nevertheless, due to the computational cost, FEM is still difficult to be implemented in applications requiring real-time measurement. The analytical model expresses the measurement of simple geometry by explicit solutions, which has fast computational speed and the advantage of gaining in-depth physical insight. The EC of the axial symmetric condition of EC probe and cylinders can be described by the scalar magnetic potential, *e.g.* the classic Dodd and Deeds (DD) model [12, 13]. The method can be extended by considering the boundary conditions of finite-long cylinders [14, 15, 16] and cracks [17, 18], which is known as the truncated region eigenfunction expansion (TREE) method [19]. For more general asymmetric cases, the EC can be modelled by the second-order vector potential. The EC field can be represented by the transverse electric (TE) potential and transverse magnetic (TM) potential. The bobbin and encircling probes can be placed in arbitrary positions and azimuth [20].

The solution of the inverse problem is usually obtained by the optimisation method solving the least squares problem between the calculated and measured inductance, and by the simplified analytical model. The optimisation method can estimate the radius and electromagnetic properties of metallic cylinders simultaneously. However, to solve the multi-variate non-linear optimisation problem, the combination of variables should be determined and the appropriate initial guess is required, as the problem is non-convex and various local minima may affect the optimisation [21]. Due to the coupling effect of electromagnetic properties on the coil inductance (different conductivities and permeabilities could have close inductance spectra), both values are sophisticated to be obtained accurately and the optimisation process could be unstable [22, 23, 24]. The simplified analytical model directly estimates a specific electromagnetic property according to the inductance at the characteristic frequencies [25, 26], *e.g.* zero-crossing frequency (the frequency where the real part of inductance change is zero) and peak frequency (the frequency where the imaginary part of inductance change reaches its maximum). The method is frequently explored for the property estimation of metallic plates, in which various functional approximation strategies have been introduced to simplify the phase of inductance induced by the metallic test pieces as a linear system, *e.g.* the first order system.Various plate properties can be estimated under the inductance characteristic frequencies using the linear equation [27]. Since the approximation only holds under certain circumstances, the applicable condition of the simplified analytical model requires to be evaluated. Few studies explore the simplified analytical model for the electromagnetic property measurement of cylinders, which could be an efficient method of cylinder property calculation.

In this study, the combination of the simplified analytical and optimisation method is investigated for the estimation of cylinder radius and permeability. The analytical model of the cylinder encircled by coaxial coils has been simplified to obtain the initial guess of objective properties, and the applicable conditions of simplification have been discussed. Furthermore, the optimisation method based on the Newton-Raphson algorithm has been investigated to optimize the cylinder radius and permeability by solving the least squares problem between the calculated and measured inductance spectra. The proposed method reduces the error of the simplified analytical model, meanwhile decreasing the influence of local minima on optimisation. Numerical simulations and experiments have been carried out to evaluate the effectiveness of the proposed method in terms of various cylinder properties. The major contribution is the cylinder property estimation method which improves the estimation accuracy of multiple variables, by optimizing the initial values obtained from the simplified analytical model.

The rest of the paper is arranged as follows. Section 2.1 introduces the simplified analytical model of the metallic cylinder measured by a coaxial encircling probe and derives the equation to calculate the initial guess of radius and permeability. The cylinder property estimation method is proposed in section 2.2. The numerical simulation and experimental results are summarized in

section 3 then conclusions are presented in section 4.

2. Methods

The flowchart of the proposed method for cylinder radius and permeability estimation is shown in Fig. 1, which consists of the initial guess obtained by the simplified analytical model and estimation by optimisation method.

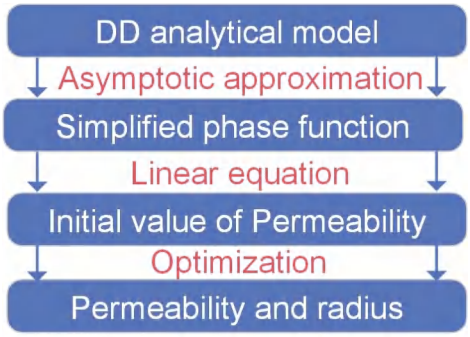

Figure 1: Flowchart of cylinder permeability estimation

2.1. Initial guess of cylinder radius and permeability

For the measurement configuration shown in Fig. 2, the mutual inductance between the Tx and Rx coils (*i.e.* mutual inductance defined in [13]), referred to as inductance hereinafter, is induced by the metallic cylinder which can be calculated by

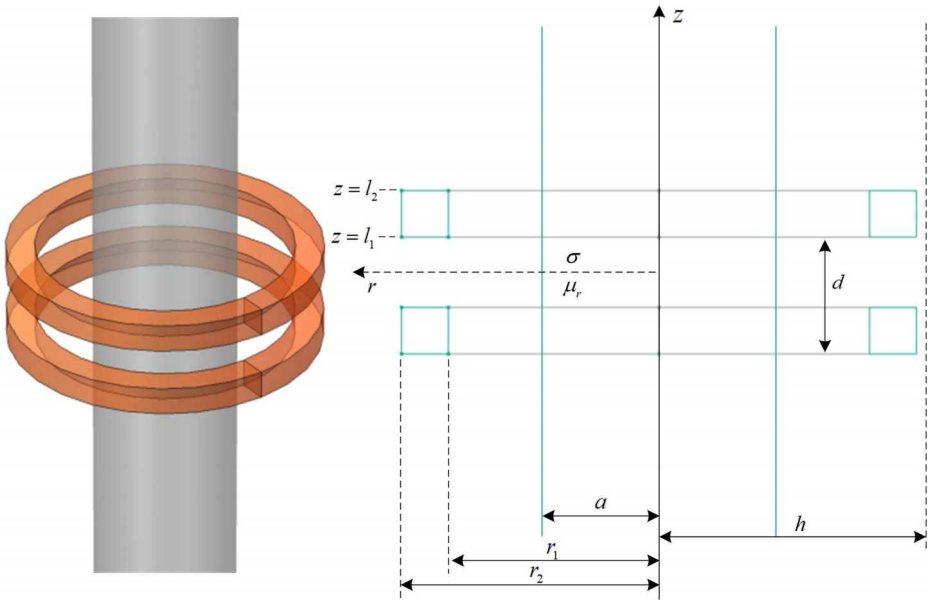

Figure 2: Induction coils encircling a coaxial metallic cylinder

$$\Delta L = k_M \int_0^\infty S(\alpha) M_s(\alpha) d\alpha \tag{1}$$

$$S(\alpha,\omega)=\frac{1}{\beta_1 I_0(\alpha_1 a)K_1(\alpha a)+\alpha I_1(\alpha_1 a)K_0(\alpha a)}\frac{I_1(\alpha_1 a)}{aK_1(\alpha a)} - I_1(\alpha a)/K_1(\alpha a) \tag{2}$$

$$M_{\mathrm{s}}(\alpha)=K^2(r_2,r_1)f\cos(\alpha)/\alpha^6 \tag{3}$$

$$K(r_2,r_1)=\int_{\alpha r_1}^{\alpha r_2}\alpha r K_1(\alpha r)d\alpha r \tag{4}$$

$$f\cos(\alpha)=2\cos(\alpha d)-\cos\left(\alpha(l_2-l_1+d)\right) - \cos\left(\alpha(l_1-l_2+d)\right) \tag{5}$$

where the phase term $S(\alpha)$ is determined by the cylinder properties and the excitation frequency, the sensor term $M_{\mathrm{s}}(\alpha)$ relates to the sensor configuration, $k_M=2N^2\mu_0/\left[(r_2-r_1)^2(l_2-l_1)^2\right]$, N is the turns of coil, μ_0 is the vacuum permeability, α is the spatial frequency of cylindrical harmonics, $\alpha_1=\sqrt{\alpha^2+j\omega\mu_0\mu_r\sigma}$, $\beta_1=\alpha_1/\mu_r$, $I(\cdot)$ and $K(\cdot)$ are the modified Bessel functions of the first and the second kind, respectively. Other parameters correspond to the dimensions of sensor.

The TREE method approximates the integral expression in equation (1) by series. The spatial frequencies are determined by $\cos(\alpha h)=0$, h denotes the truncated longitudinal calculation region, which means $\alpha_k=(k\pi+\pi/2)/h$, $k\in\{1,2,...,n_\alpha\}$ [28]. In this way, equation (1) becomes

$$\Delta L\approx k_M\sum_k S(\alpha_k,\omega)M_{\mathrm{s}}(\alpha_k) \tag{6}$$

The matrix form of the inductance spectrum calculation is

$$\mathbf{\Delta L}=\mathbf{SK} \tag{7}$$

where $\mathbf{\Delta L}\in\mathbb{C}^{n_\omega\times 1}$, $\mathbf{S}=\{S(\alpha_k,\omega_i)\}\in\mathbb{C}^{n_\omega\times n_\alpha}$, $\mathbf{K}=\{M_s(\alpha)\}\in\mathbb{R}^{n_\alpha\times 1}$, n_ω indicates the quantity of excitation frequency points.

The initial guess of radius and permeability is obtained by analysing the frequency-dependent inductance with the simplified analytical model, which is detailed as follows.

According to the limiting forms of the modified Bessel functions, as $\alpha a\to 0$ and $\alpha_1 a\to\infty$, the functions can be approximated by

$$\begin{cases} I_0(\alpha a)\approx 1, & I_0(\alpha_1 a)\approx \mathrm{e}^{\alpha_1 a}/\sqrt{2\pi\alpha_1 a} \\ I_1(\alpha a)\approx \alpha a/2, & I_1(\alpha_1 a)\approx \mathrm{e}^{\alpha_1 a}/\sqrt{2\pi\alpha_1 a} \\ K_0(\alpha a)\approx -\ln(\alpha a), & K_0(\alpha_1 a)\approx \sqrt{\pi}\mathrm{e}^{-\alpha_1 a}/\sqrt{2\alpha_1 a} \\ K_1(\alpha a)\approx 1/\alpha a, & K_1(\alpha_1 a)\approx \sqrt{\pi}\mathrm{e}^{-\alpha_1 a}/\sqrt{2\alpha_1 a} \end{cases} \tag{8}$$

Substituting the modified Bessel functions in equation (2) by equation (8), and through mathematical derivations, the phase term can be approximated by

$$S(\alpha,\omega)\approx\alpha^2 a^2\left(\frac{1}{\beta_1 a-\alpha^2 a^2\ln(\alpha a)}-\frac{1}{2}\right) \tag{9}$$

As $\alpha a \to 0$, the relationship holds for $\alpha a \ln(\alpha a) \sim 0$, then equation (9) is approximated by

$$\begin{aligned} S(\alpha,\omega) &\approx \alpha^2 a^2 \left(\frac{1}{\beta_1 a} - \frac{1}{2}\right) \\ &= \alpha^2 a^2 \left(\frac{\mu_r}{a\sqrt{j\omega\mu_0\mu_r\sigma + \alpha^2}} - \frac{1}{2}\right) \end{aligned} \tag{10}$$

For relatively high excitation frequency, conductivity and permeability, the condition $\omega\mu_0\mu_r\sigma \gg \alpha^2$ can be satisfied and the phase term can be further approximated as

$$\begin{aligned} S(\alpha,\omega) &\approx \alpha^2 a^2 \left(\frac{\mu_r}{a\sqrt{j}\sqrt{\omega\mu_0\mu_r\sigma}} - \frac{1}{2}\right) \\ &= \alpha^2 a^2 \left(\frac{\sqrt{2}(1-j)\mu_r}{2a\sqrt{\omega\mu_0\mu_r\sigma}} - \frac{1}{2}\right) \end{aligned} \tag{11}$$

At the zero-crossing frequency ω_c, it has $\mathrm{Re}\,[S(\alpha)] = 0$, which indicates that

$$\omega_c = \frac{2\mu_r}{a^2\mu_0\sigma} \tag{12}$$

At a specific frequency ω_s where the above approximation holds, substituting the simplified phase term in equation (11) to equation (6), one can obtain

$$\begin{aligned} \mathrm{Im}\,[\Delta L(\omega_s)] &\approx k_M \sum_k -\frac{{\alpha_k}^2 a^2\sqrt{2\mu_r}}{2a\sqrt{\mu_0\sigma\omega_s}} M_{\mathrm{s}}(\alpha_k) \\ &= -\frac{a\sqrt{\omega_c}}{2\sqrt{\omega_s}} M_a \\ M_a &= k_M \sum_k {\alpha_k}^2 M_{\mathrm{s}}(\alpha_k) \end{aligned} \tag{13}$$

It indicates that the cylinder radius can be calculated by

$$\tilde{a} = \left(\frac{-2\mathrm{Im}\,[\Delta L(\omega_s)]}{M_a\sqrt{\omega_c/\omega_s}}\right)^{\frac{1}{2}} \tag{14}$$

Subsequently, according to equation (12) the relative permeability can be estimated by

$$\tilde{\mu}_r = \tilde{a}^2\omega_c\mu_0\sigma/2 \tag{15}$$

The accuracy of the above radius and permeability calculation is confined by the limiting conditions of the modified Bessel functions. The condition $\alpha a \to 0$ requires small radius a and spatial frequencies of cylindrical harmonics α determined by coil radius, as shown in Fig. 3. The relatively large coil radius corresponds to the small range of dominant spatial frequency and retains adequate measurement sensitivity, which has been detailed in the previous study [21]. Other coil parameters have less influence on the range of α. The condition $\alpha_1 a \to \infty$ indicates that the product of radius a and complex spatial frequency $\alpha_1 = \sqrt{\alpha^2 + j\omega\mu_0\mu_{\mathrm{r}}\sigma}$ should be large enough, especially at the zero-crossing frequency ω_c. In addition, the frequency ω_s for radius calculation in equation (14) should be relatively high (>100 kHz).

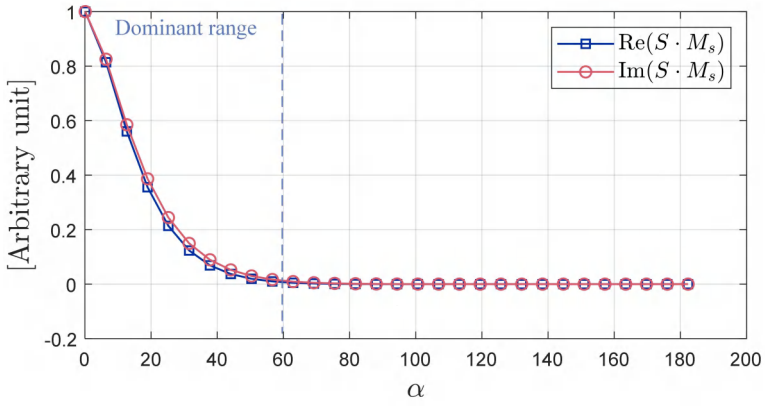

Figure 3: Relationship between the spatial frequency and normalized integrand in equation (1)

2.2. Estimation of cylinder properties

The initial guess of cylinder radius and relative permeability obtained from the simplified analytical model is applied to solve the following least squares problem. The objective function of the least squares problem is defined as

$$\min_{\mathbf{v}} \mathcal{L}_0 = \|\Delta\mathbf{L}(\mathbf{v}) - \mathbf{\Delta L}_{\mathrm{m}}\|_2^2 \tag{16}$$

where $\Delta\mathbf{L}(\mathbf{v})$ is the inductance spectrum of variable $\mathbf{v} = [a, \mu_r]^{\mathrm{T}}$ calculated by the analytical model, $\Delta\mathbf{L}_{\mathrm{m}}$ is the measured or simulated spectrum, $\|\cdot\|_2^2$ represents the ℓ_2-norm.

According to the modified Newton-Raphson method [21], the variables can be optimised iteratively by

$$\begin{aligned} \mathbf{v}^{k+1} &= \mathbf{v}^k + \Delta\mathbf{v} \\ \Delta\mathbf{v} &= -[(\mathbf{S}^k)^{\mathrm{H}}\mathbf{S}^k]^{-1}(\mathbf{S}^k)^{\mathrm{H}}(\Delta\mathbf{L}^k - \Delta\mathbf{L}_{\mathrm{m}}) \end{aligned} \tag{17}$$

where $\mathbf{S} = \{\partial L(\omega_i)/\partial\mathbf{v}\} \in \mathbb{C}^{n_w \times 2}$ is the Jacobian/sensitivity matrix, k indicates the current iterative step, the superscript H represents the Hermitian transpose.

To avoid the overflow of double precision limits calculating the modified Bessel function, the limitation of variables are employed as $\min\left\{\max\left\{a^k, \underline{a}\right\}, \overline{a}\right\}$ and $\min\{\max\{{\mu_r}^k, \underline{\mu_r}\}, \overline{\mu_r}\}$ where $\underline{a}$, $\overline{a}$, $\underline{\mu_r}$ and $\overline{\mu_r}$ represent the lower and upper limits of radius and relative permeability, respectively.

The optimisation process is summarized and illustrated in Algorithm 1.

3. Results and Discussions

In numerical simulations and experiments, the parameters of the measurement setup are provided in Table 1. The numerical analysis is performed on a PC with CPU AMD Ryzen 7 5800H 3.2 GHz and RAM 32 GB.

3.1. Numerical simulations

In the numerical simulation, the coil inductance spectra are calculated by employing the FEM model in the COMSOL software, of which the basic model structure is shown in Fig. 4. In the FEM model, the length of cylinders is 1000 mm, which is long enough to neglect the influence of edges on the eddy current signals.

For implementation, in the analytical model, the truncated calculation radius is $d = 50$ m, and the number of spatial frequencies is $n_\alpha = 1000$. The analytical solutions and FEM results

Algorithm 1 Cylinder radius and permeability optimization

Input: $\mathbf{v}^1 = [\tilde{a}, \tilde{\mu}_r]^{\mathrm{T}}$, ϵ and q_i
Output: $\mathbf{v} = [\hat{a}, \hat{\mu}_r]^{\mathrm{T}}$

initialize: Set $\Delta\mathbf{L}^1 = \Delta\mathbf{L}(\mathbf{v}^1)$
for $k = 1, 2, ..., q_i$ **do**
    $\mathbf{S}^k = \partial\Delta\mathbf{L}^k / \partial\mathbf{v}^k$
    $\mathbf{v}^{k+1} = \mathbf{v}^k - [(\mathbf{S}^k)^{\mathrm{H}}\mathbf{S}^k]^{-1}(\mathbf{S}^k)^{\mathrm{H}}(\Delta\mathbf{L}^k - \Delta\mathbf{L}_{\mathrm{m}})$
    $\Delta\mathbf{L}^{k+1} = \Delta\mathbf{L}(\mathbf{v}^{k+1})$
    if $\left\|\Delta\mathbf{L}^{k+1} - \Delta\mathbf{L}_{\mathrm{m}}\right\|_2^2 \leq \epsilon$ **then**
        Break;
    end if
end for

Table 1: Parameters of measurement setup

Parameters	Value
Inner radius of coils r_1 (mm)	53.5
Outer radius of coils r_2 (mm)	54
Lower dimension of coils l_1 (mm)	10.75
Upper dimension of coils l_2 (mm)	15.75
Span between coils d (mm)	21.5
Number of coil turns	15

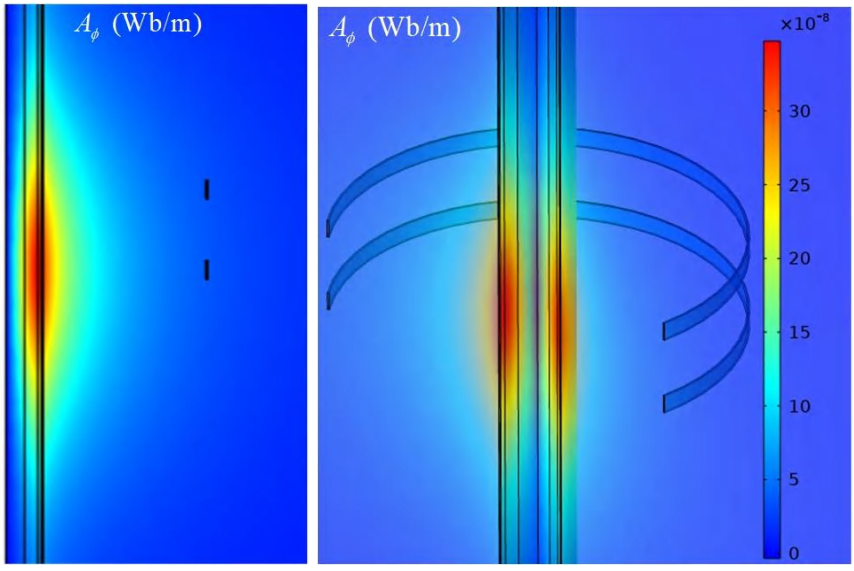

(a) (b)

Figure 4: FEM solution of a cylinder in (a) cross-sectional view and (b) 3D (rotating) view. Lines in cylinder cross-section are applied to facilitate mesh generation

of inductance spectrum measuring cylinders with various properties are shown in Fig. 5. The inductance spectrum is calculated by equation (18) from the voltage of the receiving coil. The inductance spectra calculated by FEM and DD analytical model in Fig. 5 are matched.The simplified analytical model calculates the inductance using equation (6) with the phase term by equation (9). The simplification accuracy is relatively higher for high excitation frequency, *i.e.* higher than the peak frequency. The DD analytical model alone is employed in the following sections for inductance calculation.

The relationships between the inductance zero-crossing frequency ω_c and cylinder properties are shown in Fig. 6, in which the variation of radius $a \in [5.5, 19.5]$ mm, permeability $\mu_r \in [5, 80]$, conductivity $\sigma \in [1, 7]$ MS/m. This indicates that ω_c is approximately linearly correlated to μ_r while inversely correlated to a^2 and σ, which corresponds to the proposed equation (12).

$$\Delta L = (V_{\text{sample}} - V_{\text{air}})/(I_s j\omega) \tag{18}$$

where V_{sample} and V_{air} are voltage in the receiving coil measured with and without test pieces, respectively, and the amplitude and frequency of the applied current signal in the transmitting coil is I_s and ω.

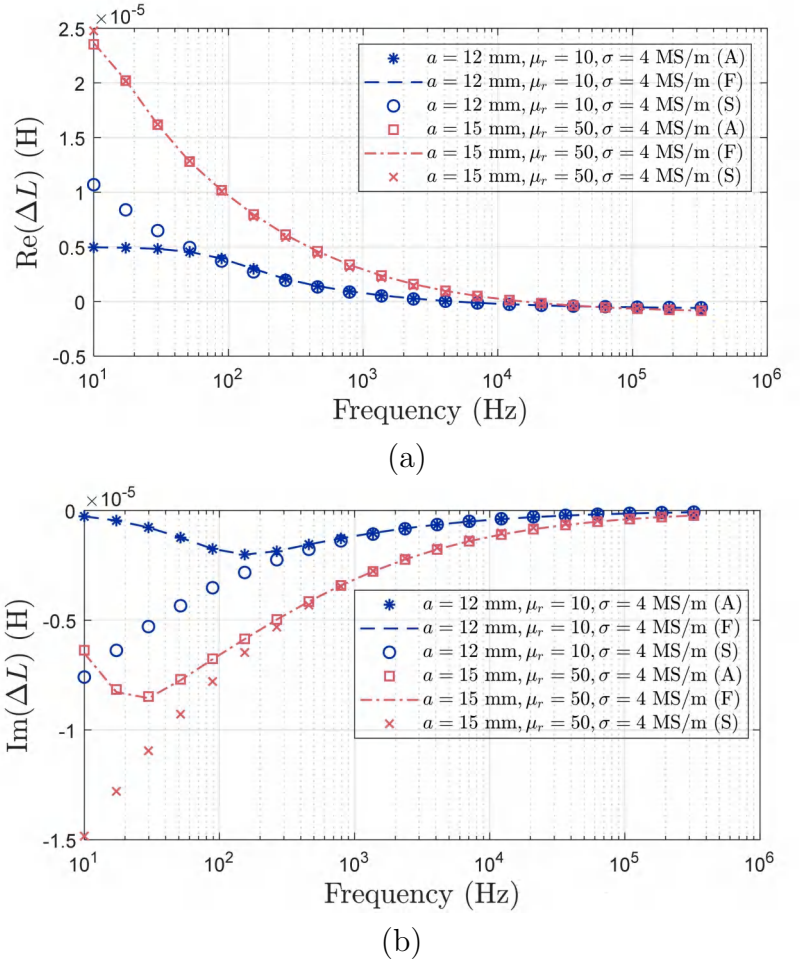

Figure 5: Inductance spectra of magnetic cylinders, (a) and (b) are real and imaginary part of the inductance . A, S and F represent the DD analytical model, simplified analytical model and FEM solutions, respectively

To evaluate the cylinder property estimation, the properties in the range of $a \in [3, 20]$ mm, $\sigma \in [1, 6]$ MS/m and $\mu_r \in [5, 80]$ are considered. The white Gaussian noise has been applied to

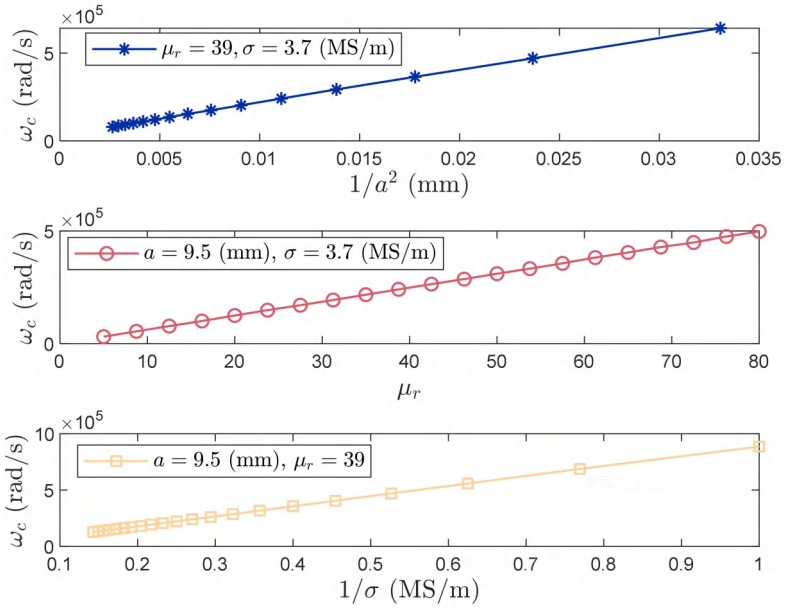

Figure 6: Relationships between the inductance zero-crossing frequency and cylinder properties

the inductance spectra of FEM results, and the equivalent signal-to-noise ratio (SNR) is 80 dB. The excitation frequency ω_s employed to calculate cylindrical radius by equation (14) is 510 kHz. The relative error of initial cylinder property guess is shown in Fig. 7, and the error of estimation is shown in Fig. 8 and Fig. 9.

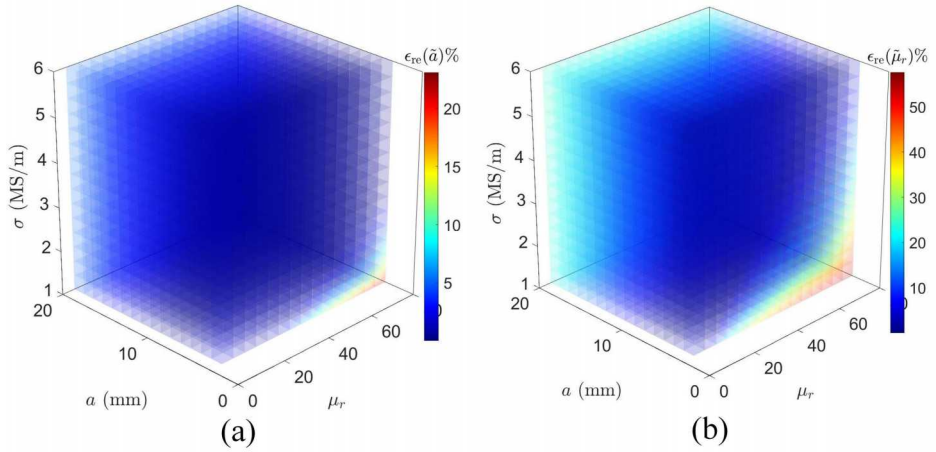

Figure 7: Relative error of radius and permeability initial guess

The error of the initial guess shown in Fig. 7 indicates that the accuracy of the simplified analytical model is influenced by cylinder properties and mainly affected by radius. The relative error of radius and permeability initial guess is generally smaller than 5% and 25 % when radius is higher than 5 mm. The error of initial guess relates to the approximation conditions that $\alpha a \to 0$ and $\alpha_1 a \to \infty$ for the proposed simplified analytical model. The error of radius guess is relatively lower due to its dependence only on the approximation at the high frequency ω_s while the error of permeability guess relies on both frequencies of ω_s and ω_c. Furthermore, the error of property estimation in Fig. 8 (a) and (b) shows that the relative error of radius and permeability is lower than 1 %, adopting the initial guess from the simplified analytical model, and the error decreases

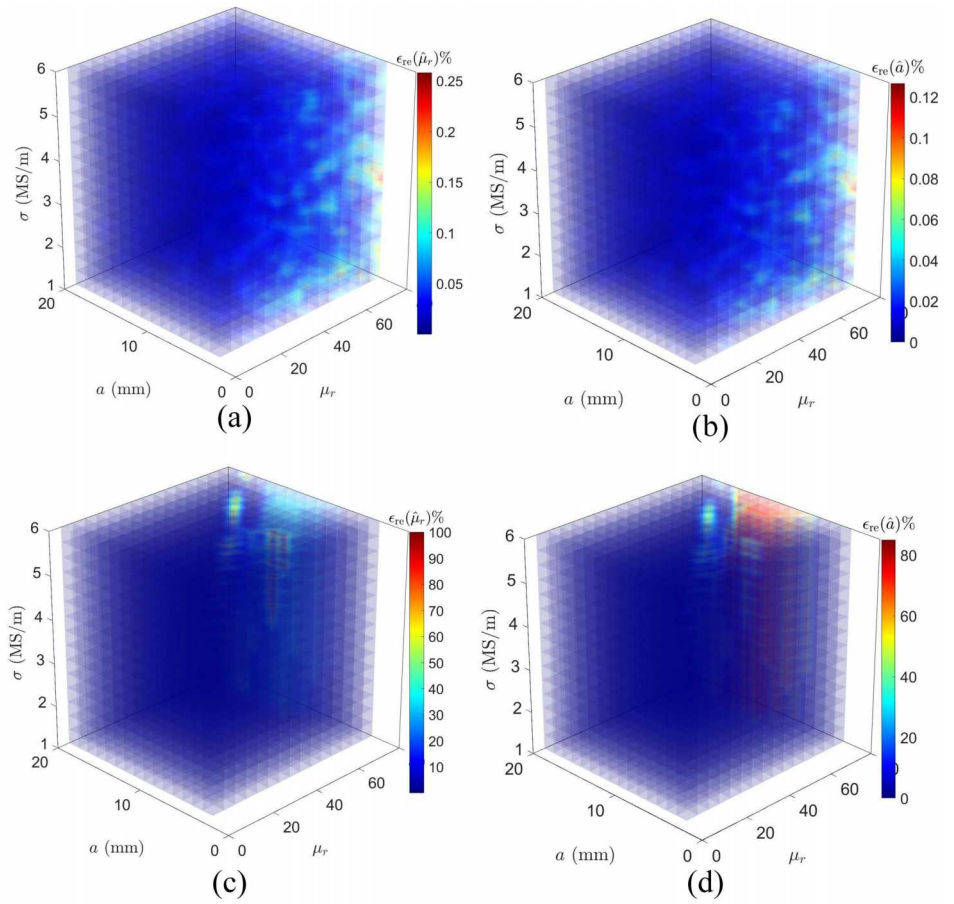

Figure 8: Relative error of permeability and radius estimation, with the initial guess of $\tilde{a}$ and $\tilde{\mu}_r$ by equation (14) and (15) for (a) and (b) and with the initial guess of $\tilde{a} = 1$ mm, $\tilde{\mu}_r = 1$ for (c) and (d), respectively

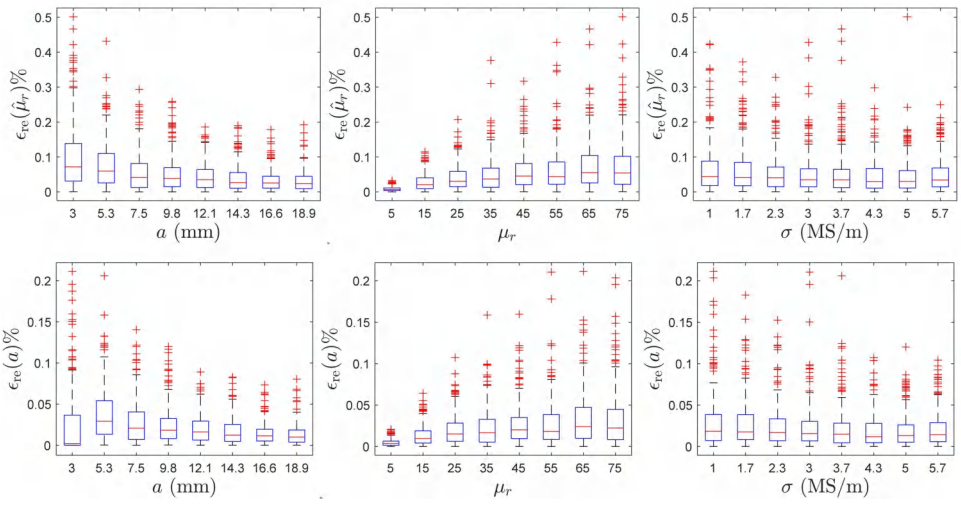

(a)

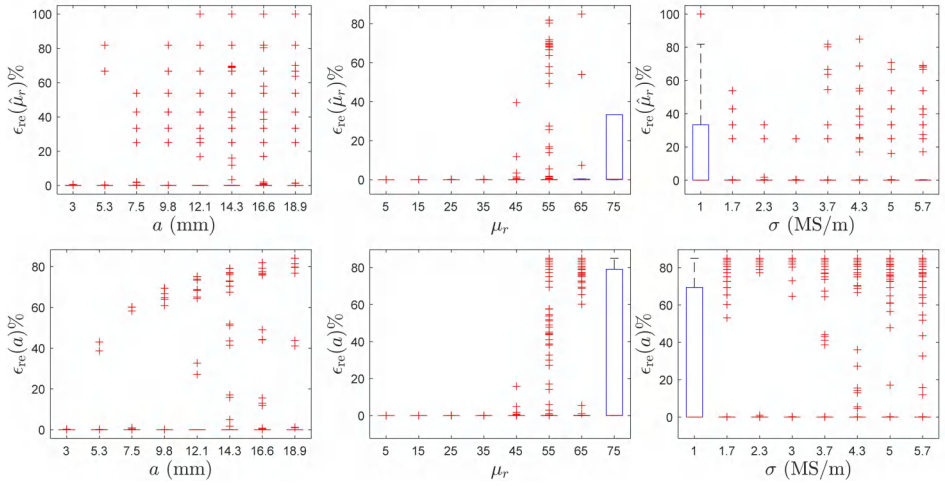

(b)

Figure 9: Box plot of permeability and radius relative estimation error, with the initial guess (a) obtained by equation (14) and (15) and (b) adopted as $\tilde{a} = 1$ mm and $\tilde{\mu}_r = 1$ (On each box, the central mark indicates the median, and the bottom and top edges of the box indicate the 25 % and 75 %, respectively. The whiskers extend to the most extreme data points not considered outliers, and the outliers are plotted individually using the '+' marker)

with the radius increase. In comparison, the estimation in Fig. 8 (c) and (d) implementing the initial guess of $\tilde{a} = 1$ mm, $\tilde{\mu}_r = 1$ shows the large error for radius close to 10 mm and relative permeability around 80. For these cases with large estimation errors, the optimisation without an appropriate initial guess fails to estimate the reasonable cylinder properties.

3.2. Experiments

The experimental setup is shown in Fig. 10 and the parameters of measurement configuration are identical to the numerical simulation. The stainless steel cylinders are measured via the Zurich impedance analyser (MFIA) which attains a measurement accuracy of 0.05% [29]. The applied martensitic stainless steels in the length of 200 mm are made with materials of AISI 416, 420 and 431.

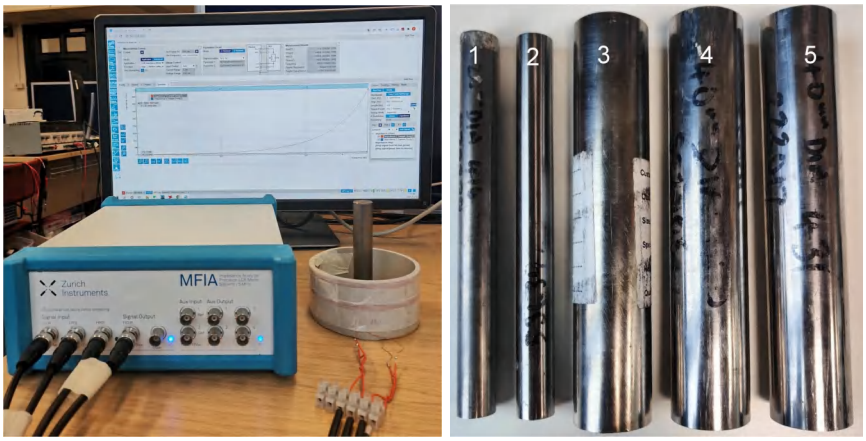

(a) (b)

Figure 10: Experimental setup. (a) measurement device and (b) measured samples

The cylinder properties are provided in Table 2, in which the nominal radius and conductivity is obtained from the product specification. The nominal value of relative permeability is obtained by evaluating the squared Euclidean distance between the calculated and measured inductance spectra, *i.e.* $\min_{\mu_r} \left\{ \|\Delta\mathbf{L}(\mu_r) - \Delta\mathbf{L}_{\mathrm{m}}\|_2^2 \right\}$, $\mu_r \in [1, 1.1, 1.2, ..., 100.0]$.

The inductance spectra of representative cylinders, *i.e.* samples 1, 4 and 5 measured by MFIA and calculated by the analytical model are shown in Fig. 11. There is a little difference between the measured and calculated inductance at the relatively low frequency near 1 kHz, which is due to the finite length of cylinders. To avoid this influence, the inductance spectrum in the frequency of $f \in [21.8, 510]$ kHz (including 11 frequency points) is selected for cylinder property estimation.

The optimisation adopts initial guess of cylinder properties calculated by the simplified analytical model using equation (14) and (15). The cylinder property estimation results are shown in Table 2.

In Table 2, the initial guess of radius is close to the nominal value while the error of initial permeability guess is relatively large for cylinders in the radius of 20 mm. Because large radius can hardly satisfies the approximation condition $\alpha a \to 0$ of the simplified analytical model. Furthermore, the permeability and radius estimation results are close to the nominal values. The largest error of radius and permeability estimation is smaller than 0.5 mm and 2, respectively, and the relative error is within 3 %. The estimation error is generally higher than numerical simulations, which is mainly caused by the finite length of cylinders and measurement error. The numerical simulation and experimental results illustrate that the proposed method can provide accurate radius permeability for metallic cylinders of various sizes and electromagnetic properties.

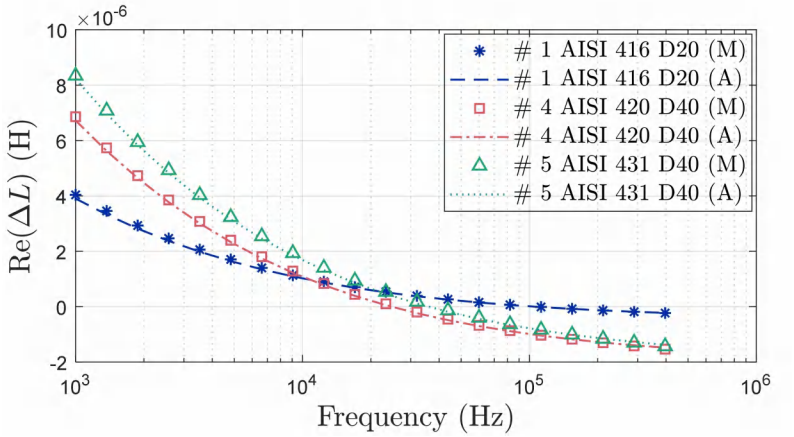

(a)

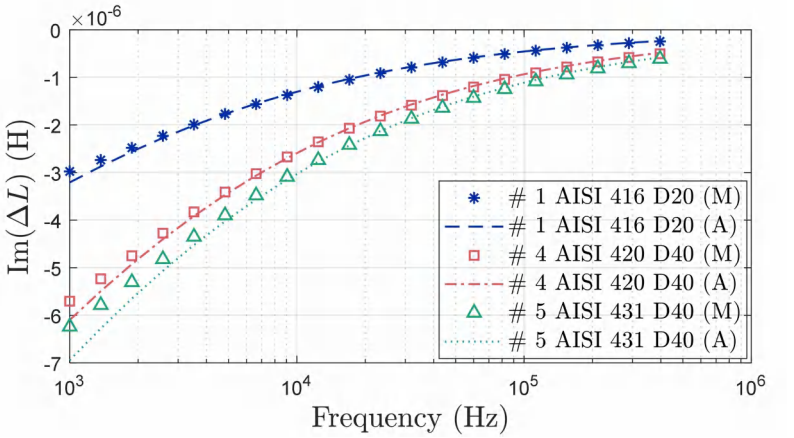

(b)

Figure 11: Experimental inductance spectra of representative cylinders in Table 2. M and A indicate measurements and analytical solutions, respectively

Table 2: Estimation results of cylinder properties in experiments

Material	AISI 416		AISI 420	AISI 431	
#	1	3	4	2	5
σ (MS/m)	1.75	1.75	1.6	1.4	1.4
a (mm)	10	20	20	10	20
$\tilde{a}$ (mm) [1]	10.14	21.11	21.09	10.45	21.14
$\hat{a}$ (mm) [2]	10.31	20.08	20.35	10.28	20.42
$\varepsilon_{\text{re}}(\hat{a})$[3]	1.4%	0.4%	1.8%	2.8%	2.1%
μ_r	72.4	59.3	56.7	62.4	72.7
$\tilde{\mu}_r$ [1]	79.37	76.14	72.79	67.56	93.59
$\hat{\mu}_r$ [2]	71.31	58.55	56.85	60.99	71.76
$\varepsilon_{\text{re}}(\hat{\mu}_r)$[3]	1.5%	1.3%	0.3%	2.3%	1.3%
Time (s)	0.17	0.18	0.18	0.18	0.18

[1] $\tilde{a}$ and $\tilde{\mu}_r$ are initial guess of cylinder radius and relative permeability, respectively

[2] $\hat{a}$ and $\hat{\mu}_r$ are estimated cylinder radius and relative permeability, respectively

[3] Relative error of estimation

4. Conclusion

This study proposes a novel method combining the analytical model and optimisation method to estimate the relative permeability of metallic cylinders. The analytical model of a metallic cylinder encircled by coaxial coils is simplified to obtain the initial guess of cylinder radius and permeability from the coil inductance spectrum. Based on the initial guess, the modified Newton-Raphson algorithm is employed to estimate the radius and permeability. In numerical simulation and experiments, the performance of the proposed method has been validated by implementing metallic cylinders in various sizes and materials. It has been validated that the initial guess can avoid some local minima of optimisation to estimate the accurate results for various cylinder properties. In the numerical simulation, the proposed method achieves the relative estimation error of cylinder properties within 0.5 %. In experiments, the relative estimation error of cylinder radius and permeability is smaller than 3 %.

References

[1] M. Bellanova, M. Carboni, R. Felicetti, A feasibility analysis on the application of eddy current testing to the detection of the most detrimental defects in historical metallic tie-rods, NDT & E International 104 (2019) 34–41.

[2] M. Rocha, S. Michel, E. Brühwiler, A. Nussbaumer, Very high cycle fatigue tests of quenched and self-tempered steel reinforcement bars, Materials and Structures 49 (2016) 1723–1732.

[3] M. Neumann, O. Stenzel, F. Willot, L. Holzer, V. Schmidt, Quantifying the influence of microstructure on effective conductivity and permeability: virtual materials testing, International journal of solids and structures 184 (2020) 211–220.

[4] O. Stenzel, O. Pecho, L. Holzer, M. Neumann, V. Schmidt, Big data for microstructure-property relationships: A case study of predicting effective conductivities, AIChE Journal 63 (9) (2017) 4224–4232.

[5] G. Tytko, Eddy current testing of small radius conductive cylinders with the employment of an i-core sensor, Measurement 186 (2021) 110219.

[6] F. Xie, X. Wu, H. Zhang, X. Zhang, Research on pulsed eddy current automatic detection technology for weld defects of pressure vessel cylinder, Measurement 176 (2021) 109081.

[7] J. Salach, Non-destructive testing of cylindrical ferromagnetic and non-magnetic materials using eddy current tomography, in: Mechatronics-Ideas for Industrial Application, Springer, 2015, pp. 373–380.

[8] C. Ni, L. Hua, X. Wang, Z. Wang, X. Qin, Z. Fang, Coupling method of magnetic memory and eddy current nondestructive testing for retired crankshafts, Journal of Mechanical Science and Technology 30 (2016) 3097–3104.

[9] M. Lu, A. Peyton, W. Yin, Acceleration of frequency sweeping in eddy-current computation, IEEE Transactions on Magnetics 53 (7) (2017) 1–8.

[10] R. Huang, M. Lu, Z. Chen, Y. Shao, Z. Xia, G. Hu, A. Peyton, W. Yin, A novel acceleration method for crack computation using finite element analysis in eddy current testing, IEEE Transactions on Instrumentation and Measurement 71 (2022) 1–9.

[11] K. Zhao, M. N. Vouvakis, J.-F. Lee, Solving electromagnetic problems using a novel symmetric fem-bem approach, IEEE Transactions on magnetics 42 (4) (2006) 583–586.

[12] C. Dodd, W. Deeds, Some Eddy-current Problems and Their Integral Solutions, ORNL.: Oak Ridge National Laboratory, Oak Ridge National Laboratory, 1969.

[13] C. V. Dodd, W. E. Deeds, Analytical solutions to eddy-current probe-coil problems, Journal of Applied Physics 39 (6) (1968) 2829–2838. doi:10.1063/1.1656680.

[14] J. R. Bowler, T. P. Theodoulidis, Eddy currents induced in a conducting rod of finite length by a coaxial encircling coil, Journal of Physics D: Applied Physics 38 (16) (2005) 2861.

[15] H. Sun, J. R. Bowler, T. P. Theodoulidis, Eddy currents induced in a finite length layered rod by a coaxial coil, IEEE Transactions on Magnetics 41 (9) (2005) 2455–2461.

[16] M. Shamgholi, S. H. H. Sadeghi, An efficient method for predicting the output signal of an eddy current probe around the edge of a conductive cylindrical rod, IEEE Transactions on Magnetics 58 (7) (2022) 1–8.

[17] T. P. Theodoulidis, J. R. Bowler, Bobbin coil signal variation due to an axisymmetric circumferential groove in a tube, in: AIP Conference Proceedings, Vol. 1096, American Institute of Physics, 2009, pp. 1922–1929.

[18] F. Jiang, S. Liu, S. Xin, H. Zhang, Electromagnetic nondestructive testing model and surface magnetic field analysis for circumferential cracks on metal rod, Journal of Nondestructive Evaluation, Diagnostics and Prognostics of Engineering Systems 2 (4) (2019).

[19] T. Theodoulidis, E. Kriezis, Eddy Current Canonical Problems (with Applications to Nondestructive Evaluation), Contemporary research on emerging science and technology, Tech Science Press, 2006.

[20] T. Theodoulidis, A. Skarlatos, Eddy current interaction of an arbitrarily positioned probe coil with a conductive cylinder, IEEE transactions on magnetics 48 (8) (2012) 2392–2394.

[21] Z. Xia, J. Yan, R. Huang, M. Lu, Z. Cui, A. Peyton, W. Yin, W. Yang, Fast estimation of metallic pipe properties using simplified analytical solution in eddy-current testing, IEEE Transactions on Instrumentation and Measurement 72 (2023) 1–13. doi:10.1109/TIM.2022.3224516.

[22] H. J. . S. Y. Lee, K. H.; Kim, Electromagnetic method for analyzing the property of steel casing, Tech. rep., University of California (1988).

[23] D. Vasic, V. Bilas, D. Ambrus, Validation of a coil impedance model for simultaneous measurement of electromagnetic properties and inner diameter of a conductive tube, IEEE Transactions on Instrumentation and Measurement 55 (1) (2006) 337–342. doi:10.1109/TIM.2005.861244.

[24] I. D. Adewale, G. Y. Tian, Decoupling the influence of permeability and conductivity in pulsed eddy-current measurements, IEEE Transactions on Magnetics 49 (3) (2013) 1119–1127. doi:10.1109/TMAG.2012.2225634.

[25] Z. Xia, R. Huang, Z. Chen, K. Yu, Z. Zhang, J. R. Salas-Avila, W. Yin, Eddy current measurement for planar structures, Sensors 22 (22) (2022) 8695.

[26] M. Lu, W. Zhu, L. Yin, A. J. Peyton, W. Yin, Z. Qu, Reducing the lift-off effect on permeability measurement for magnetic plates from multifrequency induction data, IEEE Transactions on Instrumentation and Measurement 67 (1) (2018) 167–174. doi:10.1109/TIM.2017.2728338.

[27] M. Lu, R. Huang, W. Yin, Q. Zhao, A. Peyton, Measurement of permeability for ferrous metallic plates using a novel lift-off compensation technique on phase signature, IEEE Sensors Journal 19 (17) (2019) 7440–7446.

[28] Y. Yu, K. Gao, T. Theodoulidis, F. Yuan, Analytical solution for magnetic field of cylindrical defect in eddy current nondestructive testing, Physica Scripta 95 (1) (2019) 015501.

[29] MFIA 5MHz impedance analyzer and precision lcr meter, https://www.zhinst.com/sites/default/files/documents/2021-12/zi_mfia_leaflet_latest.pdf., accessed on: Apr. 4, 2022. [Online].

6. Estimation of thickness and radius of hollow metallic spheres with a simplified forward model

Estimation of thickness and radius of hollow metallic spheres with a simplified forward model

Gang Hu[1,2], Zihan Xia[2], Wuliang Yin[2], Ruochen Huang[3], Jialong Shen[4,5], Ronghua Zhang[1,*]

***Abstract*—The measurement of metallic spherical objects in various industrial applications has a significant role in guaranteeing safety and product quality, which can be realized by the eddy-current testing technique without contact. In this study, for the measurement of thickness and radius of non-magnetic spherical shells, the original analytical model is simplified according to the asymptotic forms of the modified spherical Bessel functions. The simplified model contains only elementary functions and can therefore accelerate the sphere property estimation when employing the optimization approach based on the Newton-Raphson method. In both numerical simulation and experimental study, the proposed method can provide accurate spherical shell radii with less computational time compared with the original analytical model.**

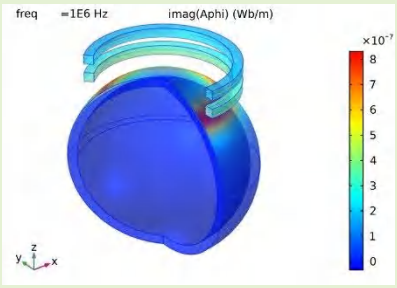

***Index Terms*—Eddy current testing, multi-frequency testing, spherical radius measurement, optimisation**

I. Introduction

Thin-walled parts are widely used in aerospace equipment, rocket nozzles and aircraft skins [1, 2]. Spherical thin-walled parts are often used in shock wave physics, and are used to develop the mechanism of various physical, chemical and mechanical phenomena. The thin-walled parts of spherical shells put forward the requirement of wall-thickness measurement [3]. To improve the accuracy and reliability of these conductive spherical shells, the eddy-current testing (ECT) technique can be employed for the thickness and radius measurement. Eddy current testing is growing in popularity as a promising tool for measuring the properties of metallic objects, which has been adopted in the metallic component testing of robots, aircraft, automotive, and medical devices [4, 5]. The relevant studies have gained interest for decades, in terms of computational viewpoint and industrial applications. The computational objective is to derive the theoretical model that accounts for the relationships between the electromagnetic measurement and physical properties of the measured objects.

The theoretical studies focus on the forward and inverse problem of ECT, most of which adopt the sensor composed of the exciting and receiving coils. The forward problem calculates the frequency-dependent inductance of the receiving coil or a given electromagnetic field generated by the exciting coil and physical properties of the metallic sphere, while the inverse problem estimates the unknown electrical conductivity, permeability, spherical radii and sensor lift-off from the inductance measurements [6].

In the forward problem study calculating the inductance (or impedance) variation of coil due to the various metallic spherical objects, the analytical and numerical methods, *e.g.* finite element method (FEM) and boundary element method (BEM), are frequently employed. Luquire, Dodd and Deeds derived the analytical model for the inductance calculation of non-magnetic double-layered spherical objects [7]. Kolyshkin and Vaillancourt calculate the coil impedance for different conductivity and permeability of the double-layer sphere [8]. Theodoros et al. proposed the truncated region eigenfunction expansion (TREE) method approximating the integral in the analytical solution by the series form, which has been applied to calculate the coil impedance measuring the multi-layered spherical structure [9, 10]. Pham and Peyton proposed a single-layered spherical model employing the BEM. They eliminate two boundary conditions involving the magnetic vector potential and its normal derivative through the transformation of exterior boundary integral equation. As a result, the computational complexity of the model is considerably reduced [11]. Furthermore, the FEM capable of the complex structure analysis is also suitable for the spherical model [12-14], of which the computational cost is relatively higher. Compared with the BEM and FEM, since the model of spherical object measurement is usually symmetric and the physical properties

Manuscript updated September 10, 2022 and submitted September 10, 2022. This research is financially supported from China Scholarship Council (CSC).

Mr. Gang Hu and Dr. Ronghua Zhang are with the School of Electronic and information engineering, Tiangong University, Tianjin 300387, China. (e-mail: gang.hu@postgrad.manchester.ac.uk; rh_zhang_2005@163.com).

Mr. Gang Hu, Mr. Zihan Xia and Dr. Wuliang Yin are with the School of Electrical and Electronic Engineering, University of Manchester, Manchester M13 9PL; U.K. (e-mail: zihan.xia-5@postgrad.manchester.ac.uk; wuliang.yin@manchester.ac.uk)

Dr. Ruochen Huang was with the School of Electrical and Electronic Engineering, University of Manchester, Manchester M13 9PL; U.K. and now with College of Electrical Engineering and Automation, Fuzhou University, Fuzhou 350108, China. (e-mail: ruochen_huang@fzu.edu.cn)

Mr. Jialong shen is with the Key Laboratory of New Processing Technology for Nonferrous Metal & Materials, Ministry of Education/ Guangxi, Guilin University of Technology, Guilin 541004, China, and with the Collaborative Innovation Center for Exploration of Nonferrous Metal Deposits and Efficient Utilization of Resources, Guilin University of Technology, Guilin 541004, China. (e-mail: jialong.shen@glut.edu.cn)

can be expressed explicitly, the analytical model is preferable for the efficient calculation of coil inductance. The analytical model can be further simplified to boost the efficiency of estimating the object properties, which has been introduced for the metallic plate measurement [15]. Nevertheless, the simplification of analytical model for the spherical objects remains to be explored.

In the inverse problem, the object physical properties can be estimated by discovering the functional relationships between the inductance characteristic frequencies, *e.g.* the zero-crossing frequency (where the real part of inductance change is zero) and peak frequency (where the imaginary part of inductance change reaches its minimum), and object properties. The relationships, in simple explicit expression, are usually derived by the simplified analytical model [16] or by the numerical analysis based on extensive simulation and experimental data [17, 18]. However, the applicable conditions are limited as the derived relationships vary with the measurement configuration, *i.e.* excitation frequency, sensor geometry *etc*, and it is sophisticated to calculate multiple properties simultaneously. Alternatively, the object properties can be obtained through the optimization methods, minimizing the error function related to the scattered field in the region outside the measured specimen [19-22]. This can be achieved by the non-linear optimization algorithm including the gradient descent, Newton-Raphson and Levenberg–Marquardt (LM) methods. Among these methods, the Newton-Raphson algorithm reaches the convergence point with less computational time, given the appropriate starting point [23, 24]. However, strong difficulties arise when minimizing the Euclidean distance, since the presence of local minima requires global optimization procedures, *e.g.* heuristic methods which work efficiently only with a limited number of variables [25, 26]. Furthermore, the variable updating process will be unstable if the correlation exists between the variables and related derivatives. This has been confirmed in the metallic pipe measurement study that the influences of conductivity and permeability on inductance measurement are strongly coupled [27-29]. To elevate the accuracy and efficiency of sphere property estimation, it is of great significance to crack the tough nut of optimization.

In this study, the original analytical model of non-magnetic spherical shell is reduced to an elementary function employing the asymptotic forms of the modified spherical Bessel functions. For the fast estimation of spherical shell properties, the simplified model is applied to the optimization method based on the Newton-Raphson algorithm, in which the issue of starting point and variable combination selection is addressed. In the numerical simulation and experiments, the performance of the proposed method has been evaluated by testing various aluminium and stainless-steel spherical shells.

II. METHOD

A. Forward method

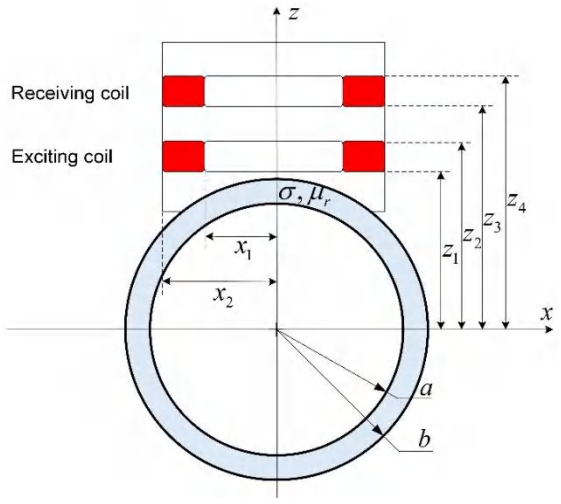

Fig. 1. Sensor structure

According to the solution of separating variables method [9], the magnetic vector potential induced by the hollow spherical object in air can be expressed by

$$A_{ec} = \frac{\mu_0 I N_S}{2\Delta z \Delta x} \sum_{n=1}^{\infty} \frac{b^{2n+1} P_n^1(\cos\theta)}{r^{n+1} n(n+1)} \times \frac{V_{11}\,\mathrm{NOMI} + V_{21}\,\mathrm{NOMK}}{V_{11}\,\mathrm{DENI} + V_{21}\,\mathrm{DENK}} P_n^1(\cos\theta) \quad (1)$$

where μ_0 is the permeability of the air, I denotes the value of the current in the exciting coil, N_S is the number of coil turns, $\Delta z = z_2 - z_1$ and $\Delta x = x_2 - x_1$ represents the thickness and height of exciting coil respectively, $P_n^1(\cos\theta)$ is the first-order associated Legendre function in degree n, V_{11} and V_{21} relate to the boundary conditions of the vector potential between the metallic layer and inner hollow space, while other terms link the conductive layer to outer space, *i.e.* NOMI, DENI, NOMK and DENK,

$$V_{11} = \frac{a^n}{\mu_2}\left\{k_n(a_2 a)[1-(n+1)\mu_2] + a_2 a k_n'(a_2 a)\right\} \quad (2)$$

$$V_{21} = -\frac{a^n}{\mu_2}\left\{i_n(a_2 a)[1-(n+1)\mu_2] + a_2 b i_n'(a_2 b)\right\} \quad (3)$$

$$\mathrm{NOMI} = i_n(a_2 b)[(n+1)\mu_2 - 1] - a_2 b i_n'(a_2 b) \quad (4)$$

$$\mathrm{NOMK} = k_n(a_2 b)[(n+1)\mu_2 - 1] - a_2 b k_n'(a_2 b) \quad (5)$$

$$\mathrm{DENI} = i_n(a_2 b)[n\mu_2 + 1] + a_2 b i_n'(a_2 b) \quad (6)$$

$$\mathrm{DENK} = k_n(a_2 b)[n\mu_2 + 1] + a_2 b k_n'(a_2 b) \quad (7)$$

where $i_n(\cdot)$ and $k_n(\cdot)$ are the modified spherical Bessel functions of the first and the second kind, respectively, $i_n'(\cdot)$ and $k_n'(\cdot)$ denote the related derivatives, and $a_2 = \sqrt{j\omega\mu_r\mu_0\sigma}$ indicates the complex special frequency of conductive layer.

The mutual inductance variation between coils L due to the measured pipe (referred to as inductance hereinafter) is expressed by

$$L=\frac{\pi\mu_0 N_{\mathrm{re}}N_{\mathrm{ex}}}{\Delta z_{\mathrm{ex}}\Delta z_{\mathrm{re}}\Delta x_{\mathrm{ex}}\Delta x_{\mathrm{re}}}\sum_{n=1}^{\infty}\frac{b^{2n+1}}{n(n+1)}\frac{V_{11}\,\mathrm{NOMI}+V_{21}\,\mathrm{NOMK}}{V_{11}\,\mathrm{DENI}+V_{21}\,\mathrm{DENK}}\times P_{n,s(\mathrm{ex})}P_{n,s(\mathrm{re})} \tag{8}$$

Furthermore, equation (8) can be expressed by the sum of the product of phase term S_n and sensor term K_n, *i.e.*,

$$\begin{aligned}
L&=\sum_n S_n K_n\\
S_n&=\frac{b^{2n+1}}{n(n+1)}\frac{V_{11}\,\mathrm{NOMI}+V_{21}\,\mathrm{NOMK}}{V_{11}\,\mathrm{DENI}+V_{21}\,\mathrm{DENK}}\\
K_n&=\frac{\pi\mu_0 N_{\mathrm{re}}N_{\mathrm{ex}}}{\Delta z_{\mathrm{ex}}\Delta z_{\mathrm{re}}\Delta x_{\mathrm{ex}}\Delta x_{\mathrm{re}}}P_{n,\mathrm{E}}P_{n,\mathrm{R}}\\
P_{n,\mathrm{E}}&=\int_{S(\mathrm{ex})}\frac{\sin\theta_o P_n^1(\cos\theta_o)}{r_o^n}dS\\
P_{n,\mathrm{R}}&=\int_{S(\mathrm{re})}\frac{\sin\theta_o P_n^1(\cos\theta_o)}{r_o^n}dS
\end{aligned} \tag{9}$$

where $S(\mathrm{ex})$ and $S(\mathrm{me})$ denote the cross-sectional region of exciting and receiving coils, respectively.

For the non-magnetic spherical objects, the phase term S_n becomes [7],

$$\begin{aligned}
S_n(\alpha)&=c_n S(\alpha)\\
S(\alpha)&=\frac{1}{bD_n(\alpha)k_n(\alpha b)}\\
&\times\{k_n(\alpha_2 b)[\alpha_2 i_n(\alpha a)i_{n-1}(\alpha_2 a)-\alpha i_n(\alpha_2 a)i_{n-1}(\alpha a)]\\
&+i_n(\alpha_2 b)[\alpha k_n(\alpha_2 a)i_{n-1}(\alpha a)+\alpha_2 k_{n-1}(\alpha_2 a)i_n(\alpha a)]\}\\
&-i_n(\alpha b)/k_n(\alpha b)\\
D_n(\alpha)&=[\alpha_2 k_{n-1}(\alpha_2 b)k_n(\alpha b)-\alpha k_{n-1}(\alpha b)k_n(\alpha_2 b)]\\
&\times[\alpha i_n(\alpha_2 a)i_{n-1}(\alpha a)-\alpha_2 i_n(\alpha a)i_{n-1}(\alpha_2 a)]\\
&+[\alpha_2 k_{n-1}(\alpha_2 a)i_n(\alpha a)+\alpha k_n(\alpha_2 a)i_{n-1}(\alpha a)]\\
&\times[\alpha i_n(\alpha_2 b)k_{n-1}(\alpha b)+\alpha_2 i_{n-1}(\alpha_2 b)k_n(\alpha b)]
\end{aligned} \tag{10}$$

where $c_n=\frac{[(2n-1)!!]^2}{\alpha^{2n+2}}$, $(\cdot)!!$ indicates the double fractional operator, $\alpha=j\sqrt{\omega^2\mu_0\varepsilon_0}$ is the spatial frequency in air, which is a very small complex value.

According to the asymptotic forms of the modified spherical Bessel functions (detailed in Appendix A.), the phase term can be simplified into,

$$S_n\approx\frac{c_n b^{2n}}{\alpha_2}\frac{\alpha_2 a+(2n+1)\tanh[\alpha_2(b-a)]}{\alpha_2 a\tanh[\alpha_2(b-a)]+2n+1}+\frac{c_n b^{2n+1}}{2n+1} \tag{11}$$

B. Inversion method

The inverse problem estimates the spherical shell properties by minimizing the Euclidean distance between the calculated and measured inductance spectra, which can be defined as a least-squares problem, *i.e.*,

$$\min_{\mathbf{v}} f=\left\|\mathbf{L}(\mathbf{v})-\mathbf{L}_{\mathrm{m}}\right\|_2^2 \tag{12}$$

The operator $\|.\|_2^2$ denotes the l_2-norm, $\mathbf{L}$ and $\mathbf{L}_{\mathrm{m}}$ ($\mathbf{L}$, $\mathbf{L}_{\mathrm{m}}\in\mathbb{C}^{n_f\times 1}$, n_f is the quantity of frequency points) are variation of the estimated and measured inductance spectra due to the sphere, respectively, $\mathbf{v}\in\mathbb{R}^{n\times 1}$ denotes the vector of the estimated variables, and n is the quantity of variables.

The local minimum $\mathbf{v}^*$ of optimisation problem satisfies the formula (13)

$$\nabla f(\mathbf{v}^*)=\mathbf{0} \tag{13}$$

where $[\nabla f]_{i,j}=\partial f_i/\partial v_j$ and $\mathbf{0}\in\mathbb{R}^{n_v\times 1}$ is a zero vector.

The reference point $\mathbf{v}_r$ can be adjusted to $\mathbf{v}^*$, then equation (13) can be approximated by using the Taylor series,

$$\nabla f(\mathbf{v}^*)=\nabla f(\mathbf{v}_r)+\nabla\nabla f(\mathbf{v}_r)\Delta\mathbf{v} \tag{14}$$

where $\Delta\mathbf{v}=\mathbf{v}^*-\mathbf{v}_r$ and $\nabla\nabla f(\mathbf{v}_r)$ denotes the Hessian matrix evaluated at $\mathbf{v}_r$ which is usually calculated by

$$\nabla\nabla f(\mathbf{v}_r)\approx[\nabla f(\mathbf{v}_r)]^{\mathrm{H}}\nabla f(\mathbf{v}_r) \tag{15}$$

where the superscript $^{\mathrm{H}}$ represents the conjugate transpose, and $\mathbf{H}(\mathbf{v}_r)=[\nabla f(\mathbf{v}_r)]^{\mathrm{H}}\nabla f(\mathbf{v}_r)$ is employed in the following analysis.

Furthermore, the first-order partial derivative of the objective function f is

$$\begin{aligned}
\nabla f(\mathbf{v}_r)&=\left[\nabla\mathbf{L}(\mathbf{v}_r)\right]^{\mathrm{H}}\left[\mathbf{L}(\mathbf{v}_r)-\mathbf{L}_{\mathrm{m}}\right]\\
&=\mathbf{S}(\mathbf{v}_r)^{\mathrm{H}}\left[\mathbf{L}(\mathbf{v}_r)-\mathbf{L}_{\mathrm{m}}\right]
\end{aligned} \tag{16}$$

where $\mathbf{S}\in\mathbb{C}^{n_f\times n_v}$ is the sensitivity/Jacobian matrix, a linearized relationship between the variation of inductance spectrum and spherical properties, which can be calculated by both the original and approximate models.

Combining equation (13)-(16), the variable difference can be calculated by

$$\Delta\mathbf{v}=-\left[\mathbf{S}(\mathbf{v}_r)^{\mathrm{H}}\mathbf{S}(\mathbf{v}_r)\right]^{-1}\mathbf{S}(\mathbf{v}_r)^{\mathrm{H}}\left[\mathbf{L}(\mathbf{v}_r)-\mathbf{L}_{\mathrm{m}}\right] \tag{17}$$

Accordingly, the optimization procedure to estimate pipe properties is illustrated in Algorithm 1, providing the starting point $\mathbf{v}_1$ and residual threshold value ϵ.

Algorithm 1 Optimization of pipe properties

Input: $\mathbf{v}^1$, ϵ and n_i
Output: $\mathbf{v}$

```
initialize: Set L^1 = L(v^1)
for k = 1, 2, ..., n_i do
    S^k = ∂L^k/∂v^k
    v^{k+1} = v^k − [(S^k)^H S^k]^{-1} (S^k)^H (L^k − L_m)
    L^{k+1} = L(v^{k+1})
    if ||L^{k+1} − L_m||_2^2 ≤ ϵ then
        Break;
    end if
end for
```

To evaluate the ill-conditioning degree of inverse problem,

the singular value feature of the Hessian matrix is introduced, which represents the ill-conditioning degree [30], $S_f: \mathbb{R}^{n_v \times n_v} \to \mathbb{R}$,

$$S_f\left(\mathbf{H}(\mathbf{v}_r)\right) = -20\log_{10}\left(\left|\lambda_{\min}\right| / \lambda_{\max}\right) \tag{18}$$

where $\lambda_{\min}$ and $\lambda_{\max}$ are the minimum and maximum singular values of $\mathbf{H}(\mathbf{v}_r)$, respectively.

This index also reflects the uncertainty of inversion, which is desired to be a small value indicating the weak correlation between the derivatives of variables. The combinations of estimated variables for non-magnetic spherical shell estimation include (a, b) and (a, b, σ). Noted that the sensor lift-off is a function of spherical outer radius for the investigated measurement configuration.

As the evaluating point $\boldsymbol{v}_r$ affects the value of $S_f(\mathbf{H}(\mathbf{v}_r))$, it is expected to calculate the average value of $\overline{S_f} = \sum_p S_f(\mathbf{v}_r^{(p)})/n_p$ ($\mathbf{v}_r^{(p)}$ denotes the p-th evaluating point and n_p is the quantity of points) on a set of points in the hyper-rectangle variable domain, $\mathcal{D} = [\underline{a}, \overline{a}] \times [\underline{b}, \overline{b}] \times [\underline{\sigma}, \overline{\sigma}]$, $\underline{a}$ and $\overline{a}$ represent the upper and lower boundaries of inner radius, respectively. For a certain measurement application, $\mathcal{D}$ can be constructed according to the possible range of variables, from which the interior point set $\mathbf{v}^{\mathcal{D}}, \mathbf{v}^{\mathcal{D}} \subset \mathcal{D}$ can be sampled. For instance, $\mathbf{v}^{\mathcal{D}}$ consists of 1000 equally spaced interior points in the variable domain $\mathcal{D}$ where $a \in [16,60]$ mm, $b - a \in [0.5,3]$ mm and $\sigma \in [1,60]$ MS/m. The index $\overline{S_f}$ evaluated on $\mathbf{v}^{\mathcal{D}}$ is shown in Table I. Obviously, the index of the former combination is much smaller than the latter, which indicates the lower ill-conditioning degree and implies the higher optimization stability. Therefore, the variable combination (a, b) is determined and σ is recommended to be measured independently beforehand.

TABLE I
SINGULAR VALUE FEATURE OF HESSIAN MATRIX COMPOSED OF VARIOUS VARIABLE DERIVATIVES

Variables	(a, b)	(a, b, σ)
$\overline{S_f}$	27.4	438.2

Furthermore, the regularization strategy can be applied to improve the optimization stability. The Hessian matrix can be decomposed by SVD as $\mathbf{H} = \mathbf{U}\sum\mathbf{V}^{\mathrm{H}}$, and one can applies.

$$\mathbf{H}^* = \mathbf{U}\sum{}^*\mathbf{V}^{\mathrm{H}},$$
$$\sum{}^* = \begin{bmatrix} \sum_{11} & 0 \\ 0 & \sum_{22} + \beta_b \sum_{11} \end{bmatrix} \tag{19}$$

where β_b is a parameter to be determined, $\sum_{11}$ and $\sum_{22}$ are elements in the diagonal matrix $\sum$.

The starting point for optimization, $\mathbf{v}_1$, influences the local minimum point that can be reached. By comparing the inductance distance between the measurement and candidate points in $\mathbf{v}^{\mathcal{D}}$, *i.e.* $\min_{\mathbf{v}_s}\{\|\mathbf{L}(\mathbf{v}_s) - \mathbf{L}_{\mathrm{m}}\|_2^2\}$, $\mathbf{v}_s \in \mathbf{v}^{\mathcal{D}}$, a suitable starting point approximate to the convergence point could be acquired.

III. RESULTS AND DISCUSSIONS

The numerical simulation and experiments are performed to evaluate the simplified analytical model of spherical shell in the forward problem and inverse problem qualitatively and quantitively.

In the numerical simulation, the aluminium ($\sigma = 38$ MS/m) and stainless-steel ($\sigma = 1.1$ MS/m) spherical shells are measured, while in the experiments, the stainless-steel spherical shells are employed. Both the simulation and experiments adopt a similar measurement configuration which is illustrated in Table II corresponding to the measurement configuration shown in Fig 1.

TABLE II
PARAMETERS OF MEASUREMENT SETUP

Parameters	Value
Inner radius of coils, x_1	53.5 mm
Outer radius of coils, x_2	54.5 mm
The vertical distance between the sphere centre and lower limit of exciting coil, z_1	$\sqrt{b^2 - 16^2} - 4$ mm
The vertical distance between the sphere centre and upper limit of exciting coil, z_2	z_1 +5 mm
The vertical distance between the sphere centre and lower limit of receiving coil, z_3	$z_1 + 22$ mm
The vertical distance between the sphere centre and upper limit of receiving coil, z_4	z_3 +5 mm
Coil turns, N_{ex} *and* N_{re}	15
Coil diameter, $\emptyset_{\mathrm{c}}$	0.25 mm
Excitation frequency	1 kHz~510 kHz

A. Numerical simulations

The inductance spectra of spherical shells are calculated by adopting the FEM, original and simplified analytical models. The FEM model is implemented in the COMSOL software, in which the representative solution of electromagnetic field is shown in Fig. 2. The comparison of inductance spectra is shown in Fig. 3, which indicates that the inductance values calculated by the FEM and original model are nearly identical, and the results of simplified model are close to them, especially for the thin thickness spherical shells.

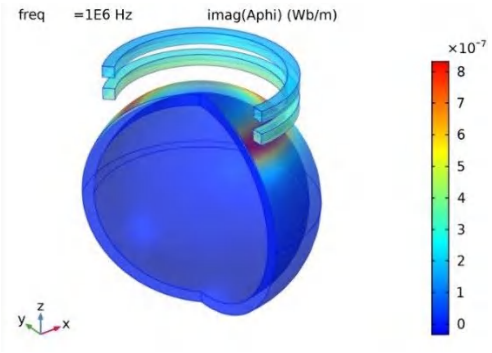

Fig. 2 Magnetic vector potential distribution of spherical shell calculated by FEM

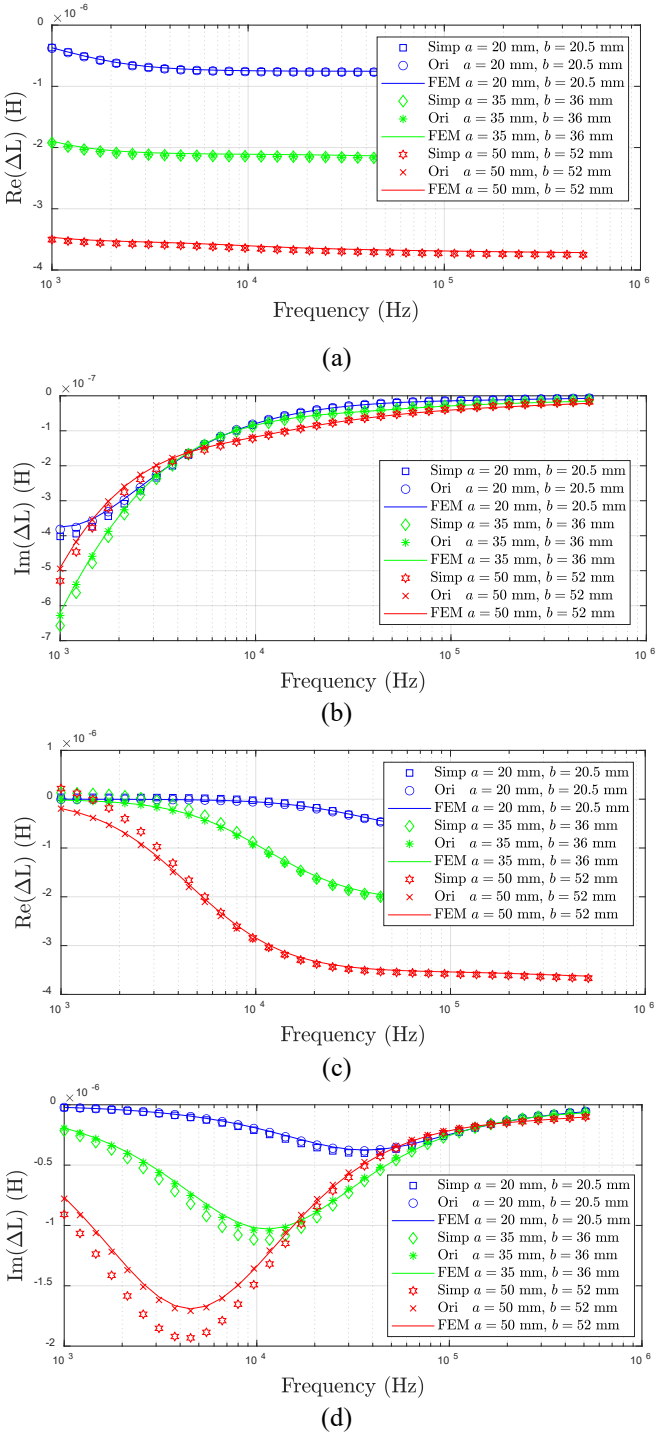

Fig. 3. Frequency sweeping inductance spectra of aluminium (a) and (b), and stainless-steel (c) and (d) spherical shells, where 'Ori' and 'Simp' indicate the original and simplified analytical model, respectively

Given a certain range of spherical shell radii that could be measured, *e.g.* the inner radius $a \in [16,60]$ mm and thickness $t = b - a \in [0.5,3]$ mm, the upper and lower bounds of relative error (RE) and correlation coefficient (CC) for the inductance calculation, in terms of the original analytical model, can be evaluated according to the interval process [31] (details can be found in Appendix B), which is shown in Table III. The indices are calculated by

$$\begin{aligned} \mathrm{RE} &= \frac{1}{n_f}\sum_{i=1}^{n_f}\left|\frac{L_{\mathrm{s},i}-L_{\mathrm{o},i}}{L_{\mathrm{o},i}}\right| \\ \mathrm{CC} &= \left|\frac{\sigma_{\mathbf{L}_\mathrm{s}\mathbf{L}_\mathrm{o}}}{\sigma_{\mathbf{L}_\mathrm{s}}\sigma_{\mathbf{L}_\mathrm{o}}}\right| \\ \sigma^2_{\mathbf{L}_\mathrm{o}} &= \frac{1}{n_f}\sum_{i=1}^{n_f}(L_{\mathrm{o},i}-\overline{\mathbf{L}}_\mathrm{o})^*(L_{\mathrm{o},i}-\overline{\mathbf{L}}_\mathrm{o}) \\ \sigma_{\mathbf{L}_\mathrm{s}\mathbf{L}_\mathrm{o}} &= \frac{1}{n_f}\sum_{i=1}^{n_f}(L_{\mathrm{s},i}-\overline{\mathbf{L}}_\mathrm{s})^*(L_{\mathrm{o},i}-\overline{\mathbf{L}}_\mathrm{o}) \end{aligned} \tag{20}$$

where the operator $(\cdot)^*$ represents the complex conjugate, $L_{\mathrm{s},i}$ and $L_{o,i}$ denote the i-th frequency-dependent inductance calculated by the simplified and original models, respectively, while $\overline{\mathbf{L}}_\mathrm{s}$ and $\overline{\mathbf{L}}_\mathrm{D}$ indicate the corresponding arithmetic mean.

The results in Table III indicate that the inductance accuracy of aluminium objects is much higher than the stainless-steel ones. Because the conductivity of aluminium is much higher and the condition that $\alpha_2 a$ and $\alpha_2 b$ are large values can be satisfied, which means that the approximation in equation (26) is more accurate and accounts for the higher accuracy for the aluminium spherical shells in thin thickness and large radius.

TABLE III
ERROR BOUNDS OF INDUCTANCE SPECTRA CALCULATED BY THE SIMPLIFIED ANALYTICAL MODEL

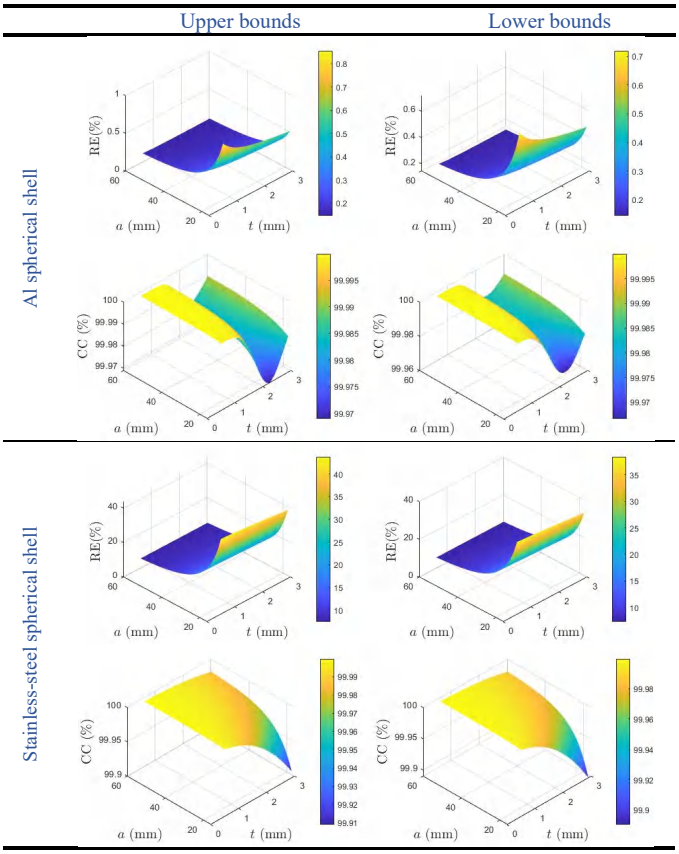

In the inverse problem, the inner radius a and thickness t of aluminium and stainless-steel spherical shells are estimated according to the proposed optimization method. The relative estimation error is shown in Table IV. The results indicate that

the estimation adopting the simplified model is accurate for both the aluminium and stainless-steel spherical shells, while the error is relatively larger for the thin thickness shells. Specifically, when measuring the aluminium shells, the relative errors of $\varepsilon_{\mathrm{re}}(a)$ and $\varepsilon_{\mathrm{re}}(t)$ are lower than 9% and 6%, while for the stainless-steel objects, the errors are within 5% and 4%, respectively.

TABLE IV
ERROR BOUNDS OF SPHERICAL SHELL INNER RADIUS a AND THICKNESS t USING THE SIMPLIFIED MODEL

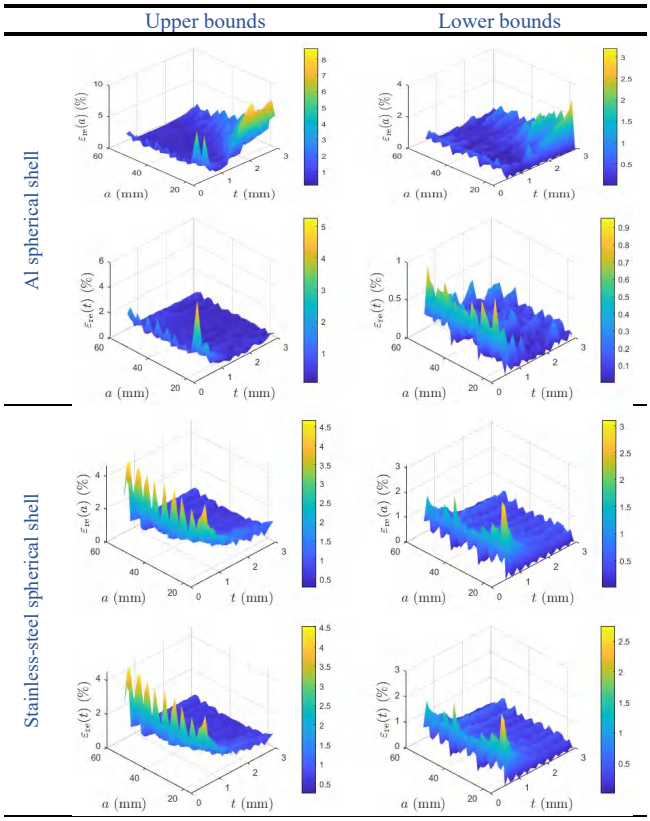

B. Experiments

The experimental setup is shown in Fig. 4, where the coil inductance is measured by the Zurich impedance analyser.

There are three representative measured stainless-steel spherical shell in radii (31 mm, 32 mm) (45 mm, 46 mm), and (49 mm, 50 mm). The measured and calculated inductance spectra are compared in Fig. 5, with mean absolute error (MAE) and correlation coefficient provided in Table V. The results indicate that the simplified analytical model can provide the inductance spectra approximate to the measurements. The discrepancy of the imaginary part of inductance is relatively larger adjacent to the peak frequency.

Fig. 4 Experimental setup and measured stainless-steel spherical shells

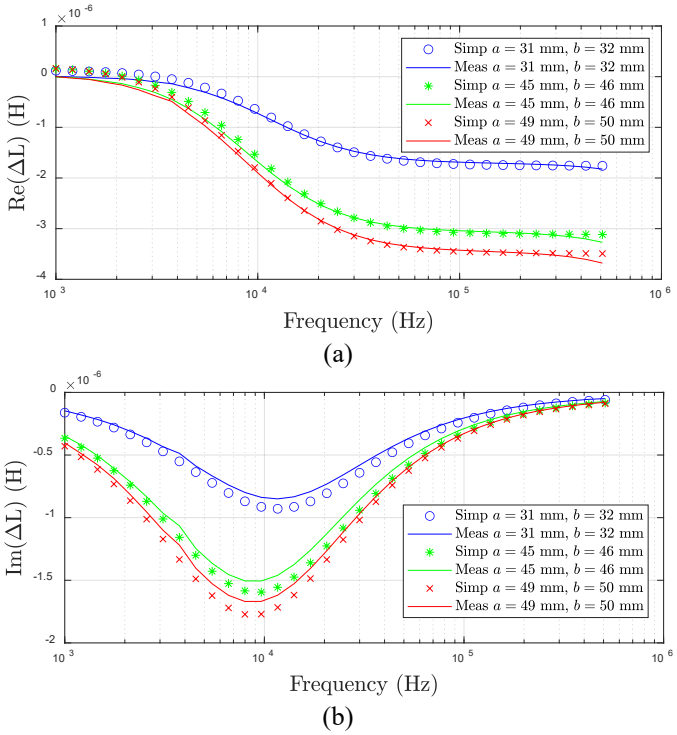

Fig. 5 The inductance spectra of stainless-steel spherical shells in experiments, (a) real part and (b) imaginary part, where 'Meas' indicate the measurements

TABLE V
MAE AND CC OF INDUCTANCE SPECTRA CALCULATED BY THE SIMPLIFIED MODEL

(a, b) (mm)	(31,32)	(45,46)	(49,50)
RE (%)	14.1	9.1	8.5
CC (%)	99.98	99.99	99.98

The estimated spherical shell radius and thickness adopting the original and simplified models are illustrated in Table VI. Both models adopt the difference equation to calculate the partial derivatives in the sensitivity matrix. The average computational time for an inductance spectrum employing the original and simplified analytical models is 0.56s and 0.10s, respectively. Compared with the original model, the simplified model can provide the estimation results in higher accuracy, except for the stainless-steel shell in radii (37, 38), while spending only 1/5 of the computational time.

TABLE VI

EXPERIMENTAL RESULTS OF SPHERICAL SHELL RADIUS ESTIMATION, WHERE (a_s, b_s) AND (a_o, b_o) ARE ESTIMATED BY THE SIMPLIFIED AND ORIGINAL MODELS, $|\Delta t_s|$ AND $|\Delta t_o|$ ARE ABSOLUTE THICKNESS ERRORS

#	1	2	3	4	5	6
a, b (mm)	19, 20	25, 26	31, 32	37, 38	45, 46	49, 50
a_s, b_s (mm)	18.2, 19.3	25.0, 26.1	31.0, 32.1	37.6, 38.6	45.1, 46.2	49.3, 50.3
$\|\Delta t_s\|$ (mm)	0.1	0.1	0.0	0.0	0.1	0.0
Time (s)	0.10	0.10	0.09	0.10	0.09	0.09
a_o, b_o (mm)	17.7, 19.0	24.6, 26.8	30.7, 31.7	37.2, 38.2	44.4, 44.5	48.6, 49.6
$\|\Delta t_o\|$ (mm)	0.2	0.1	0.0	0.0	0.1	0.0
Time (s)	0.59	0.55	0.54	0.55	0.55	0.54

IV. CONCLUSION

In order to measure the thickness and radius of non-magnetic spherical shells at a low computational cost, the analytical model of the spherical shell encircled by the coaxial coil sensor is simplified according to asymptotic forms of the modified spherical Bessel functions. The thickness and radius can be estimated through the developed optimization algorithm based on the Newton-Raphson method. In the numerical simulation and experiments, the aluminium and stainless-steel spherical shells are implemented for evaluation. The inductance calculation results indicate that the simplified model is more accurate for the spherical shells with large radius and high conductivity, while the relative error of estimation is lower than 10% for a variety of evaluating points. In the experiments, the estimation error of stainless-steel spherical shell radii is within 0.1 mm, while the calculation speed is 5 times faster than the original analytical model.

In the future, the proposed method can be developed and applied to the eddy current testing system for specific applications, *e.g.* spherical steel structures and bearing ball measurement.

APPENDIX

A.

For the inductance calculation caused by the double-layered non-magnetic spherical objects, the phase term in equation (9) can be simplified according to the asymptotic forms of the modified spherical Bessel functions.

The original phase term is

$$
\begin{aligned}
S_n(\alpha) &= c_n S(\alpha) \\
S(\alpha) &= \frac{1}{bD_n(\alpha)k_n(\alpha b)} \\
&\quad \times\{k_n(\alpha_2 b)[\alpha_2 i_n(\alpha a)i_{n-1}(\alpha_2 a) - \alpha i_n(\alpha_2 a)i_{n-1}(\alpha a)] \\
&\quad + i_n(\alpha_2 b)[\alpha k_n(\alpha_2 a)i_{n-1}(\alpha a) + \alpha_2 k_{n-1}(\alpha_2 a)i_n(\alpha a)]\} \\
&\quad - i_n(\alpha b)/k_n(\alpha b) \\
D_n(\alpha) &= [\alpha_2 k_{n-1}(\alpha_2 b)k_n(\alpha b) - \alpha k_{n-1}(\alpha b)k_n(\alpha_2 b)] \\
&\quad \times[\alpha i_n(\alpha_2 a)i_{n-1}(\alpha a) - \alpha_2 i_n(\alpha a)i_{n-1}(\alpha_2 a)] \\
&\quad + [\alpha_2 k_{n-1}(\alpha_2 a)i_n(\alpha a) + \alpha k_n(\alpha_2 a)i_{n-1}(\alpha a)] \\
&\quad \times[\alpha i_n(\alpha_2 b)k_{n-1}(\alpha b) + \alpha_2 i_{n-1}(\alpha_2 b)k_n(\alpha b)]
\end{aligned}
\tag{21}
$$

It can also be written as

$$
\begin{aligned}
S(\alpha) &= \frac{S_0}{bD(\alpha)k_n(\alpha b)} - \frac{i_n(\alpha b)}{k_n(\alpha b)} \\
S_0 &= k_n(\alpha_2 b)S_{01} + i_n(\alpha_2 b)S_{02} \\
S_{01} &= \alpha_2 i_n(\alpha a)i_{n-1}(\alpha_2 a) - \alpha i_n(\alpha_2 a)i_{n-1}(\alpha a) \\
S_{02} &= \alpha k_n(\alpha_2 a)i_{n-1}(\alpha a) + \alpha_2 k_{n-1}(\alpha_2 a)i_n(\alpha a)
\end{aligned}
\tag{22}
$$

Substituting S_{01} and S_{02} into $D(\alpha)$, $D(\alpha)$ becomes

$$
\begin{aligned}
D(\alpha) &= S_{02} \times[\alpha i_n(\alpha_2 b)k_{n-1}(\alpha b) + \alpha_2 i_{n-1}(\alpha_2 b)k_n(\alpha b)] \\
&\quad + S_{01} \times[\alpha_2 k_{n-1}(\alpha_2 b)k_n(\alpha b) - \alpha k_{n-1}(\alpha b)k_n(\alpha_2 b)] \\
&= \alpha k_{n-1}(\alpha b)S_0 + \alpha_2 k_n(\alpha b) \\
&\quad \times[i_{n-1}(\alpha_2 b)S_{02} + k_{n-1}(\alpha_2 b)S_{01}]
\end{aligned}
\tag{23}
$$

Bring equation (22) and the second equation of (23) into (21), $S(\alpha)$ becomes

$$
\begin{aligned}
S(\alpha) &= \{bk_n(\alpha b)[\alpha k_{n-1}(\alpha b) + \alpha_2 k_n(\alpha b)\, S_{\mathrm{nu}}/S_{\mathrm{de}}]\}^{-1} \\
&\quad - i_n(\alpha b)/k_n(\alpha b) \\
S_{\mathrm{nu}} &= i_{n-1}(\alpha_2 b)S_{02} + k_{n-1}(\alpha_2 b)S_{01} \\
S_{\mathrm{de}} &= k_n(\alpha_2 b)S_{01} + i_n(\alpha_2 b)S_{02}
\end{aligned}
\tag{24}
$$

By separating the terms relating to α_2 and others (α and α_1), S_{nu} and S_{de} becomes

$$
\begin{aligned}
S_{\mathrm{nu}} &= \alpha_2 i_n(\alpha a) \times[k_{n-1}(\alpha_2 a)i_{n-1}(\alpha_2 b) \\
&\quad - i_{n-1}(\alpha_2 a)k_{n-1}(\alpha_2 b)] + \alpha i_{n-1}(\alpha a) \\
&\quad \times[k_n(\alpha_2 a)i_{n-1}(\alpha_2 b) + i_n(\alpha_2 a)k_{n-1}(\alpha_2 b)] \\
S_{\mathrm{de}} &= \alpha_2 i_n(\alpha a)[k_n(\alpha_2 b)i_{n-1}(\alpha_2 a) \\
&\quad + k_{n-1}(\alpha_2 a)i_n(\alpha_2 b)] + \alpha i_{n-1}(\alpha a) \\
&\quad \times[k_n(\alpha_2 a)i_n(\alpha_2 b) - k_n(\alpha_2 b)i_n(\alpha_2 a)]
\end{aligned}
\tag{25}
$$

As $\alpha_2 = \sqrt{j\omega\mu_0\mu_r\sigma}$, for the high conductivity and excitation frequency, one can assume that $\alpha_2 a \to \infty$ and $\alpha_2 b \to \infty$. Employing the asymptotic forms (for large variable) of the modified Bessel functions in the brackets of equation (25) *i.e.* $i_n(\alpha_2 a) \approx e^{\alpha_2 a}/2\alpha_2 a$, $i_n(\alpha_2 b) \approx e^{\alpha_2 b}/2\alpha_2 b$, $k_n(\alpha_2 a) \approx$

$e^{-\alpha_2 a}/\alpha_2 a$, $k_n(\alpha_2 b) \approx e^{-\alpha_2 b}/\alpha_2 b$, the terms S_{nu} and S_{de} are approximated by

$$\begin{aligned} S_{\text{nu}} &\approx \alpha_2 i_n(\alpha a)\sinh[\alpha_2(b-a)]/(\alpha_2^2 ab) \\ &\quad +\alpha i_{n-1}(\alpha a)\cosh[\alpha_2(b-a)]/(\alpha_2^2 ab) \\ S_{\text{de}} &\approx \alpha_2 i_n(\alpha a)\cosh[\alpha_2(b-a)]/(\alpha_2^2 ab) \\ &\quad +\alpha i_{n-1}(\alpha a)\sinh[\alpha_2(b-a)]/(\alpha_2^2 ab) \end{aligned} \tag{26}$$

Substituting equation (26) into (24), $S(\alpha)$ becomes

$$\begin{aligned} S(\alpha) \approx \Big\{ & bk_n(\alpha b)\Big[\alpha k_{n-1}(\alpha b)+\alpha_2 k_n(\alpha b) \\ & \times \frac{\alpha_2 i_n(\alpha a)\tanh(\alpha_2(b-a))+\alpha i_{n-1}(\alpha a)}{\alpha_2 i_n(\alpha a)+\alpha i_{n-1}(\alpha a)\tanh(\alpha_2(b-a))}\Big]\Big\}^{-1} \\ & -i_n(\alpha b)/k_n(\alpha b) \end{aligned} \tag{27}$$

Subsequently, by applying the asymptotic forms (for small variable) of Bessel functions, *i.e.* $i_n(\alpha a) \approx \frac{(\alpha a)^n}{(2n+1)!!}$, $k_n(\alpha a) \approx \frac{(2n-1)!!}{(\alpha a)^{n+1}}$, the phase term $S_n(\alpha)$ can be simplified by

$$\begin{aligned} S_n(\alpha) = & \frac{c_n b^{2n}}{\alpha_2}\frac{\alpha_2 a+(2n+1)\tanh[\alpha_2(b-a)]}{\alpha_2 a\tanh[\alpha_2(b-a)]+2n+1} \\ & +c_n b^{2n+1}/(2n+1) \end{aligned} \tag{28}$$

B.

In the numerical simulation, the aluminium and stainless-steel spherical shells in the measurement range of inner radius $a \in [\underline{a}, \overline{a}]$ mm and thickness $t = b-a, t \in [\underline{t}, \overline{t}]$ mm are considered to analyse the uncertainty of forward and inverse models. It is assumed that the inner radius and thickness are independent and follow the uniform distributions, *i.e.* $a \sim U(\underline{a}, \overline{a})$ and $t \sim U(\underline{t}, \overline{t})$. The unit of variables is neglected in this section for simplification.

Following the interval process which is a conventional outer discretization method [31], a slicing algorithm is applied to discretize the range of a and t into a variety of intervals. Given the lower and upper boundaries $\underline{c}^{(j)}$ and $\overline{c}^{(j)}$, $j = 1, \ldots, n_c$, the variable intervals $\left[\underline{a}^{(j)}, \overline{a}^{(j)}\right]$ and $\left[\underline{t}^{(j)}, \overline{t}^{(j)}\right]$ are obtained from the corresponding cumulative distribution functions $\underline{a}^{(j)} = F_a^{-1}(\underline{c}^{(j)})$, $\overline{a}^{(j)} = F_a^{-1}(\overline{c}^{(j)})$, $\underline{t}^{(j)} = F_t^{-1}(\underline{c}^{(j)})$ and $\overline{t}^{(j)} = F_t^{-1}(\overline{c}^{(j)})$. Here $\underline{c}^{(j)} \in \{0, 0.04, \ldots, 0.96\}$, $\overline{c}^{(j)} = \underline{c}^{(j)} + 0.04$ and $n_c = 25$ are adopted, This essentially discretizes the two-dimensional variable domain into 625 hyper-rectangle $\mathcal{D}^{\boldsymbol{k}} = \left[\underline{a}^{(k_a)}, \overline{a}^{(k_a)}\right] \times \left[\underline{t}^{(k_b)}, \overline{t}^{(k_b)}\right]$, with its indices $\mathcal{K} = \{\boldsymbol{k} = (k_a, k_b), k_a, k_b \in \{1, 2, \ldots, n_c\}\}$. The probability density associated to $\mathcal{D}^{\boldsymbol{k}}$ is $p^{(\boldsymbol{k})} = p_a^{(k_a)} \cdot p_b^{(k_b)} = 1/625$.

There exist 3 equally spaced interior points in each interval of a and of t. In each hyper-rectangle $\mathcal{D}^{\mathbf{k}}$, the associated bounds of result, $\boldsymbol{y} = \{y_i\}, i = 1, \ldots, n_y$, n_y is the quantity of error indices, is estimated from the interior points by

$$\underline{y}_i^{(\mathbf{k})} = \min_{(a,b)\in\mathcal{D}^{\mathbf{k}}} \mathcal{M}(a,b), \quad \overline{y}_i^{(\mathbf{k})} = \max_{(a,b)\in\mathcal{D}^{\mathbf{k}}} \mathcal{M}(a,b)$$

where $\mathcal{M}(\cdot)$ indicates the evaluation functions of the forward and inverse problem solutions.

V. Reference

[1] H. Liu, Y. Wang, Z. Jia, and D. Guo, "Integration strategy of on-machine measurement (OMM) and numerical control (NC) machining for the large thin-walled parts with surface correlative constraint," *The International Journal of Advanced Manufacturing Technology,* vol. 80, pp. 1721-1731, 2015.

[2] N. Ahmed, M. A. Naeem, A. U. Rehman, M. Rafaqat, U. Umer, and A. E. Ragab, "High aspect ratio thin-walled structures in D2 steel through wire electric discharge machining (EDM)," *Micromachines,* vol. 12, no. 1, p. 1, 2020.

[3] J. Guo *et al.*, "A new method for precision measurement of wall-thickness of thin-walled spherical shell parts," *Micromachines,* vol. 12, no. 5, p. 467, 2021.

[4] A. N. AbdAlla, M. A. Faraj, F. Samsuri, D. Rifai, K. Ali, and Y. Al-Douri, "Challenges in improving the performance of eddy current testing: Review," *Measurement and Control,* vol. 52, no. 1-2, pp. 46-64, 2018, doi: 10.1177/0020294018801382.

[5] A. Sophian, G. Tian, D. Taylor, and J. Rudlin, "Electromagnetic and eddy current NDT: a review," *Insight,* vol. 43, no. 5, pp. 302-306, 2001.

[6] J. Garcia-Martin, J. Gomez-Gil, and E. Vazquez-Sanchez, "Non-Destructive Techniques Based on Eddy Current Testing," *SENSORS,* vol. 11, no. 3, pp. 2525-2565, MAR 2011, doi: 10.3390/s110302525.

[7] J. Luquire, W. Deeds, and C. Dodd, "Axially symmetric eddy currents in a spherical conductor," *Journal of Applied Physics,* vol. 41, no. 10, pp. 3976-3982, 1970.

[8] A. A. Kolyshkin and R. Vaillancourt, "Series solution of an eddy-current problem for a sphere with varying conductivity and permeability profiles," *IEEE Transactions on Magnetics,* vol. 35, no. 6, pp. 4445-4451, 1999, doi: 10.1109/20.809136.

[9] T. P. Theodoulidis and E. E. Kriezis, "Coil impedance due to a sphere of arbitrary radial conductivity and permeability profiles," *IEEE Transactions on Magnetics,* vol. 38, no. 3, pp. 1452-1460, 2002.

[10] T. Theodoulidis and E. E. Kriezis, "Application of the TREE method to Axisymmetric Problems," in *Eddy Current Canonical Problems (with Applications to Nondestructive Evaluation)*: Tech Science Press, 2006, p. 152−182.

[11] M. Pham and A. Peyton, "A model for the forward problem in magnetic induction tomography using boundary integral equations," *IEEE Transactions on Magnetics,* vol. 44, no. 10, pp. 2262-2267, 2008.

[12] Z. Zeng, L. Udpa, S. S. Udpa, and M. S. C. Chan, "Reduced magnetic vector potential formulation in the finite element analysis of eddy current nondestructive testing," *IEEE transactions on magnetics,* vol. 45, no. 3, pp. 964-967, 2009.

[13] R. Huang *et al.*, "A Novel Acceleration Method for Crack Computation Using Finite Element Analysis in Eddy Current Testing," *IEEE Transactions on Instrumentation and Measurement,* vol. 71, pp. 1-9, 2022, doi: 10.1109/TIM.2022.3186073.

[14] R. Huang, M. Lu, A. Peyton, and W. Yin, "A novel perturbed matrix inversion based method for the acceleration of finite element analysis in crack-scanning eddy current NDT," *IEEE Access,* vol. 8, p. 12438−12444, 2020.

[15] W. Yin, A. J. Peyton, and S. J. Dickinson, "Simultaneous measurement of distance and thickness of a thin metal plate with an electromagnetic sensor using a simplified model," *IEEE Transactions on Instrumentation and Measurement,* vol. 53, no. 4, p. 1335−1338, 2004.

[16] M. Lu, X. Meng, R. Huang, L. Chen, A. Peyton, and W. Yin, "A high-frequency phase feature for the measurement of magnetic permeability using eddy current sensor," *NDT & E International,* vol. 123, p. 102519, 2021.

[17] G. Hu, R. Huang, Y. Shao, and W. Yin, "Thickness measurement for spherical balls based on a frequency difference feature," *Insight-Non-Destructive Testing and Condition Monitoring,* vol. 64, no. 2, pp. 84-90, 2022.

[18] G. Hu, R. Huang, M. Lu, L. Zhou, and W. Yin, "Measurement of radius of a metallic ball using eddy current testing based on peak frequency difference feature," *Measurement,* vol. 184, p. 109876, 2021.

[19] Y. Li, L. Udpa, and S. S. Udpa, "Three-dimensional defect reconstruction from eddy-current NDE signals using a genetic local search algorithm," *IEEE Transactions on Magnetics,* vol. 40, no. 2, pp. 410-417, 2004.

[20] M. Salucci *et al.*, "Real-time NDT-NDE through an innovative adaptive partial least squares SVR inversion approach," *IEEE Transactions on Geoscience and Remote Sensing,* vol. 54, no. 11, pp. 6818-6832, 2016.

[21] M. Lu, Y. Xie, W. Zhu, A. Peyton, and W. Yin, "Determination of the Magnetic Permeability, Electrical Conductivity, and Thickness of Ferrite Metallic Plates Using a Multifrequency Electromagnetic Sensing System," *IEEE transactions on industrial informatics / a publication of the IEEE Industrial Electronics Society,* 2018.

[22] X.-L. Chen and Y.-Z. Lei, "Inverse problem of pulsed eddy current field of ferromagnetic plates," *Chinese Physics B,* vol. 24, no. 3, p. 030301, 2015.

[23] D. R. Hunter and K. Lange, "A tutorial on MM algorithms," *The American Statistician,* vol. 58, no. 1, pp. 30-37, 2004.

[24] W. L. Yin, S. J. Dickinson, and A. J. Peyton, "Imaging the continuous conductivity profile within layered metal structures using inductance spectroscopy," *Ieee Sensors Journal,* vol. 5, no. 2, p. 161−166, Apr 2005, doi: 10.1109/jsen.2004.842637.

[25] Z. W. Geem, J. H. Kim, and G. V. Loganathan, "A new heuristic optimization algorithm: harmony search," *simulation,* vol. 76, no. 2, pp. 60-68, 2001.

[26] M. Sambridge, "Geophysical inversion with a neighbourhood algorithm—I. Searching a parameter space," *Geophysical journal international,* vol. 138, no. 2, pp. 479-494, 1999.

[27] W. Yin, X. Hao, A. Peyton, M. Strangwood, and C. Davis, "Measurement of permeability and ferrite/austenite phase fraction using a multi-frequency electromagnetic sensor," *NDT & e International,* vol. 42, no. 1, pp. 64-68, 2009.

[28] I. D. Adewale and G. Y. Tian, "Decoupling the influence of permeability and conductivity in pulsed eddy-current measurements," *IEEE Transactions on Magnetics,* vol. 49, no. 3, p. 1119−1127, 2012.

[29] D. Vasic, V. Bilas, and D. Ambrus, "Validation of a coil impedance model for simultaneous measurement of electromagnetic properties and inner diameter of a conductive tube," *IEEE Transactions on Instrumentation and Measurement,* vol. 55, no. 1, p. 337−342, 2006.

[30] R. C. Aster, B. Borchers, and C. H. Thurber, *Parameter estimation and inverse problems*. Elsevier, 2018.

[31] R. Schöbi, "Surrogate models for uncertainty quantification in the context of imprecise probability modelling," *IBK Bericht,* vol. 505, 2019.

7. Bearing Ball Property Estimation using Multi-frequency Eddy-current Testing

Bearing Ball Property Estimation using Multi-frequency Eddy-current Testing

Zihan Xia, Gang Hu, Ruochen Huang*, Xiaofei Liu, Anthony Peyton, Wuliang Yin, *Senior Member, IEEE,* and Wuqiang Yang, *Fellow, IEEE*

***Abstract*—The quality of steel balls influences the accuracy, motion performance and service life of the rolling bearing. The eddy-current testing technique plays an important role in the measurement of bearing ball properties, including radius, electrical conductivity and relative magnetic permeability. In this study, an estimation method of bearing ball properties is proposed using the multi-frequency eddy-current testing technique. The estimation method optimizes the least squares problem between the measured and calculated coil inductance spectra through the modified Newton-Raphson algorithm. In addition, the combination of bearing ball properties to be estimated is evaluated by employing sensitivity analysis. The effectiveness of the proposed method has been evaluated by numerical simulation and experiments measuring bearing balls with various properties.**

***Index Terms*—Electromagnetic sensing, eddy current testing, bearing ball, analytical model, inverse problem.**

I. Introduction

Bearing balls are wildly employed in machine constructions, robots, aircraft, automotive, and medical devices [1, 2]. Several steps are required to make a metal bearing. The product pipeline includes quenching cooled, tempering, heat treatment, air cooling, rough grinding, shiny grinding [1] *etc.* The microstructure of the materials is changed after the heating process, such as the content of martensite and austenite, which can affect the hardness and ductility of steels [3]. The presence of contaminants in heating systems, overloading, electrical shocks, and material fatigue lead to the creation of various types of quality problems for metal bearings [4]. A variety of mechanical failures can be caused by the flaw in metal bearings. The efficient non-destructive testing method of bearing balls is an urgent requirement.

To inspect the quality of bearing balls, the non-destructive testing (NDT) techniques, including visual inspection [1, 5], optical method [6], acoustic method [7, 8], capacitance measurement [9, 10], eddy-current (EC) testing [2] *etc.*, have been introduced to measure the surface defects and geometric dimensions in previous studies. Among these techniques, EC testing characterised by the contactless, quick response and relatively low cost is suitable for the metallic bearing ball measurement. The EC measurement signals reflect the electromagnetic properties of bearing balls which relates to the hardness, micro-structure, heat state of materials and near-surface defects [11, 12].

In previous studies, the combination of the EC method and efficient spherical surface unfolding mechanism facilitates the surface defect scanning of bearing balls [1], for which the eddy-current sensor and measuring circuit have been developed extensively [13, 14]. X. Chen *et al.* proposed a least squares inverse problem for bearing ball conductivity and permeability estimation employing the pulsed EC testing, and analysed the linear coupling relationship between the conductivity and permeability [15]. It has been revealed that, for the measurement of plates and pipes, there exists the coupling effect of conductivity and permeability on the measurements in the time domain [16] and in the frequency domain [17]. However, few studies explore the estimation of bearing ball properties including radius, electrical conductivity and relative magnetic permeability, through the multi-frequency EC method and considers the appropriate properties to be estimated.

This study focuses on the measurement of bearing ball properties using the multi-frequency EC method. The analytical model to calculate the mutual inductance between the transmitting (Tx) and receiving (Rx) coils is provided based on the model of spherical objects [18, 19]. The modified Newton-Raphson method [20] has been employed to optimise the least squares problem between the measured and calculated inductance spectra, for the estimation of bearing ball properties. Furthermore, the sensitivity of inductance spectrum to bearing ball properties has been analyzed through the singular value of the Hessian matrix and variance-based sensitivity index. In numerical simulation and experiments, the performance of the proposed estimation method has been comprehensively evaluated by measuring bearing balls with different properties.

II. Methods

A. Inductance calculation

For the measurement configuration shown in Fig. 1. According to the analytical model [18], the mutual inductance between the Tx and Rx coils, referred to as inductance

Manuscript updated March 4, 2023, and submitted xxx xx, 2021.

Mr. Zihan Xia, Mr. Gang Hu, Miss Xiaofei Liu, Prof. Anthony Peyton, Dr. Wuliang Yin and Prof. Wuqiang Yang are with the School of Electrical and Electronic Engineering, University of Manchester, Manchester M13 9PL, U.K.

Dr. Ruochen Huang was with the School of Electrical and Electronic Engineering, University of Manchester, Manchester M13 9PL, U.K., and now with the College of Electrical Engineering and Automation, Fuzhou University, Fuzhou 350108, China. (*Corresponding author: Ruochen Huang email: ruochen_huang@fzu.edu.cn*)

hereinafter, induced by the metallic ball can be calculated by

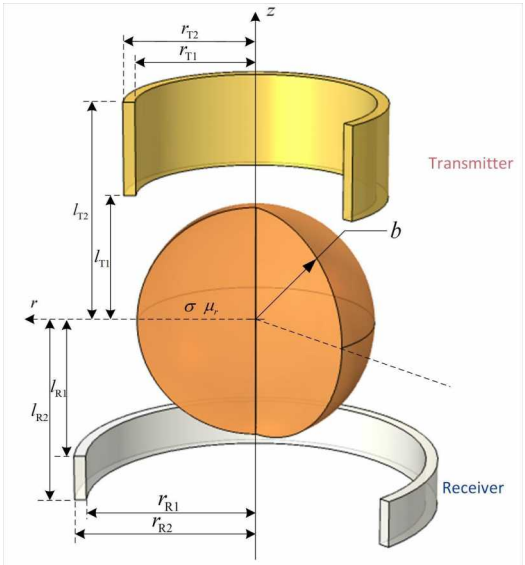

Fig. 1. Metallic bearing ball measured by the coaxial transmitting and receiving coils

$$
\begin{aligned}
\Delta L(\omega) &= \sum_n K_n \phi_n \\
\phi_n(\omega) &= b^{2n+1} \frac{n\mu_r + n + \mu_r - f_n(\alpha b)}{n\mu_r - n + f_n(\alpha b)} \\
f_n(\alpha b) &= \alpha b \frac{i_{n-1}(\alpha b)}{i_n(\alpha b)} \\
K_n &= k_l \int_{S(\mathrm{Tx})} \frac{\sin(\theta) P_n^1(\cos(\theta))}{r^n} ds \\
&\quad \times \int_{S(\mathrm{Rx})} \frac{\sin(\theta) P_n^1(\cos(\theta))}{r^n} ds \\
k_l &= \frac{\pi \mu_0 N_\mathrm{T} N_\mathrm{R}}{(r_{\mathrm{T}2} - r_{\mathrm{T}1})(r_{\mathrm{R}2} - r_{\mathrm{R}1})(l_{\mathrm{T}2} - l_{\mathrm{T}1})(l_{\mathrm{R}2} - l_{\mathrm{R}1})}
\end{aligned} \tag{1}
$$

where $\alpha = \sqrt{j\omega\mu_0\mu_r\sigma}$, b is the ball radius, $i_n(\alpha b)$ is the modified spherical Bessel function of the first kind, $P_n^1(\cdot)$ is the associated Legendre polynomial of degree n and order 1, N_T and N_R are the number of turns of the Tx and Rx coils, $S(\mathrm{Tx})$ and $S(\mathrm{Rx})$ indicate the cross-sectional area of Tx and Rx coils, respectively, ω is the angular frequency applied to the Tx coil, μ_0 is the permeability in air (free space), μ_r and σ are the relative permeability and conductivity of the metallic ball.

The matrix form of inductance equation is

$$\Delta\mathbf{L} = \phi\mathbf{K} \tag{2}$$

where $\Delta\mathbf{L} \in \mathbb{C}^{q_\omega \times 1}$, $\phi = \{\phi_n(\omega_i)\} \in \mathbb{C}^{q_\omega \times q_n}$, $\mathbf{K} = \{K_n\} \in \mathbb{R}^{q_n \times 1}$, q_ω and q_n indicate the quantity of excitation frequency points and number of the associated Legendre polynomial degree.

B. Property estimation

The bearing ball properties can be estimated by minimising the objective function,

$$\min_{\mathbf{v}} \mathcal{L}_0 = \|\Delta\mathbf{L}(\mathbf{v}) - \Delta\mathbf{L}_\mathrm{m}\|_2^2 \tag{3}$$

where $\Delta\mathbf{L}(\mathbf{v})$ is the inductance spectrum calculated by the analytical model, $\Delta\mathbf{L}_\mathrm{m}$ is the measured or simulated spectrum, $\|\cdot\|_2^2$ represents the ℓ_2-norm, $\mathbf{v} \in \mathbb{R}^{n_v \times 1}$ is the optimized bearing ball property vector, q_v denotes the quantity of variables.

According to the modified Newton-Raphson method [20], the variables can be optimised iteratively by

$$\Delta\mathbf{v} = -[(\mathbf{S}^k)^\mathrm{H}\mathbf{S}^k + \lambda]^{-1}(\mathbf{S}^k)^\mathrm{H}(\Delta\mathbf{L}^k - \Delta\mathbf{L}_\mathrm{m}) \tag{4}$$

where $\mathbf{S} = \{\partial L(\omega_i)/\partial v_j\} \in \mathbb{C}^{q_w \times q_v}$ is the Jacobian/sensitivity matrix, k indicates the current iterative step, the superscript H represents the Hermitian transpose, and λ is a diagonal regularisation matrix, $\lambda = \{\lambda_{i,i}\} \in \mathbb{R}^{q_v \times q_v}$.

The optimization process is summarized and illustrated in Algorithm 1.

Algorithm 1 Optimization of bearing ball properties

Input: $\mathbf{v}^1$, ϵ and q_i
Output: $\mathbf{v}$

```
initialize: Set ΔL^1 = ΔL(v^1)
for k = 1, 2, ..., q_i do
    S^k = ∂ΔL^k/∂v^k
    v^{k+1} = v^k − [(S^k)^H S^k + λ]^{-1} (S^k)^H (ΔL^k − ΔL_m)
    ΔL^{k+1} = ΔL(v^{k+1})
    if ‖ΔL^{k+1} − ΔL_m‖_2^2 ≤ ε then
        Break;
    end if
end for
```

C. Sensitivity analysis

The variable combination greatly influences the performance of the inverse algorithm in terms of the convergence rate and estimation accuracy. For the proposed measurement configuration shown in Fig. 1, the combination of bearing ball properties to be optimised could be (b, μ_r), (b, σ), (σ, μ_r) and (b, σ, μ_r). Local and global sensitivity analysis methods, frequently adopted in uncertainty quantification, are implemented to analyze the appropriate combination.

The local sensitivity analysis employs the singular value feature of the Hessian matrix. At a certain evaluating variable point, $\mathbf{v}_r$, the index is calculated by

$$S_l(\mathbf{H}(\mathbf{v}_r)) = -20\log_{10}(|\lambda_{\min}|/\lambda_{\max}) \tag{5}$$

where $\mathbf{H}(\mathbf{v}_r) = \mathbf{S}^\mathrm{H}\mathbf{S}|_{\mathbf{v}=\mathbf{v}_r}$, $\lambda_{\min}$ and $\lambda_{\max}$ are the minimum and maximum singular values of $\mathbf{H}(\mathbf{v}_r)$, respectively.

The singular value feature reflects the ill-conditioning degree of the inverse problem [21], and is expected to be as small as possible. If the partial derivatives of various properties are linearly correlated, *e.g.* $\partial\Delta\mathbf{L}/\partial\mu_r$ and $\partial\Delta\mathbf{L}/\partial\sigma$,

$\partial\Delta\mathbf{L}/\partial\mu_r = \{\partial\Delta L(\omega_i)/\partial\mu_r\}$, $\lambda_{\min}$ will be much smaller than $\lambda_{\max}$, which leads to a large feature value.

In the variable domain of bearing ball properties, $\mathcal{D} = [\underline{b}, \overline{b}] \times [\underline{\sigma}, \overline{\sigma}] \times [\underline{\mu_r}, \overline{\mu_r}]$ ($\underline{b}$ and $\overline{b}$ represent the upper and lower boundaries of b, respectively). One can calculate the arithmetic mean of singular value feature for evaluation,

$$\overline{S_l} = \sum_p S_l(\mathbf{v}_r^{(p)})/n_p \tag{6}$$

where $\mathbf{v}_r^{(p)}$ denotes the a sampled evaluating point and n_p is the quantity of evaluating points.

The Sobol value [22, 23], a variance-based sensitivity index aiming at evaluating the entire variable space and measuring the contribution of input variables to the output from the average point of view, is applied to investigate the global sensitivity of various variable combinations. Under the assumption that variables b, μ_r, σ are independent, the Sobol index of variable combinations is defined as follows. For the variable combination $\mathbf{v}_c$ with variable index c, $c = \{i_1, ..., i_k\} \subseteq \{1, 2, 3\}$, $\mathbf{v}_c = (v_{i_1}, ..., v_{i_k}) \subseteq (v_1, v_2, v_3) = (b, \mu_r, \sigma)$, in terms of the measurement y, the index is calculated by

$$\begin{aligned} S_c(y) &= \frac{D_c}{D} \\ D_c &= \mathrm{Var}[f_c(\mathbf{v}_c)] \\ f_c(\mathbf{v}_c) &= \sum_{N:N\subseteq c} (-1)^{|c|-|N|} E(y\,|\mathbf{v}_c) \\ D &= \sum_i D_i + \sum_i \sum_{j>i} D_{ij} + D_{123} \\ \mathrm{Var}[E(y\,|\mathbf{v}_c)] &= \int [E(y\,|\mathbf{v}_c) - E(y)]^2 p_{i_w}(v_{i_w}) dv_{i_w} \end{aligned} \tag{7}$$

where $\mathrm{Var}[\cdot]$ indicates the variance value, $p(\cdot)$ is the probability density function, $i_w \in \{i_1, i_2, ..., i_k\}$.

The properties of bearing balls are in the range of $b \in [5, 15]$ mm, $\sigma \in [1, 10]$ MS/m and $\mu_r \in [1, 100]$. The parameters of the measurement setup are shown in Table I. The inductance peak frequency w_p, the frequency where the imaginary part of the inductance researches its minimum, and corresponding inductance value $\mathrm{Im}[\Delta L(\omega_p)]$ are considered as measurement y to calculate the Sobol value. The inductance peak frequency is mainly influenced by the radius, conductivity and permeability of the bearing ball, referring to $\phi_n(\omega)$ in equation (1).

The local and global sensitivity indices of different variable combinations are shown in Tables II. The singular value feature implies that the inverse problem to estimate the variable combination (b, μ_r) has the least ill-conditioning degree and uncertainty, which is suitable for optimization. The Sobol value means that ω_p is sensitive to the bearing ball radius, conductivity and permeability, while $\mathrm{Im}[\Delta L(\omega_p)]$ is less affected by the conductivity and permeability. To guarantee the high stability of the optimization procedure and high sensitivity to the estimated properties, the combination of (b, μ_r) is selected. The bearing ball conductivity is suggested to be measured before estimation.

TABLE I
PARAMETERS OF MEASUREMENT SETUP

Parameters	Value
Inner radius of Tx coil r_{T1} (mm)	6
Outer radius of Tx coil r_{T2} (mm)	6.3
Inner radius of Rx coil r_{R1} (mm)	11
Outer radius of Rx coil r_{R2} (mm)	11.1
Lower dimension of Tx coil l_{T1} (mm)	11
Upper dimension of Tx coil l_{T2} (mm)	19
Upper dimension of Rx coil l_{R1} (mm)	13.5
Lower dimension of Rx coil l_{R2} (mm)	17
Number of Tx coil turns	20
Number of Rx coil turns	18
Range of exciting frequency (kHz)	$1 \sim 510$

TABLE II
SENSITIVITY INDICES OF VARIOUS VARIABLE COMBINATIONS

#	(b, σ)	(b, μ_r)	(σ, μ_r)	(b, σ, μ_r)
$\overline{S_l}$	386.6	162.3	243.9	494.1
$S_c(\omega_p)$	0.246	0.166	0.139	0.331
$S_c(\mathrm{Im}[\Delta L(\omega_p)])$	0.267	0.288	0.016	0.287

III. Results and Discussions

In numerical simulations and experiments, the parameters of the measurement setup are provided in Table I. Noted that the distance between the center of bearing balls to the coils is identical, and the properties to be estimated are bearing ball radius and relative permeability. The numerical analysis is performed on a PC with CPU AMD Ryzen 7 5800H 3.2 GHz and RAM 32 GB.

A. Numerical simulations

In the numerical simulation, the coil inductance spectra are calculated employing the FEM model in the COMSOL software, of which the basic model structure is shown in Fig. 2.

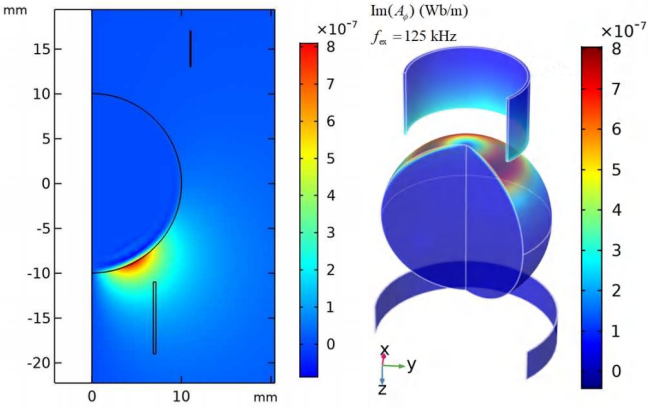

(a) (b)

Fig. 2. FEM solution of a bearing ball in (a) shaft section view and (b) 3D (rotating) view

In the evaluation procedure, the bearing ball properties are in the range of $b \in [5, 15]$ mm and $\mu_r \in [1, 101]$. The white

Gaussian noise has been applied to the inductance spectra of FEM results, and the equivalent signal-to-noise ratio is 40 dB. To apply the proposed property estimation method, in equation (4) the diagonal regularization matrix is adopted as $\lambda = \mathrm{diag}(0, \Sigma_{11} \times 10^{-6}, \Sigma_{11} \times 10^{-20})$, Σ_{11} is the largest singular value of Hessian matrix.

As a result, the relative error of estimated properties is shown in Fig. 3. The estimation results indicate that the relative estimation error of bear radius and permeability is lower than 1% and 3%. The error is relatively larger for high relative permeability and small radius. In addition, the representative evaluating points are shown in Table III, with the inductance spectra illustrated in Fig. 4. The estimated inductance spectra close to the objectives and the estimated bearing ball radius and permeability are approximate to the nominal values.

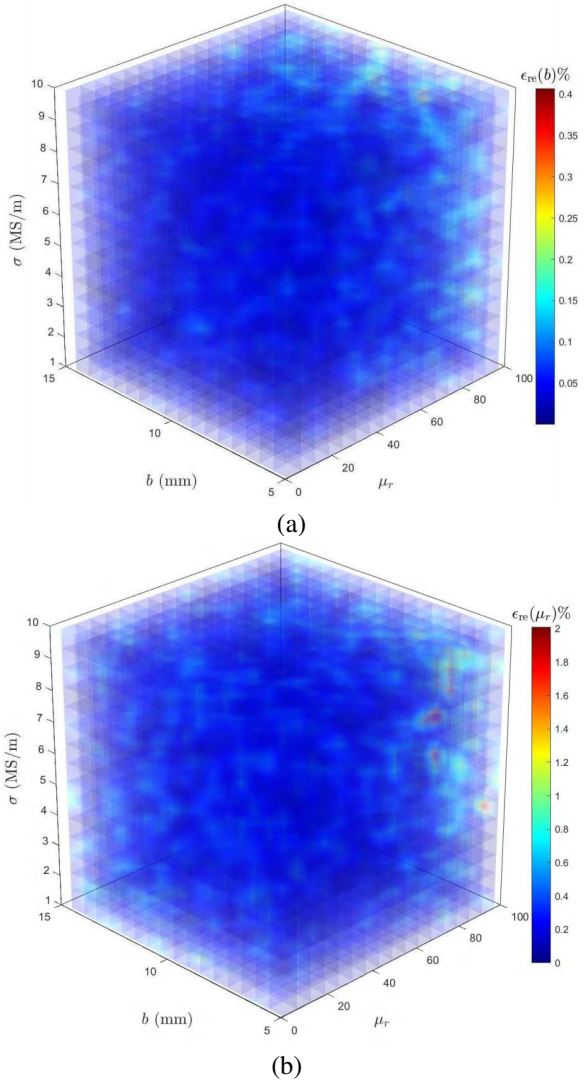

Fig. 3. Relative estimation errors of (a) bearing ball radius and (b) relative permeability

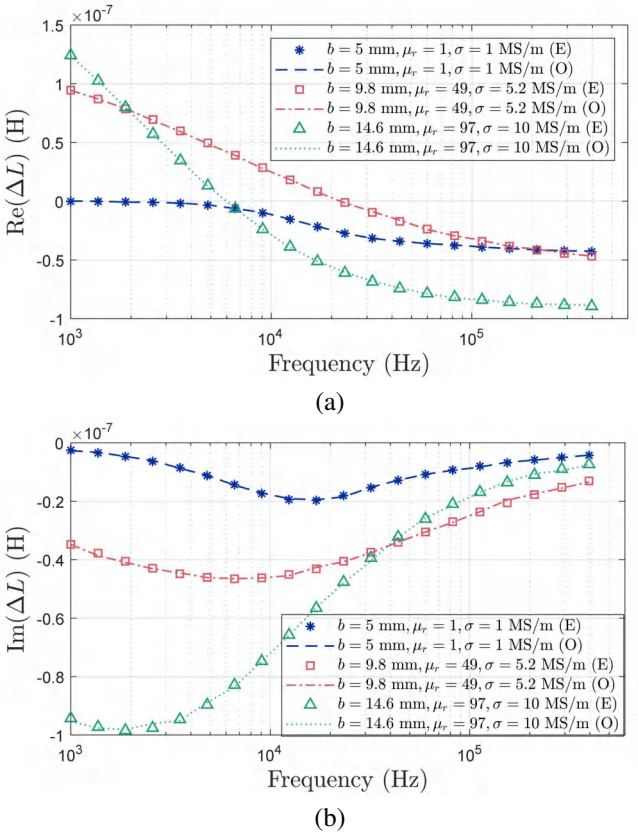

Fig. 4. Inductance spectra of bearing balls with different properties obtained from simulation (O and E represent the objective and estimated spectrum, respectively). (a) real part and (b) imaginary part

TABLE III
REPRESENTATIVE ESTIMATION RESULTS OF BEARING BALL PROPERTIES IN SIMULATIONS (b, μ_r AND σ ARE NOMINAL VALUES OF RADIUS, RELATIVE PERMEABILITY AND CONDUCTIVITY)

Sample	1	2	3
σ (SM/m)	1	5.26	10
b (mm), μ_r,	5, 1	9.8, 49	14.6, 97
$\hat{b}$ (mm), $\hat{\mu}_r$	5.00, 1.00	9.79, 48.96	14.61, 96.98

B. Experiments

The experimental setup is shown in Fig. 5. The bearing balls of various materials are measured via the Zurich impedance analyser (MFIA) with the excitation frequency ranging from 1 kHz to 510 kHz, which attains a measurement accuracy of 0.05%. The bearing ball properties are shown in the first three lines in Table IV, in which the nominal dimensions and conductivity is obtained from the product specification. The relative permeability is obtained by evaluating the squared Euclidean distance between the calculated and measured inductance spectra, *i.e.* $\min_{\mu_r} \left\{ \|\Delta \mathbf{L}(\mu_r) - \Delta \mathbf{L}_{\mathrm{m}}\|_2^2 \right\}$, $\mu_r \in [1, 2, ..., 100]$.

The estimation results of bearing ball properties are shown in Table IV, and the inductance spectra are shown in Fig. 6. The average computational time of estimation for each

TABLE IV
ESTIMATION RESULTS OF BEARING BALL PROPERTIES IN EXPERIMENTS (b, μ_r AND σ ARE NOMINAL VALUES OF RADIUS, RELATIVE PERMEABILITY AND CONDUCTIVITY)

Materials	AISI 1015	Tungsten carbide	AISI 440c	AISI 420c	AISI 52100	Brass	AISI 304
σ (MS/m)	5.75	5.56	1.47	1.39	4.65	15.9	1.4
b (mm), μ_r	6, 73	7, 2	8, 13	8.5, 24	10, 75	10, 1	7.5, 1
$\hat{b}$ (mm), $\hat{\mu}_r$	6.09, 73.08	6.69, 2.30	8.05, 14.01	8.42, 24.79	10.15, 78.78	10.08, 1.84	7.13, 1.15

bearing ball is 0.85 s. The results indicate that the estimated bearing ball properties and inductance spectra are close to the objectives. The absolute error of radius and permeability estimation is lower than 0.5 mm and 5, respectively. This could be caused by the dimensional inaccuracy of the measurement setup and due to the method acquiring the nominal value of relative permeability. The experimental estimation error is relatively larger than in the numerical simulation, while the proposed method can still provide the approximate radius and permeability for metallic bearing balls in various sizes and materials.

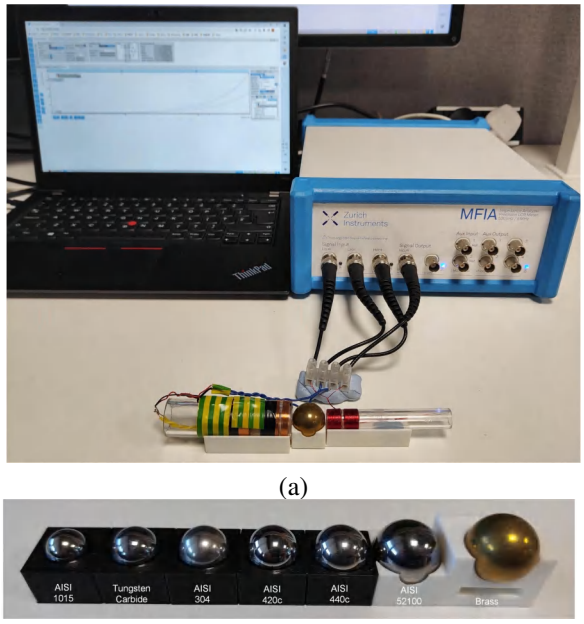

(a)

(b)

Fig. 5. Experimental setup. (a) measurement device and (b) test pieces

IV. CONCLUSION

This study proposes a theoretical method for metallic bearing ball property estimation including the radius and relative permeability. The proposed estimation method is based on the modified Newton-Raphson algorithm and the inductance of the bearing ball measured by the coaxial coils is calculated employing the analytical solution. In the numerical simulations and experiments, the accuracy of the proposed method has been validated by implementing the bearing balls in various sizes and materials. The validation results indicate that the estimation error of radius and relative permeability is within 0.5 mm and 5 for the test pieces.

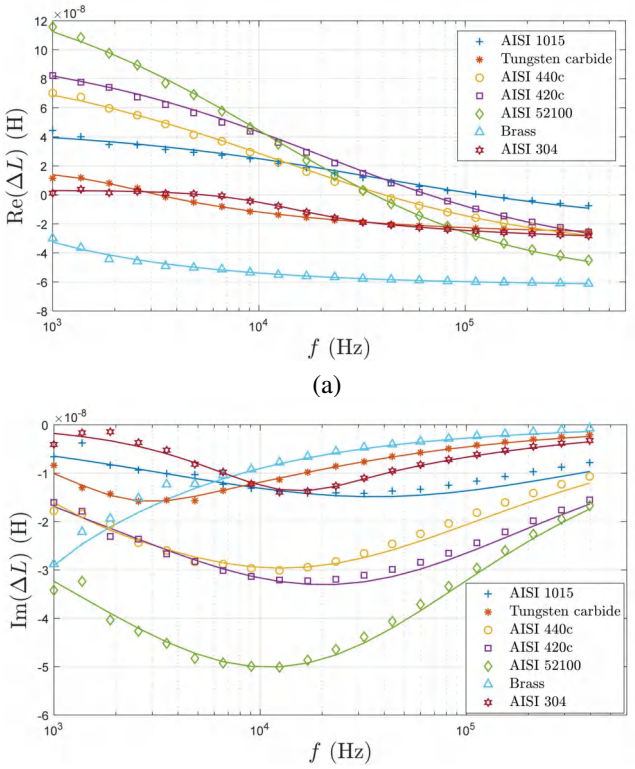

(a)

(b)

Fig. 6. Experimental inductance spectra of bearing balls with different properties (curves and points indicate the estimation and measurements, respectively)

APPENDIX A

ACKNOWLEDGMENT

The authors would like to thank the financial supports The Royal Society IEC\NSFC\211165, China Scholarship Council (CSC) and 2022 IEEE Instrumentation and Measurement Graduate Fellowship Award.

REFERENCES

[1] H. Zhang, C. Zhang, C. Wang, and F. Xie, "A survey of non-destructive techniques used for inspection of bearing steel balls," *Measurement*, vol. 159, p. 107773, 2020. [Online]. Available: https://www.sciencedirect.com/science/article/pii/S0263224120303110

[2] D.-V. Dao, J.-T. Jeng, V.-D. Doan, C.-H. Dinh, T.-T. Pham, and H.-T. Nguyen, "Classification of steel balls

by resonant eddy-current sensor," *Measurement Science and Technology*, vol. 33, no. 2, FEB 2022.

[3] W. Yin, X. Hao, A. Peyton, M. Strangwood, and C. Davis, "Measurement of permeability and ferrite/austenite phase fraction using a multi-frequency electromagnetic sensor," *NDT & E International*, vol. 42, no. 1, pp. 64–68, 2009. [Online]. Available: https://www.sciencedirect.com/science/article/pii/S0963869508000121

[4] A. Dadouche, A. Rezaei, V. Wickramasinghe, W. Dmochowski, J. W. Bird, and F. Nitzsche, "Sensitivity of air-coupled ultrasound and eddy current sensors to bearing fault detection," *Tribology Transactions*, vol. 51, no. 3, pp. 310–323, 2008.

[5] G. D'Elia, M. Cocconcelli, and E. Mucchi, "An algorithm for the simulation of faulted bearings in non-stationary conditions," *Meccanica*, vol. 53, no. 4, pp. 1147–1166, 2018.

[6] G. Li, S. Zhou, L. Ma, and Y. Wang, "Research on dual wavelength coaxial optical fiber sensor for detecting steel ball surface defects," *Measurement*, vol. 133, pp. 310–319, 2019. [Online]. Available: https://www.sciencedirect.com/science/article/pii/S0263224118309631

[7] W. L. Johnson, S. J. Norton, F. Bendec, and R. Pless, "Ultrasonic spectroscopy of metallic spheres using electromagnetic-acoustic transduction," *The Journal of the Acoustical Society of America*, vol. 91, no. 5, pp. 2637–2642, 1992.

[8] F. Deneuville, M. Duquennoy, M. Ouaftouh, F. Jenot, M. Ourak, and S. Desvaux, "Coupled analysis of high and low frequency resonant ultrasound spectroscopy: Application to the detection of defects in ceramic balls," *Review of Scientific Instruments*, vol. 80, no. 5, p. 054903, 2009.

[9] V. Schneider, N. Bader, H. Liu, and G. Poll, "Method for in situ film thickness measurement of ball bearings under combined loading using capacitance measurements," *Tribology International*, vol. 171, p. 107524, 2022. [Online]. Available: https://www.sciencedirect.com/science/article/pii/S0301679X22000974

[10] A. Kakimoto, "Detection of surface defects on steel ball bearings in production process using a capacitive sensor," *Measurement*, vol. 17, no. 1, pp. 51–57, 1996. [Online]. Available: https://www.sciencedirect.com/science/article/pii/0263224196000073

[11] W. Yin, A. Peyton, M. Strangwood, and C. Davis, "Exploring the relationship between ferrite fraction and morphology and the electromagnetic properties of steel," *Journal of materials science*, vol. 42, no. 16, pp. 6854–6861, 2007.

[12] A. V. Makarov, E. S. Gorkunov, L. K. Kogan, Y. M. Kolobylin, and A. L. Osintseva, "Eddy-current and coercive-force testing of abrasion-resistant ball bearing steel iiimx15 subjected to laser and bulk thermal processing," *Russian Journal of Nondestructive Testing*, vol. 42, no. 10, pp. 639–647, OCT 2006.

[13] H. Zhang, M. Zhong, F. Xie, and M. Cao, "Application of a saddle-type eddy current sensor in steel ball surface-defect inspection," *Sensors*, vol. 17, no. 12, p. 2814, 2017.

[14] H. Zhang, F. Xie, M. Cao, and M. Zhong, "A steel ball surface quality inspection method based on a circumferential eddy current array sensor," *Sensors*, vol. 17, no. 7, p. 1536, 2017.

[15] X. Chen and J. Li, "Pulsed eddy current testing for electromagnetic parameters of a spherical conductor," *IEEE Sensors Journal*, vol. 20, no. 7, pp. 3627–3635, 2019.

[16] D. Vasić and V. Bilas, "Lumped representation in inductive measurement of metal casing properties," in *2010 IEEE Instrumentation Measurement Technology Conference Proceedings*, 2010, pp. 841–844.

[17] W. Yin, X. Hao, A. Peyton, M. Strangwood, and C. Davis, "Measurement of permeability and ferrite/austenite phase fraction using a multi-frequency electromagnetic sensor," *NDT & E International*, vol. 42, no. 1, pp. 64–68, 2009.

[18] T. Theodoulidis and E. Kriezis, "Coil impedance due to a sphere of arbitrary radial conductivity and permeability profiles," *IEEE Transactions on Magnetics*, vol. 38, no. 3, pp. 1452–1460, 2002.

[19] G. Hu, R. Huang, M. Lu, L. Zhou, and W. Yin, "Measurement of radius of a metallic ball using eddy current testing based on peak frequency difference feature," *Measurement*, vol. 184, p. 109876, 2021. [Online]. Available: https://www.sciencedirect.com/science/article/pii/S0263224121008174

[20] Z. Xia, J. Yan, R. Huang, M. Lu, Z. Cui, A. Peyton, W. Yin, and W. Yang, "Fast estimation of metallic pipe properties using simplified analytical solution in eddy-current testing," *IEEE Transactions on Instrumentation and Measurement*, pp. 1–1, 2022.

[21] R. C. Aster, C. H. Thurber, and B. Borchers, "Parameter estimation and inverse problems (second edition)," *International Geophysics*, vol. 67, pp. 411–421, 2010.

[22] I. Sobol, "Global sensitivity indices for nonlinear mathematical models and their monte carlo estimates," *Mathematics and Computers in Simulation*, vol. 55, no. 1, pp. 271–280, 2001, the Second IMACS Seminar on Monte Carlo Methods. [Online]. Available: https://www.sciencedirect.com/science/article/pii/S0378475400002706

[23] A. Saltelli, P. Annoni, I. Azzini, F. Campolongo, M. Ratto, and S. Tarantola, "Variance based sensitivity analysis of model output. design and estimator for the total sensitivity index," *Computer physics communications*, vol. 181, no. 2, pp. 259–270, 2010.

8. Physics-guided Deep Learning for Plate Permeability Estimation with Single to Multiple Frequency Transformation of Eddy-current Testing

Physics-guided Deep Learning for Plate Permeability Estimation with Single to Multiple Frequency Transformation of Eddy-current Testing

***Abstract*— Eddy-current testing technique has been extensively explored for estimating the electromagnetic property of steel plates in various industrial applications. In this paper, a physics-guided deep learning method is proposed to estimate the permeability of plate in high thickness with probe lift-off. A simplified analytical model is derived, which realises the single to multi frequency inductance transformation and calculates the related physical properties of the measurement configuration. A constant is found, which is a fundamental coefficient describing the first-order nature of the sensor response to a plate and it is in sensitive to plate properties and probe dimensions. From the physical properties and inductance, the DL model based on the modified ResNet18-1D is trained to estimate the plate permeability. Numerical simulations and experiments have been performed to evaluate the proposed method for permeability estimation with various plate materials and probe lift-off. The method achieves real-time accurate estimation of plate permeability with a relative error lower than 3 %.**

***Index Terms*— Electromagnetic sensing, eddy current testing, analytical model, permeability measurement.**

I. Introduction

Non-destructive testing has been widely employed in a variety of industrial applications, *e.g.* steel manufacturing, oil/gas pipeline testing and aircraft structure inspection [1]–[3]. Since there is a high demand for accurately predicting the magnetic permeability of steels relating to the microstructure, eddy current testing has a promising role in estimating the steel properties. In principle, the measured signal can detect the induction field due to eddy currents in the testing target induced by the excitation field. Consequently, the estimation can be conducted from the analysis of this informative signal.

According to the measurements of eddy-current testing, *e.g.* inductance of coil probe, the electromagnetic properties of metallic objects can be estimated employing the simplified analytical model and optimization methods. The analytical model provides the explicit relationship between the measurements and electromagnetic properties, including the axial symmetric model proposed by Dodd and Deeds [4], asymmetric model expressed by the second order vector potential (SOVP) [5] and truncated eigenfunction expansion model of complex boundary condition [6]. The analytical models can be simplified, approximating the eigenfunction by the elementary and linear functions, to obtain the simple estimation equation of electromagnetic properties. For instance, the inductance zero-crossing frequency (the frequency that the real part of the inductance is zero) was found to be linearly correlated to the permeability by simplifying the phase function of the Dodd and Deeds model [7]. However, the lift-off effect, the distance between the probe and plates, causes the shift of the zero-crossing frequency and its influence on the permeability estimation requires compensation. A variety of strategies have been proposed, including sensors with multiple coils/measurements [8] (designed to estimate both lift-off and permeability) and the phenomenon of lift-off invariant inductance at a specific excitation frequency [9], [10]. Currently, the accuracy of permeability estimation by the simplified analytical models is mainly limited by the error introduced by the simplification. Furthermore, the requirement of the multi-frequency measurement or multi-coil probes for lift-off compensation increases the measurement complexity.

The optimization method estimates the metallic object properties iteratively by solving the least squares problem between the measured and calculated data which contains independent information, *e.g.* inductance spectrum and time series of pulsed eddy-current (PEC) signal. X. Chen *et al.* proposed the least squares problem of measured and calculated PEC time-series signals to estimate the pipe properties [11]. M. Lu *et al.* implemented the modified Newton-Raphson algorithm to calculate the plate properties according to the inductance spectrum [12]. The optimization method could calculate the multiple variables simultaneously with high accuracy. However, there exist inherent issues of multivariate nonlinear optimization that hinder the property estimation. It has been reported that the influence of permeability and conductivity on inductance is correlated, which causes the difficulty to optimize these variables simultaneously [13], and regularization strategies are necessary to stabilize the optimization process [14]. The objective function of optimization is non-convex, and the appropriate selection of the initial point is necessary to avoid trapping in unexpected local minima. Furthermore,

the iterative optimization process is time-consuming and can hardly be implemented in real-time applications.

In recent years, the DL method has been extensively implemented for eddy-current testing in various applications. The method learns/fits the nonlinear relationship between the measurements and objective variable, *e.g.* material properties and defect information from numerical samples by deep neural networks. It has been applied to predict the structural information of defects on plates according to the surface scanning signal of eddy-current [15]–[17]. The hardness of bearing rings has been predicted according to the receiving signal of PEC [18]. Availability of large sets of data samples is a primary issue of DL training and implementation. The samples can be obtained from the experimental measurements and numerical simulation calculated by the finite-element method (FEM) and analytical model. If the simulation model is close to the measurement configuration, the accurate estimation results of experimental test samples can be obtained from the DL model trained by the simulation samples [19]. Nevertheless, due to the lack of interpretability, the optimization method without relying on large dataset is usually preferable if the analytical model is available. Furthermore, DL models require structured data as input since the single-frequency inductance lacks enough prior information for estimation.

In this study, a physics-guided deep learning method is proposed to estimate the permeability of plate in high thickness using a single-frequency measurement of eddy-current testing. According to the simplified analytical model of the plate measured by coaxial coil, the single-frequency inductance is transformed to inductance spectrum and the physical properties including approximate lift-off and permeability can be obtained. The physical information (inductance spectrum and physical properties) from the analytical model is applied to train the DL model based on the modified ResNet18-1D for permeability estimation. In numerical simulations and experiments, the proposed method is evaluated to estimate the permeability of plates with various properties and lift-off.

The main contribution of this study includes:

1) The single to multiple frequency inductance transformation of coil measuring thick magnetic plates is proposed based on the analytical model.
2) An approximate constant of inductance spectrum is found and explained by the analytical model.
3) A physics-guided DL model is trained by physical information from analytical model to accurately estimate the plate permeability with probe lift-off, of which the model and dataset are available at Github [1] and Kaggle [2]. Feeding single frequency inductance measurement directly to the DL model does not work well compared to augmented multiple frequency data as the later embeds the eddy-current physics and hence provides physics-guidance for the DL model.

The rest of the paper is arranged as follows. Section II-A introduces the simplified analytical model to provide the physical information of plate eddy-current testing. The implementation of the DL model estimating the plate permeability is illustrated in section II-B. The numerical and experimental evaluations are summarized in section III then conclusions are presented in section IV.

II. Methods

Fig. 1 illustrates the schematic of plate permeability estimation method, which consists of the analytical model providing the physical information of plates measured by coil probe and the DL model fitting the non-linear mapping between the physical information and plate permeability. In the analytical model, the inductance spectrum transformed from a single-frequency coil inductance is applied to calculate the approximate plate permeability, probe lift-off and characteristic spatial frequency of cylindrical harmonics. In the deep learning model, the modified ResNet18-1D is employed to solve the regression problem, estimating the plate permeability from those physical information. The research highlights are detailed in the following sections.

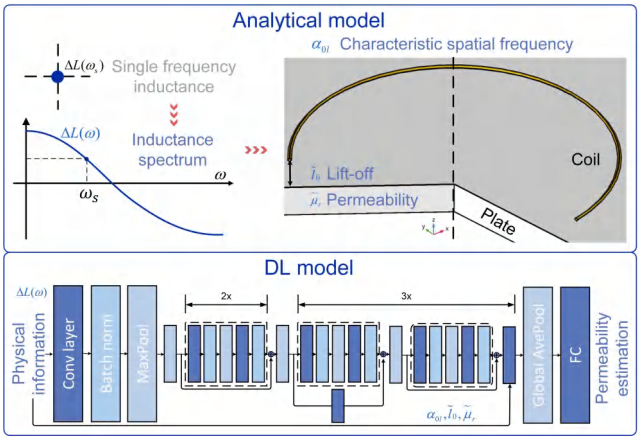

Fig. 1. Schematic of plate permeability estimation

A. Physical information from the analytical model

The Dodd and Deeds analytical model of metallic plates measured by a coaxial coil probe [4] is briefly reviewed, and its simplification is proposed to provide the physical information of plate measurement, as shown in Fig. 2.

1) Dodd and Deeds analytical model and its approximation: Considering a conductive plate, as shown in Fig. 3, the variation of coil self-inductance due to the plate [4] measured by the coil is

[1] https://github.com/rusuanjun007/Metallic-Plate-Permeability-Estimation-using-Single-Frequency-Eddy-Current-Testing

[2] https://www.kaggle.com/datasets/rusuanjun/plate-permeability-dataset

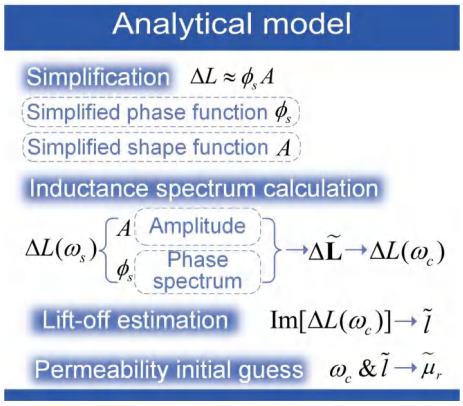

Fig. 2. Simplification of analytical model for plate permeability estimation

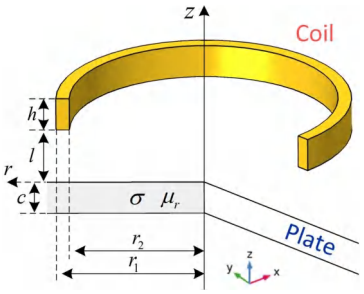

Fig. 3. A co-axial probe placed above a conductive plate

$$\Delta L(\omega) = \int_0^{\infty} K(\alpha, l)\phi(\alpha, \omega)d\alpha$$

$$K(\alpha, l) = \frac{\pi N^2 \mu_0}{h^2 (r_2 - r_1)^2} \frac{1}{\alpha^6} e^{-2\alpha l}(1 + e^{-2\alpha h} - 2e^{-\alpha h}) \times \left(\int_{\alpha r_1}^{\alpha r_2} \tau J_1(\tau) d\tau \right)^2$$

$$\phi(\alpha, \omega) = \frac{(\alpha_1 + \mu_r \alpha)(\alpha_1 - \mu_r \alpha) - (\alpha_1 + \mu_r \alpha)(\alpha_1 - \mu_r \alpha) e^{2\alpha_1 c}}{-(\alpha_1 - \mu_r \alpha)(\alpha_1 - \mu_r \alpha) + (\alpha_1 + \mu_r \alpha)(\alpha_1 + \mu_r \alpha) e^{2\alpha_1 c}} \quad (1)$$

where $K(\alpha, l)$ and $\phi(\alpha, \omega)$ are termed as the shape and phase function, respectively, N is the number of coil turns J_1 is the first-order Bessel function of the first kind, α is the spatial frequency of cylindrical harmonics, $\alpha_1 = \sqrt{\alpha^2 + j\omega\mu_0\mu_r\sigma}$ is the spatial frequency of the plate, ω is the angular frequency applied to the coil, μ_0 is the permeability in air (free space), and other parameters are shown in Fig. 3.

It was found that the bounds of integration can be approximated from 0 to α_h due to the dominant spatial frequencies of cylindrical harmonics in the inductance calculation [20], then the inductance can be calculated by

$$\Delta L(\omega) \approx \int_0^{\alpha_h} K(\alpha, l)\phi(\alpha, \omega)d\alpha \quad (2)$$

The phase function $\phi(\alpha, \omega)$ varies relatively slowly compared with the shape function $K(\alpha, l)$. Consequently, the inductance change can be simplified by extracting the phase function from the integration,

$$\Delta L(\omega) \approx \phi(\alpha_{0l}, \omega) \int_0^{\alpha_h} K(\alpha, l)d\alpha \quad (3)$$

where α_{0l} is the characteristic spatial frequency, which corresponds to the maximum value of $K(\alpha, l)$ and is influenced by the lift-off.

For the measurement without lift-off, the characteristic spatial frequency is denoted as α_{0n} which is determined by the probe parameter and can be acquired before measurement.

If the skin depth is much smaller than the thickness of the plate, the plate can be considered as the conductive and permeable half-space [6]. The phase function $\phi(\alpha_{0l}, \omega)$ can be simplified as

$$\phi(\alpha_{0l}, \omega) \approx \frac{\mu_r \alpha_{0l} - \alpha_1}{\alpha_1 + \mu_r \alpha_{0l}} = \frac{1 - \sqrt{\frac{{\alpha_{0l}}^2 + j\mu_0\mu_r\sigma\omega}{{\mu_r}^2 {\alpha_{0l}}^2}}}{1 + \sqrt{\frac{{\alpha_{0l}}^2 + j\mu_0\mu_r\sigma\omega}{{\mu_r}^2 {\alpha_{0l}}^2}}} \quad (4)$$

2) Transformation from the single frequency inductance to inductance spectrum: The simplified analytical model is employed for the single to multiple frequency inductance transformation.

For the relatively high excitation frequency, the condition that $\mu_0\mu_r\sigma\omega \gg {\alpha_{0l}}^2$ can be satisfied, then equation (4) can be approximated by a first-order system with variable $\xi = \sqrt{\mu_0\sigma/(\mu_r\alpha_{0l}^2)}$. At a specific excitation frequency ω_s, the approximation is

$$\phi(\alpha_{0l}, \omega_s) \approx \phi_s(\alpha_{0l}, \omega_s) = \frac{1 - \xi\sqrt{j\omega_s}}{1 + \xi\sqrt{j\omega_s}} = \frac{1 - \xi^2\omega_s - j\xi\sqrt{2\omega_s}}{1 + \xi^2\omega_s + \xi\sqrt{2\omega_s}} \quad (5)$$

The phase of inductance approximates to that of $\phi(\alpha_{0l}, \omega_s)$, which means

$$\frac{\mathrm{Im}[\Delta L(\omega_s)]}{\mathrm{Re}[\Delta L(\omega_s)]} \approx \frac{\mathrm{Im}[\phi_s(\alpha_{0l}, \omega_s)]}{\mathrm{Re}[\phi_s(\alpha_{0l}, \omega_s)]} = \frac{-\sqrt{2\omega_s}\xi}{1 - \xi^2\omega_s} \quad (6)$$

Variable ξ can be calculated by adopting the positive real root of quadratic equation (6), *i.e.*,

$$\xi = \frac{\sqrt{2\omega_s} + \sqrt{2\omega_s + 4\omega_s y^2}}{2\omega_s y} \quad (7)$$

where $y = \mathrm{Im}[\Delta L(\omega_s)] / \mathrm{Re}[\Delta L(\omega_s)]$.

The shape function integral $K(\alpha, l)$ in equation (3) can be approximated by

$$\int_0^{\alpha_h} K(\alpha, l)d\alpha \approx A = \Delta L(\omega_s)/\phi(\alpha_{0l}, \omega_s) \quad (8)$$

In this way, for excitation frequencies $\omega \in \mathbb{R}^{n_\omega \times 1}$, the approximate inductance spectrum can be obtained by

$$\Delta\mathbf{L}(\omega) \approx \Delta\tilde{\mathbf{L}}(\omega) = A\phi_s(\alpha_{0l}, \omega) \quad (9)$$

The approximation of inductance spectrum is shown in Fig. 4. The approximation accuracy is relatively high for excitation frequency adjacent to the calculation point ω_s.

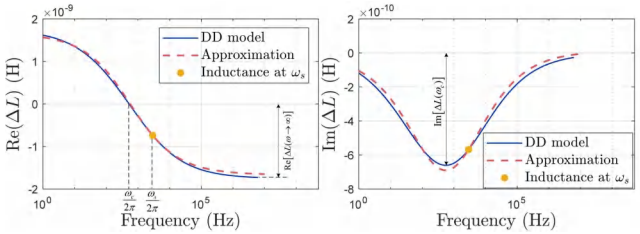

Fig. 4. Inductance spectrum transformed from the single-frequency inductance at ω_s

According to the first-order system in equation (5), at the zero-crossing frequency ω_c, *i.e.*, $\mathrm{Re}[\phi(\alpha_{0l}, \omega_c)] = 0$. It can be obtained from equation (5) that $\xi^2\omega_c$ equals to 1. Then, the frequency ω_c can be calculated by

$$\omega_c = \mu_r {\alpha_{0l}}^2 / \mu_0 \sigma \tag{10}$$

This suggests that to calculate plate permeability, the characteristic spatial frequency α_{0l} influenced by lift-off requires to be first analysed.

3) Approximate inductance constant: An approximate constant in inductance spectrum is found between the ratio of inductances at the zero-crossing frequency and high frequency, as indicated by the simplified analytical model.

According to equation (5) at the frequency ω_c, the imaginary part of the phase function becomes

$$\mathrm{Im}[\phi_s(\alpha_{0l}, \omega_c)] = -\sqrt{2}/(2+\sqrt{2}) \approx -0.4142 \tag{11}$$

For high excitation frequency $\omega \to \infty$, according to equation (5), it can be obtained that $\phi(\alpha_{0l}, \omega) \sim -1$. Therefore for high frequency and at the zero-crossing frequency, the inductance is mainly determined by the probe dimensions including lift-off. According to equation (3), an approximate constant in the inductance spectrum can be obtained, *i.e.* $\mathrm{Im}[\Delta L(\omega_c)] / \mathrm{Re}[\Delta L(\omega \to \infty)] \approx 0.4142$, as shown in Fig. 4. In addition, the approximate inductance constant is insignificantly influenced by the plate electromagnetic properties and probe dimensions.

4) Calculation of approximate lift-off, permeability and characteristic spatial frequency: The probe lift-off is determined by the inductance at the zero-crossing frequency, which is subsequently applied to calculate the characteristic spatial frequency and permeability according to the derived parametric relationships.

The calculation of probe lift-off and its influence on the characteristic spatial frequency α_{0l} is detailed as follows.

The shape function $K(\alpha, l)$ can be approximated by an elementary function, as shown in Fig. 5 (a).

$$\begin{aligned} K(\alpha, l) &\approx K_s(\alpha, l) = L_m \sin^2\left(\frac{\alpha\pi}{4\alpha_{0n}}\right) e^{-\frac{\alpha\pi}{2\alpha_{0n}}} e^{-2\alpha l} \\ L_m &= 2K(\alpha_{0n}, 0)/e^{-\pi/2} \end{aligned} \tag{12}$$

Combining equations (3), (11) and (12), after the integration of $K_s(\alpha, l)$, the inductance at the zero-crossing

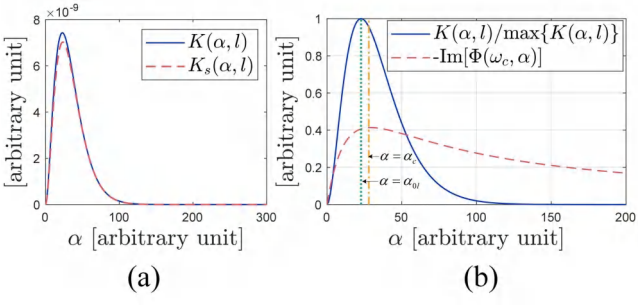

Fig. 5. (a) comparison between the shape function $K(\alpha, l)$ and its approximation $K_s(\alpha, l)$, (b) relationship between the spatial frequency α_{0l} and α_c

frequency becomes

$$\begin{aligned} \Delta L(\omega_c) \approx -0.4142j\frac{L_m}{2}\Bigg[&\frac{1-e^{-\gamma\alpha_h}}{\gamma} \\ &- \frac{\gamma - \gamma\cos\beta\alpha_h e^{-\gamma\alpha_h} + \beta\sin\beta\alpha_h e^{-\gamma\alpha_h}}{\gamma^2+\beta^2}\Bigg] \end{aligned} \tag{13}$$

where $\beta = \pi/(2\alpha_{0n})$ is a parameter relating to the shape function (probe parameters) and $\gamma = \beta + 2l$ is a inductance-dependent variable influenced by the shape function and lift-off.

For large lift-off and characteristic frequency, the condition that $\gamma\alpha_h \gg 0$ can be satisfied. Therefore, term $e^{-\gamma\alpha_h}$ in equation (13) can be omitted and the equation can be approximated by

$$\Delta L(\omega_c) \approx -0.4142j\frac{L_m}{2}\frac{\beta^2}{\gamma^3 + \gamma\beta^2} \tag{14}$$

The real root of γ in above cubic equation can be obtained by

$$\gamma = \sqrt[3]{-\frac{q}{2} + \sqrt{\left(\frac{q}{2}\right)^2 + \left(\frac{p}{2}\right)^3}} + \sqrt[3]{-\frac{q}{2} - \sqrt{\left(\frac{q}{2}\right)^2 + \left(\frac{p}{2}\right)^3}} \tag{15}$$

where $p = \beta^2$ and $q = -0.4142L_m/2$.

Subsequently, according to the relationship $\gamma = \beta + 2l$, the probe lift-off can be estimated by

$$\widetilde{l} = [\gamma - \pi/(2\alpha_{0n})]/2 \tag{16}$$

This indicates that lift-off can be determined by the plate property-independent inductance at ω_c (relating to γ) and probe parameters (corresponding to α_{0n}).

The characteristic spatial frequency α_{0l} can be calculated by

$$\alpha_{0l} = \underset{\alpha}{\mathrm{argmax}}\left\{\sin^2(\kappa\alpha)\, e^{-2\kappa\alpha} e^{-2\alpha l}\right\} \tag{17}$$

where $\kappa = \pi/4\alpha_{0n}$.

This is equivalent to calculate the maximum value of function $f(\alpha)$,

$$f(\alpha) = \sin(\kappa\alpha) e^{-\alpha(\kappa+l)} \tag{18}$$

Let $df(\alpha)/d\alpha = 0$, it has $\kappa = (\kappa + l)\tan(\kappa\alpha)$. When α is close to α_{0l} the condition that $\kappa\alpha < 1$ can be satisfied,

as the characteristic spatial frequency decreases with the increase of l. One can adopt the approximation, $\tan(\kappa\alpha) \approx \kappa\alpha$. Therefore, the solution of the problem defined in (17) can be approximated by

$$\alpha_{0l} = [\pi/(4\alpha_{0n}) + l]^{-1} \tag{19}$$

The above equation indicates the influence of probe lift-off on characteristic frequency, and especially holds for relatively large lift-off.

Substituting α_{0l} back to equation (10), the permeability of plate can be calculated by

$$\widetilde{\mu}_r = \frac{\omega_c \mu_0 \sigma}{{\alpha_{0l}}^2 \epsilon^2} \tag{20}$$

where ϵ is a compensation factor to decrease the error of inductance phase approximated by the phase function in equation (3), which is determined by $\epsilon = \alpha_c/\alpha_{0l}$, $\int_0^{\alpha_c} K_s(\alpha, l)d\alpha = k_\epsilon \int_0^{\alpha_h} K_s(\alpha, l)d\alpha$. The value of k_ϵ is empirically set between 0.5 to 0.6. This strategy selects the characteristic frequency according to the integration of the shape function rather than adopting the maximum value, as compared in Fig. 5 (b).

From the analytical model, the physical information including the approximate inductance spectrum, plate permeability and probe lift-off and characteristic spatial frequency can be obtained, while the introduced approximation limits the accuracy of the simplified analytical solutions.

B. Deep learning based permeability estimation

To estimate the permeability in high accuracy, the deep learning-based regression model is employed, of which the basic implementation is shown in Fig. 6.

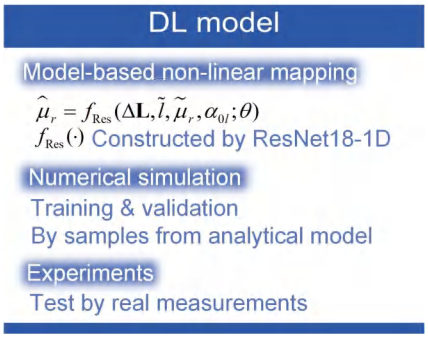

Fig. 6. Implementation of DL-based permeability estimation

The input variable are approximate plate permeability $\widetilde{\mu}_r$, by equation (20), probe lift-off $\widetilde{l}$, by equation (16), characteristic spatial frequency α_{0l}, by equation (19) and transformed inductance spectrum. The inductance spectrum in the range of $f \in [1, 510]$ kHz with 100 frequency points calculated from the single-frequency inductance at 105.64 kHz. The output variable is the estimated permeability $\hat{\mu_r}$. The non-linear mapping between the model input and output can be expressed as

$$\mu_r = f_{\text{Res}}\left(\widetilde{\mu}_r, \widetilde{l}, a_{0l}, \Delta\widetilde{\mathbf{L}}; \theta\right) \tag{21}$$

where θ represents parameters in the DL model, including weight, bias and counterparts for batch normalization.

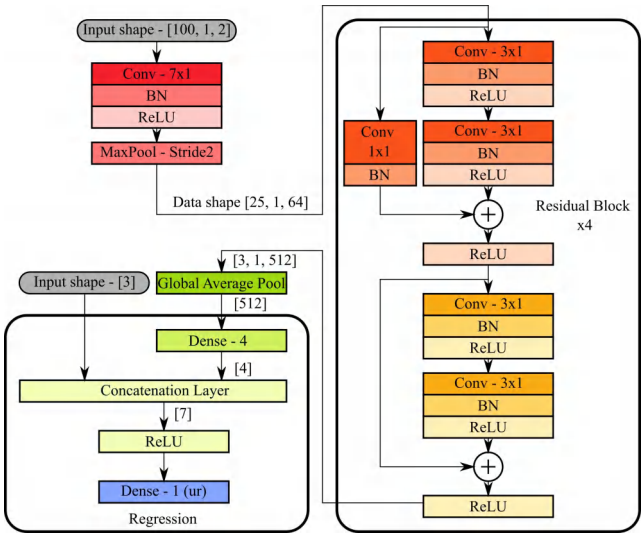

Fig. 7. Architecture of the modified ResNet18-1D model

The dataset consists of 90k simulation samples calculated by the Dodd and Deeds analytical model, the relative permeability is evenly distributed in the range of $\mu_r \in [50, 1000]$ and probe lift-off $l \in [1, 50]$ mm. The dataset is randomly divided into a training set and a validation set in a ratio of 9:1. The training set is used to update the learnable parameters of the DL model during the training phase. The validation set is relied upon to fine-tune the hyperparameters, *i.e.* model architecture, learning rate and batch normalization parameters. The test set consists of the experimental measurements, which are excluded from the training phase of the model.

The architecture of the DL model is the modified ResNet18-1D [21], as shown in Fig. 7. The inductance spectrum is fed to the input layer of the model, while other input variables $[\widetilde{\mu}_r, \widetilde{l}, a_{0l}]^{\mathrm{T}}$ is appended to the internal layer of the model, cascading with low-dimensional feature vectors extracted from the inductance spectrum.

To solve the regression problem of permeability estimation, the loss function in equation (22) is minimised. It contains the least squares error of permeability and the least absolute shrinkage and selection operator (LASSO) of model parameters for regularisation and improving the generalization ability of the model. The Adam optimiser is employed for minimisation, with parameters $\beta_1 = 0.9$ and $\beta_2 = 0.999$.

$$\min_{\theta} \mathcal{L} = \frac{1}{n_B} \sum_{i=1}^{n_B} (\mu_r - \hat{\mu}_r)^2 + \eta \frac{1}{n_\theta} \sum_{j=1}^{n_\theta} \theta_j^2 \tag{22}$$

where η is the regularization parameter adopted by $\eta = 0.0001$, n_B and n_θ indicate the batch size and quantity of model parameters, respectively.

III. Results and Discussions

A. Numerical simulations

In the numerical simulation, the estimation of probe lift-off and plate permeability is evaluated quantitatively and qualitatively. The calculation is performed on a PC with CPU AMD Ryzen 7 5800H 3.2 GHz, GPU RTX 3070 and RAM 32 GB. Details of measurement configuration are shown in Table I. The compensation factor k_ϵ relating to equation (20) is 0.6.

TABLE I
PARAMETERS OF MEASUREMENT SETUP

Parameters	Value
Inner coil radius r_1 (mm)	6
Outer coil radius r_2 (mm)	6.5
Coil hight $l_2 - l_1$ (mm)	8
Coil turns N	20
Probe lift-off l(mm)	10∼50
Conductivity of plate σ (MS/m)	1
Relative permeability of plate μ_r	10∼1000
Inductance single frequency $\omega_s/(2\pi)$ (kHz)	105.64
Frequency of inductance spectrum (kHz)	1 ∼ 510

The inductance spectra of various plate electromagnetic properties are illustrated in Fig. 8. It can be seen that inductance spectra are close for different values of μ_r and σ with the identical ratio of μ_r/σ, especially at the zero-crossing frequency. Even though only one conductivity value is evaluated, the evaluation results can represent the general cases of magnetic plates with a similar ratio of μ_r/σ.

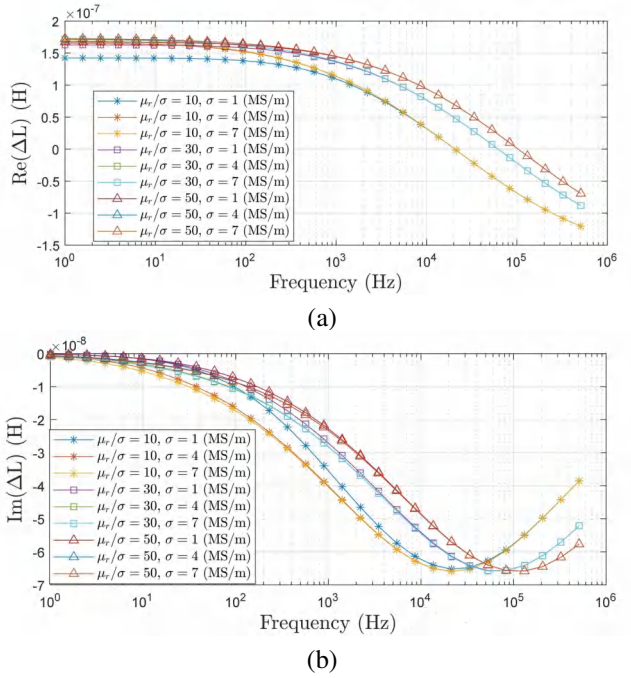

Fig. 8. Inductance spectra of magnetic plates with different electromagnetic properties for a certain probe lift-off. (a) real part and (b) imaginary part

The ratio between the inductances at the zero-crossing frequency and high frequency for various plate electromagnetic properties and probe dimensions is illustrated in Fig. 9. The ratio is close to the proposed approximate inductance constant, *i.e.* 0.4142.

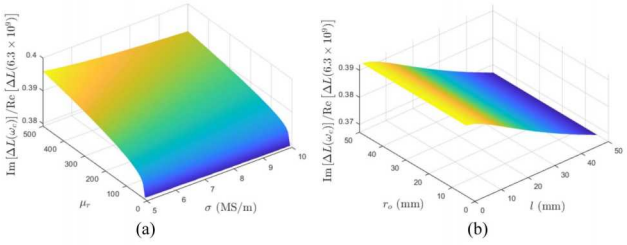

Fig. 9. Ratio between the zero-crossing frequency and high frequency inductances, r_o is the mean radius of coil

The comparison of inductance spectra calculated by the Dodd and Deeds analytical model and the single to multiple frequency transformation are shown in Fig. 10, which matches well. To evaluate the accuracy of the approximate permeability and lift-off from the analytical model, the representative results are illustrated in Table II. Furthermore, the relative error in a large evaluation range is shown in Fig. 11.

The representative cases in Table II indicate that the approximate probe lift-off and plate permeability from the analytical model are close to the nominal values when lift-off is equal to or higher than 10 mm. The relative error in Fig. 11 shows that the error is large for small lift-off and relative permeability. For lift-off higher than 10 mm and relative permeability larger than 50, the relative error is within 11% and 20% for lift-off and permeability, respectively. In addition, the lift-off calculation error shows the exponential relationship with the lift-off nominal value, while the relationship between the permeability error and nominal values is relatively complex.

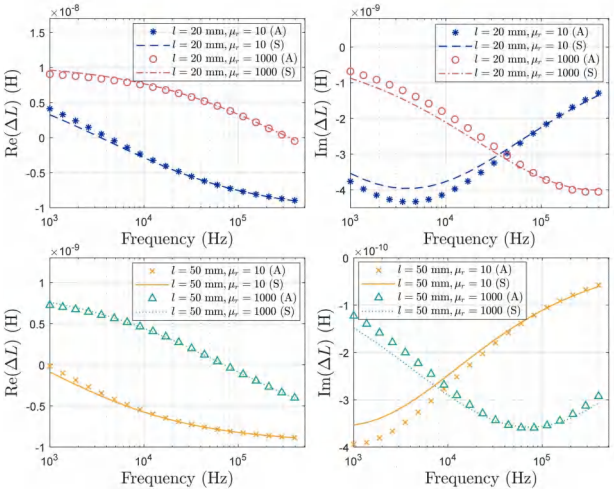

Fig. 10. Inductance spectra of representative cylinder samples in Table II. (A) and (S) indicate the spectra calculated by the Dodd and Deeds analytical method (for comparison) and through the single to multiple frequency transformation, respectively

To implement the proposed DL model, the number of training epochs is 1500, which takes 5.5 hours. The average

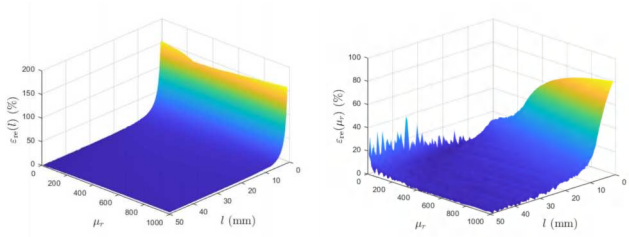

(a) (b)

Fig. 11. Relative estimation errors of (a) lift-off and (b) plate relative permeability in the evaluated range

TABLE II
APPROXIMATE LIFT-OFF AND PERMEABILITY CALCULATED BY ANALYTICAL MODEL FOR REPRESENTATIVE CASES IN SIMULATIONS

#	1	2	3	4	5	6
l (mm) [1]	20	20	30	30	50	50
$\tilde{l}$ (mm)	20.81	21.21	30.42	31.33	50.52	52.17
μ_r [1]	10	1000	10	1000	10	1000
$\tilde{\mu}_r$	10.22	927.87	10.76	957.63	11.83	965.93
$\varepsilon_{\mathrm{re}}(\tilde{\mu}_r)$ [2]	2.2 %	7.2 %	7.6 %	4.2 %	18.3%	3.4%

[1] l and μ_r are nominal values of lift-off and relative permeability
[2] $\varepsilon_{\mathrm{re}}(\tilde{\mu}_r)$ is the relative error of approximate permeability

relative error of permeability estimation on the training set described in section II-B is 0.9%, and the average estimation time for each sample is 0.1 ms. In addition, if the single-frequency inductance alone is input to the corresponding DL model, the average relative error increases to 4.7%, which indicates the necessity of physical information from the analytical model.

B. Experiments

The experimental setup is illustrated in Fig. 12. The inductance spectra are measured via the Zurich impedance analyser (MFIA) with the excitation frequency ranging from 1 kHz to 510 kHz, which attains a measurement accuracy of 0.05% [22]. The single-frequency inductance at 105.64 kHz is applied to estimate the plate permeability in experiments. The probe dimensions are identical to those in the numerical simulations, while the probe lift-off of 2 mm and 3.8 mm are considered in the experiments. The larger lift-off could lead to difficulty in impedance measurement by the impedance analyser, due to the limited sensitivity of plates measurement by small coil probe. The measured magnetic plates are generated by the hot isostatic pressing of powder mixtures. The thickness of the plates is much higher than the skin depth of eddy-current at the selected excitation frequency and the radii of plates are much larger than the coil radius. Therefore, the plates can be approximately viewed as the conductive and permeable half-space in the measurement, satisfying the applicable conditions of the analytical model. The number marked on the surface of the plates indicates the ferrite fraction of the plates. The effective electromagnetic properties (nominal values) of these plates are obtained from the studies [23].

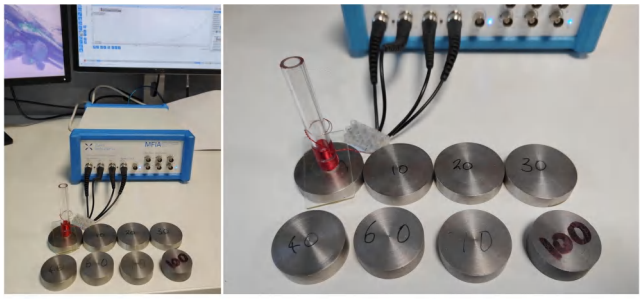

(a) (b)

Fig. 12. Experimental setup. (a) measurement device and (b) test pieces

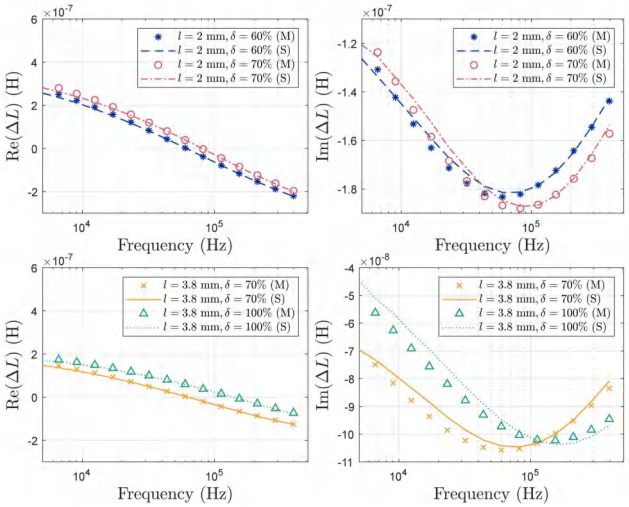

Fig. 13. Inductance spectra of measured cylinders in Table III. (M) and (S) indicate the measurements (for comparison) and through the single to multiple frequency transformation, respectively

The estimation results of the plates in ferrite fraction of 60 %, 70 % and 100 % are shown in Table III. The comparison of inductance spectra of measurements and calculation by the proposed method with equation (9) are shown in Fig. 10, which generally matches well. The approximate permeability from the simplified analytical model is generally close to the nominal value, while the error of approximate lift-off is relatively larger. Because the relative error of lift-off is large for small lift-off values, as validated in simulations. Furthermore, the DL model estimates the accurate permeability from the physical information obtained from the analytical model. Specifically, the largest error of permeability estimation is 2.9%, for the plate with nominal permeability of $\mu_r = 104.1$ and probe lift-off $l = 2$ mm. Compared with numerical simulations, the permeability estimation error in experiments is relatively larger. This is mainly due to the discrepancy between the simulation and experimental samples, which is induced by the finite-size plates, inaccuracy of sensor dimensions and measurement errors.

By combining the analytical and DL models, abundant physical information is obtained by analytical solutions, of which the feature is extracted and utilized by the DL model

for permeability estimation. The proposed method provides the accurate estimation results for various probe lift-off and plate electromagnetic properties in both numerical simulations and experiments.

TABLE III
ESTIMATION RESULTS IN EXPERIMENT

δ [1]	60 %	70 %	100 %	60 %	70 %	100 %
$l\ (mm)$ [2]	2	2	2	3.8	3.8	3.8
$\tilde{l}$ (mm)	3.43	3.36	3.40	4.85	4.75	4.85
μ_r [2]	78.9	104.1	200	78.9	104.1	200
$\tilde{\mu}_r$	76.82	99.50	188.46	86.39	115.31	206.58
$\varepsilon_{\mathrm{re}}(\tilde{\mu}_r)$ [3]	2.3%	4.4%	5.8%	9.5%	10.8%	3.3%
$\hat{\mu}_r$	76.71	107.16	196.32	76.89	102.87	203.76
$\varepsilon_{\mathrm{re}}(\hat{\mu}_r)$ [3]	2.8%	2.9%	1.8%	2.5%	1.2%	1.9%

[1] δ is the ferrite fraction of samples
[2] l and μ_r are nominal values of lift-off and relative permeability
[3] $\varepsilon_{\mathrm{re}}(\tilde{\mu}_r)$ and $\varepsilon_{\mathrm{re}}(\hat{\mu}_r)$ are relative error of approximate permeability and its estimation, respectively

IV. CONCLUSIONS

This study proposes a physics-guided DL for plate permeability estimation employing the single to multiple frequency transformation of eddy-current testing. The measured plates are in high thickness and the proposed method can reduce the influence of probe lift-off. The measured single-frequency inductance is transformed to inductance spectrum and the related physical properties of measurement configuration is obtained, employing the simplified analytical model. An approximate inductance constant in the inductance spectrum is investigated by the analytical model. The DL model based on the modified ResNet18-1D is constructed to estimate plate permeability from the physical information. The eddy-current physics provides physics-guidance for the DL model. In numerical simulations, the accuracy and characteristics of the proposed analytical model have been comprehensively evaluated concerning various plate properties. The physics-guided DL model outperforms the counterpart without physical information. In the experiment, the samples in various ferrite fractions are measured and the proposed method achieves the real-time permeability estimation with a relative estimation accuracy of 3 %.

REFERENCES

[1] J. Kral, R. Smid, H. M. G. Ramos, and A. L. Ribeiro, "The lift-off effect in eddy currents on thickness modeling and measurement," *IEEE Transactions on Instrumentation and Measurement*, vol. 62, no. 7, pp. 2043–2049, 2013.

[2] N. Ulapane, A. Alempijevic, J. Valls Miro, and T. Vidal-Calleja, "Non-destructive evaluation of ferromagnetic material thickness using pulsed eddy current sensor detector coil voltage decay rate," *NDT & E International*, vol. 100, pp. 108–114, 2018. [Online]. Available: https://www.sciencedirect.com/science/article/pii/S096386951730600X

[3] R. Huang, M. Lu, Z. Chen, Y. Shao, Z. Xia, G. Hu, A. Peyton, and W. Yin, "A novel acceleration method for crack computation using finite element analysis in eddy current testing," *IEEE Transactions on Instrumentation and Measurement*, vol. 71, pp. 1–9, 2022.

[4] C. V. Dodd and W. E. Deeds, "Analytical solutions to eddy-current probe-coil problems," *Journal of Applied Physics*, vol. 39, no. 6, pp. 2829–2838, 1968.

[5] D. Wu, F. Yang, X. Wang, and T. He, "Impedance calculation of arbitrary-shaped thin-walled coils for eddy-current testing of planar media," *Sensors and Actuators A: Physical*, vol. 279, pp. 537–542, 2018.

[6] T. Theodoulidis and E. Kriezis, *Eddy Current Canonical Problems (with Applications to Nondestructive Evaluation)*, ser. Contemporary research on emerging science and technology. Tech Science Press, 2006.

[7] W. Zhu, W. Yin, A. Peyton, and H. Ploegaert, "Modelling and experimental study of an electromagnetic sensor with an h-shaped ferrite core used for monitoring the hot transformation of steel in an industrial environment," *Ndt & E International*, vol. 44, no. 7, pp. 547–552, 2011.

[8] M. Lu, X. Meng, L. Chen, R. Huang, W. Yin, and A. Peyton, "Measurement of ferromagnetic slabs permeability based on a novel planar triple-coil sensor," *IEEE Sensors Journal*, vol. 20, no. 6, pp. 2904–2910, 2020.

[9] G. Y. Tian, Y. Li, and C. Mandache, "Study of lift-off invariance for pulsed eddy-current signals," *IEEE Transactions on Magnetics*, vol. 45, no. 1, pp. 184–191, 2009.

[10] Z. Jin, Y. Meng, R. Yu, R. Huang, M. Lu, H. Xu, X. Meng, Q. Zhao, Z. Zhang, A. Peyton, and W. Yin, "Methods of controlling lift-off in conductivity invariance phenomenon for eddy current testing," *IEEE Access*, vol. 8, pp. 122 413–122 421, 2020.

[11] X. Chen and X. Liu, "Pulsed eddy current-based method for electromagnetic parameters of ferromagnetic materials," *IEEE Sensors Journal*, vol. 21, no. 5, pp. 6376–6383, 2021.

[12] M. Lu, Y. Xie, W. Zhu, A. Peyton, and W. Yin, "Determination of the magnetic permeability, electrical conductivity, and thickness of ferrite metallic plates using a multifrequency electromagnetic sensing system," *IEEE Transactions on Industrial Informatics*, vol. 15, no. 7, pp. 4111–4119, 2019.

[13] D. Vasić and V. Bilas, "Lumped representation in inductive measurement of metal casing properties," in *2010 IEEE Instrumentation Measurement Technology Conference Proceedings*, 2010, pp. 841–844.

[14] Z. Xia, J. Yan, R. Huang, M. Lu, Z. Cui, A. Peyton, W. Yin, and W. Yang, "Fast estimation of metallic pipe properties using simplified analytical solution in eddy-current testing," *IEEE Transactions on Instrumentation and Measurement*, vol. 72, pp. 1–13, 2023.

[15] P. Zhu, Y. Cheng, P. Banerjee, A. Tamburrino, and Y. Deng, "A novel machine learning model for eddy current testing with uncertainty," *ndt & e International*, vol. 101, pp. 104–112, 2019.

[16] X. Tao, L. Peng, Y. Tao, and C. Ye, "Inspection of defects in weld using differential array ect probe and deep learning algorithm," *IEEE Transactions on Instrumentation and Measurement*, vol. 70, pp. 1–9, 2021.

[17] T. Meng, Y. Tao, Z. Chen, J. R. S. Avila, Q. Ran, Y. Shao, R. Huang, Y. Xie, Q. Zhao, Z. Zhang, H. Yin, A. J. Peyton, and W. Yin, "Depth evaluation for metal surface defects by eddy current testing using deep residual convolutional neural networks," *IEEE Transactions on Instrumentation and Measurement*, vol. 70, pp. 1–13, 2021.

[18] J. Sha, M. Fan, and B. Ye, "Intelligent hardness prediction of bearing rings using pulsed eddy current testing," *IEEE Sensors Journal*, vol. 22, no. 23, pp. 23 320–23 327, 2022.

[19] S. Kucheryavskiy, A. Egorov, and V. Polyakov, "Coupling analytical models and machine learning methods for fast and reliable resolution of effects in multifrequency eddy-current sensors," *Sensors*, vol. 21, no. 2, p. 618, 2021.

[20] W. Yin and K. Xu, "A novel triple-coil electromagnetic sensor for thickness measurement immune to lift-off variations," *IEEE Transactions on Instrumentation and Measurement*, vol. 65, no. 1, pp. 164–169, 2016.

[21] K. He, X. Zhang, S. Ren, and J. Sun, "Identity mappings in deep residual networks," in *Computer Vision–ECCV 2016: 14th European Conference, Amsterdam, The Netherlands, October 11–14, 2016, Proceedings, Part IV 14*. Springer, 2016, pp. 630–645.

[22] "MFIA 5MHz impedance analyzer and precision lcr meter," https://www.zhinst.com/sites/default/files/documents/2021-12/zi_mfia_leaflet_latest.pdf., accessed on: Apr. 4, 2022. [Online].

[23] W. Yin, A. Peyton, M. Strangwood, and C. Davis, "Exploring the relationship between ferrite fraction and morphology and the electromagnetic properties of steel," *Journal of materials science*, vol. 42, no. 16, pp. 6854–6861, 2007.

9. Thickness and permeability estimation of metallic plates by triple-frequency eddy-current testing with probe lift-off

Thickness and permeability estimation of metallic plates by triple-frequency eddy-current testing with probe lift-off

Ruochen Huang, *Member, IEEE*, Zihan Xia*, Mingyang Lu, *Member, IEEE*, and Wuliang Yin, *Senior Member, IEEE*

***Abstract*—Eddy-current testing is one of the contactless nondestructive testing technique for the physical property measurement (*e.g.* thickness, electrical conductivity and magnetic permeability) of steel plates in various industrial applications. In this study, an estimation method of plate thickness and permeability has been proposed using the triple-frequency coil inductance with probe lift-off. The functional relationship between the plate properties, probe lift-off and characteristics of coil inductance is suggested with the simplified analytical model, which is employed for the initial guesses of optimisation. The proposed method can decrease the influence of the local minimum issue of optimisation on property estimation. Numerical simulations and experiments have been performed to evaluate the property estimation with various probe lift-off. Compared with the estimation results without the appropriate initial guesses, the proposed method is more robust and accurate for various cases, with a relative estimation error smaller than 8 %.**

***Index Terms*—Eddy current testing, analytical model, thickness measurement, permeability measurement, probe lift-off.**

I. Introduction

Non-destructive testing of metallic plates has been widely studied for a variety of industrial applications. Since there is a high demand for accurately testing the physical properties of metallic plates, including thickness and electromagnetic properties, eddy-current (EC) testing has a promising role in measurement. In principle, the EC signals are sensitive to the dimensions and electromagnetic properties of metals which influences the EC diffusion. The property estimation can be achieved by analysing the informative signals.

According to the measurements of EC signals, *e.g.* inductance of coil probe, the electromagnetic properties of metallic objects can be estimated employing the simplified analytical model and optimisation method.

The analytical model provides the explicit relationship between the measurements, plate properties and probe parameters. This includes the Dodd and Deeds [1] model for axial-symmetric cases, the second-order vector potential (SOVP) method for asymmetric model [2] and truncated eigenfunction expansion model for complex geometries [3]. The analytical function can be simplified mathematically to obtain the estimation equation of electromagnetic properties, usually at characteristic frequencies of the inductance spectrum (complex mutual inductance between the transmitting and receiving coils). The simplified analytical model reveals that the zero-crossing frequency of the real part of the inductance (the frequency that the real part of the inductance is zero) relates to the permeability-to-conductivity ratio of plates [4], by approximating to the first-order system. For thin plates, the peak frequency of the imaginary part of the inductance relates to the conductivity and thickness of plates [5]. By approximating the phase of the inductance at the high frequency where plates almost completely reflect the incident electromagnetic waves, the real part of the inductance corresponds to the probe lift-off [6]. At the low frequency where part of the electromagnetic waves penetrate the measured plates, the simplified phase of inductance is influenced by the thickness and electromagnetic properties of plates [7]. The accuracy of plate property estimation by the simplified analytical models is mainly limited by the inaccuracy due to model approximation.

The optimisation method optimises the properties of test pieces by solving the least squares problem between the measured and calculated measurement signals. X. Chen *et al.* proposed the least squares problem of the pulsed eddy-current signals in time domain to estimate the pipe properties [8]. M. Lu *et al.* employed the Newton-Raphson algorithm to calculate the plate properties according to the inductance spectrum [9]. The optimisation method could calculate the multiple properties simultaneously with high accuracy if the global minimum can be reached. However, there exist difficulties in optimisation. It has been reported that a certain permeability-to-conductivity ratio leads to a similar inductance spectrum for relatively high excitation frequency [10], which causes the difficulty in simultaneous estimation of magnetic permeability and electrical conductivity. Furthermore, the objective function minimising the Euclidean distance of the inductance spectrum is non-convex, and the appropriate selection of the initial point is necessary to avoid trapping in unexpected local minima [11], [12]. In addition,

Manuscript updated June 25, 2023, and submitted xxx xx, 2021.

Mr. Zihan Xia and Dr. Wuliang Yin are with the School of Electrical and Electronic Engineering, University of Manchester, Manchester M13 9PL, U.K.

Dr. Ruochen Huang is with the College of Electrical Engineering and Automation, Fuzhou University, Fuzhou 350108, China. (*Corresponding author: Ruochen Huang. email: ruochen_huang@fzu.edu.cn*)

Dr. Mingyang Lu is with the Nondestructive Evaluation (CNDE), Iowa State University, Iowa 50011-3041, U.S.A.

to overcome the undetermined issue of the inverse problem, the quantity of frequency points in the inductance spectrum should be equal to or more than the number of optimised properties.

In this study, an estimation method of plate thickness, permeability and probe lift-off has been proposed using the triple-frequency inductance of EC testing. Through the simplified analytical model, the initial guesses of probe lift-off, plate permeability and thickness are calculated according to the characteristics of the triple-frequency inductance, and are optimised by the modified Newton-Raphson method. The initial guesses alleviate the influence of local minimum on optimisation. In numerical simulations, the relationship between the estimated properties and inductance characteristics suggested by the simplified analytical model has been validated. In both numerical simulations and experiments, the performance of the proposed method has been evaluated for various properties of metallic plates.

The rest of the paper is arranged as follows. Section II-A introduces the simplified analytical model to obtain the initial guesses of plate properties and probe lift-off. The implementation of the optimisation based on the Newton-Raphson method is detailed in section II-B. The numerical and experimental evaluations are summarised in section III then conclusions are presented in section IV.

II. Methods

The basis of plate property estimation is shown in Fig. 1. The characteristics of the triple-frequency inductance is applied to infer the initial guesses of the plate properties and probe lift-off which are optimised for accurate estimation. The research highlights are detailed in the following sections.

A. Plate property initial guesses

The Dodd and Deeds analytical model of metallic plates measured by a coaxial coil probe [1], shown in Fig. 2, is briefly reviewed, and its approximation is proposed, regarding the relatively high, medium and low frequencies for plate property estimation.

Measuring a conductive plate, as shown in Fig. 2, the variation of the mutual inductance between the transmitting and receiving coils due to the plate [1] (referred to as inductance hereinafter) is

$$\Delta L(\omega) = \int_0^\infty K(\alpha, l)\phi(\alpha, \omega)d\alpha$$

$$K(\alpha, l) = \frac{\pi N^2 \mu_0}{h^2 (r_2 - r_1)^2} \frac{1}{\alpha^6} e^{-2\alpha l} e^{-\alpha(h+g)} \left(1 - e^{-\alpha h}\right)^2 \times \left(\int_{\alpha r_1}^{\alpha r_2} \tau J_1(\tau) d\tau \right)^2$$

$$\phi(\alpha, \omega) = \frac{(\alpha_1 + \mu_r \alpha)(\alpha_1 - \mu_r \alpha) - (\alpha_1 + \mu_r \alpha)(\alpha_1 - \mu_r \alpha) e^{2\alpha_1 c}}{-(\alpha_1 - \mu_r \alpha)(\alpha_1 - \mu_r \alpha) + (\alpha_1 + \mu_r \alpha)(\alpha_1 + \mu_r \alpha) e^{2\alpha_1 c}} \quad (1)$$

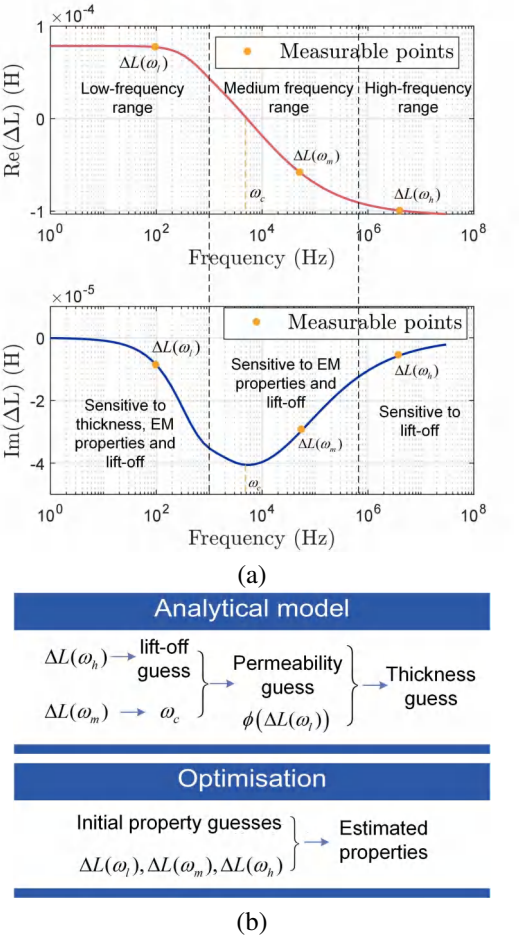

Fig. 1. (a) relationship between the characteristics of coil inductance and plate properties, (b) flowchart of property estimation

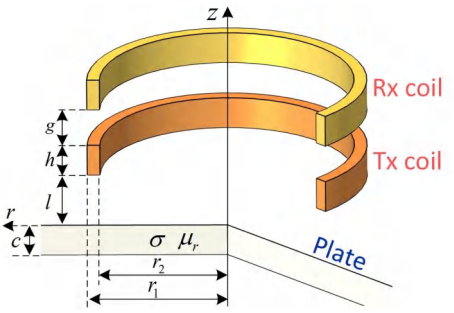

Fig. 2. Schematic of the metallic plate measured by coil probe

where $K(\alpha, l)$ and $\phi(\alpha, \omega)$ are termed as the shape and phase function, respectively, N is the number of coil turns J_1 is the first-order Bessel function of the first kind, α is the spatial frequency of cylindrical harmonics, $\alpha_1 = \sqrt{\alpha^2 + j\omega\mu_0\mu_r\sigma}$ is the spatial frequency of the plate, ω is the angular frequency applied to the coil, μ_0 is the permeability in air (free space), and other parameters are shown in Fig. 2.

It was found that the bounds of integration can be approximated from 0 to α_h due to the dominant spatial frequencies

of cylindrical harmonics in the inductance calculation [13], then the inductance can be calculated by

$$\Delta L\left(\omega\right) \approx \int_0^{\alpha_h} K(\alpha, l)\phi(\alpha, \omega)d\alpha \tag{2}$$

1) Initial guess of probe lift-off: The high-frequency inductance is applied to obtain the initial guess of lift-off with the approximation of the shape function.

For relatively high excitation frequency, the condition $\omega_h \to \infty$ can be satisfied, the phase function $\phi(\alpha, \omega)$ in equation (1) can be simplified by $\phi(\alpha, \omega_h) \approx -1$, which indicates that the plate reflects completely the electromagnetic wave generated by coils.

The shape function $K(\alpha, l)$ composed of the exponential and Bessel function can be approximated by the product of the exponential and sinusoidal function,

$$\begin{aligned} K\left(\alpha, l\right) &\approx K_s(\alpha, l) \\ &= L_m \sin^2\left(\frac{\alpha\pi}{4\alpha_{0n}}\right) e^{-\frac{\alpha\pi}{2\alpha_{0n}}} e^{-2\alpha l} \\ L_m &= 2K(\alpha_{0n}, 0)/e^{-\pi/2} \\ \alpha_n &= \arg\max_{\alpha}\left\{K(\alpha, 0)\right\} \end{aligned} \tag{3}$$

The comparison of the shape function and its approximation is shown in Fig. 3.

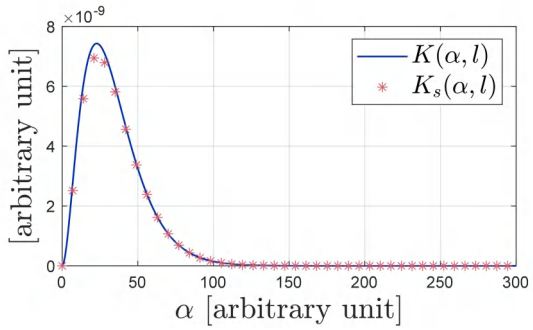

Fig. 3. Comparison between the shape function $K(\alpha, l)$ and its approximation $K_s(\alpha, l)$

Substituting $K(\alpha, l)$ in equation (1) by $K_s(\alpha, l)$ and through integral, the inductance becomes

$$\begin{aligned} \Delta L(\omega_h) \approx -j\frac{L_m}{2}\Bigg[&\frac{1 - e^{-\gamma\alpha_h}}{\gamma} \\ &- \frac{\gamma - \gamma\cos\beta\alpha_h e^{-\gamma\alpha_h} + \beta\sin\beta\alpha_h e^{-\gamma\alpha_h}}{\gamma^2 + \beta^2}\Bigg] \end{aligned} \tag{4}$$

where $\beta = \pi/(2\alpha_n)$ is a parameter relating to the shape function (probe parameters) and $\gamma = \beta + 2l$ is an inductance-dependent variable influenced by the shape function and lift-off.

The probe lift-off, the only unknown, can be obtained by solving equation (4) which is further simplified. For the large value of upper limit of integral α_h, the condition $\gamma\alpha_h \gg 0$ holds. The function $e^{-\gamma\alpha_h}$ in equation (4) can be omitted to obtain

$$\Delta L(\omega_c) \approx -j\frac{L_m}{2}\frac{\beta^2}{\gamma^3 + \gamma\beta^2} \tag{5}$$

This is a cubic equation of γ, of which the real root is applied to calculate the lift-off,

$$\widetilde{l} = \left[\gamma - \pi/(2\alpha_n)\right]/2 \tag{6}$$

2) Initial guess of plate permeability: The initial guess of plate permeability is obtained from inductance of medium frequency, with the approximation of the phase function.

According to the mean value theorem for integrals, the inductance can be calculated by

$$\Delta L\left(\omega\right) = \phi(\alpha_s, \omega)\int_0^{\alpha_h} K(\alpha, l)d\alpha \tag{7}$$

where α_s is referred to as the characteristic spatial frequency.

Noted that α_s depends on both shape and phase function, which is difficult to be obtained accurately without the known plate properties. In previous study [14], one can still approximate it by

$$\begin{aligned} \Delta L\left(\omega\right) &\approx \phi(\epsilon\alpha_l, \omega)\int_0^{\alpha_h} K(\alpha, l)d\alpha \\ \alpha_l &= \arg\max_{\alpha}\left\{K(\alpha, l)\right\} \\ &\approx \arg\max_{\alpha}\left\{K_s(\alpha, l)\right\} \end{aligned} \tag{8}$$

where ϵ is a compensating factor that can be set empirically and is selected as 1 previously.

In the medium excitation frequency where the skin depth is much smaller than the plate thickness. The plate can be approximately viewed as a conductive permeable half-space [3]. The phase function can be approximated by

$$\begin{aligned} \phi(\alpha, \omega) &\approx \frac{\mu_r\alpha - \alpha_1}{\alpha_1 + \mu_r\alpha} \\ &= \frac{1 - \sqrt{\frac{\alpha^2 + j\mu_0\mu_r\sigma\omega}{{\mu_r}^2\alpha^2}}}{1 + \sqrt{\frac{\alpha^2 + j\mu_0\mu_r\sigma\omega}{{\mu_r}^2\alpha^2}}} \end{aligned} \tag{9}$$

For plates with high conductivity and permeability, the condition that $\mu_0\mu_r\sigma\omega \gg {\alpha_{0l}}^2$ can be satisfied. A first-order system is applied to approximate equation (9) with variable $\eta = \sqrt{\mu_0\sigma/(\mu_r\alpha^2)}$. At the medium frequency ω_m,

$$\begin{aligned} \phi\left(\alpha, \omega_m\right) &\approx \phi_s\left(\alpha, \omega_m\right) \\ &= \frac{1 - \eta\sqrt{j\omega_m}}{1 + \eta\sqrt{j\omega_m}} = \frac{1 - \eta^2\omega_m - j\eta\sqrt{2\omega_m}}{1 + \eta^2\omega_m + \eta\sqrt{2\omega_m}} \end{aligned} \tag{10}$$

According to equation (8), as $K(\alpha, l)$ is a real function, the phase of inductance is

$$\begin{aligned} \frac{\mathrm{Im}\left[\Delta L(\omega_m)\right]}{\mathrm{Re}\left[\Delta L(\omega_m)\right]} &\approx \frac{\mathrm{Im}\left[\phi_s(\alpha_s, \omega_m)\right]}{\mathrm{Re}\left[\phi_s(\alpha_s, \omega_m)\right]} \\ &= \frac{-\sqrt{2\omega_m}\eta}{1 - \eta^2\omega_m} \end{aligned} \tag{11}$$

The variable η can be obtained by adopting the positive real root of its quadratic equation (11). Furthermore, the phase spectrum $\phi_s\left(\alpha, \omega_m\right)$ can be obtained by bring the calculated η back to equation (10).

At the zero-crossing frequency of the real part of the inductance ω_c, it has $\mathrm{Re}[\phi(\alpha_s, \omega_c)] = 0$. From equation (10), one can derive $\eta^2\omega_c = 1$, indicating that

$$\omega_c = \mu_r {\alpha_s}^2/\mu_0\sigma \tag{12}$$

This means that ω_c is determined by the permeability-to-conductivity ratio and characteristic spatial frequency. From equation (3) and (8), the spatial frequency α_l can be obtained by

$$\alpha_l = \underset{\alpha}{\mathrm{argmax}} \left\{ \sin(\kappa\alpha) e^{-\alpha(\kappa+l)} \right\} \tag{13}$$

where $\kappa = \pi/4\alpha_n$.

Rendering $\partial[\sin(\kappa\alpha)e^{-\alpha(\kappa+l)}]/\partial\alpha = 0$ leads to $\kappa = (\kappa + l)\tan(\kappa\alpha)$. The approximation of the tangential function can be applied, *i.e.* $\tan(\kappa\alpha) \approx \kappa\alpha$, as $\kappa\alpha < 1$ can be satisfied. Subsequently, the spatial frequency is approximated by

$$\alpha_l \approx [\pi/(4\alpha_n) + l]^{-1} \tag{14}$$

This indicates the relationship between the spatial frequencies at the peak points and probe lift-off.

According to equation (12) and (14), with approximation $\alpha_s \approx \epsilon\alpha_l$, the relative permeability of the plate can be solved by

$$\widetilde{\mu}_r = \frac{\omega_c \mu_0 \sigma}{{\alpha_l}^2 \epsilon^2} \tag{15}$$

3) Initial guess of plate thickness: The initial guess of plate thickness is obtained from the low-frequency inductance with phase function simplification.

Through some mathematical derivation [15], the phase function can be written as

$$\phi(\alpha, \omega) = \frac{\alpha^2 {\mu_r}^2 - \alpha^2}{\left[\alpha\mu_r \tanh\left(\frac{\alpha_1 c}{2}\right) + \alpha_1\right]\left[\alpha_i \mu_r \coth\left(\frac{\alpha_1 c}{2}\right) + \alpha_1\right]} \tag{16}$$

Employing the variable transform, $\xi = -j\alpha_1 c/2$ and $\lambda = 2/(\alpha\mu_r c)$, the phase function becomes

$$\phi(\alpha, \omega) = \frac{1 + \xi^2\lambda^2}{1 + \xi\lambda(\cot\xi - \tan\xi) - \xi^2\lambda^2} \tag{17}$$

According to equation (7), for low excitation frequency ω_l, the phase function can be calculated by

$$\begin{aligned} \phi(\alpha_s, \omega_l) &= \Delta L(\omega_l) / \int_0^{\infty} K(\alpha, l) d\alpha \\ &\approx \Delta L(\omega_l) / \int_0^{\alpha_h} K(\alpha, l) d\alpha \end{aligned} \tag{18}$$

In equation (17), the function $\cot\xi - \tan\xi$ can be expressed by a function of ϕ,

$$\begin{aligned} \cot\xi - \tan\xi &= f(\phi) \\ &= \frac{\frac{1+\xi^2\lambda^2}{\phi(\alpha_s, \omega_l)} + \xi^2\lambda^2 - 1}{\xi\lambda} \end{aligned} \tag{19}$$

According to the relationship $\cot\xi - \tan\xi = 1/\tan\xi - \tan\xi$, $\tan\xi$ can be solved by adopting the positive real root of equation (20).

$$\tan^2\xi + \tan\xi f(\phi) - 1 = 0 \tag{20}$$

Subsequently, the thickness of plate can be calculated by

$$\begin{aligned} c &= \frac{2\arctan(\tan\xi)}{-j\sqrt{{\alpha_s}^2 + j\mu_0\mu_r\sigma}} \\ &\approx \frac{2\arctan(\tan\xi)}{-j\sqrt{\epsilon^2{\alpha_l}^2 + j\mu_0\mu_r\sigma}} \end{aligned} \tag{21}$$

From the simplified analytical model, the approximate plate thickness, permeability and probe lift-off can be obtained, while the introduced approximation limits the accuracy.

B. Optimisation of plate properties

The modified Newton-Raphson method is applied to accurately estimate the plate properties with the calculated initial guesses. The objective function of optimisation is

$$\min_{\mathbf{v}} \mathcal{L} = \|\Delta\mathbf{L}(\mathbf{v}) - \mathbf{\Delta L}_{\mathrm{m}}\|_2^2 \tag{22}$$

where $\Delta\mathbf{L}(\mathbf{v})$ is the inductance spectrum of variable $\mathbf{v} = [c, \mu_r, l]^{\mathrm{T}}$ calculated by the Dodd and Deeds analytical model, $\Delta\mathbf{L}_{\mathrm{m}}$ is the measured or simulated spectrum, $\|\cdot\|_2^2$ represents the ℓ_2-norm.

According to the modified Newton-Raphson method [12], the variables can be optimised iteratively by

$$\begin{aligned} \mathbf{v}^{k+1} &= \mathbf{v}^k + \Delta\mathbf{v} \\ \Delta\mathbf{v} &= -[(\mathbf{S}^k)^{\mathrm{H}}\mathbf{S}^k]^{-1}(\mathbf{S}^k)^{\mathrm{H}}(\Delta\mathbf{L}^k - \Delta\mathbf{L}_{\mathrm{m}}) \end{aligned} \tag{23}$$

where $\mathbf{S} = \left[\begin{array}{ccc} \partial\Delta\mathbf{L}/\partial c & \partial\Delta\mathbf{L}/\partial\mu_r & \partial\Delta\mathbf{L}/\partial l \end{array}\right] \in \mathbb{C}^{3\times3}$ is the sensitivity matrix, $\mathbf{L} = \left[\begin{array}{ccc} \Delta L(\omega_l) & \Delta L(\omega_m) & \Delta L(\omega_h) \end{array}\right]^{\mathrm{T}}$, k indicates the current iterative step, and the superscript H represents the Hermitian transpose.

To stabilise the optimisation, a regularisation strategy is applied to the Hessian matrix, *i.e.* $(\mathbf{S}^k)^{\mathrm{H}}\mathbf{S}^k = \mathbf{U\Sigma V}^{\mathrm{H}} \approx \mathbf{U\Sigma}^*\mathbf{V}^{\mathrm{H}}$, where $\Sigma^* = \mathrm{diag}(\Sigma_{11}, \Sigma_{22} + s_\mu\Sigma_{11}, \Sigma_{33} + s_l\Sigma_{22})$. Σ_{11}, Σ_{22} and Σ_{33} are singular values of the original Hessian matrix, s_μ and s_l are regularisation parameters to be determined.

To avoid the divergence of optimisation, the limitation of variables is employed as $\min\left\{\max\left\{c^k, \underline{c}\right\}, \overline{c}\right\}$, $\min\{\max\{\mu_r{}^k, \underline{\mu_r}\}, \overline{\mu_r}\}$ and $\min\left\{\max\left\{l^k, \underline{l}\right\}, \overline{l}\right\}$ where $\underline{c}$ and $\overline{c}$ represent the lower and upper limits of possible thickness, respectively.

The optimisation process is summarised and illustrated in Algorithm 1.

III. Results and Discussions

A. Numerical simulations

In the numerical simulation, the estimation of plate properties is evaluated quantitatively, on a PC with CPU AMD Ryzen 7 5800H 3.2 GHz and RAM 32 GB. Details of measurement configuration are shown in Table I.

In the numerical simulation, the coil inductance spectra are calculated by employing the Dodd and Deeds analytical model. For implementation, the discrete spatial frequencies

Algorithm 1 Optimisation of plate properties

Input: $\mathbf{v}^1 = [\tilde{c}, \tilde{\mu}_r, \tilde{l}]^{\mathrm{T}}$, ϵ_o and q_i
Output: $\mathbf{v} = [\hat{c}, \hat{\mu}_r, \hat{l}]^{\mathrm{T}}$
initialize: Set $\Delta\mathbf{L}^1 = \Delta\mathbf{L}(\mathbf{v}^1)$
for $k = 1, 2, ..., q_i$ **do**
  $\mathbf{S}^k = \partial\Delta\mathbf{L}^k/\partial\mathbf{v}^k$
  $\mathbf{v}^{k+1} = \mathbf{v}^k - [(\mathbf{S}^k)^{\mathrm{H}}\mathbf{S}^k]^{-1}(\mathbf{S}^k)^{\mathrm{H}}(\Delta\mathbf{L}^k - \Delta\mathbf{L}_{\mathrm{m}})$
  $\Delta\mathbf{L}^{k+1} = \Delta\mathbf{L}(\mathbf{v}^{k+1})$
  if $\left\|\Delta\mathbf{L}^{k+1} - \Delta\mathbf{L}_{\mathrm{m}}\right\|_2^2 \leq \epsilon_o$ **then**
    Break;
  end if
end for

TABLE I
PARAMETERS OF MEASUREMENT SETUP

Parameters	Value
Inner coil radius r_1 (mm)	19
Outer coil radius r_2 (mm)	19.3
Coil hight $l_2 - l_1$ (mm)	11.5
Coil turns N	30
Probe lift-off l(mm)	1∼40
Conductivity of plate σ (MS/m)	5
Relative permeability of plate μ_r	100∼500
Thickness of plate c (mm)	0.1∼3
Low frequency $\omega_l/(2\pi)$ (kHz)	0.1
Medium frequency $\omega_m/(2\pi)$ (kHz)	1
High frequency $\omega_h/(2\pi)$ (kHz)	100

are employed for numerical integral of inductance calculation, which adopts the roots of $J_1(\alpha_i) = 0$, $i = 1, ..., 500$. The compensating factor k_ϵ in equation (15) and (21) is 13/20.

To evaluate the cylinder property estimation, the properties in the range of $c \in [0.1, 3]$ mm, $\mu_r \in [100, 500]$ and $l \in [1, 40]$ mm are considered. The white Gaussian noise has been applied to the inductance spectra, leading to the equivalent signal-to-noise ratio (SNR) of 60 dB. The relationship between the characteristics of the triple-frequency inductance, *i.e.* Re[$\Delta L(\omega_h)$], ω_c and phase of $\Delta L(\omega_l)$, and estimated properties are shown in Fig. 4. The relative error of the initial cylinder property guess is shown in Table. II, and the error of estimation results is shown in Table III and Table IV. The average computational time for each evaluation point is 23 ms.

The relationship between the inductance characteristics and estimate properties in Fig. 4 shows that the real part of the high-frequency inductance Re[$\Delta L(\omega_h)$] correlates to the lift-off l. The zero-crossing frequency ω_c mainly relies on the plate permeability and lift-off while is less influenced by the thickness in the evaluation range. The phase of the low-frequency inductance $\Phi(\Delta L(\omega_l))$ is affected by the plate thickness, permeability and lift-off. This suggests that the initial guess error of lift-off could affect the error of permeability, and these errors influence the thickness calculation. The relative error of initial guesses in Table. II indicates that the error decreases with the increase of the lift-off. The error of thickness initial guess is relatively higher

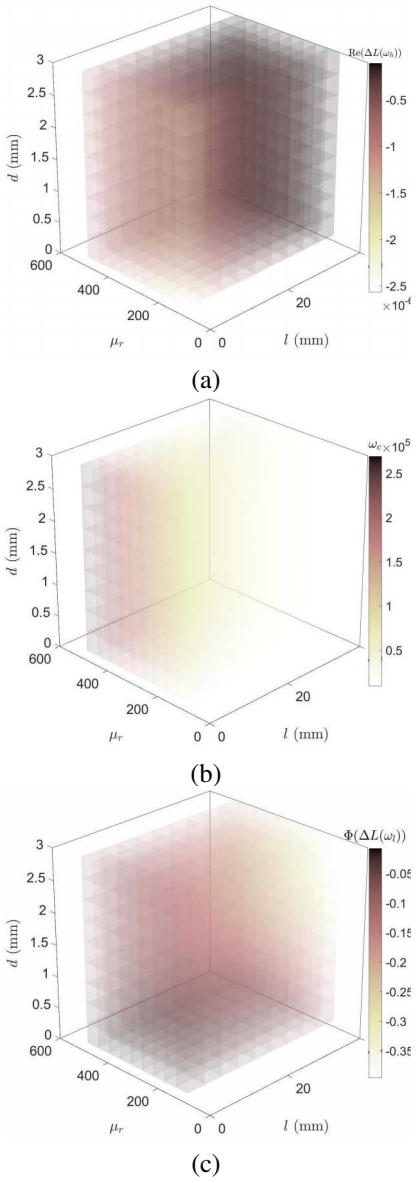

Fig. 4. Illustration of relationship between the inductance characteristics, (a) Re[$\Delta L(\omega_h)$], (b) ω_c and (c) phase of $\Delta L(\omega_l)$, and estimated properties

than permeability and lift-off.

The property estimation results in Table II and III show that the optimisation method can provide results close to the nominal values for most of the evaluation points. There exist several points with large estimation error when average values of properties serve as the initial guesses. In comparison, the proposed method employing the initial guesses from the simplified analytical model attains the relative errors within 0.3 %, 0.01 % and 0.02 % for thickness, permeability and lift-off, respectively.

B. Experiments

The experimental setup is illustrated in Fig. 5. The inductance measuring S275 steel plates is acquired via the Zurich impedance analyser (MFIA), which attains a measurement

TABLE II
RELATIVE ERROR OF INITIAL GUESSES FROM THE SIMPLIFIED ANALYTICAL MODEL

Map of relative error	
Thickness	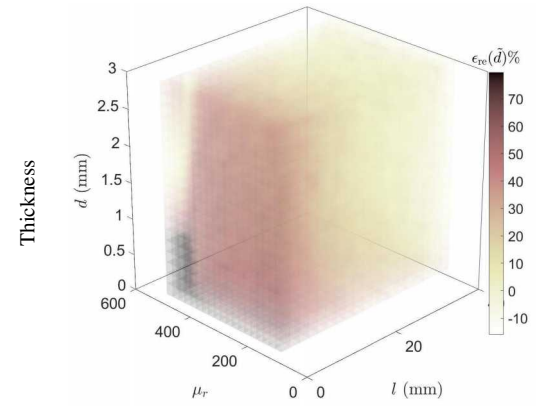
Permeability	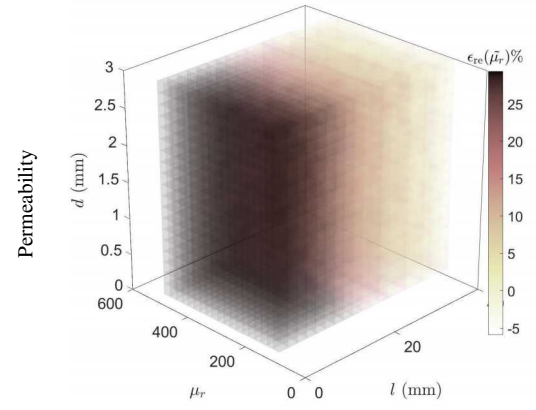
Lift-off	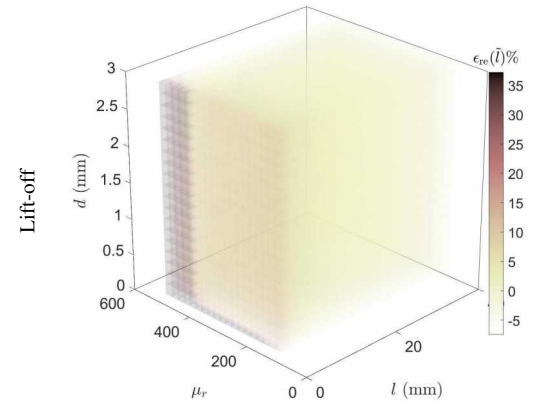

TABLE III
RELATIVE ESTIMATION ERROR WITH THE INITIAL GUESSES OF THE AVERAGE VARIABLE VALUES

Map of relative error	
Thickness	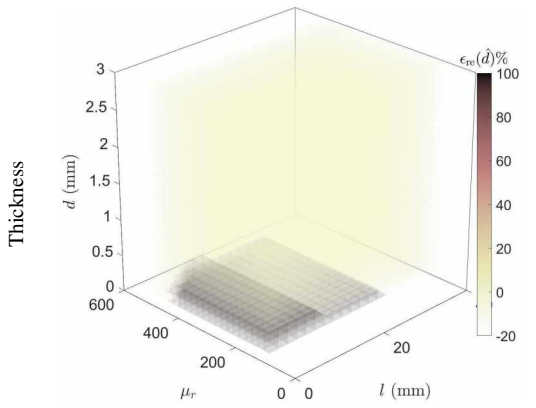
Permeability	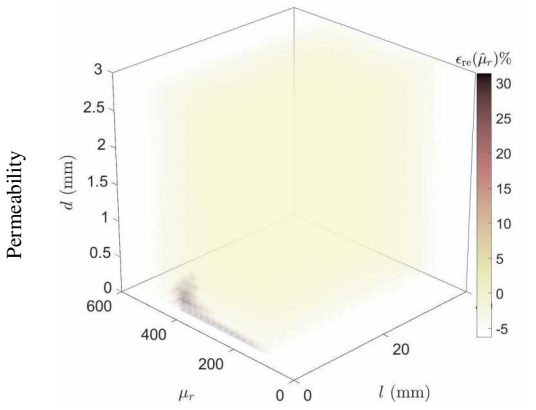
Lift-off	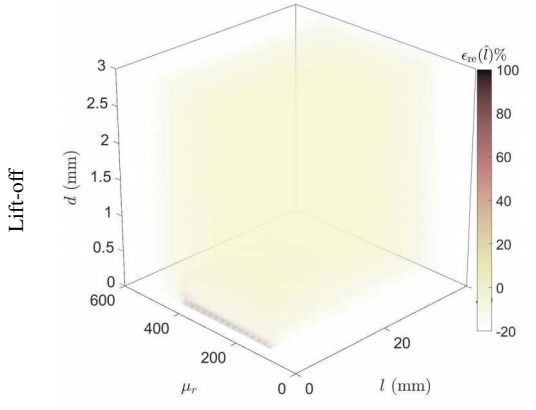

accuracy of 0.05% [16], with thickness ranging from 0.84 mm to 1.7 mm. The excitation frequencies are 0.3 kHz, 1.8 kHz and 59.7 kHz, corresponding to the EC skin-depth in the measured materials of 1 mm, 0.42 mm and 0.07 mm. Lower excitation frequency could be employed for higher plate thickness, while the impedance of the receiving coil is too small to be accurately measured by the instrument. The measured plates are in the length/width of 200 mm and electrical conductivity of 6.7 MS/m, with other properties shown in Table V. The nominal value of relative permeability is obtained by evaluating the squared Euclidean distance between the calculated and measured inductance spectra, *i.e.* $\min_{\mu_r} \left\{ \|\Delta\mathbf{L}(\mu_r) - \Delta\mathbf{L}_{\mathrm{m}}\|_2^2 \right\}$, $\mu_r \in [1, 2, ..., 300]$. In addition, probe dimensions and parameters of the applied algorithm is identical to the counterparts in numerical simulations.

The comparison of the measured and calculated inductance using the analytical model is shown in Fig. V, which generally matches well. The discrepancy between measurement and calculation is relatively higher at the frequency

TABLE IV
RELATIVE ESTIMATION ERROR WITH THE INITIAL GUESSES FROM THE SIMPLIFIED ANALYTICAL MODEL

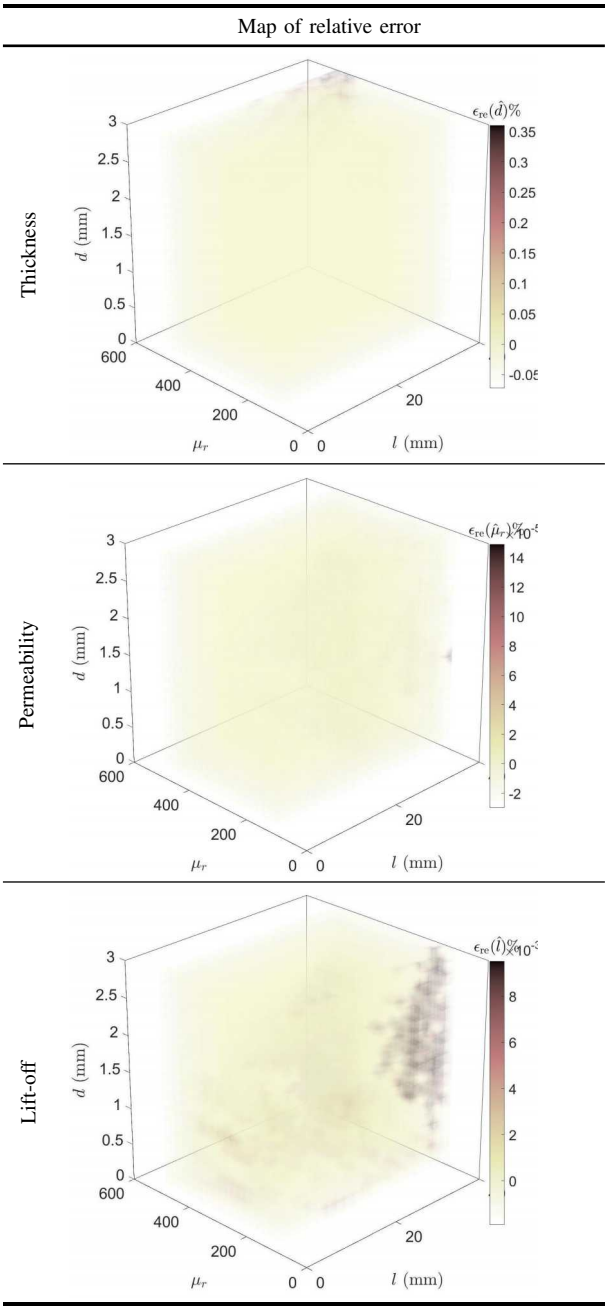

of 0.3 kHz, mainly due to the low coil impedance. For various plate thickness, the phase of inductance is different at the frequency of 0.3 kHz, and becomes closer at the frequency of 1.8 kHz and 59.7 kHz, because of the similar electromagnetic properties. The inductance is insensitive to the thickness at the middle and high frequencies. For various probe lift-off, the amplitude of inductance varies while the phase is close.

The estimation results of the properties of the plates are shown in Table V, in which the estimation is close to the nominal values. Specifically, the largest estimation errors

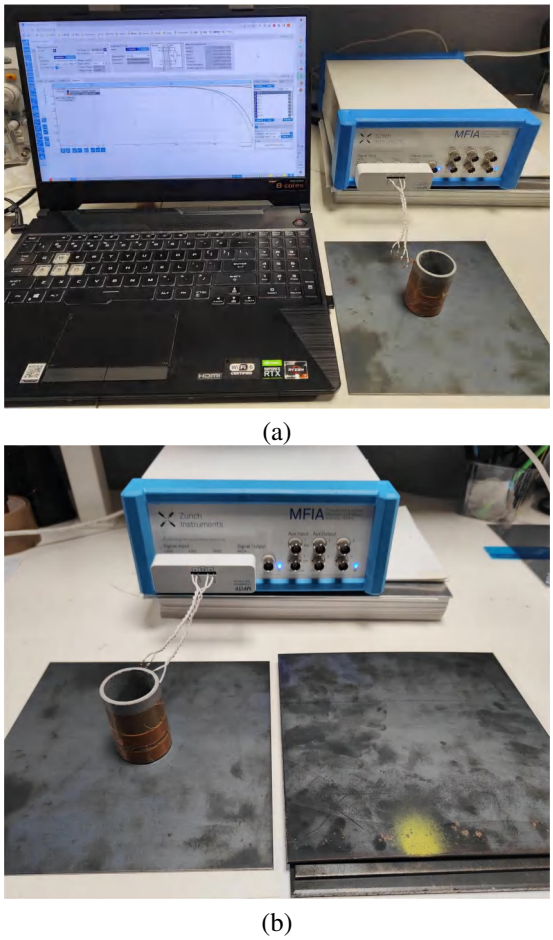

Fig. 5. Experimental setup. (a) measurement device and (b) test pieces

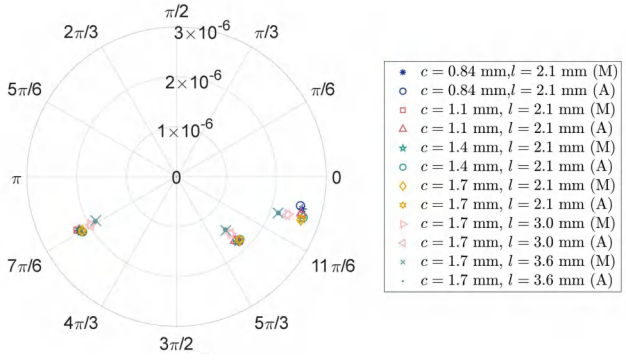

Fig. 6. Experimental inductance of plates in Table V. M and A indicate measurements and analytical solutions, and c and l are plate thickness and probe lift-off, respectively.

of thickness, permeability and lift-off are 7.05 %, 6.89 % and 9.26 %, respectively. Compared with the numerical simulation, the estimation error in experiments is relatively higher, which is mainly caused by the following factors. The plates are in finite size and the permeability of S275 plate which is not homogenous is difficult to be determined accurately. The relatively thinner plates are not strictly flat, which influences the distribution of eddy-current in plates.

TABLE V
ESTIMATION RESULTS IN EXPERIMENT

#	1	2	3	4	5	6
$c\ (mm)$ [1]	0.84	1.1	1.4	1.7	1.7	1.7
$\hat{c}$ (mm)	0.88	1.16	1.30	1.69	1.71	1.77
$\varepsilon_{\mathrm{re}}(\hat{c})$ [2]	4.34%	5.65%	7.05%	0.68%	0.81%	3.94%
μ_r [1]	120	115	128	121	121	121
$\hat{\mu}_r$	119.49	114.84	119.18	123.94	124.89	125.81
$\varepsilon_{\mathrm{re}}(\hat{\mu}_r)$ [2]	0.42%	0.14%	6.89%	2.43%	3.21%	3.98%
$l\ (mm)$ [1]	2.1	2.1	2.1	2.1	3.0	3.6
$\hat{l}$ (mm)	1.91	1.93	2.08	2.07	2.98	3.61
$\varepsilon_{\mathrm{re}}(\hat{l})$ [2]	9.26%	8.07%	0.91%	0.34%	0.65%	0.03%

[1] c, μ_r and l are nominal values of plate thickness, relative permeability and lift-off, respectively

[2] $\varepsilon_{\mathrm{re}}(\hat{c})$, $\varepsilon_{\mathrm{re}}(\hat{\mu}_r)$ and $\varepsilon_{\mathrm{re}}(\hat{l})$ are relative error of corresponding estimation

IV. CONCLUSIONS

This study proposes an estimation method of plate thickness and permeability with probe lift-off. The method calculates the initial guesses of the estimated properties according to the simplified analytical model and further optimises them through the optimisation approach. The estimation only requires three inductance measurements, at the low, medium and high frequencies, for thickness, permeability and lift-off estimation, respectively. In numerical simulations, the accuracy of the estimation method has been comprehensively evaluated for various plate properties. The proposed method can alleviate the influence of the local minimum on property estimation. In the experiment, the S275 plate samples in various thickness are measured and the proposed method achieves the relative estimation accuracy of 8 % and 7 % for thickness and permeability, respectively.

REFERENCES

[1] C. V. Dodd and W. E. Deeds, "Analytical solutions to eddy-current probe-coil problems," *Journal of Applied Physics*, vol. 39, no. 6, pp. 2829–2838, 1968.

[2] D. Wu, F. Yang, X. Wang, and T. He, "Impedance calculation of arbitrary-shaped thin-walled coils for eddy-current testing of planar media," *Sensors and Actuators A: Physical*, vol. 279, pp. 537–542, 2018.

[3] T. Theodoulidis and E. Kriezis, *Eddy Current Canonical Problems (with Applications to Nondestructive Evaluation)*, ser. Contemporary research on emerging science and technology. Tech Science Press, 2006.

[4] W. Zhu, W. Yin, A. Peyton, and H. Ploegaert, "Modelling and experimental study of an electromagnetic sensor with an h-shaped ferrite core used for monitoring the hot transformation of steel in an industrial environment," *Ndt & E International*, vol. 44, no. 7, pp. 547–552, 2011.

[5] M. Lu, L. Yin, A. J. Peyton, and W. Yin, "A novel compensation algorithm for thickness measurement immune to lift-off variations using eddy current method," *IEEE Transactions on Instrumentation and Measurement*, vol. 65, no. 12, pp. 2773–2779, 2016.

[6] X. Meng, M. Lu, W. Yin, A. Bennecer, and K. J. Kirk, "Inversion of lift-off distance and thickness for nonmagnetic metal using eddy current testing," *IEEE Transactions on Instrumentation and Measurement*, vol. 70, pp. 1–8, 2020.

[7] W. Cheng, "Thickness measurement of metal plates using swept-frequency eddy current testing and impedance normalization," *IEEE Sensors Journal*, vol. 17, no. 14, pp. 4558–4569, 2017.

[8] X. Chen and X. Liu, "Pulsed eddy current-based method for electromagnetic parameters of ferromagnetic materials," *IEEE Sensors Journal*, vol. 21, no. 5, pp. 6376–6383, 2021.

[9] M. Lu, Y. Xie, W. Zhu, A. Peyton, and W. Yin, "Determination of the magnetic permeability, electrical conductivity, and thickness of ferrite metallic plates using a multifrequency electromagnetic sensing system," *IEEE Transactions on Industrial Informatics*, vol. 15, no. 7, pp. 4111–4119, 2019.

[10] D. Vasić and V. Bilas, "Lumped representation in inductive measurement of metal casing properties," in *2010 IEEE Instrumentation Measurement Technology Conference Proceedings*, 2010, pp. 841–844.

[11] J. Martin, L. C. Wilcox, C. Burstedde, and O. Ghattas, "A stochastic newton mcmc method for large-scale statistical inverse problems with application to seismic inversion," *SIAM Journal on Scientific Computing*, vol. 34, no. 3, pp. A1460–A1487, 2012.

[12] Z. Xia, J. Yan, R. Huang, M. Lu, Z. Cui, A. Peyton, W. Yin, and W. Yang, "Fast estimation of metallic pipe properties using simplified analytical solution in eddy-current testing," *IEEE Transactions on Instrumentation and Measurement*, vol. 72, pp. 1–13, 2023.

[13] W. Yin and K. Xu, "A novel triple-coil electromagnetic sensor for thickness measurement immune to lift-off variations," *IEEE Transactions on Instrumentation and Measurement*, vol. 65, no. 1, pp. 164–169, 2016.

[14] W. Yin, X. Hao, A. Peyton, M. Strangwood, and C. Davis, "Measurement of permeability and ferrite/austenite phase fraction using a multi-frequency electromagnetic sensor," *NDT & E International*, vol. 42, no. 1, pp. 64–68, 2009.

[15] T. Theodoulidis, "Developments in calculating the transient eddy-current response from a conductive plate," *IEEE Transactions on magnetics*, vol. 44, no. 7, pp. 1894–1896, 2008.

[16] "MFIA 5MHz impedance analyzer and precision lcr meter," https://www.zhinst.com/sites/default/files/documents/2021-12/zi_mfia_leaflet_latest.pdf., accessed on: Apr. 4, 2022. [Online].

10. Through Thickness Inspection of Layered Magnetic Material Using Pulsed Eddy Current Testing

Through Thickness Inspection of Layered Magnetic Material Using Pulsed Eddy Current Testing

Lei Xiong, Zihan Xia, Ruochen Huang*, *Member, IEEE*, Shupei Wang, Xinnan Zheng, Jialong Shen, Xiaochu Pang, and Wuliang Yin, *Senior Member, IEEE*

***Abstract*—Steel microstructure determines the mechanical properties of steel such as hardness and tensile strength. To monitor steel microstructure evolution during thermal processing such as hot rolling, online measurement of microstructure is vital to steel quality control. Previous studies using multi-frequency eddy-current testing to monitor the change of electromagnetic properties and infer steel microstructures have achieved remarkable success, yet due to the high-frequency excitation signal, the inspected thickness of steel microstructures is constrained on the surface due to the skin effect. This study introduces the pulsed eddy-current (PEC) method to characterise the electromagnetic property profile along the depth of thick steel plates. The low-frequency square wave signal enables PEC to reflect multi-layer characteristics in a single measurement with good penetration ability. An explicit analytical equation for calculating the time domain PEC response is derived for the first time which shows advantages in terms of speed and gaining in-depth physical insights. A custom PEC system has been designed and built with a TMR sensor as the receiver. Theoretical and numerical analysis are performed. A time domain intersection point on the Tau curve is found to be a useful indication of the properties of a planar structure. Experimental results on layered planar structures of various electromagnetic properties are analysed and validated.**

***Index Terms*—Pulsed eddy-current testing, thickness inspection, steel microstructure**

I. Introduction

The production of steels with dual or multi-phase microstructures by direct rolling and cooling requires accurate process control. It is of great significance to analyse the microstructures of plates in various depths to guarantee the uniformity of the mechanical properties of steel [1, 2, 3]. The electromagnetic properties, *i.e.* electrical conductivity and permeability, are closely related to the microstructure of the steels [4, 5]. The effective medium approximation (EMA) theory bridges the gaps between the ferrite fraction and electromagnetic properties [6, 7]. The characteristic variations of effective electromagnetic properties can be tested and evaluated by non-destructive testing (NDT) methods, *e.g.* magnetic Barkhausen noise analysis (MBNA) [8, 9, 10]. The EMA theory indicates that electromagnetic properties reflect the steel plate ferrite fraction and the eddy-current testing method could be explored to measure the plate properties along the plate depth.

The pulsed eddy-current (PEC) technique, which features wide frequency spectrum and high sensitivity to conductivity and permeability of metals in high thickness, has been intensively studied for decades and improves the detection of multi-layer characteristics [11, 12, 13, 14]. The technique can overcome the high lift-off of probes and is suitable for inspection under thick insulation. J. Sha *et al.* studied the principal component analysis of the microstructure of heat-treated bearing rings using the PEC technique and realize 90% accuracy in classifying samples by summation features [15]. K. Rao *et al.* realized subsurface flaws detection in stainless steel using a high-sensitivity PEC system [16]. X. Chen *et al.* investigates the electrical conductivity and permeability measurement for ferromagnetic materials by optimizing the least squares problem [17]. Furthermore, great efforts have been made to explore the analytical model of PEC. F. Fu and J. Bowler proposed to solve the time domain response of eddy-current signal from the frequency spectrum through the inverse Laplace transform and derived the approximating form for conductive half-space [18]. T. Theodoulidis introduced the residue theorem to calculate the complex integral with numerical solutions of poles, improving the efficiency of the inverse Laplace transform, and analysed the response of exponential current excitation employing convolution [19]. D. Desjardins *et al.* studied the PEC testing of metallic rods with coaxial driver and pickup coil. The analytical solutions of coil current match well with measurements [20], by incorporating all electromagnetic interactions. In addition, through the Laplace transform of coil current signals, it was revealed that the permeability and conductivity of metallic rods can be inverted separately from the signals [21]. The time domain signal can also be calculated through the inverse Fourier transform which can be realized through the inverse fast Fourier transform (IFFT) in software packages, *e.g.* MATLAB and Mathematica. G. Tian *et al.* derived the time domain analytical solution of

Manuscript updated June 11, 2023, and submitted xxx xx, 2021.

Mr. Lei Xiong, Mr. Zihan Xia, Mr. Xinnan Zheng, Mr. Jialong Shen, Mr. Xiaochu Pang and Dr. Wuliang Yin are with the School of Electrical and Electronic Engineering, University of Manchester, Manchester M13 9PL, U.K.

Dr. Shupei Wang is with the MAIERIC Ltd, Manchester, UK, M15 6SZ;

Dr. Ruochen Huang is with the College of Electrical Engineering and Automation, Fuzhou University, Fuzhou 350108, China. (*Corresponding author: Ruochen Huang. email: ruochen_huang@fzu.edu.cn*)

magnetic field sensor and analysed the eddy-current signal of multi-layer plates [22].

Based on the fact that the receiving signal in the time domain reflects the eddy-current diffusion in various depths of the measured plates, we propose using the PEC technique to inspect the microstructure along the depth of thick steel plates in either online manufacturing process or off-line applications. This study derives the analytical solution of the PEC signal received by a magnetic field sensor through the inverse Laplace transform which is calculated by the residue theorem. With the approximation of poles in the complex plane, the solution achieves an explicit analytical form. The relationship between the plate properties and rate of eddy-current diffusion has been proposed for the analysis of effective electromagnetic properties in steel plates. Furthermore, a PEC system has been developed to measure the steel plates and evaluate microstructures. Numerical simulations have been performed to evaluate the accuracy and speed of the proposed analytical model. In addition, experiments are carried out with the stacked S275 and S355 mild steel plates, in which the receiving signal can characterize the variation of material electromagnetic properties along the plate depth.

The rest of the paper is arranged as follows: In Section II, we describe the analytical model calculating the magnetic field signal and derive the relationship between the rate of signal rising/decay and plate properties; In Section III, we illustrate the details of a custom-designed PEC system including the architecture, probe and applied excitation signal; In Section IV, we provide the numerical simulation and experiments evaluating the proposed analytical model and developed system then discuss the phenomenon of receiving signal regarding various plate properties.

II. Theoretical Analysis of PEC

The diffusion equation for the magnetic inductance is

$$\nabla^2 \mathbf{B} = \mu_0 \mu_r \sigma \frac{\partial \mathbf{B}}{\partial t} \tag{1}$$

The equation also holds for magnetic vector potential $\mathbf{A}$ and electric field $\mathbf{E}$. The form of the diffusion equation provides an estimation for diffusion time τ_D of an initial configuration of the electromagnetic field with typical spatial variation defined by the characteristic length l of metallic materials which is the thickness of plates with large radial dimensions. One can put $\nabla^2 \mathbf{B} = O(\mathbf{B}/l^2)$ and $\partial \mathbf{B}/\partial t = O(\mathbf{B}/\tau_D)$, then $\tau_D = O(\mu_0 \mu_r \sigma l^2)$ [23, 24, 25].

The time domain receiving signal of magnetic field sensors is derived through the Laplace transform and the long-time signal decaying rate which corresponds to the diffusion time is investigated as follows.

The receiving signal of magnetic field sensors, tunnel magneto-resistance (TMR) sensor here, in the frequency domain measuring a single-layer plate can be formulated as [19, 26],

$$B_z(\omega) = \sum_{\alpha_i} K(\alpha_i) \left[1 + e^{-\alpha_i (c_1 + c_2)} \phi(\alpha_i, \omega)\right] i_0(\omega) \tag{2}$$

$$K(\alpha_i) = \frac{2\mu_0}{r_0 (c_2 - c_1)} \frac{J(r_2, r_1) J_1(\alpha_i r_0)}{{\alpha_i}^5 [b J_0(\alpha_i b)]} \times \left(e^{\alpha_i c_2} - e^{\alpha_i c_1}\right) \left(e^{-\alpha_i z_1} - e^{-\alpha_i z_2}\right) \tag{3}$$

$$\phi(\alpha_i, \omega) = \frac{(\alpha_1 + \mu_r \alpha_i)(\alpha_1 - \mu_r \alpha_i) - (\alpha_1 + \mu_r \alpha_i)(\alpha_1 - \mu_r \alpha_i) e^{2\alpha_1 d}}{-(\alpha_1 - \mu_r \alpha_i)(\alpha_1 - \mu_r \alpha_i) + (\alpha_1 + \mu_r \alpha_i)(\alpha_1 + \mu_r \alpha_i) e^{2\alpha_1 d}} = \frac{\alpha_i^2 {\mu_r}^2 - \alpha_1^2}{\left[\alpha_i \mu_r \tanh\left(\frac{\alpha_1 d}{2}\right) + \alpha_1\right] \left[\alpha_i \mu_r \coth\left(\frac{\alpha_1 d}{2}\right) + \alpha_1\right]} = \frac{\Gamma_1}{\Gamma_2} \tag{4}$$

$$i_0(t) = I_0 (1 - e^{-t/\tau}) u(t) \tag{5}$$

where $J(r_2, r_1) = \int_{\alpha r_1}^{\alpha r_2} \alpha r J_1(\alpha r) \alpha r$, $J_1(\alpha r)$ is the Bessel function of the first kind, $\alpha_1 = \sqrt{\alpha_i^2 + j\omega\mu_r\mu_0\sigma}$, α_i indicates a spatial frequency of the cylindrical harmonics, $i_0(t)$ is the excitation signal applied to the transmitting coil, $i_0(\omega) = F[i_0(t)]$ is the applied signal in the frequency domain, $u(t)$ is the step function, I_0 is the signal magnitude, τ is the time constant depending on the transmitting coil, and other dimensions are shown in Fig. 1.

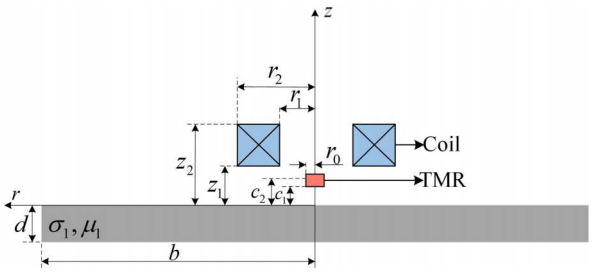

Fig. 1. Metallic plate measured by a transmitting coil and TMR sensor which is simplified as a small cylinder

The above time domain solution can be achieved through the inverse Fourier transform, however, the computation process is relatively time consuming and the formula is not explicit to provide physical insights. A Laplace inverse solution is derived as follows: Letting $s = j\omega$, equation (2) can be rewritten by the counterpart in the complex plane by

$$B_z(s) = \sum_{\alpha_i} K(\alpha_i) \left[1 + e^{-\alpha_i (c_1 + c_2)} \phi(\alpha_i, s)\right] i_0(s) \tag{6}$$

The receiving signal in the time domain can be obtained through the inverse Laplace transform,

$$\begin{aligned} B_z(t) &= L^{-1}[B_z(s)] \\ &= B_{z0}(t) + \sum_{\alpha_i} K(\alpha_i) e^{-\alpha_i (c_1 + c_2)} L^{-1}[\phi(\alpha_i, s) i_0(s)] \\ &= B_{z0}(t) + \sum_{\alpha_i} K(\alpha_i) e^{-\alpha_i (c_1 + c_2)} [B_{z\phi_u}(t) - B_{z\phi_e}(t)] I_0 \end{aligned} \tag{7}$$

$$B_{z0}(t) = \sum_{\alpha_i} K(\alpha_i) i_0(t) \tag{8}$$

$$B_{z\phi_u}(t) = L^{-1}\left[\phi(\alpha_i, s)/s\right] \tag{9}$$

$$B_{z\phi_e}(t) = L^{-1}\left[\phi(\alpha_i, s)\right] * \left[e^{-t/\tau}u(t)\right] \tag{10}$$

The inverse Laplace transform can be calculated employing the residue theorem, which leads to

$$B_{z\phi_u}(t) = \sum_{s_{t,c,0}} \mathrm{Res}\left[\phi(\alpha_i, s)/s, s_{t,c,0}\right] \tag{11}$$

$$B_{z\phi_e}(t) = \left\{\sum_{s_{t,c}} \mathrm{Res}\left[\phi(\alpha_i, s), s_{t,c}\right]\right\} * \left[e^{-t/\tau}u(t)\right] \tag{12}$$

where $s_0 = 0$, s_t and s_c are poles of $\phi(\alpha_i, s)$, *i.e.* roots of equation (13) and (14), respectively.

$$\alpha_i \mu_r \tanh(\alpha_1 d/2) + \alpha_1 = 0 \tag{13}$$

$$\alpha_i \mu_r \coth(\alpha_1 d/2) + \alpha_1 = 0 \tag{14}$$

The residue of $\phi(\alpha_i, s)$ is calculated by

$$\mathrm{Res}\left[\phi(\alpha_i, s), s_{t,c}\right] = \frac{\Gamma_1\big|_{s=s_{t,c}}}{\partial\Gamma_2/\partial s\big|_{s=s_{t,c}}} \tag{15}$$

In this way, function $B_{z\phi_u}(t)$ and $B_{z\phi_e}(t)$ can be calculated by

$$B_{z\phi_u}(t) = \phi(\alpha_i, s=0) + \sum_{s_t} A_t e^{s_t t}/s_t + \sum_{s_c} A_c e^{s_c t}/s_c \tag{16}$$

$$B_{z\phi_e}(t) = \left(\sum_{s_t} A_t e^{s_t t} + \sum_{s_c} A_c e^{s_c t}\right) * \left[e^{-t/\tau}u(t)\right] \tag{17}$$

The factors A_t and A_c in equation (16) and (17) are

$$\begin{cases} A_t = -\dfrac{1+(\xi_t\lambda)^2}{\left[\cot(\xi_t) - \lambda\xi_t\right]\left[\lambda + \sec^2(\xi_t)\right]} \dfrac{2\xi_t}{\mu_r\mu_0\sigma h^2} \\ A_c = \dfrac{1+(\xi_c\lambda)^2}{\left[\tan(\xi_c) + \lambda\xi_c\right]\left[\lambda + \csc^2(\xi_c)\right]} \dfrac{2\xi_c}{\mu_r\mu_0\sigma h^2} \end{cases} \tag{18}$$

where $\xi = -j\sqrt{\alpha^2 + s\mu_0\mu_r\sigma}h$, $h = d/2$ and $\lambda = 1/(\alpha\mu_r h)$.

Because of the variable transform from s to ξ, the poles of $\phi(\alpha_i, \xi)$ are the roots of $\tan(\xi_t) = -\lambda\xi_t$ and $\cot(\xi_c) = \lambda\xi_c$, respectively, of which the distribution is shown in Fig. 16. The values of ξ_t and ξ_c are usually obtained by the numerical method [17, 19], which is a time-consuming process. However, the values can be approximated by applying the Taylor series of Tangent and Cotangent functions, as detailed in Appendix A, leading to

$$\begin{aligned} \xi_t &\approx -2\sqrt{\frac{p}{3}}\sinh\left[\mathrm{arcsinh}\left(\frac{3q_t}{2p}\sqrt{\frac{3}{p}}\right)\right] + n\pi \\ \xi_c &\approx -2\sqrt{\frac{p}{3}}\sinh\left[\mathrm{arcsinh}\left(\frac{3q_c}{2p}\sqrt{\frac{3}{p}}\right)\right] + n\pi - \frac{\pi}{2} \end{aligned} \tag{19}$$

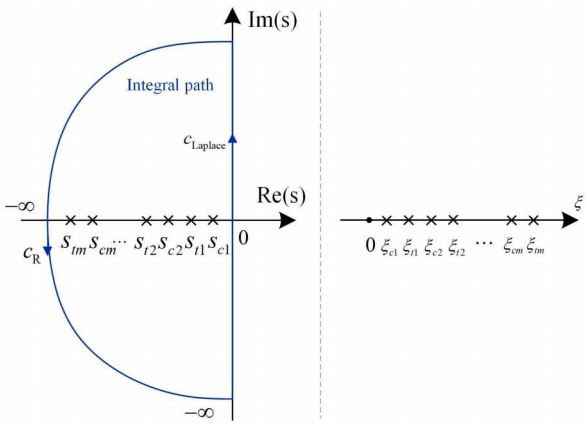

Fig. 2. Distribution of the poles of $\phi(\alpha_i, s)$ and $\phi(\alpha_i, \xi)$

where $p = 3(\lambda+1)$, $q_t = 3\lambda n\pi$, $q_c = 3\lambda(n\pi - \pi/2)$ and $n = 1, ..., m$.

Bring equations (8), (16), (18) and (19) back to (7), a new equation, the explicit analytical expression of receiving signal in the magnetic field sensor, can be obtained by

$$\begin{aligned} B_z(t) &= \sum_{\alpha_i} K(\alpha_i) i_0(t) + \sum_{\alpha_i} K(\alpha_i) I_0 e^{-\alpha_i(c_1+c_2)} \\ &\times \left[\phi(\alpha_i, s=0) + \sum_{s_t} A_t e^{s_t t}/s_t + \sum_{s_c} A_c e^{s_c t}/s_c \right. \\ &\left. - \left(\sum_{s_t} A_t \frac{\left(e^{s_t t} - e^{-t/\tau}\right)}{s_t + 1/\tau} + \sum_{s_c} A_c \frac{\left(e^{s_c t} - e^{-t/\tau}\right)}{s_c + 1/\tau}\right)\right] \end{aligned} \tag{20}$$

As the time constant τ is usually a small value, the rate of signal $B_z(t)$ rising/decay is usually dominated by the term $\sum_{s_t} A_t e^{s_t t}/s_t + \sum_{s_c} A_c e^{s_c t}/s_c$. In the late phase of eddy-current diffusion, as shown in Fig. 3, when the concentration region of eddy-current is adjacent to the centre of the tested plate, the rate of signal rising/decay is mainly determined by the maximum root of s_t and s_c, *i.e.* the root of equation $\cot(\xi_{cp}) = \lambda\xi_{cp}$, $\xi_{cp} \in [0, \pi/2]$. In the scenario of high-permeability thick plate measurement, the condition that $\lambda = 1/(\alpha\mu_r h) \ll 1$ is satisfied. $\lambda\xi_{cp} \ll 1$ because $\xi_{cp} \sim \pi/2$ as shown in Fig 3. This indicates that

$$s_{cp} \approx -\frac{(\xi_{cp}/h)^2 + \alpha^2}{\mu_r\mu_0\sigma} \tag{21}$$

According to equation (21), the rate of signal decay in the late phase of eddy-current diffusion is inversely correlated to the plate properties $\mu_r\sigma$ and thickness.

III. Hardware Design of the PEC System

The hardware architecture of the PEC system is shown in Fig. 4. The system consists of four components, including a detachable probe sensor, an ARM-based microcontroller with support modules, front-end circuits and a host PC. An STM32F4 series micro-controller with a 32-bit ARM Cortex-M4 core is the main processor of the system which

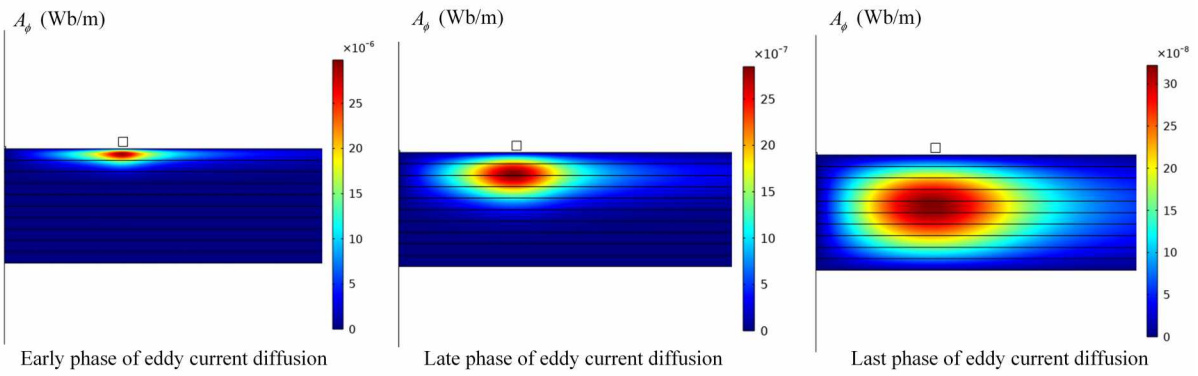

Fig. 3. Eddy-current diffusion process in the measured plate

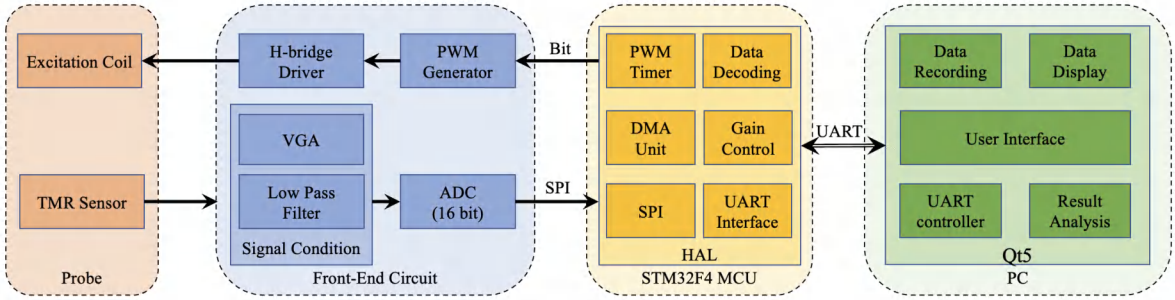

Fig. 4. Block diagram of hardware architecture of the PEC system

takes charge of excitation signal generation, signal acquisition, data processing and board-level communication. The system can excite the coil with the frequency range of 0.1 Hz to 100 Hz and receive the signal at a sample rate of 100 kHz. The front-end circuits are comprised of a pulse width modulation (PWM) signal generator, an H-bridge driver, a 16-bit analogue-to-digital converter (ADC) and signal conditioning circuits with a filter and a variable gain amplifier. The host PC with Qt5 graphical user interface (GUI) software provides real-time data feedback and visualization for result analysis.

In terms of the sensor probe, the excitation coil is connected to an H-bridge driver which amplifies the square wave excitation signal. Instead of using the receiving coil, a TMR sensor is implemented inside the probe to collect the pulsed eddy-current signal as its better performance in low-frequency circumstances and succinct support circuits. The TMR sensor provides a sensitivity of 45 – 65 mV/V/Oe. A low-pass filter and a variable gain amplifier are placed to condition the receiving signal from the TMR sensor and transfer the signal to the ADC for data acquisition. The STM32F4 microcontroller collects the data from the ADC via the serial peripheral interface (SPI) and then transmits it to the host PC via universal asynchronous receiver-transmitter (UART) serial communication. The data transmission speed can reach up to 10 Mbit/s. The related parameters such as excitation signal frequency and amplification gain can be set easily from the GUI. The integrated portable PEC system provides good compatibility for different probe designs and can be used in various applications with different metals, *e.g.* aluminum and ferrite steel.

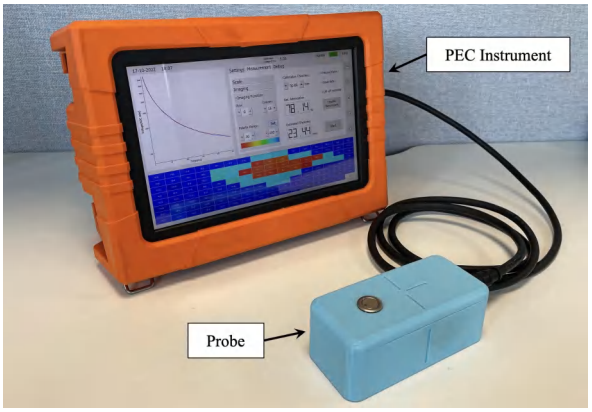

Fig. 5. Picture of the PEC system and the probe

The basic setup of the PEC system and the probe is shown in Fig. 5. The results from the probe can be seen on the display promptly in the form of the measurement curve and surface rendering. The plates can be stacked to simulate the variation of thickness, conductivity and permeability. A probe with a circular coil and TMR sensor is designed, of which the schematic is shown in Fig. 6.

With the excitation amplitude set to 24 V, the ability to penetrate samples is closely related to the excitation

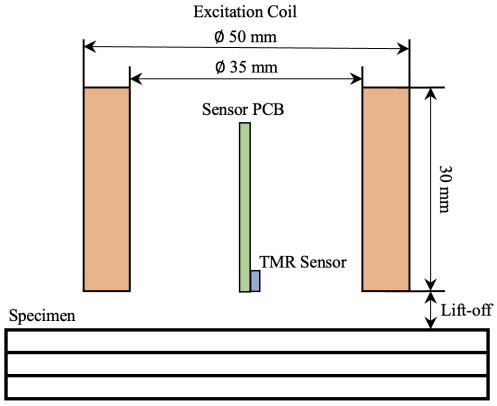

Fig. 6. Schematic and dimensions of the probe

frequency. The skin depth δ of the electromagnetic field of a certain frequency in the tested material is limited by the skin depth effect, which can be described by equation (22). Generally, the lower excitation frequency results in deeper penetration depths.

$$\delta = (\sigma \pi f \mu_r \mu_0)^{-\frac{1}{2}} \tag{22}$$

The performance of the PEC system can be evaluated by the maximum distinguishable thickness. When the test is performed on a certain type of metal, the descending rate of the curve can characterize the thickness of the material. Generally, the thicker sample results in a slower rate of curve decay. The results measuring S355 steel plates with 5 mm probe lift-off are shown in Fig. 7, where the distinguishable thickness is around 25 mm.

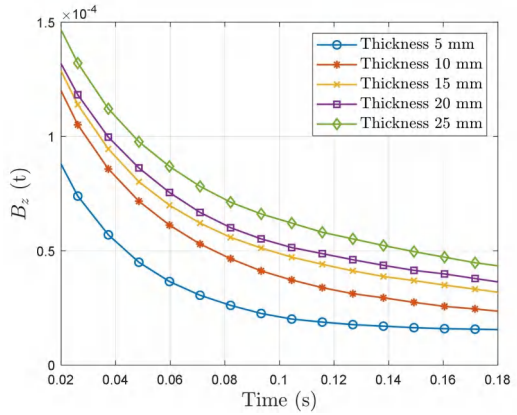

Fig. 7. A-scan results of S355 steel plates from the PEC system

IV. Results and Discussions

A. Numerical simulations

The numerical simulation is performed to evaluate the calculation of the PEC receiving signal and relating phenomenon, which is performed on a PC with CPU AMD Ryzen 7 5800H 3.2 GHz and RAM 32 GB. The parameters of the measurement setup are provided in Table I.

TABLE I
Parameters of Measurement Setup

Parameters	Value
Plate thickness d (mm)	$\{5, 50\}$
Plate electric conductivity σ (MS/m)	$\{10, 60\}$
Plate relative magnetic permeability μ_r (μ_0)	$\{1, 1000\}$
Radius of TMR r_0 (mm)	0.5
Lower dimension of TMR c_1 (mm)	$\{0, 5\}$
Upper dimension of TMR c_2 (mm)	$c_1 + 1$
Inner radius of coil r_1 (mm)	17.5
Outer radius of coil r_2 (mm)	25
Lower dimension of coil z_1 (mm)	c_1
Upper dimension of coil $z_2(mm)$	$c_1 + 30$
Number of coil turns N	400
Amplitude of current excitation I_0 (A)	0.5
Time constant τ (s)	0.0001
Truncated calculation boundary b (mm)	1000

The analytical model is employed to calculate the average magnetic induction intensity in the region of the TMR sensor. The results are compared with FEM solutions constructed in COMSOL, of which the basic model structure is shown in Fig 8. In the FEM model, the radius of plates is 1000 mm, which is much larger than the coil radius and the influence of plate size can be neglected. The average computational time for each of the signal curves adopting the proposed analytical model is 0.68 s, which is faster than 6.76 s employing the method transforming the frequency spectrum to the time domain by the IFFT [27], using 4096 sampling points and 2k spatial frequencies. Various values of plate thickness, conductivity, permeability and probe lift-off are considered in the evaluation. The calculation results of receiving signals are shown in Fig. 9.

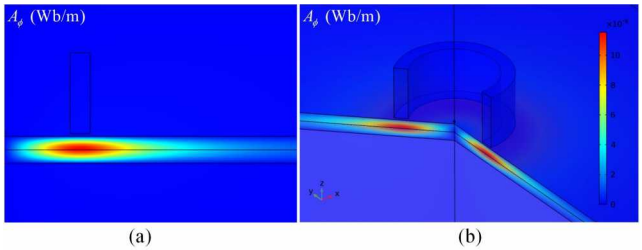

Fig. 8. FEM solution of a double-layer plate in (a) axial cross-sectional view and (b) 3D (rotating) view

The receiving signals in Fig. 9. indicate that the results of the analytical model are close to FEM for different plate properties and probe lift-off. For various plate thicknesses in Fig. 9 (c), the signals are close near the starting point of the curves while in the late phase, the rate of curve decay decreases with the increase of thickness. Because the early phase of eddy-current diffusion of different thickness is similar while the rate of diffusion in the late phase is inversely correlated to the plate thickness. The signal decays slower with the increase of conductivity, permeability and plate thickness. This generally corresponds to the rate of signal decay described by equation (21).

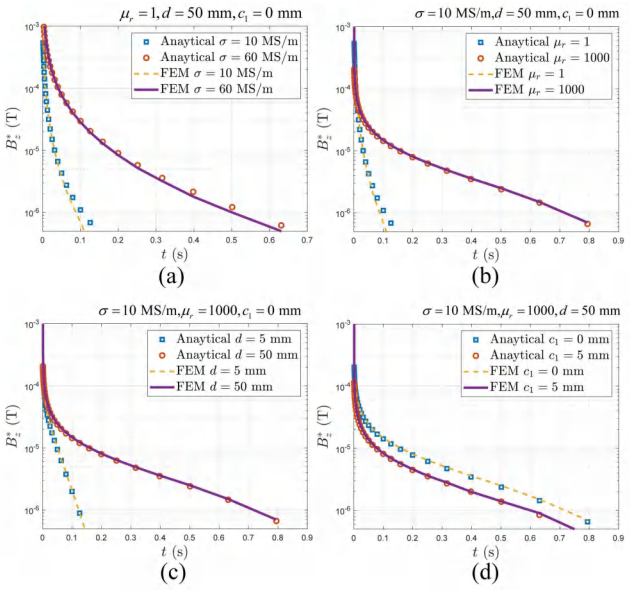

Fig. 9. Receiving signals of TMR sensor obtained from simulation for various (a) plate conductivity, (b) magnetic permeability, (c) thickness and (d) probe lift-off, $B_z^*(t) = \max\{B_z(t)\} - B_z(t)$

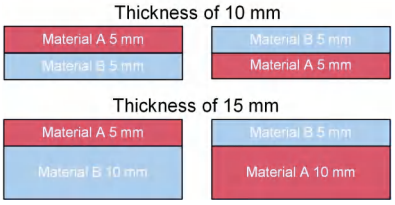

Fig. 10. Double-layer plates of various materials, material A: $\sigma_A = 5$ MS/m, $\mu_{rA} = 500$, material B: $\sigma_B = 4.5$ MS/m, $\mu_{rB} = 550$ ($\sigma_A\mu_{rA} > \sigma_B\mu_{rB}$)

Furthermore, to investigate the relationship between the PEC diffusion and variation of plate properties, the double-layer plates, as shown in Fig. 10, are modelled in FEM. The electrical conductivity and relative magnetic permeability of material A and material B are close to the electromagnetic properties of S275 and S355 steel. The calculation results of the decaying period of signals are shown in Fig. 11. The long-time approximation of the receiving signal takes the form

$$B_z(t) = A_0 e^{-t/\tau_s(t)} \tag{23}$$

where τ_s is calculated by

$$\tau_s(t) = -\left\{\frac{d\ln\left[B_z(t)/A_0\right]}{dt}\right\}^{-1} \tag{24}$$

Noted that τ_s relates to the diffusion time τ_D, reflecting the thickness of plates with large radial dimensions and electromagnetic properties of the eddy-current diffused region.

The results in Fig. 11 indicate that for a certain thickness of double-layer plates, the signals and corresponding rate of decay vary with the electromagnetic properties of the plate along the depth. For double-layer plates with a thickness of

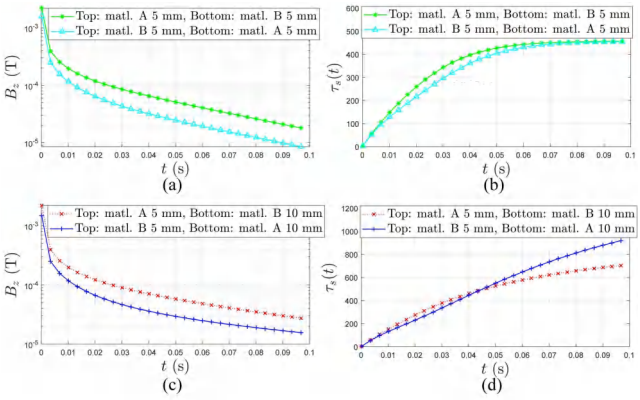

Fig. 11. Receiving signals of TMR sensor obtained from simulation of double-layered plates with thickness of 10 mm, (a) and (b), and thickness of 15 mm, (c) and (d)

10 mm, once material A is on the top layer, $\tau_s(t)$ is higher when $t \in (0.01, 0.06)$ s according to Fig. 11 (b), while $\tau_s(t)$ of two measurement conditions tends to be similar when $t \in (0.07, 0.1)$ s, corresponding to the last phase of eddy-current diffusion shown in Fig. 3. This is consistent with the phenomenon described by equation (21). For double-layer plates with the thickness of 15 mm, in the early phase of measurement when material A is on the top layer the value of $\tau_s(t)$ is larger, and there is an intersection of the signal curves corresponding to the center of eddy-current near the interface of the two materials, as shown in Fig. 12. In the late phase of signals, the value of $\tau_s(t)$ is higher when material A is on the bottom layer. The results imply that when eddy-current is mainly distributed in the material with larger electromagnetic properties of $\sigma\mu_r$, the rate of signal decay and eddy-current diffusion is slower.

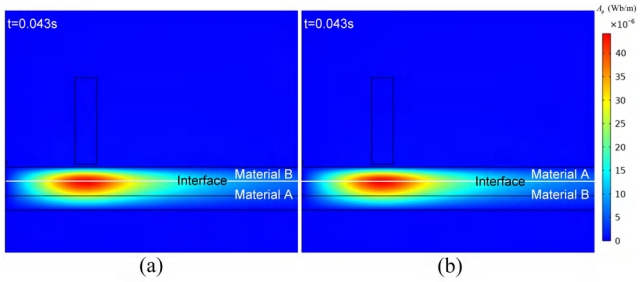

Fig. 12. Eddy-current distribution in the stacked plates at the intersection point in Fig. 11 (d)

B. Experiments

In the experiments, the S355 and S275 mild steel plates are measured by the developed PEC system, to validate the relationship between the PEC signal and plate properties. The frequency of the applied excitation signal to the transmitting coil is 5 Hz.

The plates are stacked in a different order to simulate different microstructure distribution along the depth of the

plates, as shown in Table II. The test pieces of plates are shown in Fig. 13. The measurements from the PEC system are shown in Fig. 14. In addition, for the measurement of stacked plates in the thickness of 10 mm and 15 mm, the $\tau_s(t)$ curve representing the PEC diffusion process is shown in Fig. 15. Before calculating $\tau_s(t)$, the receiving signals are fitted by the exponential function to reduce the influence of measurement noise on calculation, *i.e.*,

$$\widetilde{B}_z(t) = E_a e^{E_b t} + E_c e^{E_d t} \tag{25}$$

where E_a, E_b, E_c and E_d are parameters which can be obtained through the curve-fitting method.

The reason adopting this fitting function is as follows. The long-time approximation of $B_z(t)$ in equation (23) merely adopts one exponential term corresponding to the pole of the phase function $\phi(\alpha_i, s)$ nearest to the center of the complex plane. For a stacked plate of two different materials, the diffusion time τ_D in these materials needs to be considered separately, as the diffusion is affected by various electromagnetic properties along the plate depth. In addition, to approximate the $B_z(t)$ signal covering the short-time region, more exponential terms are necessary to accurately fit the series form of the analytical solutions [23, 24].

TABLE II
COMBINATION OF STACKED PLATES

Top Layer	Bottom Layer
S355 5 mm	S275 5 mm S275 10 mm
S275 5 mm	S355 5 mm S355 10 mm
S355 10 mm	S275 10 mm
S275 10 mm	S355 10 mm

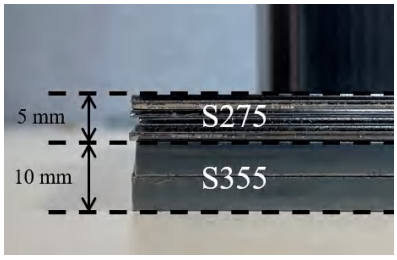

Fig. 13. Test pieces of stacked S355 and S275 mild steel plates

The receiving TMR signal in Fig. 14 indicates that the thickness of stacked plates can be distinguished according to the magnitude of $B_z(t)$ especially when $t \in (0.04, 0.07)$ s. In this period, the eddy-current intensity increases with plate thicknesses. The calculated $\tau_s(t)$ curves in Fig. 15 show that for the stacked plates in the thickness of 10 mm, the rate of eddy-current diffusion is slower in the early phase of measurement when S275 plates are on the top layer while the rate of diffusion tends to be similar in the late phase of measurement as eddy-current tends to be evenly distributed

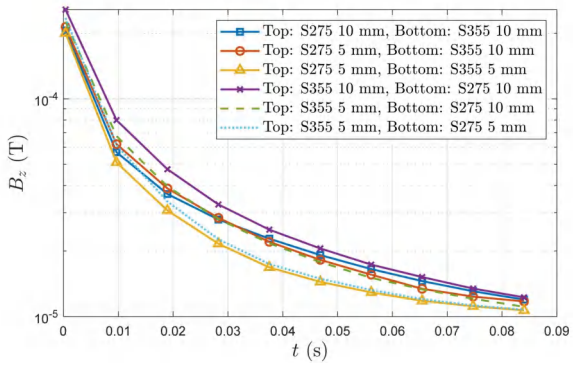

Fig. 14. Experimental receiving signals of TMR sensor measuring stacked plates

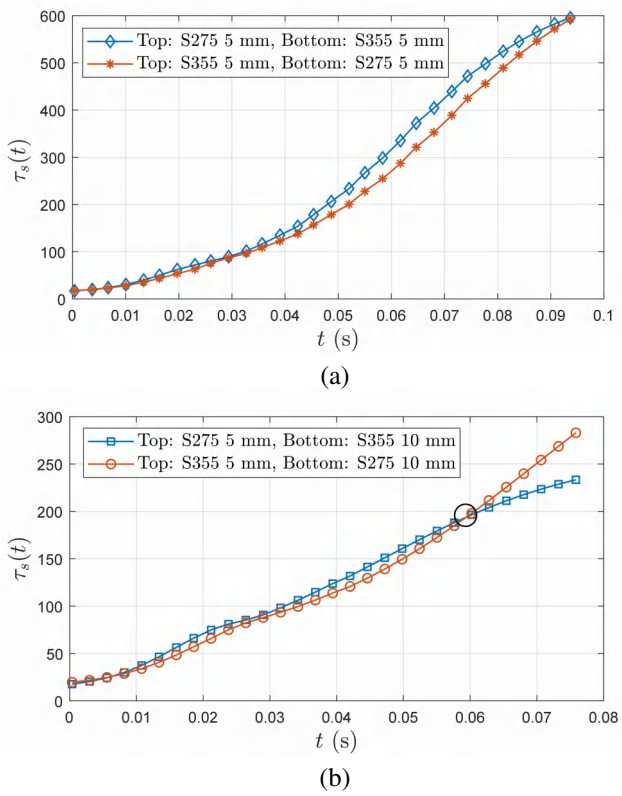

Fig. 15. The $\tau_s(t)$ curves of stacked plates in the thickness of (a) 10 mm and (b) 15 mm

in the top and the bottom layers. For the stacked plate thickness of 15 mm, the rate of eddy-current diffusion is slightly higher in the early phase of testing when S275 plates are on the top layer, and the rate of diffusion is higher in the last phase when S275 plates are at the bottom layer. In addition, there is a curve intersection around 0.06 s. After this moment, the eddy-current is mainly distributed in the bottom layer and its rate of diffusion is influenced by the plate properties of this layer. The phenomenon is generally consistent with the numerical simulation. There is a slight difference in intersection time in Fig. 11 (d) and Fig. 15

(b), *i.e.* 0.043 s and 0.058 s, respectively. This could be caused by the time-constant difference of the transmitting coil in the simulation and experiments, and the influence of measurement noise.

V. Conclusion

This study explores the PEC method for the characterisation of steel plate electromagnetic properties profile along the depth of a thick steel plate. The new analytical model has been derived to provide explicit link between the plate electromagnetic properties and the rate of signal decay and also accelerate the computation process. In the numerical simulation, the proposed analytical model has been evaluated in comparison with the FEM model and they agree well. A custom PEC system with a probe composed of a transmitting coil and a TMR sensor has been implemented to provide the measurements of steel plates in high thickness. Furthermore, the observation that the rate of eddy-current diffusion is inversely correlated to the plate thickness and electromagnetic properties along the depth of the plates is confirmed by the experiments from the receiving signal of the TMR sensor. The intersection point in the time domain receiving signal curve also show consistency between simulation and experiments. Currently, the proposed analytical model to calculate the PEC receiving signal of magnetic field sensors is only suitable for single-layer plate measurement. For other test pieces, the fast computation of the Laplace transform requires further study. The qualitative analysis indicates the relationship between the PEC signal decaying rate and plate properties, while the quantitative estimation of plate properties along the plate depth remains to be investigated. In addition, the calibration procedure of the customized PEC system will be developed to obtain the measurement signals with high accuracy.

Appendix A

The method to approximate multiple roots of equations $\tan(x) + \lambda x = 0$ and $\cot(x) - \lambda x = 0$, $x \in (0, \infty)$ is illustrated as follows. The roots of these transcendental equations can be observed in Fig. 16. Because $\tan(x - \pi/2) = -\cot(x)$, the roots of equation $\cot(x) = \lambda x$ can be obtained by solving $\tan(x - \pi/2) + \lambda x = 0$.

The problem is converted to solve equation $\tan(x - n\pi/2) + \lambda x = 0, n = 1, 2, ..., m$. The odd and even numbers of n correspond to the roots of the Cotangent and Tangent equation, respectively. Replacing x by $x = x' + n\pi/2$, $x' \in (-\pi/2, \pi/2)$, the equation to be solved becomes

$$\tan x' + \lambda(x' + \frac{n\pi}{2}) = 0 \tag{26}$$

According to the Taylor series of the Tangent function, it has

$$\begin{aligned} \tan x &= \sum_{n=1}^{\infty} \frac{(2^{2n} - 1)\, 2^{2n} B_n}{(2n)!} x'^{2n-1} \\ &= x' + \frac{x'^3}{3} + \frac{2}{15} x'^5 + \cdots \end{aligned} \tag{27}$$

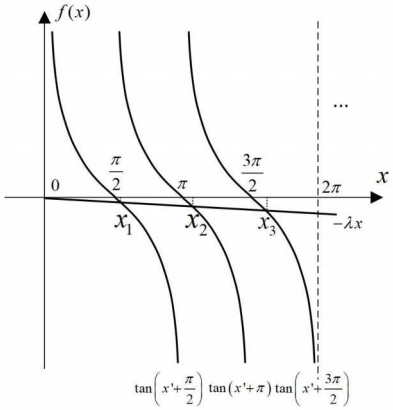

Fig. 16. Roots of transcendental equations

where B_n indicates the Bernoulli numbers.

Approximating the Tangent function by the first and the second terms of the Taylor series and bringing them back to equation (26), it has

$$x' + \frac{x'^3}{3} + \lambda(x' + \frac{n\pi}{2}) = 0 \tag{28}$$

The real root of this cubic equation is

$$x' = -2\sqrt{\frac{p}{3}} \sinh\left[\operatorname{arcsinh}\left(\frac{3q}{2p}\sqrt{\frac{3}{p}}\right)\right] \tag{29}$$

where $p = 3(\lambda + 1)$, $q = 3(\lambda n\pi/2)$.

Substituting x' by x, one can obtain the roots of $\tan(x) + \lambda x = 0$ and $\cot(x) - \lambda x = 0$ by

$$\begin{aligned} x_t &\approx -2\sqrt{\frac{p}{3}} \sinh\left[\operatorname{arcsinh}\left(\frac{3q_t}{2p}\sqrt{\frac{3}{p}}\right)\right] + n\pi \\ x_c &\approx -2\sqrt{\frac{p}{3}} \sinh\left[\operatorname{arcsinh}\left(\frac{3q_c}{2p}\sqrt{\frac{3}{p}}\right)\right] + n\pi - \frac{\pi}{2} \end{aligned}$$

where $q_t = 3\lambda n\pi$, $q_c = 3\lambda(n\pi - \pi/2)$ and $n = 1, ..., m$.

Acknowledgment

The authors would like to thank the financial supports from The Royal Society IEC\NSFC\211165, China Scholarship Council (CSC), 2022 IEEE Instrumentation and Measurement Graduate Fellowship Award and the Research Fund for Coal and Steel of the European Union under the grant agreement No.847296, which is gratefully acknowledged.

References

[1] W. Zhu, H. Yang, A. Luinenburg, F. Van Den Berg, S. Dickinson, W. Yin, and A. Peyton, "Development and deployment of online multifrequency electromagnetic system to monitor steel hot transformation on runout table of hot strip mill," *Ironmaking & Steelmaking*, vol. 41, no. 9, pp. 685–693, 2014.

[2] X. Hao, W. Yin, M. Strangwood, A. Peyton, P. Morris, and C. Davis, "Characterization of decarburization of steels using a multifrequency electromagnetic sensor:

experiment and modeling," *Metallurgical and Materials Transactions A*, vol. 40, pp. 745–756, 2009.

[3] S. J. Dickinson, R. Binns, W. Yin, C. Davis, and A. J. Peyton, "The development of a multifrequency electromagnetic instrument for monitoring the phase transformation of hot strip steel," *IEEE Transactions on Instrumentation and Measurement*, vol. 56, no. 3, pp. 879–886, 2007.

[4] M. Neumann, O. Stenzel, F. Willot, L. Holzer, and V. Schmidt, "Quantifying the influence of microstructure on effective conductivity and permeability: virtual materials testing," *International journal of solids and structures*, vol. 184, pp. 211–220, 2020.

[5] O. Stenzel, O. Pecho, L. Holzer, M. Neumann, and V. Schmidt, "Big data for microstructure-property relationships: A case study of predicting effective conductivities," *AIChE Journal*, vol. 63, no. 9, pp. 4224–4232, 2017.

[6] W. Yin, A. Peyton, M. Strangwood, and C. Davis, "Exploring the relationship between ferrite fraction and morphology and the electromagnetic properties of steel," *Journal of materials science*, vol. 42, pp. 6854–6861, 2007.

[7] Z. Cui, Q. Zhang, K. Gao, Z. Xia, and H. Wang, "Electrical impedance sensors for multi-phase flow measurement: A review," *IEEE Sensors Journal*, vol. 21, no. 24, pp. 27 252–27 267, 2021.

[8] V. Moorthy, S. Vaidyanathan, T. Jayakumar, and B. Raj, "Microstructural characterization of quenched and tempered 0.2% carbon steel using magnetic barkhausen noise analysis," *Journal of magnetism and magnetic materials*, vol. 171, no. 1-2, pp. 179–189, 1997.

[9] O. Saquet, J. Chicois, and A. Vincent, "Barkhausen noise from plain carbon steels: analysis of the influence of microstructure," *Materials Science and Engineering: A*, vol. 269, no. 1-2, pp. 73–82, 1999.

[10] C. H. Gür and I. Cam, "Comparison of magnetic barkhausen noise and ultrasonic velocity measurements for microstructure evaluation of sae 1040 and sae 4140 steels," *Materials Characterization*, vol. 58, no. 5, pp. 447–454, 2007.

[11] A. Sophian, G. Y. Tian, D. Taylor, and J. Rudlin, "A feature extraction technique based on principal component analysis for pulsed eddy current ndt," *NDT & e International*, vol. 36, no. 1, pp. 37–41, 2003.

[12] D. Vasic, V. Bilas, and D. Ambrus, "Pulsed eddy-current nondestructive testing of ferromagnetic tubes," *IEEE transactions on instrumentation and measurement*, vol. 53, no. 4, pp. 1289–1294, 2004.

[13] X. Chen and X. Liu, "Pulsed eddy current-based method for electromagnetic parameters of ferromagnetic materials," *IEEE Sensors Journal*, vol. 21, no. 5, pp. 6376–6383, 2020.

[14] V. Arjun, B. Sasi, B. P. C. Rao, C. Mukhopadhyay, and T. Jayakumar, "Optimisation of pulsed eddy current probe for detection of sub-surface defects in stainless steel plates," *Sensors and Actuators A: Physical*, vol. 226, pp. 69–75, 2015.

[15] J. Sha, M. Fan, B. Cao, and B. Liu, "Noncontact and nondestructive evaluation of heat-treated bearing rings using pulsed eddy current testing," *Journal of Magnetism and Magnetic Materials*, vol. 521, p. 167516, 2021.

[16] K. S. S. Rao, B. P. C. Rao, and S. Thirunavukkarasu, "Development of pulsed eddy current instrument and probe for detection of sub-surface flaws in thick materials," *IETE Technical Review*, vol. 34, no. 5, pp. 572–578, 2017.

[17] X. Chen and Y. Lei, "Electrical conductivity measurement of ferromagnetic metallic materials using pulsed eddy current method," *Ndt & E International*, vol. 75, pp. 33–38, 2015.

[18] F. Fu and J. Bowler, "Transient eddy-current driver pickup probe response due to a conductive plate," *IEEE Transactions on magnetics*, vol. 42, no. 8, pp. 2029–2037, 2006.

[19] T. Theodoulidis, "Developments in calculating the transient eddy-current response from a conductive plate," *IEEE Transactions on magnetics*, vol. 44, no. 7, pp. 1894–1896, 2008.

[20] D. Desjardins, T. Krause, and L. Clapham, "Transient response of a driver-pickup coil probe in transient eddy current testing," *NDT & E International*, vol. 75, pp. 8–14, 2015.

[21] D. Desjardins, T. Krause, and L. Clapham, "Transient eddy current method for the characterization of magnetic permeability and conductivity," *NDT & E International*, vol. 80, pp. 65–70, 2016.

[22] Y. Li, T. Theodoulidis, and G. Y. Tian, "Magnetic field-based eddy-current modeling for multilayered specimens," *IEEE Transactions on magnetics*, vol. 43, no. 11, pp. 4010–4015, 2007.

[23] J. Jackson, "Magnetostatics, faraday's law, quasi-static fields," *Classical Electrodynamics*, vol. 3, pp. 219–223, 1999.

[24] H. Wilhelm, "Initial-boundary-value problem for diffusion of magnetic fields into conductors with external electromagnetic transients," *Journal of Mathematical Physics*, vol. 23, no. 10, pp. 1765–1768, 1982.

[25] H. C. Ohanian, "On the approach to electro-and magneto-static equilibrium," *American Journal of Physics*, vol. 51, no. 11, pp. 1020–1022, 1983.

[26] G. Y. Tian, Y. Li, and C. Mandache, "Study of lift-off invariance for pulsed eddy-current signals," *IEEE transactions on magnetics*, vol. 45, no. 1, pp. 184–191, 2009.

[27] Y. Li, G. Y. Tian, and A. Simm, "Fast analytical modelling for pulsed eddy current evaluation," *NDT & E International*, vol. 41, no. 6, pp. 477–483, 2008.

11. Conclusions and future works

11.1 Conclusions

The forward and inverse problems of eddy current testing models are studied using the analytical method which is applied to the measurement of metallic plates, pipes and spheres.

The approximate functional relationships between the coil inductance and object properties are derived through the simplification of the shape function and phase function of the analytical models. The simplification is accurate only if the approximation conditions can be held. All human-invented methods have limited applicable scopes.

To solve the inverse problem of object property estimation. The primary issue is to determine the appropriate variable combinations, which influence the ill-conditioning degree. This can be analyzed by sensitivity analysis. The initial guess is also significant as it affects the convergence points that can be reached, which can be selected according to the approximate functional relationships.

The eddy-current diffusion process of multi-frequency testing and pulsed testing is related in the frequency and time domain, both of which are determined by the phase function (reflection coefficient) of the measured objects.

11.2 Future works

The inverse problem of defect scanning, accurately estimating the dimensions of defects could be studied.

The FEM model for forward problem calculation would be investigated for the thin-skin regime and combined with the analytical model for complex geometry calculation.

The estimation of the electromagnetic property profile along the depth of object thickness would be investigated for pulsed EC testing.

References

[1] J. Garcia-Martin, J. Gomez-Gil, and E. Vazquez-Sanchez, "Non-Destructive Techniques Based on Eddy Current Testing," *SENSORS,* vol. 11, no. 3, pp. 2525-2565, MAR 2011, doi: 10.3390/s110302525.

[2] D. Rifai, A. N. Abdalla, K. Ali, and R. Razali, "Giant Magnetoresistance Sensors: A Review on Structures and Non-Destructive Eddy Current Testing Applications," *Sensors,* vol. 16, no. 3, p. 298, 2016. [Online]. Available: https://www.mdpi.com/1424-8220/16/3/298.

[3] C. J. Hellier, *Handbook of nondestructive evaluation*. McGraw-Hill Education, 2013.

[4] L. Pedersen, K.-Å. Magnusson, and Y. Zhengsheng, "Eddy current testing of thin layers using co-planar coils," *Journal of Research in Nondestructive Evaluation,* vol. 12, no. 1, pp. 53-64, 2000.

[5] A. Sethuraman and J. H. Rose, "Rapid inversion of eddy current data for conductivity and thickness of metal coatings," *Journal of nondestructive evaluation,* vol. 14, no. 1, pp. 39-46, 1995.

[6] D. Mercier, J. Lesage, X. Decoopman, and D. Chicot, "Eddy currents and hardness testing for evaluation of steel decarburizing," *Ndt & E International,* vol. 39, no. 8, pp. 652-660, 2006.

[7] G. Y. Dymkin, A. V. Kurkov, Y. G. Smorodinskii, and A. V. Shevelev, "On the Sensitivity of Eddy Current Testing of Parts of Railway Rolling Stock," *Russian Journal of Nondestructive Testing,* vol. 55, no. 8, pp. 610-616, Aug 2019, doi: 10.1134/s1061830919080059.

[8] J. Rajamaki, M. Vippola, A. Nurmikolu, and T. Viitala, "Limitations of eddy current inspection in railway rail evaluation," *Proceedings of the Institution of Mechanical Engineers Part F-Journal of Rail and Rapid Transit,* vol. 232, no. 1, pp. 121-129, Jan 2018, doi: 10.1177/0954409716657848.

[9] L. Cheng and G. Y. Tian, "Surface Crack Detection for Carbon Fiber Reinforced Plastic (CFRP) Materials Using Pulsed Eddy Current

Thermography," *Ieee Sensors Journal,* vol. 11, no. 12, pp. 3261-3268, Dec 2011, doi: 10.1109/jsen.2011.2157492.

[10] F. Ciampa, P. Mahmoodi, F. Pinto, and M. Meo, "Recent Advances in Active Infrared Thermography for Non-Destructive Testing of Aerospace Components," *Sensors,* vol. 18, no. 2, Feb 2018, Art no. 609, doi: 10.3390/s18020609.

[11] X. Ma, A. J. Peyton, S. R. Higson, A. Lyons, and S. J. Dickinson, "Hardware and software design for an electromagnetic induction tomography (EMT) system for high contrast metal process applications," *Measurement Science and Technology,* vol. 17, no. 1, pp. 111-118, Jan 2006, doi: 10.1088/0957-0233/17/1/018.

[12] Z. Q. Liu, B. K. Li, and M. F. Jiang, "Transient Asymmetric Flow and Bubble Transport Inside a Slab Continuous-Casting Mold," *Metallurgical and Materials Transactions B-Process Metallurgy and Materials Processing Science,* vol. 45, no. 2, pp. 675-697, Apr 2014, doi: 10.1007/s11663-013-9972-z.

[13] Y. T. Yu, Y. Yan, F. Wang, G. Y. Tian, and D. J. Zhang, "An approach to reduce lift-off noise in pulsed eddy current nondestructive technology," *Ndt & E International,* vol. 63, pp. 1-6, Apr 2014, doi: 10.1016/j.ndteint.2013.12.012.

[14] K. Bin Ali, A. N. Abdalla, D. Rifai, and M. A. Faraj, "Review on system development in eddy current testing and technique for defect classification and characterization," *Iet Circuits Devices & Systems,* vol. 11, no. 4, pp. 338-351, Jul 2017, doi: 10.1049/iet-cds.2016.0327.

[15] W. L. Yin *et al.*, "Custom edge-element FEM solver and its application to eddy-current simulation of realistic 2M-element human brain phantom," *Bioelectromagnetics,* vol. 39, no. 8, pp. 604-616, Dec 2018, doi: 10.1002/bem.22148.

[16] M. Wang, *Industrial tomography: systems and applications*. Elsevier, 2015.

[17] Y. Le Bihan, "3-D finite-element analysis of eddy-current evaluation of curved plates," *IEEE transactions on magnetics,* vol. 38, no. 2, pp. 1161-1164, 2002.

[18] H. Huang, T. Takagi, and T. Uchimoto, "Crack shape reconstruction in ferromagnetic materials using a novel fast numerical simulation method," *IEEE transactions on magnetics,* vol. 40, no. 2, pp. 1374-1377, 2004.

[19] B. Gupta, B. Ducharne, G. Sebald, and T. Uchimoto, "A space discretized ferromagnetic model for non-destructive eddy current evaluation," *IEEE Transactions on Magnetics,* vol. 54, no. 3, pp. 1-4, 2018.

[20] Z. Chen, M. Rebican, N. Yusa, and K. Miya, "Fast simulation of ECT signal due to a conductive crack of arbitrary width," *IEEE Transactions on Magnetics,* vol. 42, no. 4, pp. 683-686, 2006.

[21] M. Zolgharni, P. Ledger, and H. Griffiths, "Forward modelling of magnetic induction tomography: a sensitivity study for detecting haemorrhagic cerebral stroke," *Medical & biological engineering & computing,* vol. 47, no. 12, pp. 1301-1313, 2009.

[22] K. Zhao, M. N. Vouvakis, and J.-F. Lee, "Solving electromagnetic problems using a novel symmetric FEM-BEM approach," *IEEE Transactions on magnetics,* vol. 42, no. 4, pp. 583-586, 2006.

[23] Y. Du, S. Xie, X. Li, Z. Chen, T. Uchimoto, and T. Takagi, "A fast forward simulation scheme for eddy current testing of crack in a structure of carbon fiber reinforced polymer laminate," *IEEE access,* vol. 7, pp. 152278-152288, 2019.

[24] M. Morozov, G. Rubinacci, A. Tamburrino, and S. Ventre, "Numerical models of volumetric insulating cracks in eddy-current testing with experimental validation," *IEEE transactions on magnetics,* vol. 42, no. 5, pp. 1568-1576, 2006.

[25] M. Lu, A. Peyton, and W. Yin, "Acceleration of frequency sweeping in eddy-current computation," *IEEE Transactions on Magnetics,* vol. 53, no. 7, pp. 1-8, 2017.

[26] R. Huang, M. Lu, A. Peyton, and W. Yin, "A novel perturbed matrix inversion based method for the acceleration of finite element analysis in crack-scanning eddy current NDT," *IEEE Access,* vol. 8, pp. 12438-12444, 2020.

[27] R. Huang *et al.*, "A novel acceleration method for crack computation using finite element analysis in eddy current testing," *IEEE Transactions on Instrumentation and Measurement,* pp. 1-1, 2022, doi: 10.1109/TIM.2022.3186073.

[28] M. Brideson, "Electromagnetic induction tomography : a feasibility study," *Queensland University of Technology,* 2000.

[29] J. E. Cruz Serrallés, "Global Maxwell Tomography: inverse scattering via magnetic resonance and volume integral equations," Massachusetts Institute of Technology, 2016.

[30] J. Bowler, S. Jenkins, L. Sabbagh, and H. Sabbagh, "Eddy-current probe impedance due to a volumetric flaw," *Journal of Applied Physics,* vol. 70, no. 3, pp. 1107-1114, 1991.

[31] A. Skarlatos, G. Pichenot, D. Lesselier, M. Lambert, and B. Duchene, "Electromagnetic modeling of a damaged ferromagnetic metal tube by a volume integral equation formulation," *IEEE transactions on magnetics,* vol. 44, no. 5, pp. 623-632, 2008.

[32] J. R. Bowler, T. P. Theodoulidis, and N. Poulakis, "Eddy current probe signals due to a crack at a right-angled corner," *IEEE transactions on magnetics,* vol. 48, no. 12, pp. 4735-4746, 2012.

[33] Z. Jin *et al.*, "Boundary-element analysis of magnetic polarization tensor for metallic cylinder," *IEEE Access,* vol. 9, pp. 63250-63256, 2021.

[34] M. Pham and A. Peyton, "A model for the forward problem in magnetic induction tomography using boundary integral equations," *IEEE Transactions on Magnetics,* vol. 44, no. 10, pp. 2262-2267, 2008.

[35] C. Dodd and W. Deeds, "Analytical solutions to eddy-current probe-coil problems," *Journal of applied physics,* vol. 39, no. 6, pp. 2829-2838, 1968.

[36] C. V. Dodd, J. Luquire, W. Deeds, and W. Spoeri, "SOME EDDY-CURRENT PROBLEMS AND THEIR INTEGRAL SOLUTIONS," Oak Ridge National Lab., Tenn., 1969.

[37] J. Luquire, W. Deeds, and C. Dodd, "Axially symmetric eddy currents in a spherical conductor," *Journal of Applied Physics,* vol. 41, no. 10, pp. 3976-3982, 1970.

[38] S. Fortin, Y. Yang, J. Ma, and F. P. Dawalibi, "Electromagnetic fields of energized conductors in multilayer soils," in *Asia-Pacific Conference on Environmental Electromagnetics*, Dalian, PEOPLES R CHINA, Aug 01-04 2006, 2006, pp. 893-+, doi: 10.1109/ceem.2006.258096. [Online]. Available: <Go to ISI>://WOS:000241457100201

[39] A. Seliem, "Evaluation of the transient electromagnetic field in evaporation duct," *Applied Mathematics and Computation,* vol. 151, no. 2, pp. 411-421, Apr 2004, doi: 10.1016/s0096-3003(03)00351-5.

[40] J. O. Fava and M. C. Ruch, "Calculation and simulation of impedance diagrams of planar rectangular spiral coils for eddy current testing," *Ndt & E International,* vol. 39, no. 5, pp. 414-424, Jul 2006, doi: 10.1016/j.ndteint.2005.12.002.

[41] X. F. Mao and Y. Z. Lei, "Analytical solutions to eddy current field excited by a probe coil near a conductive pipe," *Ndt & E International,* vol. 54, pp. 69-74, Mar 2013, doi: 10.1016/j.ndteint.2012.11.010.

[42] T. P. Theodoulidis and J. R. Bowler, "The Truncated Region Eigenfunction Expansion Method for the Solution of Boundary Value Problems in Eddy Current Nondestructive Evaluation," *AIP Conference Proceedings,* vol. 760, no. 1, pp. 403-408, 2005/04/09 2005, doi: 10.1063/1.1916704.

[43] Y. Li, T. Theodoulidis, and G. Y. Tian, "Magnetic Field-Based Eddy-Current Modeling for Multilayered Specimens," *IEEE Transactions on Magnetics,* vol. 43, no. 11, pp. 4010-4015, 2007, doi: 10.1109/TMAG.2007.904930.

[44] W. Yin, A. J. Peyton, and S. J. Dickinson, "Simultaneous measurement of distance and thickness of a thin metal plate with an electromagnetic sensor using a simplified model," *IEEE Transactions on Instrumentation and Measurement,* vol. 53, no. 4, pp. 1335-1338, 2004.

[45] R. Huang *et al.*, "Measurement of the radius of metallic plates based on a

novel finite region eigenfunction expansion (FREE) method," *IEEE Sensors Journal,* vol. 20, no. 24, pp. 15099-15106, 2020.

[46] R. Huang, M. Lu, X. He, A. Peyton, and W. Yin, "Measuring coaxial hole size of finite-size metallic disk based on a dual-constraint integration feature using multifrequency eddy current testing," *IEEE Transactions on Instrumentation and Measurement,* vol. 70, pp. 1-7, 2020.

[47] R. Huang, M. Lu, A. Peyton, and W. Yin, "Thickness measurement of metallic plates with finite planar dimension using eddy current method," *IEEE Transactions on Instrumentation and Measurement,* vol. 69, no. 10, pp. 8424-8431, 2020.

[48] W. Yin, S. J. Dickinson, and A. J. Peyton, "Evaluating the permeability distribution of a layered conductor by inductance spectroscopy," *IEEE transactions on magnetics,* vol. 42, no. 11, pp. 3645-3651, 2006.

[49] G. Hu, R. Huang, Y. Shao, and W. Yin, "Thickness measurement for spherical balls based on a frequency difference feature," *Insight-Non-Destructive Testing and Condition Monitoring,* vol. 64, no. 2, pp. 84-90, 2022.

[50] M. Lu, X. Meng, R. Huang, A. Peyton, and W. Yin, "Analysis of tilt effect on notch depth profiling using thin-skin regime of driver-pickup eddy-current sensor," *Sensors,* vol. 21, no. 16, p. 5536, 2021.

[51] M. Lu, X. Meng, R. Huang, L. Chen, A. Peyton, and W. Yin, "A high-frequency phase feature for the measurement of magnetic permeability using eddy current sensor," *NDT & E International,* vol. 123, p. 102519, 2021.

[52] T. Theodoulidis and A. Skarlatos, "Eddy current interaction of an arbitrarily positioned probe coil with a conductive cylinder," *IEEE transactions on magnetics,* vol. 48, no. 8, pp. 2392-2394, 2012.

[53] M. Shamgholi and S. H. H. Sadeghi, "Simultaneous Measurement of Radius and Coating Thickness of Finite Length Metal Rods by Eddy Current Surface Probes," *IEEE Transactions on Instrumentation and Measurement,* pp. 1-1, 2022, doi: 10.1109/TIM.2022.3187738.

[54] G. Hu, R. Huang, M. Lu, L. Zhou, and W. Yin, "Measurement of radius of a

metallic ball using eddy current testing based on peak frequency difference feature," *Measurement,* vol. 184, p. 109876, 2021.

[55] M. Lu, X. Meng, R. Huang, L. Chen, A. Peyton, and W. Yin, "Measuring lift-off distance and electromagnetic property of metal using dual-frequency linearity feature," *IEEE Transactions on Instrumentation and Measurement,* vol. 70, pp. 1-9, 2020.

[56] M. Lu, X. Meng, L. Chen, R. Huang, W. Yin, and A. Peyton, "Measurement of ferromagnetic slabs permeability based on a novel planar triple-coil sensor," *IEEE Sensors Journal,* vol. 20, no. 6, pp. 2904-2910, 2019.

[57] W. L. Yin, S. J. Dickinson, and A. J. Peyton, "Imaging the continuous conductivity profile within layered metal structures using inductance spectroscopy," *Ieee Sensors Journal,* vol. 5, no. 2, pp. 161-166, Apr 2005, doi: 10.1109/jsen.2004.842637.

[58] J. Xu, J. Wu, W. Xin, and Z. L. Ge, "Measuring Ultrathin Metallic Coating Properties Using Swept-Frequency Eddy-Current Technique," *Ieee Transactions on Instrumentation and Measurement,* vol. 69, no. 8, pp. 5772-5781, Aug. 2020, doi: 10.1109/tim.2020.2966359.

[59] H. Tesfalem, A. J. Peyton, A. D. Fletcher, M. Brown, and B. Chapman, "Conductivity Profiling of Graphite Moderator Bricks From Multifrequency Eddy Current Measurements," *Ieee Sensors Journal,* vol. 20, no. 9, pp. 4840-4849, May 2020, doi: 10.1109/jsen.2020.2965201.

[60] M. Y. Lu, Y. D. Xie, W. Q. Zhu, A. Peyton, and W. L. Yin, "Determination of the Magnetic Permeability, Electrical Conductivity, and Thickness of Ferrite Metallic Plates Using a Multifrequency Electromagnetic Sensing System," *Ieee Transactions on Industrial Informatics,* vol. 15, no. 7, pp. 4111-4119, Jul 2019, doi: 10.1109/tii.2018.2885406.

[61] X. L. Chen, J. W. Li, and Z. H. Wang, "Inversion Method in Pulsed Eddy Current Testing for Wall Thickness of Ferromagnetic Pipes," *Ieee Transactions on Instrumentation and Measurement,* vol. 69, no. 12, pp. 9766-9773, Dec 2020, doi: 10.1109/tim.2020.3005114.

[62] K. H. Lee, H. J. Kim, and Y. Song, "Electromagnetic method for analyzing the property of steel casing," *Office of Scientific & Technical Information Technical Reports,* 1998.

[63] I. D. Adewale and G. Y. Tian, "Decoupling the Influence of Permeability and Conductivity in Pulsed Eddy-Current Measurements," *IEEE Transactions on Magnetics,* 2013.

[64] T. P. Theodoulidis and E. E. Kriezis, "Coil impedance due to a sphere of arbitrary radial conductivity and permeability profiles," *IEEE Transactions on Magnetics,* vol. 38, no. 3, pp. 1452-1460, 2002.

Table 1: Gantt chart of project plane

Plan \ Monthly	Jul	Aug	Sep	Oct	Nov	Dec	Jan	Feb	Mar	Apr	May	Jun
1. Crack detection of planar structures by solving the inverse problem												
1.1 Acquire the measurements of surface cracks with multi-channel sensors												
1.2 Evaluate the proposed method of crack dimension inversion												
1.3 Writing a manuscript summarising the research outcomes												
2. Development of the FEM solver for thin-structure testing												
2.1 Study of FEM using Galerkin A-V equations of EC testing												
2.2 Improve the high-order FEM and complete the programming												
2.3 Evaluate the solver comparing with commercial softwares												
3. Automatic surface defect scanning with robotic arm												
3.1 Theoretical study controlling the EC probe lift-off and tilt angle												
3.2 EC probe design and manufactory												
3.3 Programming and evaluation of the proposed method												
Research summary												